Structural defects in CdTe

Ken Durose

STRUCTURAL DEFECTS IN CdTe

by

Ken Durose

This thesis is presented in candidature
for the degree of
Doctor of Philosophy

in the

University of Durham

December 1986

This thesis is dedicated to

Mr Trevor Harcourt

ABSTRACT

This thesis is primarily concerned with the characterisation of the native defects present in CdTe crystals grown from the vapour phase using two different methods. The principal characterisation techniques used were TEM, SEM and etching/optical microscopy. Crystal defects in bulk CdTe are of great importance since this material is in demand as a substrate for the epitaxial growth of $Cd_xHg_{1-x}Te$ for use in large area infra-red imaging devices.

Large single crystals grown using the 'Durham' technique invariably contain first order twin boundaries lying on {111} planes and these are of the 'ortho'-type. Twin boundaries on other planes were characterised using the coincidence site lattice models of twin boundaries in sphalerite which were developed during this work. First order lateral twin boundaries lying on {511}-{111}, {112}-{112}, {001}-{221} and {110}-{114} and second order twin boundaries lying on {111}-{115} {114}-{114} and {221}-{221} are discussed. Twinning in CdTe is thought to be due to post-growth stress rather than to a growth phenomenon. The dislocations which are present in crystals grown by the 'Durham' method are predominantly concentrated into well-formed arrays which are sometimes associated with other crystal defects. These arrays were shown by EBIC studies to be electrically active and the average sub-grain dimension was found to be $\sim$ 150 μm. It is thought that the arrays form as a result of dislocation polygonisation during the latter stages of growth. Precipitates, which were identified as being comprised of Te, are found in the bulk of the crystals although they are more often seen on twin boundaries. The relationship between boundary type and the density of precipitates is discussed.

Sub-grain boundaries and precipitates were also examined in a small number of CdTe crystals which had been grown by a modified 'Piper-Polich' technique. The differences between the defects in this material and those in CdTe crystals grown by the 'Durham' method are fully explained in terms of the differences in the crystal growth conditions employed in the two techniques. Networks of dislocations in $Cd_{0.95}Zn_{0.05}Te$ crystals grown by the 'Durham' technique were also investigated.

A mechanochemical polishing machine which was developed during the course of this work and which is capable of producing high quality chemically polished surfaces is described. Also the use of chemical etchants to determine the crystallographic polarity of {111} oriented surfaces is clarified.

Important features of this work include; the development of coincidence site lattice models of first order lateral and second order twin boundaries in the sphalerite structure and the thorough characterisation of these boundaries in as-grown CdTe crystals, and the comparison of the sub-grain boundaries and precipitates present in material grown from the vapour phase by two different techniques.

ACKNOWLEDGEMENTS

It gives me great pleasure to acknowledge those people who contributed to the unique atmosphere of the Department of Applied Physics and Electronics which I enjoyed while preparing this thesis.

First and foremost I offer my sincere thanks to my supervisor Dr Graham Russell. He knows why. To my co-supervisor and Head of Department, Dr J Woods I owe an apology : early on during my studies Dr Woods looked at one of my micrographs and said "Yes, but how can we get rid of these defects?" I have to admit that I'm still not entirely sure of the answer, although this thesis does offer some suggestions.

I am deeply grateful to Norman Thompson who grew all the crystals examined during this work and to Trevor Harcourt who cut and polished them.

The Applied Physics workshop, while providing a first-class service, was just as valuable as a bolt-hole to sanity. Special thanks to Brian Blackburn, Frank Spence and Roger Little. Sue Little typed the manuscript magnificently, and Janet Hails helped with the proof reading.

Finally I wish Paul Brown well in his PhD work on the structure of epitaxial systems at Durham.

STRUCTURAL DEFECTS IN CdTe

CONTENTS

Page

CHAPTER ONE

INTRODUCTION

CdTe has a number of important applications, including solar cells [1,2,3], infra-red windows [1,3,4], electrooptic modulators [1,6,7] and nuclear radiation detectors [1,8,9]. Relatively recently CdTe has also been used extensively as a substrate material for the epitaxial deposition of $Cd_xHg_{1-x}Te$ [10,11]. This ternary compound is an important infra-red detector material for use in the 8-12 μm range when $x \simeq 0.2$ [12]. However, problems encountered in the preparation of bulk crystals of this material for use in large area infra-red imaging devices have led to the development of an extensive epitaxial technology: $Cd_xHg_{1-x}Te$ epilayers have been grown by liquid phase epitaxy (LPE) [13], molecular beam epitaxy (MBE) [14] and metal-organic vapour phase epitaxy (MOVPE) [15-19] on a variety of substrates. CdTe is a leading candidate for use as a substrate material for the growth of epitaxial CdTe for the following reasons:-

i) The lattice mismatch of CdTe to $Cd_{0.2}Hg_{0.8}Te$ is 2.5×10^{-3} at room temperature, which is favourable for good epitaxy.

ii) The thermal expansion coefficients of the two materials are compatible.

iii) CdTe contains no foreign species which could diffuse into and hence contaminate $Cd_xHg_{1-x}Te$ epilayers.

However, the presence of crystal defects in CdTe substrates is detrimental to good epitaxy since such defects are known to propagate into the epilayers from the substrates upon which they were grown. Any electrical activity or compositional inhomogeneity which

is caused by the presence of these defects in $Cd_xHg_{1-x}Te$ epilayers will have a deleterious effect upon the performance of imaging devices fabricated on such layers.

Comparatively recently some interest has also been shown in $Cd_yHg_{1-y}Te$ ($y \simeq 0.95$) as an alternative substrate to CdTe [20] since the composition of this material can be adjusted to give an exact lattice match to $Cd_{0.2}Hg_{0.8}Te$ for epitaxy [21]. Furthermore, $Cd_{0.95}Zn_{0.05}Te$ substrates have been reported as having a more favourable dislocation content than bulk CdTe [20,22].

The techniques for growing large CdTe crystals which are most frequently referred to in the literature are melt-growth methods involving growth from either a congruent melt, or from a solution of CdTe in one or the other of the elements [23]. However, in this laboratory considerable expertise has been developed in the growth of a wide range of II-VI crystals from the vapour phase [24]. Crystal growth by the so-called 'Durham' technique proceeds in the specially designed sealed silica growth capsules which are described in §2.2.2. In excess of 80 boules of CdTe weighing up to 160g each and being up to 29 mm in diameter have been grown using this technique, and these crystals have provided a source of substrate material for an extensive programme of growing $Cd_xHg_{1-x}Te$ epilayers by MOVPE in this laboratory. A smaller number of bulk $Cd_{0.95}Zn_{0.05}Te$ crystals have also been grown by the 'Durham' technique. In addition, the growth of large CdTe crystals was also attempted using a second vapour phase method which is a modification of that developed by Piper and Polich (see §2.2.3) [24].

This project is concerned with the characterisation of the grown-in structural defects in these crystals. Owing to the success of

the 'Durham' technique of growing CdTe crystals having large grain size most of the characterisation work described in this thesis was performed on this material. Nevertheless, significant characterisation studies have been carried out on CdTe grown by the modified Piper-Polich technique and on the $Cd_{0.95}Zn_{0.05}Te$ crystals grown by the 'Durham' method.

The techniques of characterisation used during this work include transmission electron microscopy (TEM), scanning electron microscopy (SEM) and the electron beam induced current mode of the SEM (SEM/EBIC), energy dispersive analysis of X-rays (EDAX) and reflection high energy electron diffraction (RHEED). These are all described in Chapter 2. Chemical etching in conjunction with optical microscopy has been used extensively in this work to characterise a variety of defects and the properties of the etchants used are reviewed in Chapter 5. The use of chemical etchants to determine the crystallographic polarity of CdTe surfaces and the development of a mechanochemical polishing technique which is capable of producing pristine crystal surfaces for epitaxy are also described in that Chapter.

Three types of defects which are encountered in the as-grown crystals have received particular attention in this work and these are:-

i) Twin bands and boundaries (Chapters 6 and 7).

ii) Sub-grain boundaries (dislocation arrays) (Chapter 8).

iii) Precipitates(Chapter 9).

CdTe crystals are inherently prone to twinning [25] and a great variety of twin boundaries and intersecting twin structures have been observed in some of the 60 boules of 'Durham'-grown CdTe which were examined. The crystallography of these twins has been fully

characterised with reference to the geometric models of twin boundaries which were developed during the course of this work (see Chapter 7). Dislocation arrays (sub-grain boundaries) have been observed in CdTe crystals grown by both of the vapour phase techniques and also in the $Cd_{0.95}Zn_{0.05}Te$ crystals grown by the 'Durham' method. The structures of these boundaries have been found to be considerably different in each of the three materials. A comparison between the form and distribution of precipitates in CdTe grown by the modified Piper-Polich and 'Durham' techniques has also been made in Chapter 9.

Throughout this work, efforts have been made not only to characterise the defects present in the crystals studied, but also to establish their origins and to relate the structures and distribution of these defects to the crystal growth conditions. Whenever possible the effect that the defects in the substrate materials examined might have upon the quality of any epitaxial layers grown upon these substrates is discussed.

REFERENCES FOR CHAPTER ONE

1 F.V.Wald, Rev.Phys.Appl., 12 (2) (1977) p.277.

2 M.Rodot, ibid, p.411.

3 K.Zanio in Semiconductors and Semimetals Vol.13 'Cadmium Telluride'. Academic Press, New York, 1978. Eds. R.K.Willardson and A.C.Beer, p.6.

4 R.O.Bell, Rev.Phys.Appl., 12(2) (1977) p.392.

5 K.Zanio, as reference 3, p.191.

6 D.L.Spears and A.J.Strauss, Rev.Phys.Appl., 12(2) (1977) p.401.

7 K.Zanio, as reference 3, p.186.

8 L.T.Jones, Rev.Phys.Appl., 12 (2) (1977) p.380.

9 K.Zanio, as reference 3, p.164.

10 W.F.H.Micklethwaite in Semiconductors and Semimetals, Vol.18, 'Cadmium Mercury Telluride'. Academic Press, New York, 1981. Eds. R.K.Willardson and A.C.Beer, Ch.3.

11 K.Zanio, as reference 3, p.209.

12 P.W.Kruse in Semiconductors and Semimetals, Vol.18. 'Cadmium Mercury Telluride'. Academic Press, New York, 1981. Eds. R.K.Willardson and A.C.Beer, Ch.1. p.1.

13 M. Astles, G.Blackmore, N.Gordon and D.R.Wight, J.Crystal Growth, 72 (1985) p.61.

14 J.P.Faurie, M.Boukersche, J.Reno, S.Sivanathan and C.Hsu, J.Vacuum Sci.Technol., A3 (1985) p.55.

15 J.B.Mullin, S.J.C.Irvine and D.J.Ashen, J.Crystal Growth, 55 (1981) p.92.

16 J.B.Mullin, S.J.C.Irvine and J.Tunnicliffe, J.Crystal Growth, 68 (1984) p.214.

17 J.Geiss, J.S.Gough, S.J.C.Irvine, G.W.Blackmore, J.B.Mullin and A.Royle, J.Crystal Growth, 72 (1985) p.120.

18 J.E.Hails, G.J.Russell, A.W.Brinkman and J.Woods, In press in J.Crystal Growth.

19 J.E.Hails, G.J.Russell, A.W.Brinkman and J.Woods, In press in J.Appl.Phys.

20 S.L.Bell and S.Sen, J.Vac.Sci.Technol., A3 (1) (1985) p.112.

21 H.Booyens and J.H.Basson, Phys.Stat.Sol., (a) 85 (1984) p.449.

22 J.C.Tranchart, B.Latorre, C.Foucher and Y. Le Gouge, J.Crystal Growth, 72 (1985) p.468.

23 K.Zanio, as reference 3, p.11.

24 G.J.Russell, N.F.Thompson and J.Woods, J.Crystal Growth, 71 (1985) p.621.

25 A.W.Vere, S.Cole and D.J.Williams, J.Electronic Materials, 12 (3) (1983) p.551.

CHAPTER TWO

CRYSTAL GROWTH AND EXPERIMENTAL TECHNIQUES

§2.1 Introduction

This Chapter is comprised of two sections which deal with the growth of large CdTe crystals from the vapour phase (§2.2) and the principal techniques of structural assessment used in this work (§2.3). The basic experimental features of transmission electron microscopy (TEM), scanning electron microscopy (SEM), energy dispersive analysis of X-rays (EDAX) and reflection high energy electron diffraction (RHEED) are outlined while a discussion of electron diffraction and image contrast is postponed until Chapter 3.

The author is indebted to Mr N.F. Thompson and Dr G.J. Russell who grew all of the crystals examined in this work.

§2.2 Crystal Growth

§2.2.1 The Growth of CdTe Crystals From the Vapour Phase

The most popular methods of growing bulk CdTe crystals are from the liquid phase, either from the stoichiometric melt or from Te rich solutions (see reference [1]). However, this work is concerned with the quality of CdTe crystals which were grown from the vapour phase using the methods described in the next two sections. The vapour phase technique is thought to offer the advantage of growth at low temperatures in comparison to the congruent melting point of CdTe, which is 1092 ^{o}C. By employing lower growth temperatures the possibility of contamination is reduced. Also, if a reservoir containing one of the elements is connected to the growth capsule, some degree

of stoichiometric control over the vapour, and therefore the crystals, may be achieved. Consequently it is expected that the defect content of vapour-grown crystals may differ from that of those grown by melt techniques.

CdTe for use in crystal growth was synthesised directly from the elements. Ingots of Cd and Te of 'six 9s' purity were purchased from M.C.P. Electronic Materials Ltd. The elements were loaded into a silica capsule which was evacuated, sealed, and heated at 940 ^{o}C for three days. In practice, a small excess of Te ($\sim$1%) was included in the material before synthesis, since this is thought to reduce the sticking of CdTe to silica glass which is sometimes encountered. $Cd_yZn_{1-y}Te$, with $y \simeq 0.95$, for use in crystal growth was synthesised in the same way with the addition of the appropriate quantity of high purity Zn.

§2.2.2 The 'Durham' Technique

This technique of vapour phase crystal growth has been used in Durham for many years and has been used to grow a variety of bulk II-VI crystals. These include CdS[2,3,4], CdSe[6], ZnS[7], ZnSe[4,5,8], ZnS-Se, CdZnS and, more recently CdTe[9,10]. The technique employs a sealed, evacuated silica capsule of the type which is illustrated in Figure 2.1. A 'charge' of CdTe is placed in the bottom of this capsule and is transported to the conical growth tip at the top of the tube by sublimation in a temperature gradient. During growth, the temperature difference between the growth face and the charge material is maintained by pulling the crystal growth tube through the temperature profile of the furnace at a rate of 1-2 mm per hour. An important feature of the 'Durham' technique is that the growth

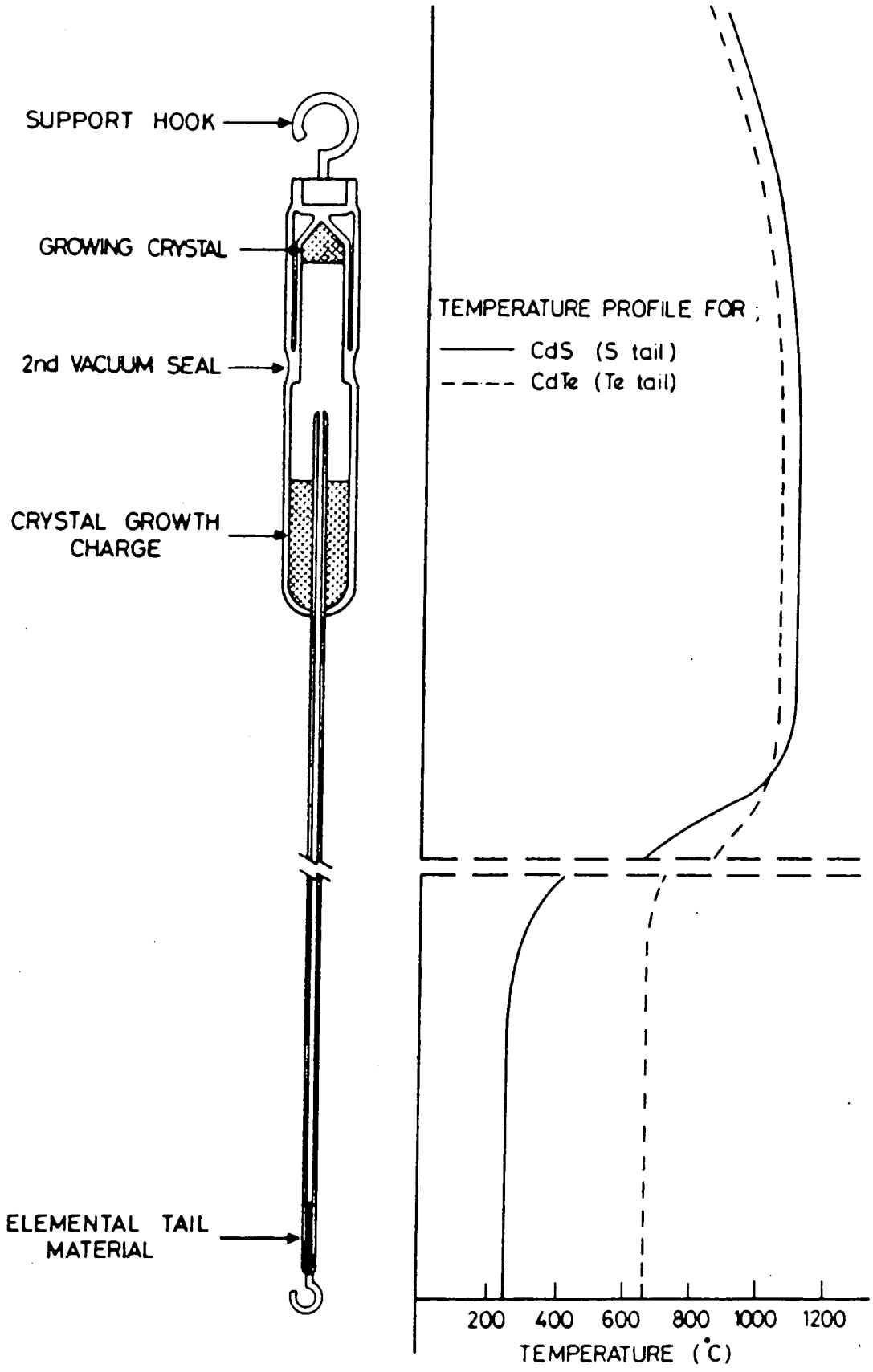

Figure 2.1 Crystal growth by the 'Durham' method.

capsule is coupled, via a narrow orifice, to a tail tube which contains one of the elements. This enables the stoichiometry of the vapour to be maintained close to the P_{min} condition which is known to be the optimum for crystal growth [5]. The element in the tail tube is usually Te, since it has been reported elsewhere that a slight excess of Te enhances growth from the vapour phase [10]. Growth takes place over a period of 4-5 days, after which the crystal is cooled to room temperature in a controlled manner over a further three day period. Crystals grown using this technique are maintained at high temperatures for long periods of time and this might be expected to influence their structural and electrical properties. Boules up to 29 mm in diameter and weighing up to 160 g have been grown routinely using the Durham technique and an example is shown in the photograph in Figure 6.1 in Chapter 6.

§2.2.3 The Modified Piper-Polich Technique

A second vapour phase technique which is a modification of that described by Piper and Polich [12] has been used to grow crystals of ZnS[7], ZnS-Se[7], CdS[10] and CdTe[10] in this laboratory. The design of the silica growth tube employed is shown in Figure 2.2. A charge of CdTe which was synthesised using the direct combination method described in §2.2.1 was loaded into the growth capsule, which is open to an argon atmosphere at the beginning of the growth process. The capsule was fabricated from silica tubes of two different bores, the narrow one of which is open ended and is constricted at intervals, as shown in the figure. During growth a temperature difference of $\sim$ 40 - 50 ^{o}C was maintained between the charge material and the conical end of the growth tube. However, before crystal growth

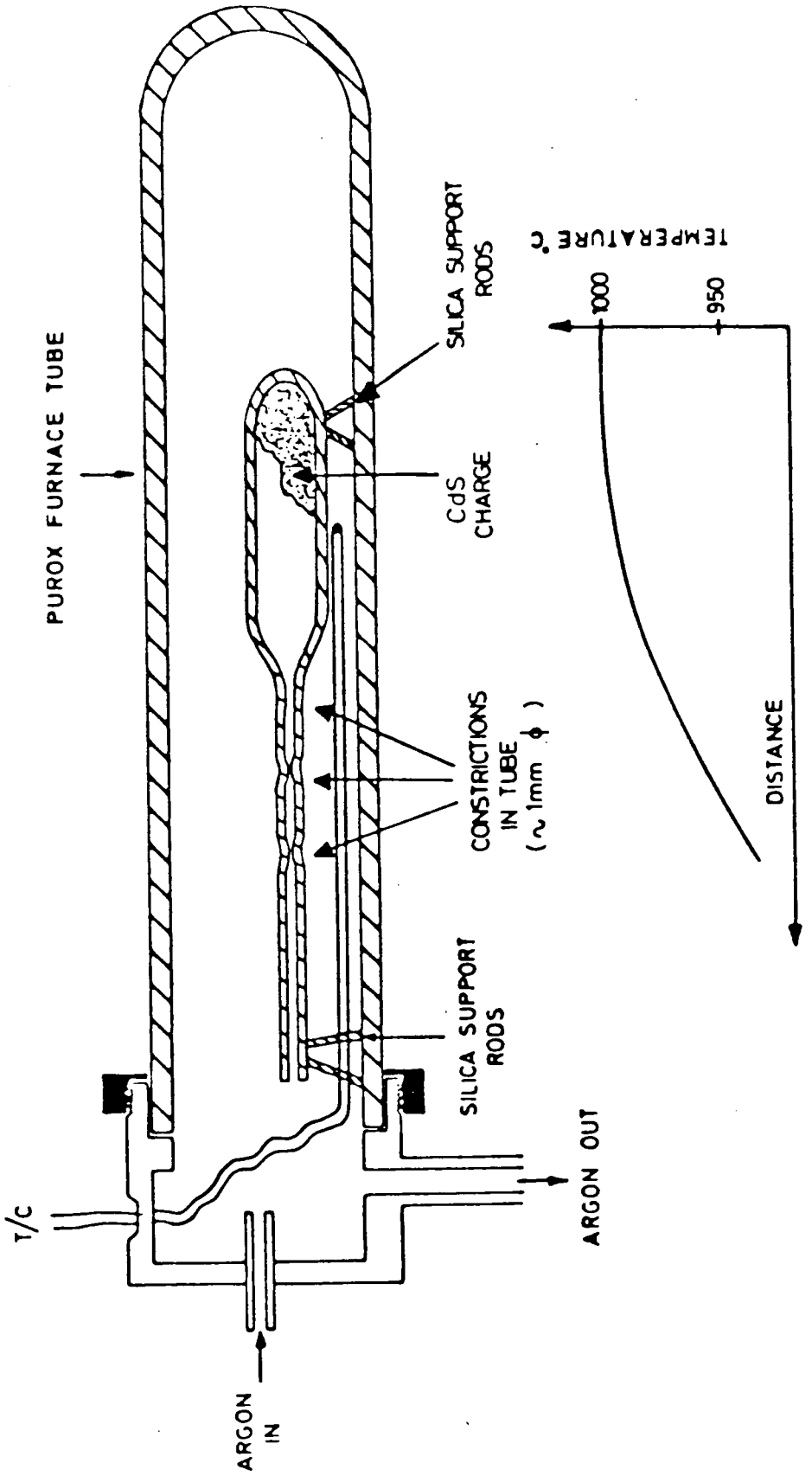

Figure 2.2 Crystal growth by the modified Piper-Polich method.

commences the first of the material to sublime nucleates at the coolest constriction thereby sealing off the narrow bore tube which results in subsequent nucleation at the colder constrictions and finally at the neck of the main growth capsule.

In this method, no pulling is involved and complete transport of material occurs in a period of about one day, after which the growth tubes are cooled to room temperature simply by switching off the furnace. CdTe boules up to 15 mm in diameter and weighing up to 30 g have been grown in this way.

§2.2.4 A Comparison of the Two Growth Techniques

The 'Durham' and modified Piper-Polich vapour phase growth techniques differ from one another substantially: in the case of the 'Durham' method the temperature gradient during growth is much smaller and as a consequence these crystals grow much more slowly than those grown by the modified Piper-Polich technique. Furthermore, in the 'Durham' method, the maintenance of the crystals at a high temperature during growth combined with their subsequent slow cooling to room temperature is equivalent to subjecting them to a post-growth annealing process. This contrasts with the fast growth and cooling conditions encountered in the modified Piper-Polich technique. The rate of transport during growth is also affected by the composition of the gases and vapours present in the growth capsules. These differ in two ways. Firstly, growth in the modified Piper-Polich technique is in an argon ambient whereas the sealed 'Durham' growth capsules are evacuated. Secondly, the tail tube incorporated in the 'Durham' capsules enables the composition of the vapour to be controlled. In the case of Piper-Polich crystals the vapour composition is governed

by the conditions under which the capsules self-seal, and these may vary from one growth-run to another.

Due to these differences in growth conditions it is expected that the structural and electrical properties of the two types of crystal will differ considerably. Indeed, during early trials of CdTe crystal growth using 10 mm diameter growth tubes, those crystals grown by the modified Piper-Polich technique had a larger grain size. However, upon increasing the growth tube diameter to 15 mm this trend was reversed. Following the trials some 60 boules of CdTe with diameters up to 29 mm have been grown by the 'Durham' method. Accordingly, much of the structural assessment work presented in this thesis was performed on 'Durham' grown materials. However, some work on crystals grown by the modified Piper-Polich technique was done and this enabled comparisons of the dislocation and precipitate content of the two materials to be made.

§2.3 Experimental Techniques

This section draws attention to the experimental techniques used in this work. These are all well established and the reader is referred to relevant textbooks and review articles whenever appropriate.

§2.3.1 Transmission Electron Microscopy

Detailed descriptions of the construction and operation of transmission electron microscopes (TEM's) may be found in the textbooks by Hirsch et al [13], Thomas [14] and Loretto and Smallman [15]. However, the basic modes of operation of the TEM are described in the next four sections while the preparation of thin specimens of

CdTe crystals is described in §2.3.1.5.

§2.3.1.1 Bright Field Microscopy

A schematic ray path diagram showing the formation of an electron-optical image in a TEM is shown in Figure 2.3 (The 'illumination' system consisting of an electron gun and two condenser lenses is omitted). The imaging system itself is comprised of objective, intermediate and projector (electromagnetic) lenses which give individual magnifications of 25, 10 and 100 respectively. These lead to an overall magnification which is typically 25 x 10 x 100 = 25,000 times. Under microscopy conditions the parallel beam of illumination is diffracted by the crystalline sample and a diffraction pattern is formed in the back focal plane of the objective lens. By inserting a 30 μm objective aperture into the path of the beam in this plane, only those electrons which are not diffracted by the sample may be selected to contribute to the image. This is termed 'bright field' imaging. If electrons are strongly diffracted from a particular region of a crystalline sample, then this area will appear dark in the bright field image, since the local intensity of the undeviated beam will be diminished in that region. Some fundamental aspects of this 'diffraction contrast' are reviewed in Chapter 3.

§2.3.1.2 Selected Area Diffraction

If the intermediate lens is focussed on the back focal plane of the objective lens then the image of the diffraction pattern located there will be projected onto the viewing screen. This is illustrated in the ray path diagram in Figure 2.4. Furthermore, the area of the sample which contributes to the diffraction pattern may be

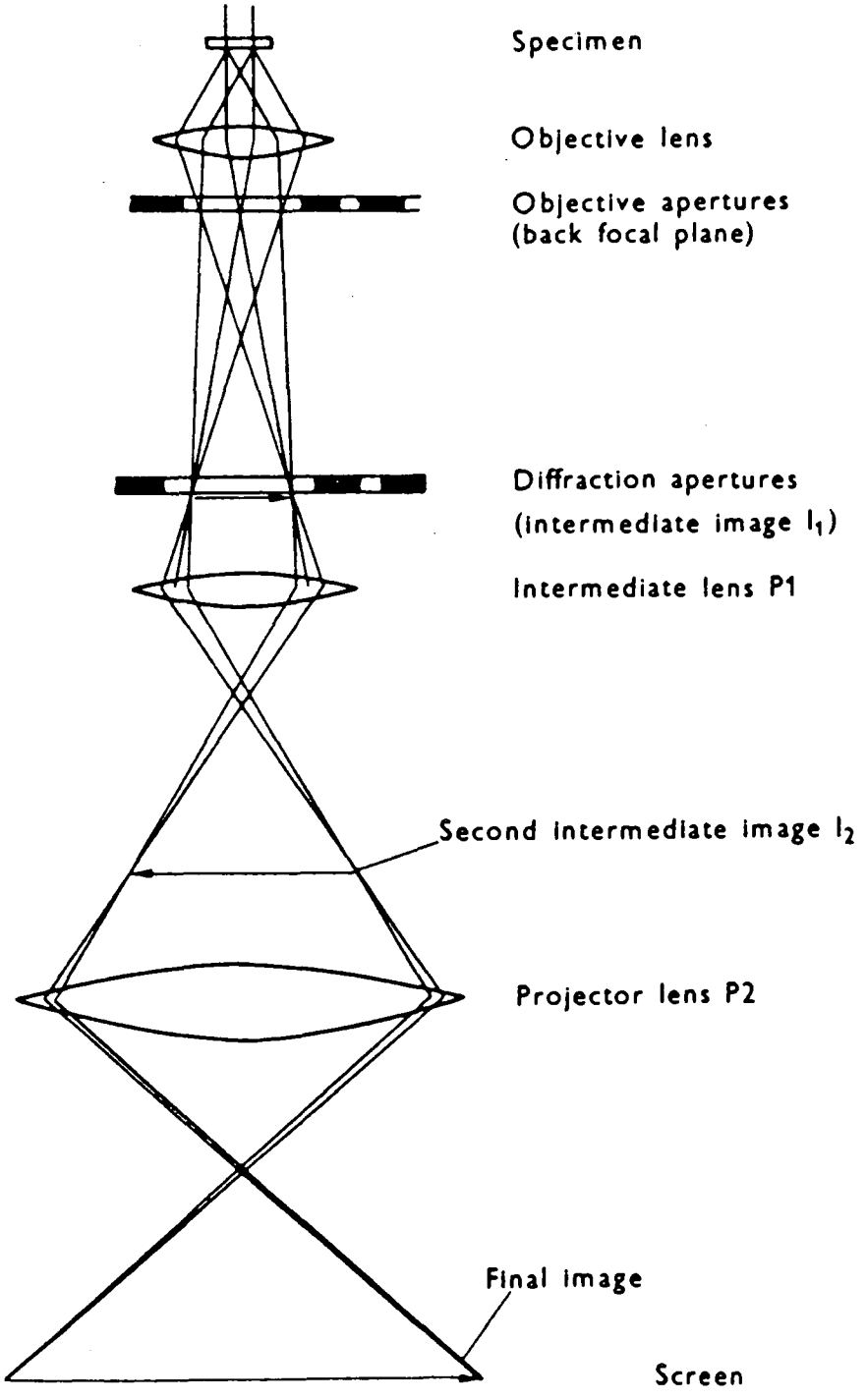

Figure 2.3 Ray paths under imaging conditions.

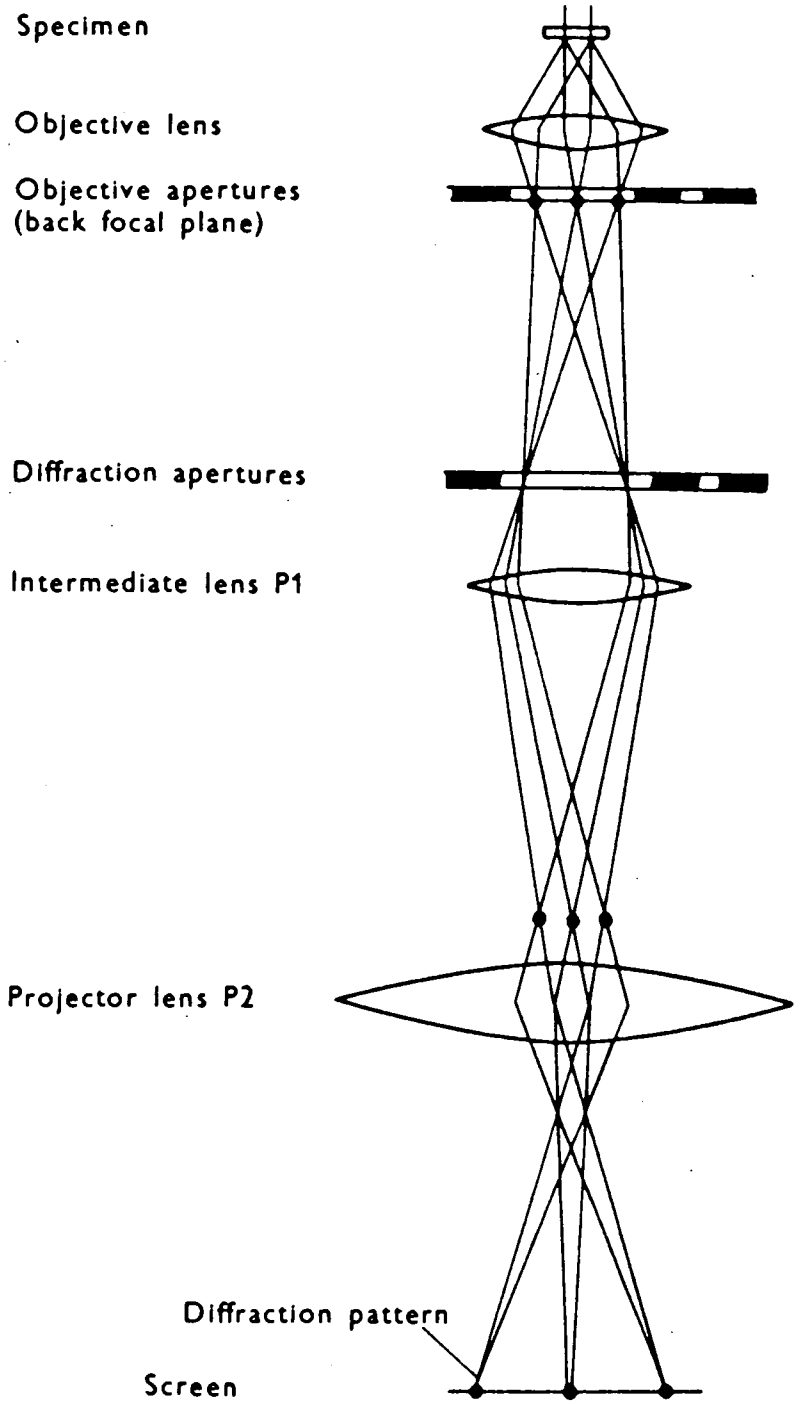

Figure 2.4 Ray paths under diffraction conditions.

selected by inserting an aperture into the plane of the first intermediate image, as shown in the figure. This aperture may be positioned accurately on regions of interest by viewing both the sample and the aperture in the bright field condition. Selected area diffraction (SAD) is therefore a useful technique for analysing multi-phase or multi-grained samples.

§2.3.1.3 Dark Field Microscopy

If only those electrons which are diffracted by a particular set of crystal planes are allowed to pass through the objective aperture then a 'dark field' image is obtained. The best way to arrange this imaging condition is to tilt the illuminating beam so that the diffracted beam passes along the optic axis of the microscope. Beam tilting in this way, usually with the aid of deflection coils, avoids the spherical aberration suffered if a diffracted beam is selected by simply moving the objective aperture off the lens axis to intercept a diffracted beam.

§2.3.1.4 Scanning Transmission Electron Microscopy

Modern analytical electron microscopes are capable of imaging in the scanning transmission electron microscopy (STEM) mode. This employs an electron beam of much smaller diameter than conventional transmission electron microscopy ($\sim$0.01 μm as compared to $\sim$10 μm) and the beam is scanned across the sample in a raster fashion. The transmitted electrons are collected by a detector comprised of a scintillator and a photomultiplier tube which is located beneath the viewing screen of the microscope. The signal from this is displayed on a CRT which is scanned synchronously with the electron

beam scan on the specimen. STEM is particularly useful if X-ray microanalysis is to be performed on thin sections since the small electron beam probe may be positioned so as to focus on specific regions of the specimen. X-ray microanalysis is discussed in §2.3.2.4

§2.3.1.5 Specimen Preparation

Thin, electron transparent sections of CdTe bulk crystals for examination in the TEM were prepared from $\frac{1}{2}$ mm thick slices which were cut from the boules using a diamond saw. These were then polished on both sides by chemical hydroplane polishing using a 1% solution of Br_2 in methanol + ethylene glycol (4+1) (see § 5.2.3.3). Discs with a diameter of 3 mm were then cut from the slices with an ultrasonic drill and these were masked around their edges using 'Lacomit' varnish. Further chemical polishing was performed using a 1% solution of bromine in methanol (see § 5.2.3.2) and was terminated by immersing the samples in methanol when perforation occured. The specimens were then dried in a slow stream of air and inserted directly into the transmission electron microscope.

§2.3.2 Scanning Electron Microscopy

§2.3.2.1 The Scanning Electron Microscope

The construction, modes of operation and uses of the scanning electron microscope (SEM) are described in detail in the textbooks by Goldstein et al [16,17] and Holt et al [18].

A schematic diagram of an SEM is shown in Figure 2.5. The microscope is essentially an electron probe forming instrument which makes use of a focused electron beam that has been accelerated through up to 50kV. Scan coils enable the electron beam to be deflected in

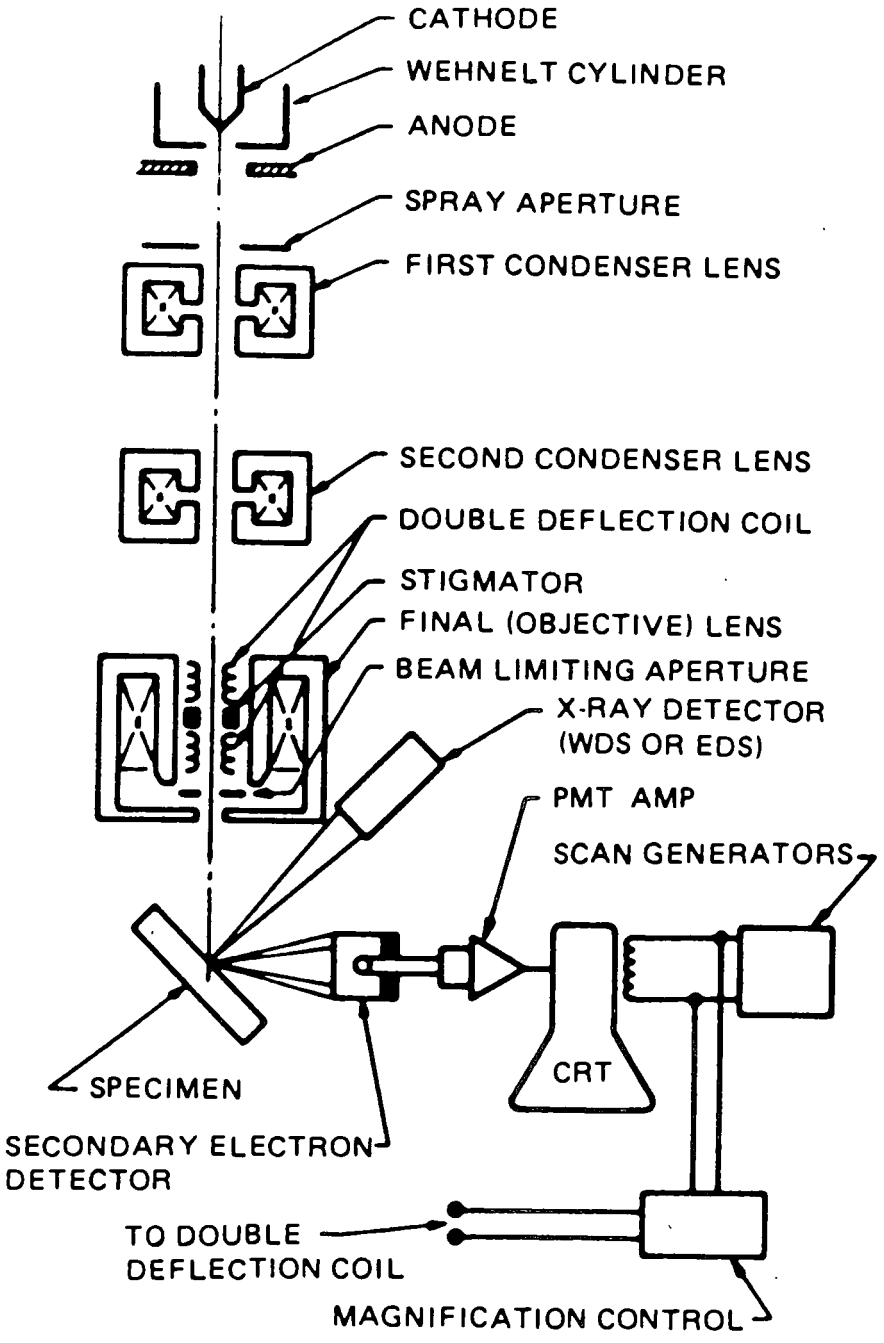

Figure 2.5 Schematic diagram of an SEM.

a raster fashion over the specimen, which is maintained at earth potential. A number of different signals excited in the specimen by the high energy incident electron beam can be detected and used to modulate the output of a display CRT which is scanned synchronously with the electron beam in the microscope. The magnification is given by the ratio of the width of the image on the CRT to that of the electron beam raster on the sample surface. Most modern SEMs offer a range of magnifications extending from x20 to x100,000. The physical effects resulting from electron beam-specimen interactions which give rise to signals which may be used for imaging purposes are indicated in the next section.

§2.3.2.2 Electron Beam - Specimen Interactions

When an electron beam impinges on the surface of a semiconductor sample, a number of interactions occur in various parts of the excitation region within the sample, as illustrated in Figure 2.6. Effects which can be used in image formation and analysis is the SEM include the emission of:-

i) secondary emitted electrons with energy 0-50 eV.
ii) Elastically scattered, primary or backscattered electrons.
iii) Auger electrons.
iv) Characteristic and continuous X-rays.
v) Cathodoluminescence.

Beam-induced currents may also be used in the formation of images when the generation volume intersects, or is within the diffusion length of, a potential barrier such as a p-n junction of a Schottky diode.

In the next three sections the use of the SEM in the secondary

Figure 2.6 Electron beam-specimen interactions.

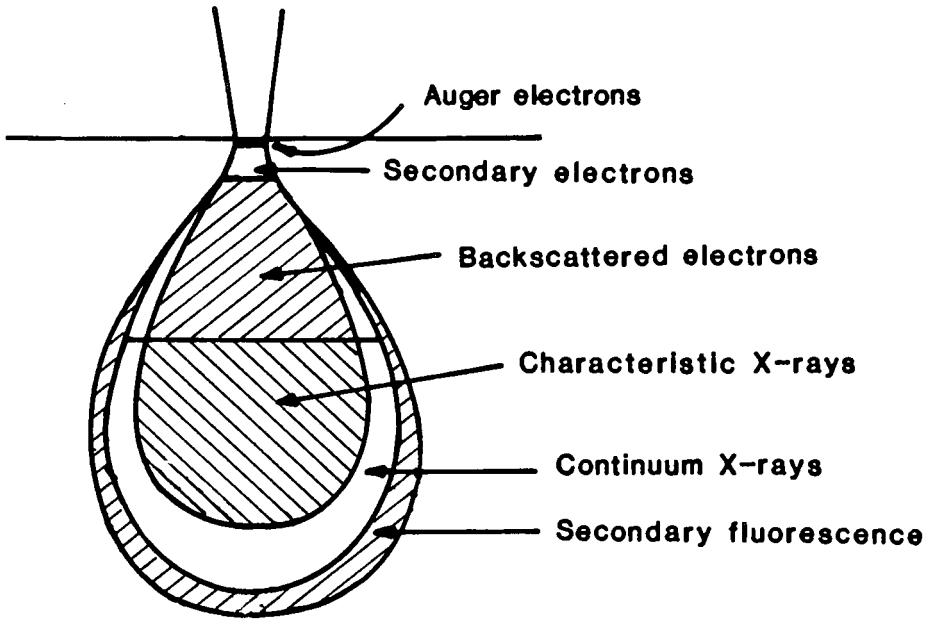

emission, backscattered, X-ray (analysis) and beam induced conductivity modes is briefly described.

§2.3.2.3 Secondary and Backscattered Electron Emission Modes

Images formed using either the combined signal from the high energy elastically scattered, primary and inelastically scattered secondary electrons, or just the primary electrons may be formed with the aid of a single detector of the type first described by Everhart and Thornley [19]. This detector is able to select the electrons which contribute to the image according to their energies by means of a biased metal grid. If a grid voltage of +250V is used then both the high energy primaries and the low energy secondaries are able to impinge on an Al coated scintillator which is maintained at about +10 kV. The light from the scintillator is amplified by a photomultiplier tube and the signal from this is used to modulate

the intensity of the electron beam in a display CRT. Since the number of secondary electrons emitted from a surface greatly exceeds the number of primaries, when using a grid bias of +250V the image formed is essentially a secondary electron image. However, if a grid bias of -50V is used, the secondary electrons are excluded from the detector and a backscattered image is produced.

There are a number of constrast mechanisms which operate when imaging in these two modes. The most important of these are:-

i) Topographic contrast in the secondary electron emission mode.

This arises primarily as a result of the different probabilities of secondary electrons being collected from parts of the sample surface that are inclined differently with respect to the detector. The position of the electron detector with respect to both the sample and the electron beam is thus of major importance in this mode of image formation.

ii) Atomic number contrast in the backscattered mode.

The backscattering coefficient of electrons increases with the atomic number of the specimen, thus enabling compositional contrast to be obtained from flat samples containing separate phases of material differing significantly in atomic number.

Compositional contrast may also be obtained by X-ray mapping, as described in the next section.

§2.3.2.4 X-ray Microanalysis

If an SEM is fitted with a suitable X-ray detector system then characteristic X-rays may be used to perform both microanalysis and compositional mapping. Both wavelength and energy dispersive X-ray analyses are available, although the latter are more frequently

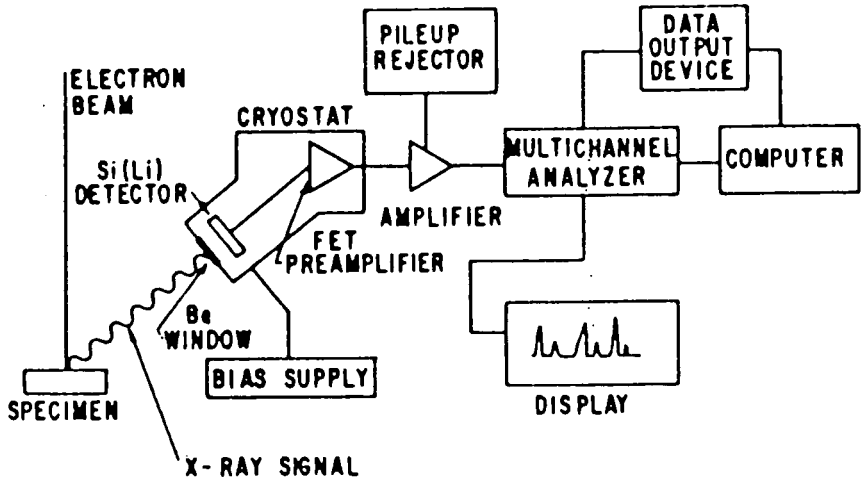

Figure 2.7 Energy dispersive X-ray analyser.

encountered in routine analytical microscopy. Whereas wavelength dispersive systems have the advantages of greater resolution and lower detection limits, energy dispersive systems are both easier and faster to operate. Moreover, they are sufficiently accurate and sensitive for many general analytical investigations.

A schematic diagram of an energy dispersive analyser is shown in Figure 2.7. The X-ray signal from the sample passes through a Be window into a cooled, reversed-biased p-n Si (Li) detector. This leads to the formation of electron-hole pairs which are swept away by the voltage bias to form a charge pulse which is then converted to a voltage pulse by a charge sensitive amplifier. The detector works on the principle that the voltage pulse produced is proportional to the energy of the incident X-ray photon. The signal is further

amplified and passed on to a multi-channel analyser (MCA) where the pulses are sorted by voltage. The contents of the MCA's memory may then be passed on to a computer for peak identification, by comparison with the known positions of the characteristic X-ray lines of all elements, and is then displayed on a monitor.

The technique may be used to analyse special features of interest if the SEM is used in the stationary 'spot' mode. Use of the microscope in 'spot' mode enables elemental maps to be formed from selected portions of the X-ray spectrum. The resolution of X-ray microanalysis is governed by the width of the beam-induced excitation region in the sample and is typically of the order of 1 μm. X-ray techniques in the scanning electron microscope are reviewed at length by Goldstein et al [17].

§2.3.2.5 Electron Beam-Induced Conductivity

The basis of this technique rests in the ability of an electron beam to excite electron-hole pairs in a semiconductor sample. These are then separated under the influence of the bias field of a p-n junction or a Shottky diode. In constant voltage conditions the regions through which the carriers move before recombining yield 'charge collection current' pulses in an external circuit. Regions in which charge collection occurs appear bright in the image. This mode of imaging is commonly referred to as the electron beam-induced conductivity (EBIC) or β-conductivity mode.

In most cases, the investigation of the distribution of recombination centres in a bulk semiconductor sample necessitates the fabrication of a Schottky diode to which a bias voltage may be applied. Schottky diodes on CdTe were made for this purpose by evaporating

a thin gold film (rectifying) on to one side of a chemically polished slice, and soldering an indium contact (ohmic) onto the other.

§2.3.3 Reflection High Energy Electron Diffraction

A detailed review of reflection high energy electron diffraction (RHEED) is provided by Russell [20].

A high energy beam of electrons ($\sim$100 KV) is capable of undergoing diffraction upon intersecting the surface of a bulk crystal at a glancing angle: this is the basis of the RHEED technique. RHEED may be carried out conveniently in a TEM which has been modified to accept a goniometer stage and an air-lock. These are usually positioned in the space directly below the projector lens. Such goniometers are usually capable of holding specimens measuring $\sim$ 10 mm x 10 mm x 2 mm. The diffraction geometry employed in RHEED is illustrated in Figure 2.8. Crystal spacings may be calculated from RHEED patterns by combining Bragg's law, $\lambda = 2d_{hkl}\sin\theta$ and the expression which describes the diffraction geometry, $R_{hkl} = L\tan 2\theta$. (All symbols have their usual meanings - see Figure 2.8).
Applying the small θ approximation yields:

$$\lambda L = R_{hkl}d_{hkl}.$$

λL is the 'camera constant' which is a constant for a given set of diffraction conditions.

The types of information which can be obtained using RHEED include:

i) The amount of crystalline order.

ii) The interplanar spacings and crystal structure of the material.

iii) The content of the unit cell, which may be determined in some cases by analysing the intensities of the

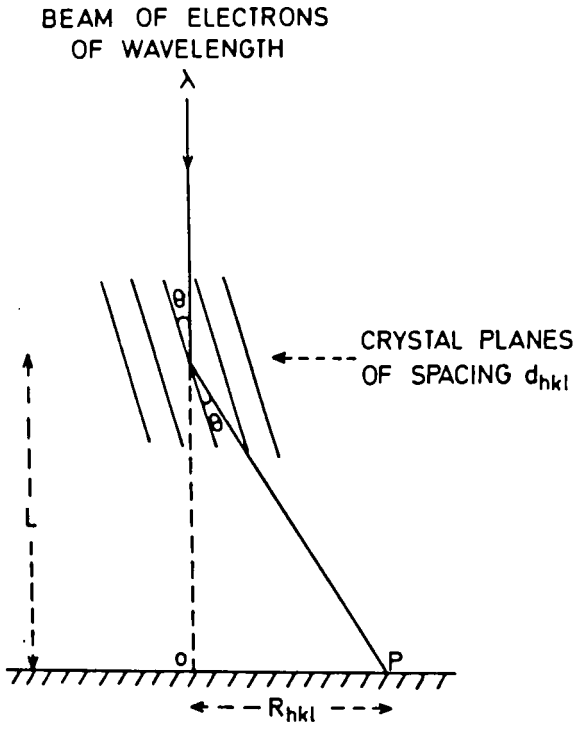

Figure 2.8 Diffraction geometry in RHEED.

diffracted beams

iv) The texture of the specimen surface, which may be assessed from the shape of the diffraction spots.

v) The crystal quality of the surface, which may be assessed by examining the sharpness of Kikuchi lines.

The main advantages of RHEED are that it is a technique which is capable of assessing the crystallography or crystallinity of the surfaces of bulk crystals nondestructively with minimal sample preparation.

§2.3.4 Equipment Available

The Department of Applied Physics and Electronics has a JEOL JEM 120 TEM (1967) which is capable of operating at 80, 100 and 120kV.

It has been adapted to accept a RHEED stage. In April 1985 a JEOL 100CX TEM with STEM and EDAX was purchased. The Department also has a Cambridge Stereoscan 600 SEM which is equipped with a Link Systems EDAX facility.

REFERENCES FOR CHAPTER TWO

1 K.Zanio in, Semiconductors and Semimetals, Volume 13 (1978) Academic Press, New York, Eds. R.K.Willardson and A.C.Beer. p.11.

2 L.Clark and J.Woods, Brit.J.Appl.Phys, 17 (1966) p.319.

3 L.Clark and J.Woods, J.Crystal Growth, 3,4 (1968) p.127.

4 G.J.Russell and J.Woods, J.Crystal Growth, 46 (1979) p.323.

5 J.R.Cutter and J.Woods, J.Crystal Growth, 47 (1979) p.405.

6 I.E.Ture, G.J.Russell and J.Woods, J.Crystal Growth, 59 (1982) p.223.

7 G.J.Russell and J.Woods, J.Crystal Growth, 47 (1979) p.647.

8 J.R.Cutter, G.J.Russell and J.Woods, J.Crystal Growth, 32 (1976) p.179.

9 G.J.Russell, N.F.Thompson and J.Woods, J.Crystal Growth,71 (1985) p.621.

10 K.Durose, G.J.Russell and J.Woods, J.Crystal Growth, 72 (1985) p.85.

11 N. Yellin and S.Szapiro, J.Crystal Growth, 69 (1984) p.555.

12 W.W.Piper and S.J.Polich, J.Appl.Phys, 32 (1961) p.1278.

13 P.B.Hirsch, A.Howie, R.B.Nicholson, D.W.Pashley and M.J.Whelan, 'Electron Microscopy of Thin Crystals', Butterworths, London (1965).

14 G.Thomas, 'Transmission Electron Microscopy of Metals'. John Wiley and Sons, New York, (1964).

15 M.Loretto and R.E.Smallman, 'Defect Analysis in Electron Microscopy'. Chapman and Hall, London (1975).

16 J.I.Goldstein, H.Yakowitz, D.E.Newbury, E.Lifshin, J.W.Colby and J.R.Coleman, 'Practical Scanning Electron Microscopy', Plenum, New York, (1975) Ed. J.I.Goldstein and H.Yakowitz.

17 J.I.Goldstein, D.E.Newbury, P.Echlin, D.C.Joy, C.Fiori and E.Lifshin, 'Scanning Electron Microscopy and X-ray Microanalysis'. Plenum Press, New York, (1981).

18 D.B.Holt, M.D.Muir, P.R.Grant and I.M.Boswarva, 'Quantitative Scanning Electron Microscopy', Academic Press, London, (1974).

19 T.E.Everhart and R.F.M.Thornley, J.Sci.Inst.,37 (1960) p.246.

20 G.J.Russell, Prog.Crystal Growth and Characterisation, 5 (1982) p.291.

CHAPTER THREE

ELECTRON DIFFRACTION AND CONTRAST IN THE TRANSMISSION ELECTRON MICROSCOPE

§3.1 Introduction

The interpretation of the images of crystalline samples obtained in the transmission electron microscope requires considerable understanding of electron diffraction. In particular, the ways in which the presence of crystal defects modifies the transmission and diffraction of electrons by thin crystals is of fundamental importance. In the first part of this Chapter (§3.2), the geometric conditions necessary for the diffraction of radiation by a crystalline specimen are outlined. The implications of these conditions with reference to electron diffraction from thin crystals is then considered. The fundamental features of the 'kinematical' treatment of diffraction which is necessary for the understanding of image contrast are described in §3.3.2 while the remainder of that section is devoted to descriptions of the characteristics of the image contrast associated with crystal defects. The treatment is limited to those defects which were encountered during this work - there is extensive and detailed literature on the interpretation of diffraction contrast arising at all forms of crystal defect and the reader is referred to the relevant textbooks whenever appropriate.

§3.2 Electron Diffraction

§3.2.1 The Reciprocal Lattice

An important concept which is necessary in order to gain a proper

understanding of diffraction phenomena is the idea of the reciprocal lattice. In order to construct the reciprocal lattice from the real lattice, lines are drawn from a point which is chosen to be the origin of reciprocal space in directions which are perpendicular to the crystal planes in the real lattice. The reciprocal lattice point corresponding to the plane (hkl) lies at a distance of $1/d_{hkl}$ from the origin along the line which is perpendicular to this plane. In this way a space lattice of reciprocal lattice points may be formed for any crystal structure. For a real lattice having the unit cell vectors $\underline{a}_1$, $\underline{a}_2$, $\underline{a}_3$, the reciprocal lattice will have the reciprocal lattice unit cell vectors $\underline{b}_1$, $\underline{b}_2$, $\underline{b}_3$, and for the cubic system, the two sets of axes are coincident. Furthermore, the reciprocal lattice point corresponding to the (hkl) plane may be described by the reciprocal lattice vector $\underline{g}_{hkl} = h\underline{b}_1 + k\underline{b}_2 + l\underline{b}_3$. Full details of the properties of the reciprocal lattice may be found in Cullity's text on X-ray diffraction [1].

§3.2.2 The Laue Equations

The Laue equations describe the conditions necessary for the constructive interference of waves which have been elastically scattered from two scattering centres. In the case of electron diffraction elastic scattering occurs as a result of the interaction of electrons with the nuclei of atoms. The diffraction of inelastically scattered electrons is considered in §3.2.5.

In order for constructive interference to occur between waves scattered from two centres, the path difference between them must equal a whole number of wavelengths. Consider the two centres illustrated in Figure 3.1, one of which lies at the origin of the real

lattice, O and the other at A whose coordinates are $p\underline{a}_1$, $q\underline{a}_2$, $r\underline{a}_3$, where p,q and r are integers. The vector $\underline{OA}$ is thus given by $\underline{OA} = p\underline{a}_1 + q\underline{a}_2 + r\underline{a}_3$. The incident and diffracted beams of radiation (electrons having a wavelength λ) are represented by vectors $\underline{K}o$ and $\underline{K}$ respectively. To determine the conditions under which diffraction occurs we must consider the phase difference between waves scattered from the centres O and A. The lines Ou and Ov in the diagram are the wavefronts of the incident and diffracted beams respectively. Let δ be the path difference for waves scattered by O and A.

We see that $\delta = uA + Av$

$$= Om + On$$

$$= \underline{K}o \cdot \underline{OA} + (-\underline{K}).\underline{OA}$$

$$= -\underline{OA} \cdot (\underline{K} - \underline{K}o)$$

The corresponding phase difference is given by

$$\phi = \frac{2\pi\delta}{\lambda}$$

$$= -2\pi \left(\frac{\underline{K} - \underline{K}o}{\lambda} \right) \cdot \underline{OA}$$

$\left(\frac{\underline{K} - \underline{K}o}{\lambda} \right)$ may be represented as a vector in the reciprocal lattice, that is

$$\left(\frac{\underline{K} - \underline{K}o}{\lambda} \right) = h\underline{b}_1 + k\underline{b}_2 + l\underline{b}_3$$

In general h, k and l are continuously variable and may assume any values. The expression for the phase difference may be rewritten as

$$\phi = -2\pi (h\underline{b}_1 + k\underline{b}_2 + l\underline{b}_3).(p\underline{a}_1 + q\underline{a}_2 + r\underline{a}_3)$$

$$= -2\pi (hp + kq + lr)$$

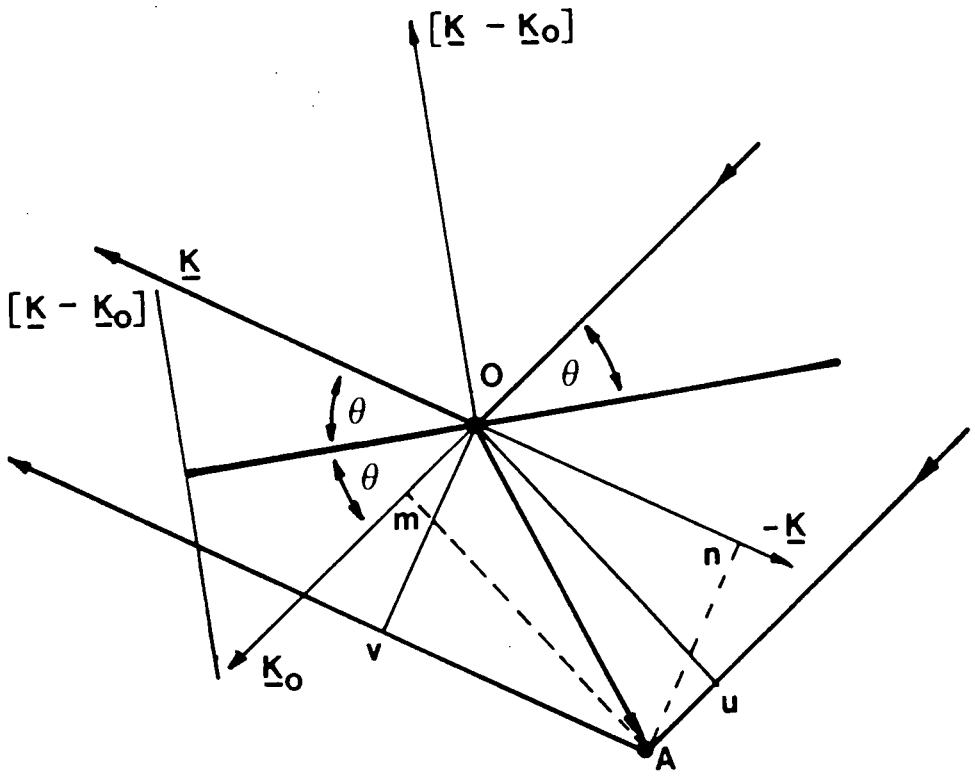

Figure 3.1 Scattering from two centres, O and A.

In order for constructive interference to occur the phase difference must be a multiple of 2π and so h, k and l must be integers: the condition for diffraction is therefore that the vector $\frac{\underline{K} - \underline{K}o}{\lambda}$ ends at a reciprocal lattice point, that is

$$\left(\frac{\underline{K} - \underline{K}o}{\lambda} \right) = h\underline{b}_1 + k\underline{b}_2 + l\underline{b}_3 = \underline{g}_{hkl}$$

where $\underline{g}_{hkl}$ is a reciprocal lattice vector termed the diffraction vector. By resolving the diffraction vector along the three orthogonal axes of the real lattice of a cubic structure the Laue equations are obtained. For example,

$$\underline{a}_1 \cdot \left(\frac{\underline{K} - \underline{K}o}{\lambda} \right) = \underline{a}_1 \cdot (h\underline{b}_1 + k\underline{b}_2 + l\underline{b}_3) = h$$

and so $\underline{a}_1 \cdot (\underline{K} - \underline{K}o) = h\lambda$

$\underline{a}_2 \cdot (\underline{K} - \underline{K}o) = k\lambda$

$\underline{a}_3 \cdot (\underline{K} - \underline{K}o) = l\lambda$.

Since the vector $(\underline{K} - \underline{K}o)$ bisects the angle between $\underline{K}$ and $\underline{K}o$, we may consider the diffracted beam $\underline{K}$ to be reflected from a set of planes perpendicular to $(\underline{K} - \underline{K}o)$, that is perpendicular to $\underline{g}$. The unit vectors $\underline{K}$ and $\underline{K}o$ both make an angle θ, the Bragg angle with these planes, as is shown in Figure 3.1, and so $(\underline{K} - \underline{K}o) = 2 \sin\theta$.

Therefore $$\frac{2\sin\theta}{\lambda} = \left(\frac{\underline{K} - \underline{K}o}{\lambda}\right) = \underline{g} = \frac{1}{d}$$

or $\lambda = 2d \sin\theta$ which is Bragg's law.

§3.2.3 The Ewald Construction

The conditions for diffraction outlined in the final paragraph of the previous section may be represented in graphical form using the Ewald construction, which is shown in Figure 3.2. All of those lattice points, such as P(h,k,l), which lie on the surface of the reflecting sphere satisfy the condition $\underline{K} - \underline{K}o = \underline{g}$, that is Bragg's law.

In the application of the Ewald construction to electron diffraction there are two important features of note:-

i) The wavelength of 100 keV electrons is small (0.037Å) and so the radius of the Ewald sphere is about 27 Å^{-1} in reciprocal space. In comparison with a typical value for $|\underline{g}|$, which is about 0.4 Å^{-1} for a (220) reflection for CdTe, the curvature of the reflecting sphere is large and may be considered to be planar over a region containing a considerable number of reciprocal lattice points.

ii) The reciprocal lattice 'points' representing planes in a thin film are distorted and take the form of rods which lie perpendicular to the foil. Their lengths are inversely proportional to the thickness of the foil [2]. This effect increases the probability of the reflecting sphere intersecting a reciprocal lattice 'point'.

As a consequence of these effects, electron diffraction patterns containing many orders of reflections can easily be obtained from thin samples. For crystals having high symmetry, the two dimensional array of diffraction spots can be indexed simply by comparing them with the standard patterns corresponding to orientations of low index (see [4] and [9] for instance).

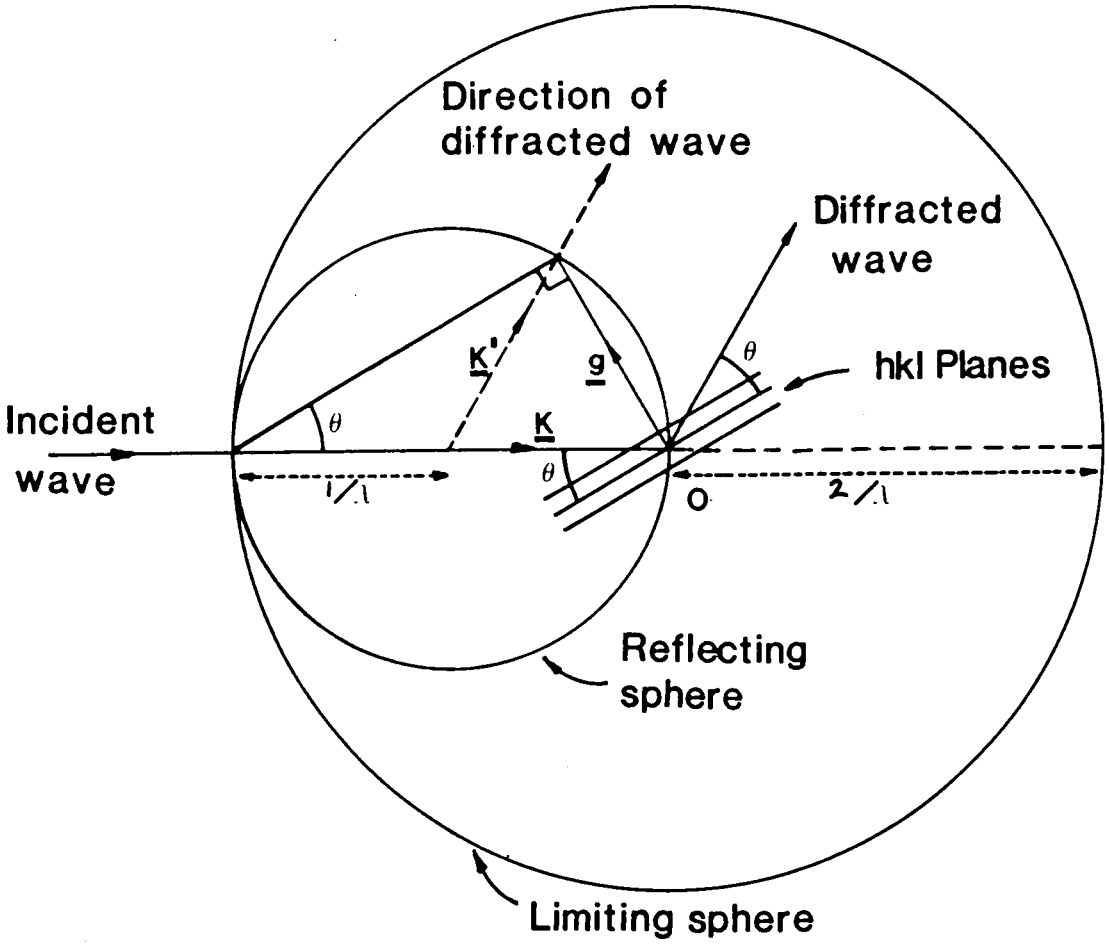

Figure 3.2 The Ewald construction.

§3.2.4 Structure Factor

By considering the phase differences of waves which are scattered from all of the atoms in a unit cell, it is possible to calculate the total amplitude of a wave scattered by that unit cell. The expression for this total amplitude is called the structure factor, F_{hkl}. For a reflection from the (hkl) plane in a structure whose unit cell has N atoms F_{hkl} is given by the relationship

$$F_{hkl} = \sum_{1}^{N} f_n(\theta)\, e^{2\pi i(hu_n + kv_n + lw_n)}$$

where u_n, v_n and w_n are the fractional coordinates of atom n and $f_n(\theta)$ is the atomic scattering factor for electrons for that atom [3]. The intensity of a wave diffracted by a set of planes (hkl) at an angle given by Bragg's law is thus $|F_{hkl}|^2$.

§3.2.5 Kikuchi Lines

An effect which is observed in electron diffraction patterns from fairly thick samples is the presence of pairs of light and dark lines which run across the pattern. These so called Kikuchi lines originate from inelastically scattered electrons which are subsequently diffracted by crystal planes which are at the Bragg angle to those electrons. This is illustrated in Figure 3.3. Some of the electrons incident at point P in the figure will be inelastically scattered and those which make the Bragg angle with a set of crystal planes at Q and R will be diffracted in the directions QQ' and RR' to form the Kikuchi lines. However, since the intensity of inelastically scattered electrons in directions close to the foreward beam direction (eg PQ) is greater than in directions which make a larger angle to

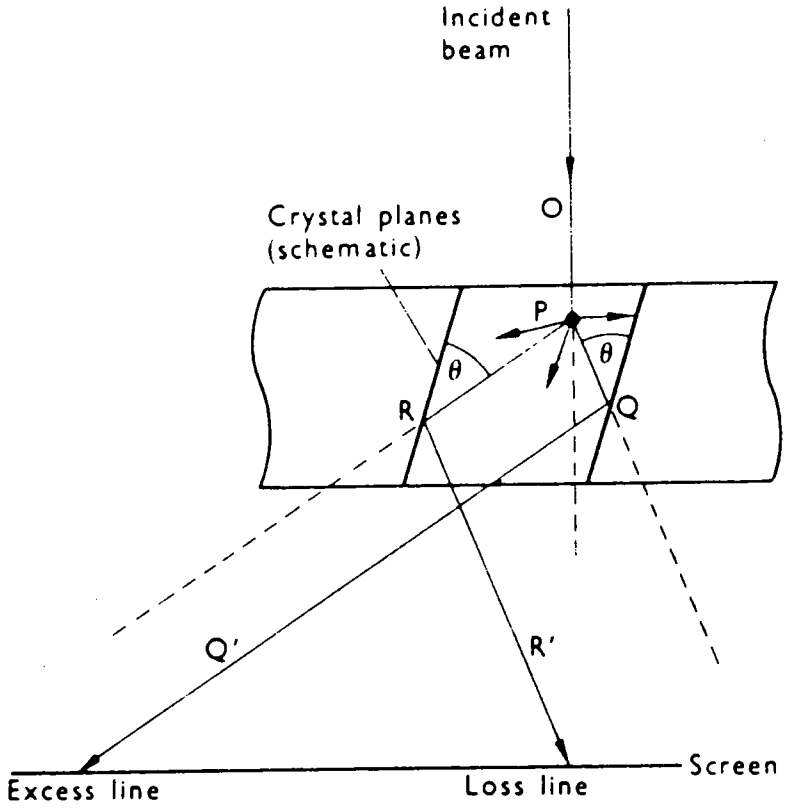

Figure 3.3 The origin of Kikuchi lines.

the foreward beam direction (eg PR), the intensities of the two Kikuchi lines will differ, as is indicated in the figure. The angular separation of each pair of Kikuchi lines is 2θ and so each spot in the diffraction pattern is associated with a pair of these lines. By considering Figure 3.3 it can be appreciated that if the sample is tilted slightly the Kikuchi lines will move while the diffraction spots, even though they may change in intensity, remain fixed.

When a bright Kikuchi line is coincident with a diffraction spot having the same Miller indices, then the exact Bragg condition is satisfied exactly for that particular reflection. Deviations from the exact Bragg condition are indicated if the Kikuchi line is displaced to one side of its corresponding diffraction spot.

This is characterised by the deviation parameter, $\underline{s}$, which is defined as the distance from the Ewald sphere to the reciprocal lattice point measured in a direction parallel to $\underline{B}$, the direction of the incident beam. While the beam direction may be determined by taking the cross product of two diffraction vectors represented in a diffraction pattern, such a calculation may be in error by as much as a few degrees since the reflections used may have been excited even though the exact Bragg condition was not satisfied. The displacements of Kikuchi lines and poles from diffraction spots may be used to calculate the incident beam direction exactly.

§3.3 Image Contrast

§3.3.1 Introduction

Calculation of image contrast in the transmission electron microscope effectively involves the computation of the intensities of the electron beams which are transmitted and diffracted by thin crystalline specimens taking particular account of the effects introduced by specific crystalline defects. In the next section, the essential features of the 'kinematical' approach to determining image contrast are outlined. Some of the fundamental aspects of contrast associated with twin boundaries, dislocations and inclusions, all of which were encountered in this work, are described in the subsequent sections.

§3.3.2 The Kinematical Theory of Electron Diffraction

The kinematical theory of electron diffraction [5] represents the most straight forward formulation of a set of equations which are capable of describing image contrast in the transmission electron microscope. It is based on the following assumptions:-

i) That a 'two beam' condition is in operation, ie there is only one diffracted beam.

ii) The intensity of the diffracted beam is small with respect to that of the incident beam. This implies that there is a significant deviation from the exact Bragg condition.

iii) There is negligable absorption and no multiple diffraction effects occur. This implies that the sample is very thin in the direction of the electron beam.

If these assumptions are made then it is possible to prove that the total amplitude, Ψ_D, of the wave which is scattered by a crystal of thickness t, is given by the integral

$$\Psi_D = \int_{-t/2}^{t/2} \exp\left[2\pi i\,(\underline{g} + \underline{s}).\underline{r}_n\right] dr$$

where $\underline{r}$ is a lattice vector whose magnitude varies from t/2 to -t/2, and $\underline{s}$ is the deviation parameter.

Upon integrating and substituting the limits it is found that the intensity, I_D, of the diffracted wave is given by

$$I_D = |\Psi_D|^2 \simeq \frac{\sin^2 \pi\, ts}{(\pi s)^2}$$

If the incident intensity, I_I, is taken as unity, then the transmitted intensity, I_T, is given by

$$I_T \simeq 1 - \left[\frac{\sin^2 \pi\, ts}{(\pi s)^2}\right]$$

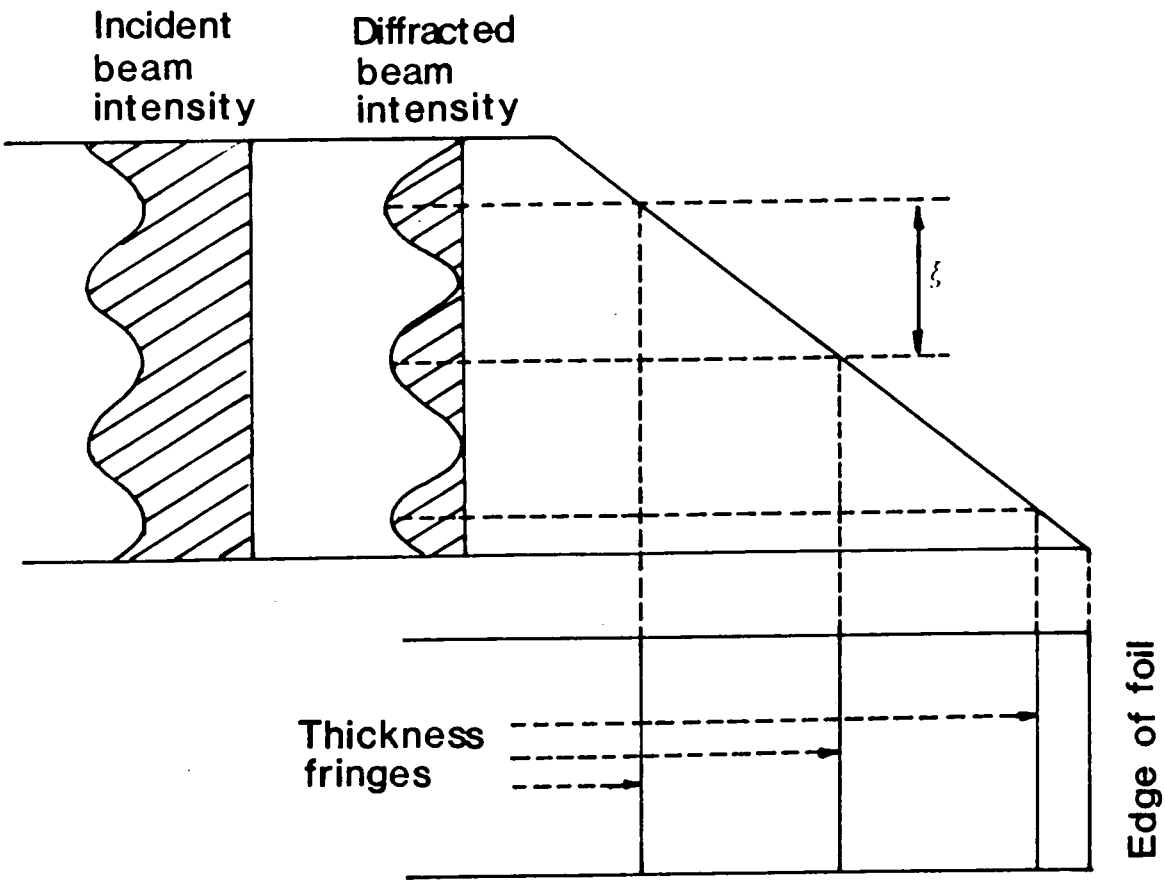

Figure 3.4 The origin of thickness fringes.

These two equations show how the intensities of both the transmitted and diffracted waves vary periodically with both the thickness of the crystal, t, and the deviation parameter, $\underline{s}$. The variation of I_T and I_D for an undistorted wedge-shaped crystal is illustrated in Figure 3.4. This shows how 'thickness fringes' are associated with images of such crystals when they are imaged in a two-beam condition.

In order to determine the influence that crystal imperfections such as dislocations have on the image contrast, the displacement, $\underline{R}$, of a unit cell from its position in the perfect crystal needs to be known. The modified expression for the amplitude of the diffracted wave then becomes

$$\Psi_D = \int_o^t \exp [2\pi i \underline{g}.\underline{R}] \exp [2\pi i \underline{s}.\underline{r}]dr$$

where the phase factor $2\pi i\underline{g}.\underline{R}$ accounts for the presence of the lattice defect. Clearly, if the product $\underline{g}.\underline{R} = 0$ then the equation for the amplitude of the diffracted wave is identical to that for a perfect crystal. Under such conditions a defect would not be visible in either a bright or a dark field image. Knowledge of a function describing $\underline{R}$ which is appropriate to a specific defect enables an image profile to be computed for that particular defect.

Although kinematical calculations of this type are capable of explaining the qualitative features of image contrast which are observed in practice, the necessary approximations limit their applicability in most experimental instances and make them quantitatively inaccurate. Accurate computation of the image profiles of defects imaged in the TEM requires the dynamical theory of electron diffraction which takes into account both absorption and multiple scattering phenomena [6]. This theory has been used extensively to enable quantitative calculations of the image profiles associated with a wide range of crystal defects to be made. However, the dynamical theory is considerably more complex than the kinematical one and the latter remains an extremely useful means of gaining an understanding of the image contrast effects encountered in practical transmission electron microscopy.

§3.3.3 Contrast at Twin Boundaries

When a twin boundary (see § 4.4.2) is imaged in a condition in which a single set of planes in the matrix diffracts strongly, and no strong reflections are excited from the twin, then characteristic fringes are seen at the twin boundary which lie parallel to the intersection of the boundary with the sample's surface. The presence

of these fringes can be explained with reference to the phenomenon of thickness fringes which was described in §3.3.2. Since the twin does not diffract strongly in the conditions described above, the situation is qualitatively similar to one in which the material having the twin orientation is replaced by a vacuum and the matrix crystal is bounded by an inclined facet at the position previously occupied by the twin boundary. In this way it can be seen that fringes which are similar in appearance to closely spaced thickness fringes will be visible at twin boundaries providing that they are imaged using the correct diffraction conditions. A number of workers have applied the dynamical theory to the problem of calculating the image profiles of twin boundaries and this has yielded quantitative information concerning the contrast associated with these defects (see [11,12 and 13] for example).

§3.3.4 Contrast from Dislocations

It was pointed out in §3.3.2 that the introduction of a defect into a crystal is taken into account in the kinematical equations by including an additional phase factor term in the equations which describe electron transmission through a perfect crystal. This phase factor is $2\pi i(\underline{g}.\underline{R})$ where $\underline{R}$ is a displacement term associated with the crystal defect. For a dislocation, $\underline{R}$ is equivalent to the Burgers vector, $\underline{b}$ of that dislocation. When perfect dislocations (that is those having Burgers vectors which are unit lattice vectors) are considered then the product $\underline{g}.\underline{b}$ is always an integer or zero. In general, at the exact Bragg condition, if $\underline{g}.\underline{b} = 0$ then a dislocation will be invisible, or else represented by only weak contrast, whereas if $\underline{g}.\underline{b} = 1$ or 2 single and double images respectively will be observed.

By careful selection of diffraction conditions these properties of dislocation images can be used to determine the Burgers vectors of dislocations. However, since partial dislocations have Burgers vectors which are non-lattice vectors, the product $\underline{g}.\underline{b}$ can be fractional and the interpretation of the images of these dislocations is correspondingly more complex.

Detailed descriptions of the contrast effects associated with dislocations may be found in references [7] and [10].

§3.3.5 Diffraction Contrast From Inclusions

The diffraction contrast effects associated with coherent spherical precipitates in isotropic media, such as that shown in Figure 3.5, have been studied extensively. Mott and Nabarro [14] were able to show that the displacements both within and surrounding such a precipitate may be described by simple radial functions. These displacement formulae have been used in a number of image profile calculations for this type of precipitation. Kinematical calculations have been performed by Whelan [15] and Phillips and Livingston [16]. This work yielded the qualitative features of the image contrast and is summarised in reference [8]. The essential results of the application of the dynamical theory to this problem obtained by Ashby and Brown [17,18] are given in reference [19].

Briefly, a strain field of the type illustrated in Figure 3.5 is imaged as a pair of lobes of contrast if only one reflection is operating. The lobes are separated by a 'line of no contrast' as illustrated in Figure 3.6 which is always perpendicular to the diffracting vector, $\underline{g}$. Thus the orientation of the line of no contrast

may be changed by varying the diffraction conditions. As illustrated in Figure 3.7, the symmetry of the lobe contrast varies according to the position of the precipitate in the foil and may also change if the imaging is performed in dark field conditions. Ashby and Brown [17,18] have outlined how, given favourable experimental conditions, quantitative information regarding precipitate coherency strains may be derived from measurements of their images.

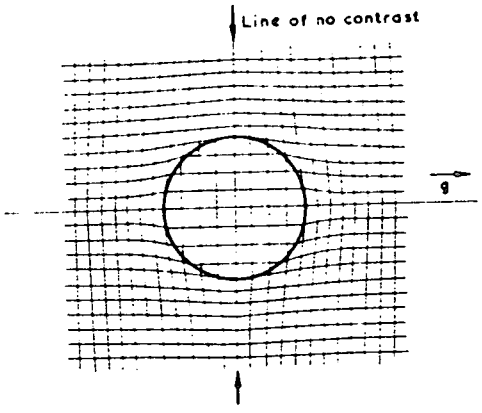

Figure 3.5 Lattice displacements near a coherent precipitate.

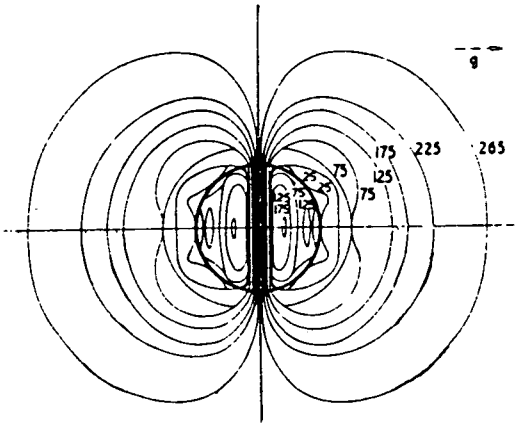

Figure 3.6 Contrast surrounding a spherically strained inclusion.

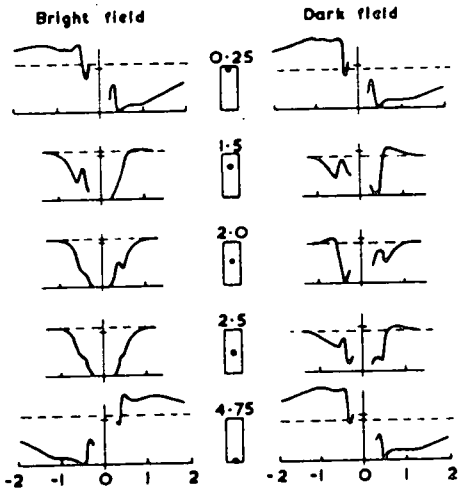

Figure 3.7 Image profiles of inclusions at various positions within a thin crystalline sample.

REFERENCES FOR CHAPTER THREE

1 B.D.Cullity, 'The Elements of X-ray Diffraction', Addison Wesley, (1967) p.490.

2 G. Thomas, 'Transmission Electron Microscopy of Metals', John Wiley and Sons, New York, (1964) p.38.

3 G. Thomas, ibid, p.17.

4 P.B.Hirsch, A.Howie, R.B.Nicholson, D.W.Pashley and M.J.Whelan, 'Electron Microscopy of Thin Crystals', Butterworths, London, (1965) Appendix 5 p.498.

5 Idem., ibid, Ch.4 p.85.

6 Idem., ibid, Ch.8-12 p.195.ff.

7 Idem., ibid, Ch.11 p.247.ff.

8 Idem., ibid, p.188.

9 M.H.Loretto and R.E.Smallman, 'Defect Analysis in Electron Microscopy', Chapman and Hall, London, (1975) Appendix 2 p.115.

10 M.H.Loretto and R.E.Smallman, ibid, p.49,63,74.

11 J. van Landuyt, R.Gevers and S.Amelinckx, Phys.Stat.Sol.,9 (1965) p.135.

12 G. Remaut, R.Gevers, A. Lagasse and S.Amelinckx, Phys.Stat.Sol.,10 (1965) p.121.

13 G. Remaut, R.Gevers, A.Lagasse and S.Amelinckx, Phys.Stat.Sol.,13 (1966) p.125.

14 N.F.Mott and F.R.N. Nabarrow, Proc.Phys.Soc.,52 (1940) p.86.

15 M.J.Whelan, J.Inst.Met.,87 (1958-59) p.392.

16 V.A.Phillips and J.D.Livingston, Phil.Mag.,7 (1962) p.969.

17 M.E.Ashby and L.M.Brown, Phil.Mag.,8 (1963) p.1083.

18 M.E.Ashby and L.M.Brown, ibid, p.1649.

19 K.F.Hale in Electron Microscopy and Microanalysis of Metals, Ed. J.A.Belk and A.L.Davis, Elsevier, Amsterdam, (1968) Ch.7 p.121.

CHAPTER FOUR

CRYSTAL DEFECTS

§ 4.1 Introduction

The purpose of this Chapter is to describe some of the defects which are encountered in crystals having the sphalerite structure. The discussion is limited to those topics which are relevant to the experimental observations described in later chapters. Those covered include the sphalerite structure, crystallographic polarity (unique to noncentrosymmetric crystal structures), dislocations, dislocation arrays, 'special' grain boundaries and twinning. For a more detailed discussion of the structure and defect content of II-VI compounds the reader is referred to the reviews by Roth [1] and Hartmann [2].

§ 4.2 The Sphalerite Structure

The stable crystalline form of CdTe at room temperature and pressure is the sphalerite or zincblende structure [3]. It is comprised of two interpenetrating fcc lattices one of which consists of metal atoms and the other of which contains the non-metal atoms. These two lattices are displaced from one another by $\frac{1}{4}$ <111> as shown in Figure 4.1. Alternatively the structure may be described in terms of the stacking sequence of the {111} planes. Using Roman letters for metal atoms and Greek ones for non-metal atoms the sphalerite structure is represented by the sequence A αB βC γA αB β.... where α, β and γ are located vertically above A, B and C respectively as shown in Figure 4.2. An important

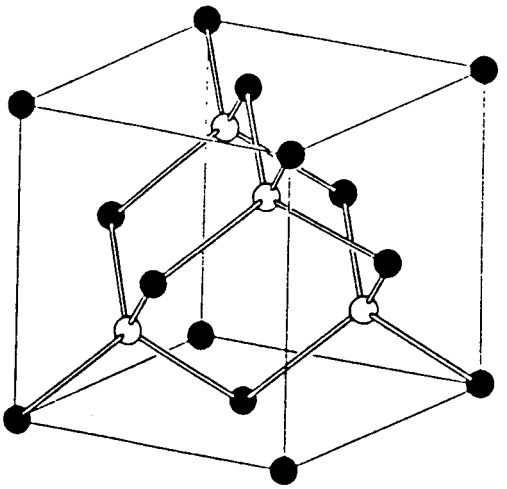

Figure 4.1 A sphalerite unit cell.

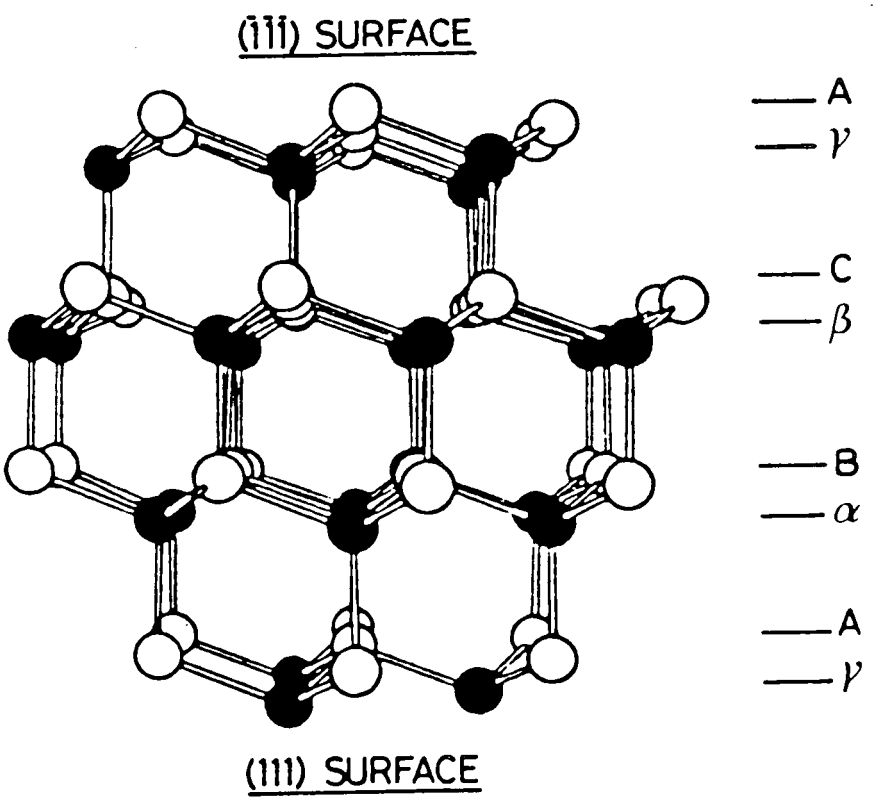

Figure 4.2 Polar {111} surfaces in the sphalerite structure.

feature of this structure is the absence of any centre of symmetry. This gives rise to the piezoelectric, electrooptic and piezobirefringent properties encountered in CdTe [3]. Some crystal surfaces, notably {111} , exhibit crystallographic polarity, that is (hkl) and $(\bar{h}\bar{k}\bar{l})$ planes are non-equivalent (see Figure 4.2). This is a result of the absence of a centre of symmetry and the high density of bonds present in the double atomic layers such as those labelled γA, αB and βC in Figure 4.2. Conventionally [4] the close packed plane terminated by metal atoms is called the (111) or A face whereas that terminated by non-metal atoms is called the $(\bar{1}\bar{1}\bar{1})$ or B face. Many properties of polar {111} surfaces in CdTe differ considerably. For example etch pit geometries [5], the bulk growth rate from the vapour phase [6] and the quality of epitaxial films of CdTe and $Cd_xHg_{1-x}Te$ grown by MOCVD [7] are markedly different on (111) and $(\bar{1}\bar{1}\bar{1})$. In the case of X-ray diffraction from centrosymmetric crystal structures, the intensities from (hkl) and $(\bar{h}\bar{k}\bar{l})$ planes are identical. This is known as Friedel's law. However, when the radiation used in a diffraction experiment is chosen so as to be below the absorbtion edge of one of the elements in a sphalerite compound, then Friedel's law does not apply. Using this so called anomalous X-ray diffraction effect, Warekois et al [8] identified the (111) and $(\bar{1}\bar{1}\bar{1})$ faces of a range of II-VI compounds and correlated the results with the differences in etching behaviour observed on opposite polar faces. Fewster and Whiffin [9] repeated the experiment for CdTe and obtained the definition of polarity in that material which is currently accepted (see §5.2.1).

Crystallographic polarity introduces the possibilities of

some important geometric variants to defects in the sphalerite structure which need not be considered in crystals having the diamond cubic structure. The dangling bonds at dislocation cores may be either metal or non-metal types for example [5]. Also the crystallographic polarity of adjacent grains can have a profound effect upon the properties of grain boundaries. An interesting example of this is the case of first order twin boundaries described in §4.4.2.2.

§ 4.3 Dislocations

§ 4.3.1 Introduction

In this section some properties of dislocations which are of relevance to experimental observations discussed later in the thesis are reviewed. Since sphalerite is based on a fcc lattice many of the properties of dislocations present in it correspond closely to those in the fcc structure. For this reason the literature available on the subject of dislocations in fcc metals is of particular relevance to the present work. More detailed coverage of the topics discussed in this section can be found in the books by Cotterel [10], Hirthe and Lothe [11], Hull [12] and Read [13].

§ 4.3.2 Perfect a/2<110> and Partial a/6<211> Dislocations

A common dislocation in both the fcc and sphalerite structure has a Burgers vector of a/2 <110> and is illustrated in Figure 4.3a for the fcc structure. The observed slip direction in the sphalerite structure is <110> . However, consideration of the close packed layer of spheres in Figure 4.4 shows how it is energeti-

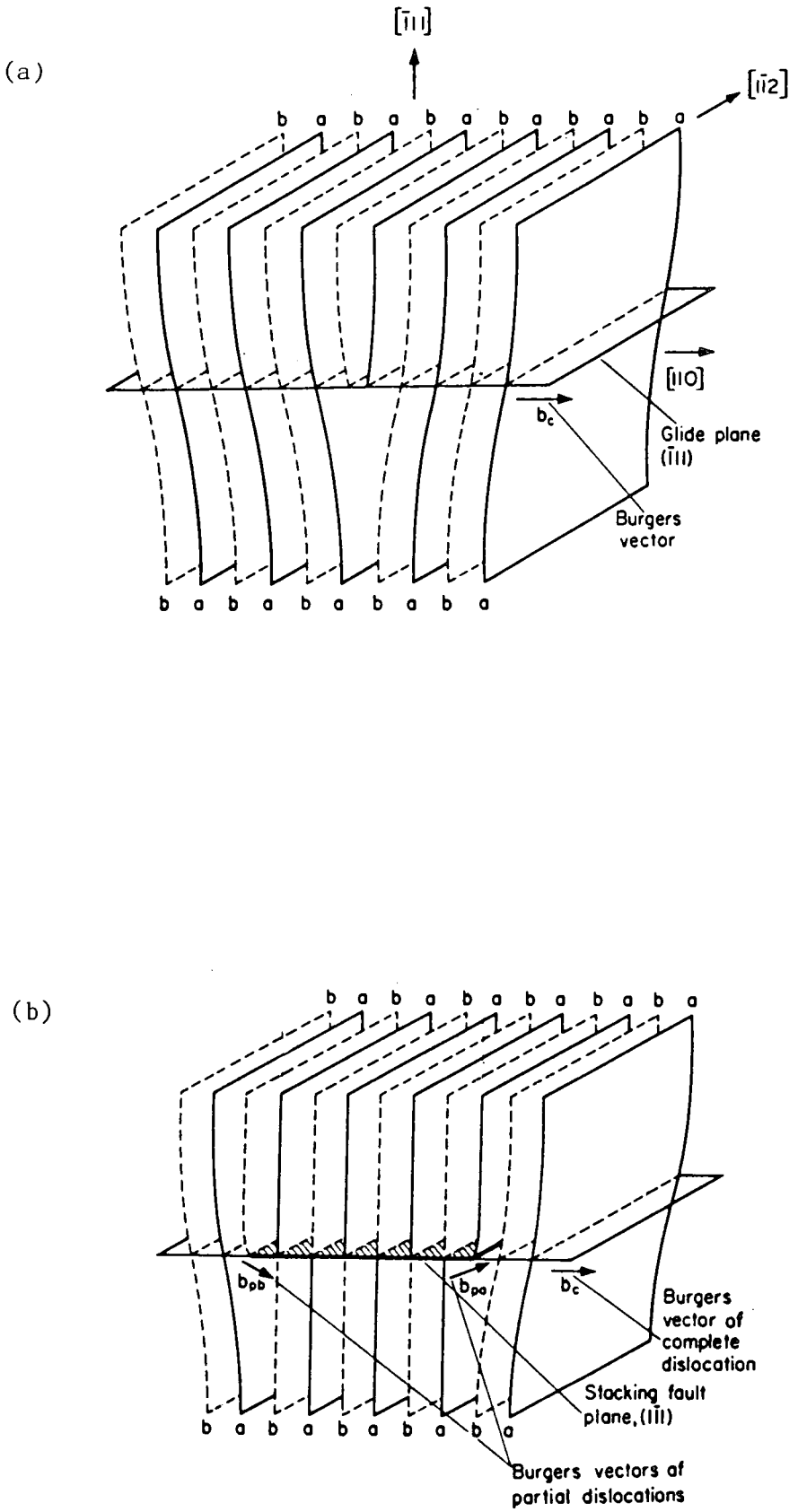

Figure 4.3 Undissociated (a) and dissociated dislocations (b) in the fcc structure.

cally favourable for slip to proceed via two <211> directions rather than directly along <110>. It is for this reason that a/2 <110> dislocations can dissociate into two a/6 <211> partial dislocations to form an extended dislocation. Frank's rule [12] states that the energy of a dislocation is proportional to the square of it's Burgers vector. Using this relationship we see that the dislocation reaction $a/2\ \langle 10\bar{1}\rangle \rightarrow a/6\ \langle 2\bar{1}\bar{1}\rangle + a/6\ \langle 11\bar{2}\rangle$ is energetically favourable. The relationship between the Burgers vectors of the dislocations involved in this reaction is illustrated in Figure 4.4. Figure 4.3a shows how an a/2 <110> edge dislocation in the fcc structure is comprised of two extra {110} half planes of atoms. The dissociation of a dislocation involves the independent movement of these two partial dislocations as in Figure 4.3b.

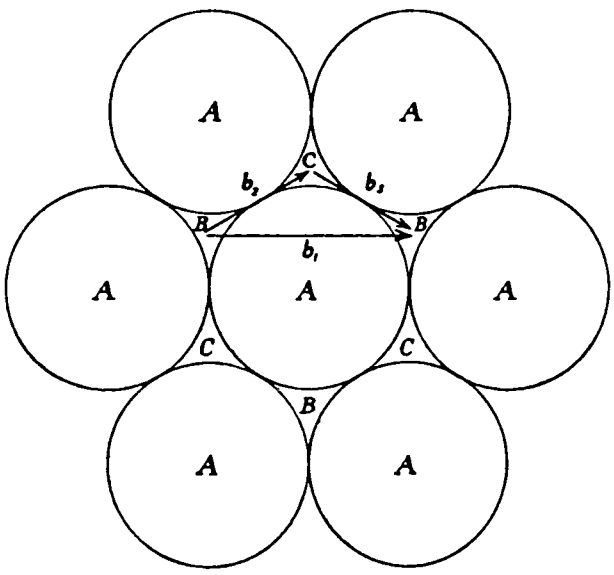

Figure 4.4 Slip directions on a close packed plane of spheres.
$b_1 = a/2[10\bar{1}]$, $b_2 = a/6[2\bar{1}\bar{1}]$, $b_3 = a/6[11\bar{2}]$.

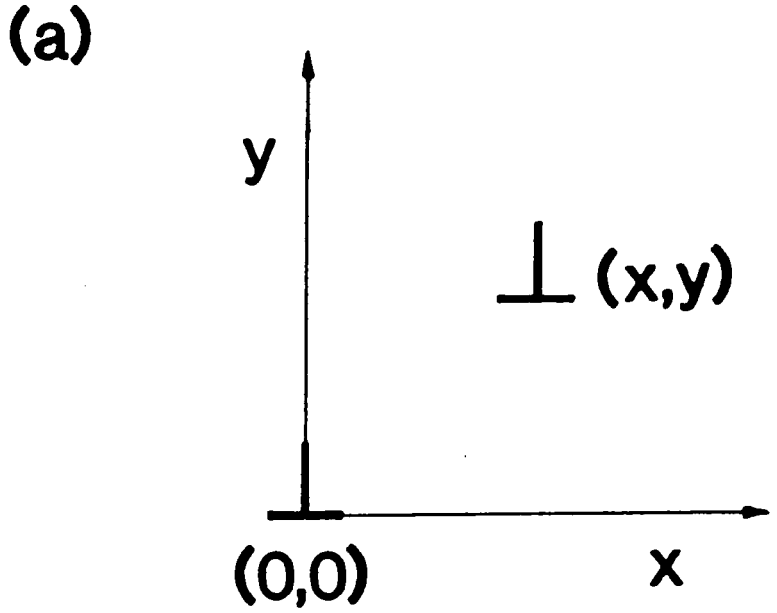

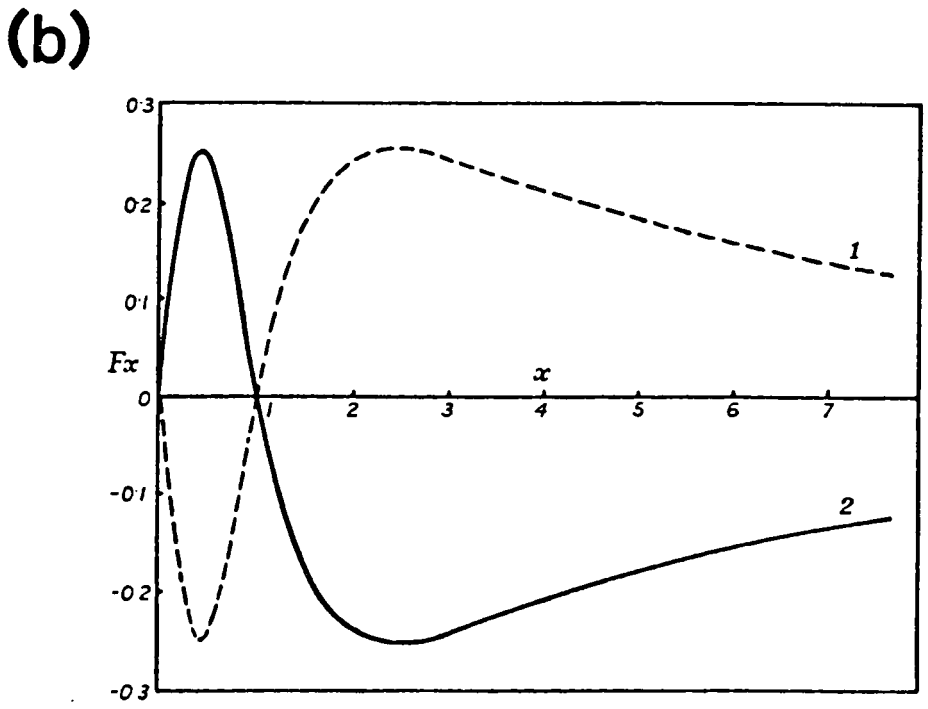

Figure 4.5 The forces of interaction between parallel edge dislocations.
(a) Positions of the dislocations.
(b) Interaction forces for (1), dislocations of like sign and (2), dislocations of opposite sign. The units of Fx are $\mu b^2 / 2\,\Pi(1-\nu)y$ (see ref[10]).

the most stable configuration of parallel edge dislocations of like sign is achieved when they lie one above another. This is the arrangement of dislocations found in low angle tilt boundaries.

§ 4.3.4 Polygonisation and Dislocation Arrays

If a crystal is plastically bent then edge dislocations will form on a number of parallel slip planes to accomodate the strain, as in Figure 4.6a. Subsequent annealing can lead to the formation of straight dislocation arrays, as shown in Figure 4.6b. This behaviour was first shown experimentally for Al [15] and silicon-iron [16]. Such dislocation rearrangement reduces the strain energy stored in the material after deformation and the dislocations also achieve the stable energy configuration described in §4.3.3. This process of rearrangement by slip and dislocation climb is called polygonisation. Since dislocation climb involves the movement of point defects, complete polygonisation can only occur at high homologous annealing temperatures. Dislocation arrays formed in this way constitute simple low angle grain boundaries as illustrated in Figure 4.7. The distance D between adjacent dislocations in the boundary is given by $D = b/\theta$ where b is the Burgers vector and θ is a small angle of tilt between adjacent grains. As the tilt angle increases the distance between adjacent dislocations decreases: The term low angle grain boundary is only applied to those boundaries in which the dislocations remain discre . In practice this implies a tilt angle of less than about 1^{o}. More complex dislocation structures are found at low energy boundaries which do not lie on symmetric positions with respect to the adjacent grains or else are not simple tilt boundaries.

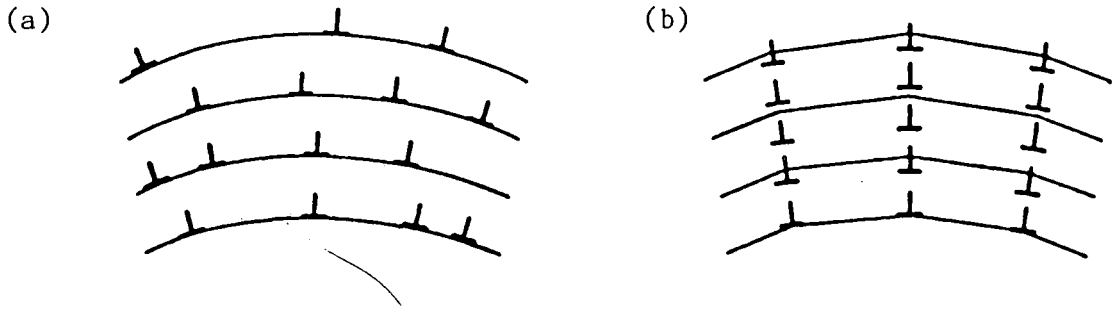

Figure 4.6 Slip and polygonisation.
(a) Edge dislocations in a plastically bent crystal.
(b) Polygonisation walls formed during annealing.

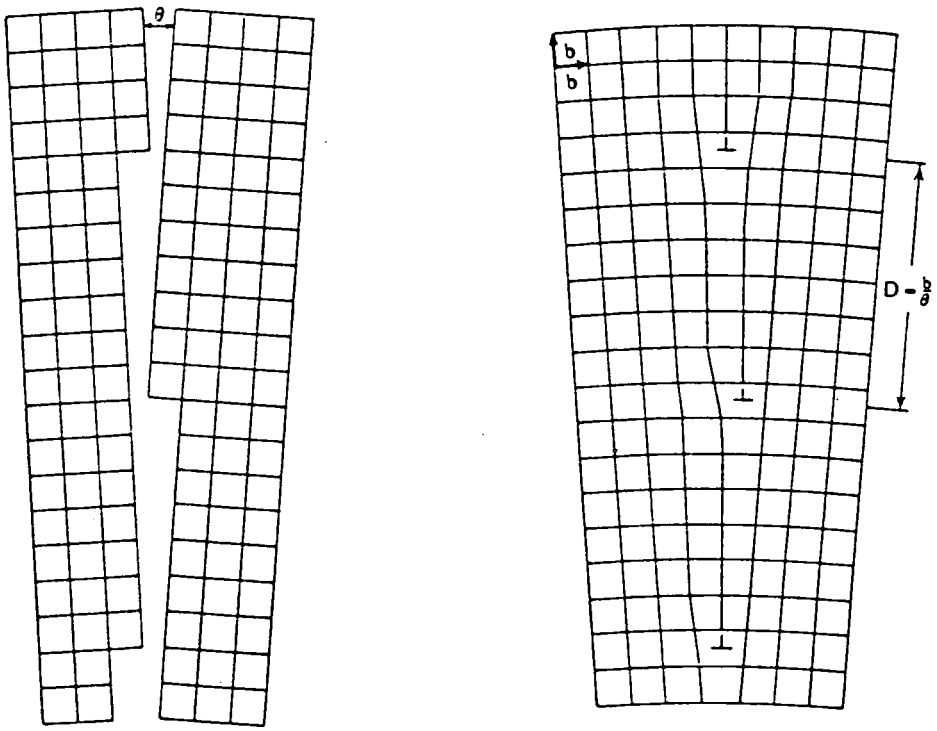

Figure 4.7 A symmetric low angle tilt boundary.

A number of these are described by Read [13]. Low angle grain boundaries are sometimes referred to as sub-grain boundaries or polygonisation walls.

§ 4.4 Grain Boundaries and Twins

§ 4.4.1 Grain Boundaries

In an arbitrary grain boundary both the interfacial plane and the axis of relative rotation of the grains may have any orientation. Thus a general grain boundary has five degrees of freedom: Three account for the orientation of the axis of rotation between adjacent grains and two define the orientation of the interfacial plane. The simplest type of grain boundary to visualise is the symmetric tilt boundary where the grains are related by symmetric rotations about an axis which lies in the boundary plane. Figure 4.7 shows how this type of boundary is associated with a dislocation array. The energies of boundaries of this type having low tilt angles were calculated by Read and Schockley [17]. They found the relationship between the energy per unit area, E and the tilt angle, θ to be of the form

$E = E_o \theta (A_o - \ln\theta)$ where A_o is a parameter related to the core energy of the dislocations and E_o is a constant related to the elastic constants of the material. This relationship has been verified experimentally for a number of systems. A comparison of the theoretical curve with the experimental data obtained by Aust and Chalmers [18] for tilt boundaries in lead is given in Figure 4.8. This shows that there is excellent agreement between the theoretical and experimental results even at high values of θ where the assumption that the boundary dislocations

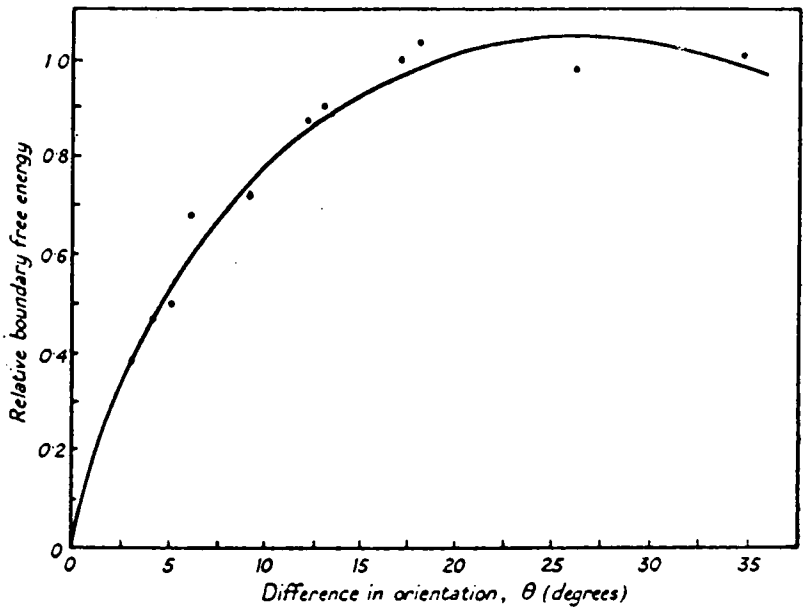

Figure 4.8 A comparison of experimentally obtained values of grain boundary energies (•) with the theoretical curve (–) for tilt boundaries in lead (see ref.[18]).

remain discreet is invalid. However, cusps or minima in the E– θ curves are expected when values of θ corresponding to 'special' low energy grain boundaries are encountered. Such boundaries correspond to 'coincidence' boundaries for which the superimposition of atoms from the two grains generates a set of lattice points which are common to both grains. This is termed the coincidence lattice. The ratio of the density of lattice points to the density of coincidence lattice points is the Friedel index, Σ [19] which is unique for a given type of boundary. Table 4.1 lists the angles of tilt about <110> axes associated with the five coincidence boundaries having the lowest Σ values, that is the highest densities of coincidence lattice points. Similar data for a variety of low index tilt axes is listed by Brandon et al [20]. Friedel indices of $\Sigma = 3$ and $\Sigma = 9$ for <110> tilt axes correspond to first and second order twin boundaries respectively. Twinning is discussed

in the next section.

Table 4.1 Tilt Angles About a <110> Axis Associated With Low Index Coincidence Site Lattices. (From Reference [20]).

Σ	Tilt Angle
3	70.5°
9	38.9°
11	50.5°
17	86.6°
19	26.5°

§ 4.4.2 Twins

§ 4.4.2.1 Introduction

Grains which are related to one another by a simple symmetry relationship involving low index crystal directions and planes are said to be in twin orientation to one another. Common twinning relationships between grains are characterised by reflections or rotations which bring atoms on each side of the boundary into coincidence. Alternatively, twin boundaries in cubic structures may be described as tilt boundaries about <110> axes. The interfacial energies of twin boundaries have been measured for Cu, Cu-Al alloys, Ni and stainless steels and were found to have energies of between 0.01 and 0.04 of those of random grain boundaries [21]. The tilt angles corresponding to twin orientations are

therefore at cusp (low energy) positions on the E-θ curves described in §4.4.1. If part of a crystal is in a twin orientation with respect to an adjacent part, it is usual to refer to the smaller grain as the twin and the larger one as the host crystal or matrix. Twins may constitute large grains, lamellae or small regions within the bulk of the host crystal (microtwins). The following sections outline some of the features of twinning which are relevant to the observations of twins in CdTe described in Chapter 6 and the geometric models of twin boundaries presented in Chapter 7.

§ 4.4.2.2 First Order Twins

The simplest and most commonly observed type of twin in materials having the fcc, diamond and sphalerite structures is the first order 'coherent' twin. This type of twin boundary is a <110> tilt boundary with $\Sigma = 3$ and a tilt angle of $70^{\circ}32'$ [22], the most common boundary plane being {111}. Twins of this type are common in fcc metals such as Au [23] and Ag [24], in diamonds [25] and cast Ge [26] which has the diamond cubic structure and also in crystals of both III-V [27,28] and II-VI compounds [1] having the sphalerite structure. Coincidence site lattice models (see Chapter 7) of $\Sigma = 3$ boundaries in the diamond cubic structure were first drawn by Ellis and Treuting [22]. Kohn [29] later systematically drew coincidence site lattice models for this and other types of twin boundaries. Hornstra subsequently produced models of a variety of <110> [30] and <100> [31] tilt boundaries in the diamond cubic structure.

A tilt angle of $70^{\circ}32'$ corresponds exactly with the angle

between two different {111} planes. Hence the first order coherent twin boundary contains no wrong bonds and its formation may be described in terms of the shifting of successive double atomic layers from one stacking position to another. For example, in the diamond cubic structure the close packed layers of atoms are stacked according to the sequence AABBCCAABB... where atoms designated by the same letter are stacked one above the other along a <111> axis. The stacking positions are indicated in Figure 4.4. In the twinned crystal this arrangement becomes AABBCCBBAA..., that is the double atomic layer AA moves to BB, BB to CC and CC to AA. The slip of a close packed layer of atoms from one stacking position to another can be effected by the passage of a partial dislocation having a Burgers vector of the type a/6 <211> over the close packed plane (see Figure 4.4). If equivalent a/6 <211> dislocations pass over successive planes in a crystal having either the fcc, diamond or sphalerite structure then the area swept out by the partial dislocations becomes a twin.

Holt [32] pointed out that for each grain boundary in the diamond structure there are two alternatives in sphalerite since the crystallographic polarity of each grain has to be taken into account. Hence the first order twin boundary in sphalerite could have a tilt angle of either $\theta = 70^{\circ}32'$ or $\Theta = \theta + 180^{\circ} = 250^{\circ}32'$. This gives rise to two possible forms of first order twin boundary in the sphalerite structure which have been named 'para-' and 'ortho-' respectively [32]. (Aminoff and Broomé [33] first recognised the possibility of different types of twin boundary in the sphalerite structure but did not consider them as tilt boundaries). The

structures of the two types of boundary and the stacking sequences of {111} planes in each case are shown in Figure 4.9. From the figure it is apparent that the para-configuration may be described in terms of a reflection over a {111} mirror plane and the ortho-configuration in terms of a twist of 180^{o} about a <111> axis. In the para-configuration the crystallographic polarity of the matrix is in the opposite sense to that of the twin whereas in the case of the ortho-twin the polarities of both are in the same sense. This simple difference has a profound effect on the structure and properties of these boundaries. The bonding at the ortho-twin boundary is undistorted from that in the bulk sphalerite structure while that at the para-twin boundary is comprised of Te-Te or Cd-Cd wrong bonds. The para-boundary might therefore be expected to have a higher grain boundary energy than that of the ortho-twin. It is also likely to be electrically active since the wrong bonds will act as recombination centres.

Boundaries lying on planes other than {111} which separate grains having the first order twin orientation with respect to one another are referred to as 'lateral' or 'incoherent' twin boundaries. The boundary planes and atomic structures of lateral twin boundaries in the diamond cubic structure have been evaluated using a simple coincidence site lattice model by Kohn [29] (see §7.1). In Cu, Cu-Al alloys, Ni and stainless steels, the interfacial energies of lateral twin boundaries were found to be from 0.25 to 0.8 of the energies of random grain boundaries [21]. Thus lateral boundaries have considerably higher interfacial energies than coherent twin boundaries but are nevertheless more energetically favourable than random grain boundaries.

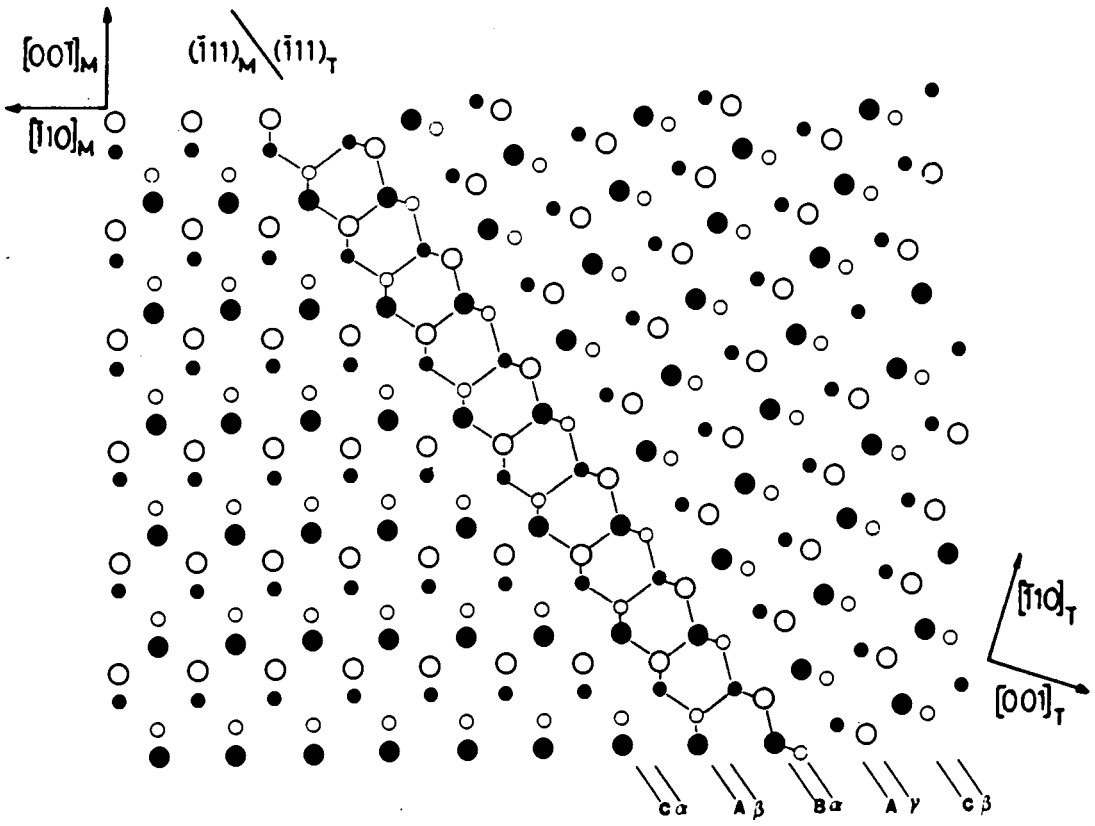

Figure 4.9a Ortho-twin boundary, $\theta = 250^{o}32'$.

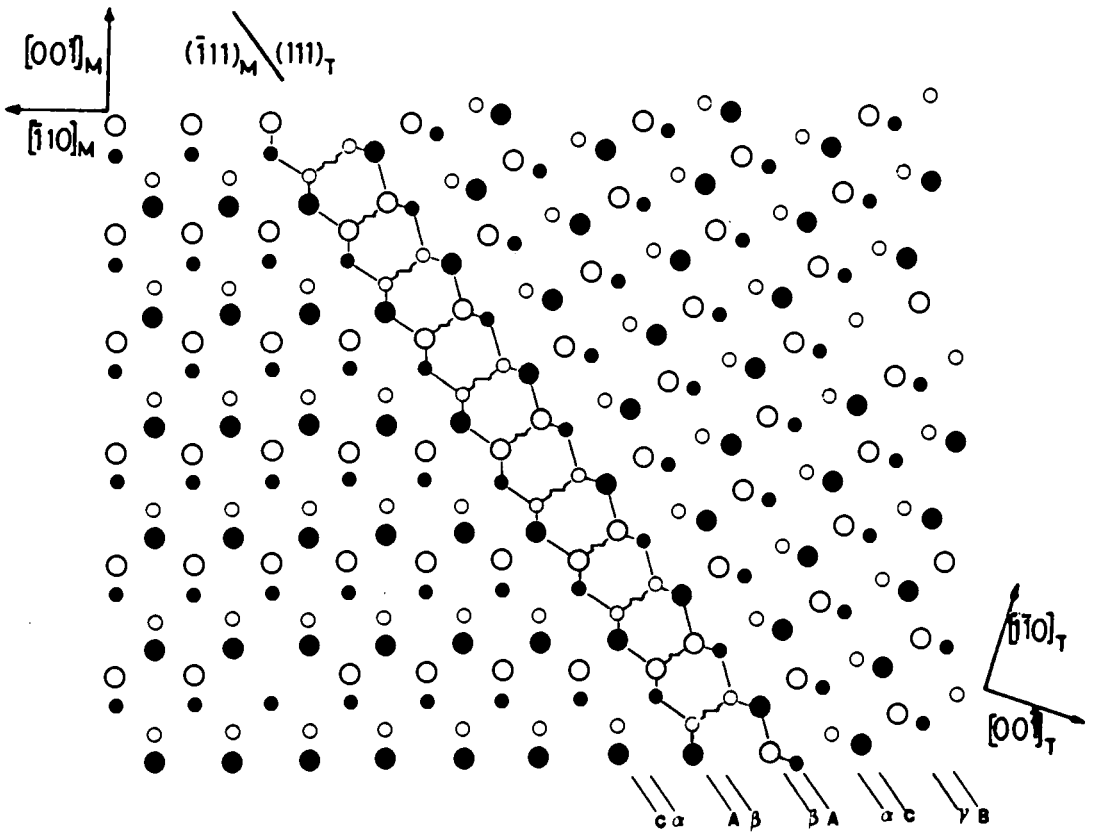

Figure 4.9b Para-twin boundary, $\theta = 70^{o}32'$.

§4.4.2.3 Second and Higher Order Twins

If part of a grain which has undergone a twinning transformation with respect to the matrix itself undergoes a second twinning transformation such that the matrix orientation is not restored, then the new grain is a second order twin. Regions of contact between the matrix and second order twins are second order twin boundaries. In general if a grain has undergone n different twinning transformations from the matrix orientation the grain will be an nth order twin. All such higher order twin boundaries may be described as <110> tilt boundaries and the tilt angle, θ for the fcc and diamond cubic structures varies according to the series $\theta = 180^{o} - n \times 70^{o}32'$ (even n) and $\theta = n \times 70^{o}32' - 180^{o}$(odd n) [29]. The Friedel index of an nth order twin boundary is $\Sigma = 3^{n}$.

§4.4.2.4 Twinning Matrices

Twinning and other crystallographic transformations may be described using a matrix notation [27,34]. Matrices characteristic of twinning operations may be used to transform the indices of planes and directions from the axes of the matrix to those of the twin. The elements of a twinning matrix may be evaluated by considering the effect of the twinning transformation on the three orthogonal unit vectors [100], [010] and [001]. The matrix elements are the indices of these directions after transformation. For example, the ortho-twinning relationship corresponds to the rotation of one part of the crystal with respect to another by 180^{o} about a <111> axis. If the twist axis is $[\bar{1}11]$ then the unit vectors transform as follows:-

$[100] \rightarrow 1/9\ [\bar{1}\bar{2}\bar{2}]$

$[010] \rightarrow 1/9\ [\bar{2}\bar{1}2]$

$[001] \rightarrow 1/9\ [\bar{2}2\bar{1}]$

The twinning matrix is thus $1/9 \begin{pmatrix} -1 & -2 & -2 \\ -2 & -1 & 2 \\ -2 & 2 & -1 \end{pmatrix} = \underline{T}_{\bar{1}11}$

First order twinning matrices corresponding to the four <111> twist axes may be derived. These are:-

$$\underline{T}_{\bar{1}11} = \begin{pmatrix} -1 & 2 & 2 \\ 2 & -1 & 2 \\ 2 & 2 & -1 \end{pmatrix} \qquad \underline{T}_{1\bar{1}\bar{1}} = \begin{pmatrix} -1 & -2 & 2 \\ -2 & -1 & -2 \\ 2 & -2 & -1 \end{pmatrix}$$

$$\underline{T}_{\bar{1}\bar{1}1} = \begin{pmatrix} -1 & -2 & -2 \\ -2 & -1 & 2 \\ -2 & 2 & -1 \end{pmatrix} \qquad \underline{T}_{11\bar{1}} = \begin{pmatrix} 1 & 2 & -2 \\ 2 & 1 & -2 \\ -2 & -2 & -1 \end{pmatrix}$$

In order to transform a direction or plane, its indices must be written as a 1 x 3 matrix which is then premultiplied by the twinning matrix. For example, if the twin axis is $[\bar{1}11]$, the indices of the plane (hkl) in the twin which is parallel to the Cd(111) matrix plane are given by

$$\begin{pmatrix} h \\ k \\ l \end{pmatrix} = \underline{T}_{\bar{1}11} \begin{pmatrix} 1 \\ 1 \\ 1 \end{pmatrix} = \begin{pmatrix} -1 & -2 & -2 \\ -2 & -1 & 2 \\ -2 & 2 & -1 \end{pmatrix} \begin{pmatrix} 1 \\ 1 \\ 1 \end{pmatrix} = \begin{pmatrix} -5 \\ -1 \\ -1 \end{pmatrix}$$

Thus (hkl) = $(\bar{5}\bar{1}\bar{1})$. Similarly the Te $(\bar{1}\bar{1}\bar{1})$plane transforms to (511). Second and higher order twins are grains which have undergone twinning transformations involving more than one twin axis. The matrix representing nth order twinning may be generated by combining the n first order matrices which define each step of the overall

transformation. In general, a transformation $\underline{T}_N$ which is achieved by performing the transformations $\underline{T}_1$, $\underline{T}_2$ ... $\underline{T}n$ in succession may be represented by the product of the transformation matrices $\underline{T}n$ ..... $\underline{T}_2\underline{T}_1 = \underline{T}_N$. In the case of second order twinning, the second order twin matrix may take one of three forms. For example, if $\underline{T}_1 = \underline{T}_{\bar{1}11}$, then $\underline{T}_2$ may be either $\underline{T}_{1\bar{1}1}$, $\underline{T}_{11\bar{1}}$ or T_{111}. The three second order twinning matrices are:-

$$\underline{T}_{2a} = \underline{T}_{111} \cdot \underline{T}_{\bar{1}11} = \begin{pmatrix} -7 & 4 & 4 \\ -4 & 1 & -8 \\ -4 & -8 & 1 \end{pmatrix}$$

$$\underline{T}_{2b} = \underline{T}_{1\bar{1}1} \cdot \underline{T}_{\bar{1}11} = \begin{pmatrix} 1 & 8 & -4 \\ 8 & 1 & 4 \\ 4 & -4 & -7 \end{pmatrix}$$

$$\underline{T}_{2c} = \underline{T}_{11\bar{1}} \cdot \underline{T}_{\bar{1}11} = \begin{pmatrix} 1 & -4 & 8 \\ 4 & -7 & -4 \\ 8 & 4 & 1 \end{pmatrix}$$

These transform the Cd(111) plane to $(1\ \bar{1}\bar{1}\ \bar{1}\bar{1})$, $(5\ 13\ \bar{7})$ and $(5\ \bar{7}\ 13)$ respectively, and thus the surface of a second order twin can have either of these orientations.

§ 4.5 Summary

This chapter has drawn attention to those types of crystal defects which were encountered during this study of as-grown CdTe crystals.

Some of the properties of dislocations were reviewed in §4.3, and in particular, the forces of interaction between parallel edge

dislocations were discussed (§ 4.3.3). The most energetically favourable arrangement of dislocations having the same Burgers vector is in the form of an array in which the dislocations lie one above another. This type of array constitutes a low angle grain boundary : Such boundaries may form by a process of dislocation polygonisation (§ 4.3.4) in crystals which have been deformed and subsequently annealed.

High angle grain boundaries were considered in §4.4.1 and in particular the relationship between the grain boundary energy and the tilt angle of simple tilt boundaries was discussed. Cusps or minima in the theoretical relationship between grain boundary energy and tilt angle occur at tilt angles which correspond to grain boundaries which are characterised by coincidence site lattices (see §4.4.1). Twin boundaries are recognised as being coincidence boundaries for which the Friedel index Σ is of the form $\Sigma = 3^n$, where n is the order of twinning. First order, lateral and second order twin boundaries were described in §4.4.2 and the formation of deformation twins by the passage of a/6 <211> dislocations over successive {111} planes is mentioned in §4.4.2.2. The variants of grain and twin boundaries in the sphalerite structure which are geometrically possible as a result of crystallographic polarity are emphasised with particular reference to the ortho- and para- forms of the first order coherent twin boundary in §4.4.2.2. Finally, a simple method of calculating the equivalent indices of planes and directions in twins and their host lattices was described in §4.4.2.4.

REFERENCES FOR CHAPTER FOUR

1 W.L. Roth in The Physics and Chemistry of II-VI Compounds. Ed. M. Aven and J.S. Prener, North Holland, Amsterdam (1967) Ch.3 p.117.

2 H. Hartmann, R. Mach and B. Selle, Current Topics in Materials Science. Ed. E. Kaldis, 9 (1982) p.20.

3 K. Zanio in Semiconductors and Semimetals, Vol.13, Ed. R.K. Willardson and A.C. Beer.

4 J.F. Dewald, J. Electrochem. Soc. 104 (1957) p.244.

5 M. Inoue, I. Teramoto and S. Takayanagi, J. Appl. Phys. 33 (8) (1962) p.2578.

6 I. Teramoto and M. Inoue, Phil. Mag.8 (1963) p.1593.

7 J.E. Hails, G.J. Russell, A.W. Brinkman and J. Woods, J. Crystal Growth - In press.

8 E.P. Warekois, M.C. Lavine, A.N. Mariano and H.C. Gatos, J.Appl. Phys. 33 (1962) p.690.

9 P.F. Fewster and P.A.C. Whiffin, J.Appl.Phys. 54 (8) (1983) p.4668.

10 A.H. Cotterel, Dislocations and Plastic Flow in Crystals, Clarendon Press, Oxford (1953).

11 J.P. Hirth and J.Lothe, Theory of Dislocations, McGraw-Hill (1968).

12 D. Hull, An Introduction to Dislocations, Pergammon Press. 2nd Ed. (1975).

13 W.T. Read, Dislocations in Crystals, McGraw-Hill, London (1953).

14 S. Takeuchi, K. Suzuki and K.Maeda, Phil.Mag.A. 50(2) (1984) p.171.

15 R.W. Cahn, J.Inst. Metals,76 (1949) p.121.

16 C.G.Dunn and F.W. Daniels, Trans.Amer.Inst.Min. Met.Engrs.191 (1951) p.147.

17 W.T. Read and W.Schockley, Phys.Rev.78(1950) p.275.

18 K.T.Aust and B.Chalmers, Proc.Roy.Soc.A204 (1950) p.359.

19 D.Whitwham, M.Mouflard and P.Lacombe, Trans.Amer.Inst.Min. (Metall) Engr. 191 (1951) p.1070.

20 D.G. Brandon, B.Ralph, S.Ranganathan and M.S.Wald, Acta Met. 12 (1964) p.813.

21 L.E. Murr, Interfacial Phenomena in Metals and Alloys. Addison-Wesley. (1975).

22 W.C.Ellis and R.G. Treuting, Trans Amer.Inst.Min.(Metall)Engrs, 191 (1951) p.53.

23 D.W.Pashley and M.J.Stowell, Phil.Mag.8 (1963) p.1605.

24 J.W.Matthews, Phil.Mag.7 (1962) p.915.

25 C.B.Slawson, Am.Min.,35 (1950) p.193.

26 W.C.Ellis and J.Fageant, Trans.Amer.Inst.Min.(Metall)Engrs. 200 (1954) p.291.

27 K.F.Hulme and J.B.Mullin,Solid State Electronics, 5 (1962) p.211.

28 A.Steinemann and U.Zimmerli, Solid State Electronics, 6 (1963) p.597.

29 J.A.Kohn, Am.Min.43 (1958) p.263.

30 J.Hornstra, Physica 25 (1959) p.409.

31 J. Hornstra, Physica 26 (1960) p.198.

32 D.B. Holt, J.Phys.Chem.Solids. 25 (1964) p.1385.

33 G.Aminoff and B.Broomé, Zeitschrift für Kristallographie und Mineralogie (Leipzig) 80 (1931) p.355.

34 A.Kelly and G.W. Groves, Crystallography and Crystal Defects, Longmann, London (1970) Ch.10 p.290.

CHAPTER FIVE

POLISHING AND ETCHING CdTe

§5.1 Introduction

This Chapter is concerned with the polishing and etching of CdTe crystals. The cutting and mechanical polishing procedures employed in this work are described in §5.2.2 while chemical polishing is discussed in §5.2.3. Particular attention is paid to the selection of a suitable chemical polish for CdTe (§5.2.3.1), to the appraisal of surfaces which have been polished with a solution of bromine in methanol (§5.2.3.2) and to the development of a mechanochemical polishing machine for CdTe substrates (§5.2.3.3). The use of chemical etchants to reveal the crystallographic polarity of CdTe is reviewed in §5.3.2 and the ability of three different etchants to distinguish between {111} polar surfaces is correlated in §5.3.3. The characteristics of three specific defect etchants used elsewhere in this work are described in §5.4, and in particular the formation of faceted etch pits by Inoue's EAg-1 reagent is examined.

§5.2 Polishing CdTe Substrates

§5.2.1 Introduction

The preparation of pristine crystal surfaces is of utmost importance in the fabrication of semiconductor devices [1,2]. For example, the presence of mechanical damage, surface contaminant layers, or nonstoichiometric films on a substrate's surface will undoubtedly have an effect upon the quality of epitaxial layers grown on such surfaces [3,4]. Moreover, the behaviour of electrical

contacts made on imperfect surfaces will also be influenced [5]. The production of good quality surfaces is also an essential part of sample preparation prior to the investigation of the structure of crystalline specimens by either transmission electron microscopy or chemical etching. In the sections which follow the choice of polishing reagents and the polishing procedures used during this work are described, together with an assessment of the quality of the crystal surfaces produced.

§5.2.2 Cutting and Mechanical Polishing

Crystal boules were mounted on a goniometer and the largest grains in them were oriented using the Laue X-ray back reflection technique. The goniometer was then transferred directly to a Meyer and Burger diamond wheel cutting machine. The cutting process produced heavily work damaged and uneven surfaces which necessitated mechanical polishing to obtain flat surfaces which were free from cutting damage. Throughout this work mechanical polishing was usually carried out in two stages. There were:-

i) Hand polishing using 10-12 μm α-alumina powder on a glass plate to remove coarse saw marks.

ii) Polishing on a Beuhler polishing pad with 1 μm α-alumina powder, either by hand or on a 'Logitech' polishing machine. This stage of polishing yielded flat scratch-free surfaces.

The polycrystalline surface which results from mechanical polishing [6] was removed by chemical dissolution with a solution of bromine in methanol as described in the next section.

§5.2.3 Chemical Polishing CdTe

§5.2.3.1 Choice of a Chemical Polish for CdTe

A chemical polishing agent is distinct from a chemical etchant in that it dissolves a crystal's surface uniformly without preferentially removing material from the sites of crystal defects. Ideally a chemical polish should also produce a stoichiometric surface, although this is unlikely to be the case in practice.

A number of chemical polishes (and etches) for CdTe are listed by Tuck [1], Hartmann et al [2] and Gaugash and Milnes [7]. The most frequently used polish cited in the recent literature is a 2% solution of bromine in methanol which dissolves CdTe to form the soluble species $CdBr_2$ and $TeBr_4$ [5]. Other polishes such as the E reagent [8], which consists of $K_2Cr_2O_7 + HNO_3 + H_2O$, produce relatively thick surface layers which are severely depleted of Cd and contain some oxides of Te [5]. While bromine in methanol is one of the better polishes from the point of view of maintaining surface stoichiometry, the composition of surfaces of CdTe polished with this reagent is not ideal. A number of studies of bromine-methanol polished surfaces have been published, but the results are not conclusive. For example, while Gaugash and Milnes [7], using X-ray photoelectron spectroscopy (XPS), found surfaces polished with bromine in methanol to be stoichiometric, Patterson and Williams [9] detected a surface layer composed of TeO_2, Te and possibly some $TeBr_2$ using the same technique of analysis. Further XPS studies by Werthen et al [5] concluded that the surface layer was comprised of Te and some $TeBr_4$ or hydrolysed forms of it. Evidence of a 10-10Å thick layer of Te on similarly treated surfaces was obtained by Amirtharaj and Pollak [10] using Raman

scattering.

Polishing with 2% bromine in methanol was employed throughout this work. The next two sections describe the use of this solution both as a 'free' polish and in a mechanochemical polishing machine.

§5.2.3.2 Chemical Polishing With a 2% Bromine in Methanol Solution

Initial tests using the 2% bromine in methanol polish were conducted by 'free' polishing the samples, that is by immersing them in a beaker of the polishing solution and agitating gently. After polishing the samples were thoroughly rinsed in methanol and then blown dry in air. If sawn surfaces were 'free' polished without any mechanical polishing then the surfaces produced, although bright and shiny, exhibited undulations corresponding to the saw marks and were therefore unsuitable for device fabrication or defect studies. Consequently in all cases it was necessary to polish CdTe surfaces mechanically with alumina powder, as described in §5.2.2, prior to 'free' polishing. The polishing rate of a 2% solution of bromine in methanol at room temperature was determined by weight loss to be 10-15 μm per minute. The progress of the chemical polishing action of this solution on CdTe was monitored using RHEED. This technique revealed that mechanically polished surfaces of CdTe are polycrystalline which is in accordance with the findings of Russell et al [6]. A short period of chemical polishing (one or two minutes) is sufficient to remove some of the polycrystalline layer and expose the single crystal material beneath. RHEED patterns taken from such surfaces consist of patterns of spots corresponding to the single crystal substrate and sets of rings due to the presence of polycrystalline

CdTe. When a surface has been chemically polished for approximately 10 minutes all evidence of these polycrystalline rings disappears and a single crystal spot pattern, such as that in Figure 5.1 is obtained. However, two surface effects following polishing in a 2% bromine in methanol solution have been observed by RHEED in some cases.

The first of these is the presence, in RHEED patterns taken from chemically polished surfaces, of spotty polycrystalline rings which do not correspond to polycrystalline CdTe. A particularly severe example of this is shown in Figure 5.2. In this particular case evidence of this ring pattern persisted even after the chemical polishing was continued for up to 40 minutes. The interplanar spacings corresponding to these rings match with those of α-alumina

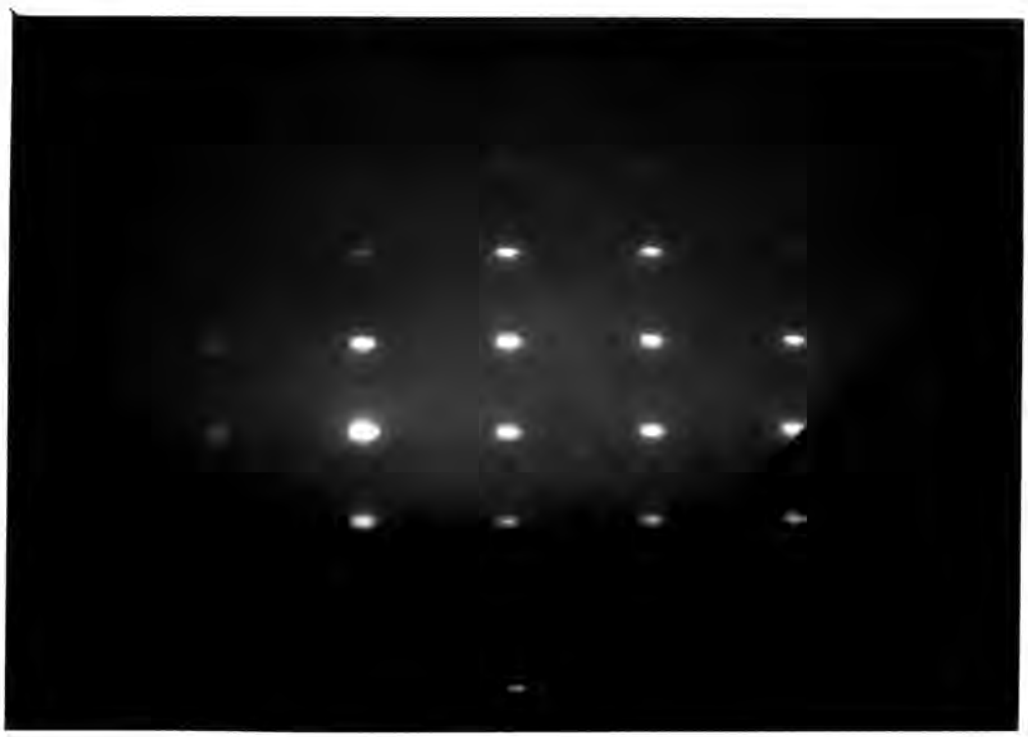

Figure 5.1 [211] RHEED pattern taken from a chemically polished surface.

given in the ASTM X-ray Powder Diffraction File (see Table 5.1). α-alumina is of course the abrasive powder used in the mechanical polishing which precedes chemical polishing. In order to investigate more fully the association of α-alumina particles with surfaces which have been both mechanically and chemically polished, 'plan view' samples were prepared for examination in the transmission electron microscope in the following way: CdTe discs, 3mm in diameter and $\frac{1}{2}$ mm thick were polished on both sides using 1 μm alumina powder before being chemically polished with a 2% solution of bromine in methanol for 1-2 minutes. They were then masked on one side using 'Lacomit' varnish and chemically thinned until perforation occured. Examination in the TEM revealed a random distribution of particles $\sim$1 μm in diameter embedded in the samples, as shown in the micrograph in Figure 5.3. The particles were confirmed to contain Al using EDAX. Characteristic lobe contrast was seen to be associated with each particle when imaged in a two beam condition. The 'line of no contrast' separating the two lobes is approximately perpendicular to the diffracting vector, as shown in Figure 5.3. These contrast features are similar to those associated with the precipitate coherency strains described in Chapter 3, although in this case they are due to the plastic strain associated with alumina particles which have become embedded in the CdTe surface. Some evidence of polycrystalline CdTe also seen in a selected area diffraction pattern taken from the area in Figure 5.3. This is undoubtedly due to the presence of some damaged material left by the mechanical polishing process on the side of the sample which had been masked off during chemical polishing.

Figure 5.2 RHEED pattern taken from a surface polished with alumina after a short period of chemical polishing.

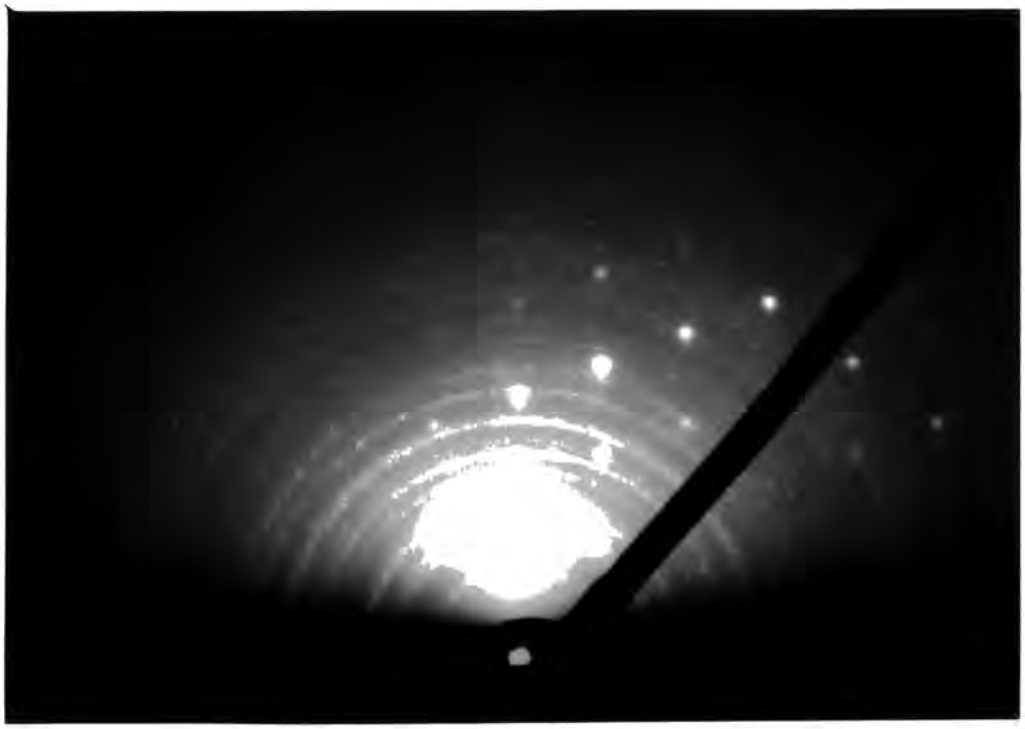

Table 5.1 Comparison of the d spacings calculated from the RHEED pattern above with those for α-alumina from the ASTM Powder File.

Observed data			ASTM data	
Ring No.	d spacing Å	Intensity	d spacing Å	Intensity %
1	3.833	(CdTe line)		
2	2.612	strong	2.552	90
3	2.423	medium	2.379	40
			2.165	<1
4	2.103	strong	2.085	100
			1.964	<1
5	1.795	medium	1.740	45
6	1.611	strong	1.601	80
			1.546	3
7	1.519	weak	1.514	5
			1.510	7
8	1.408	strong	1.404	30
9	1.379	strong	1.374	50
			1.337	1
			1.276	3
			1.239	15
10	1.2383	medium	1.2343	7

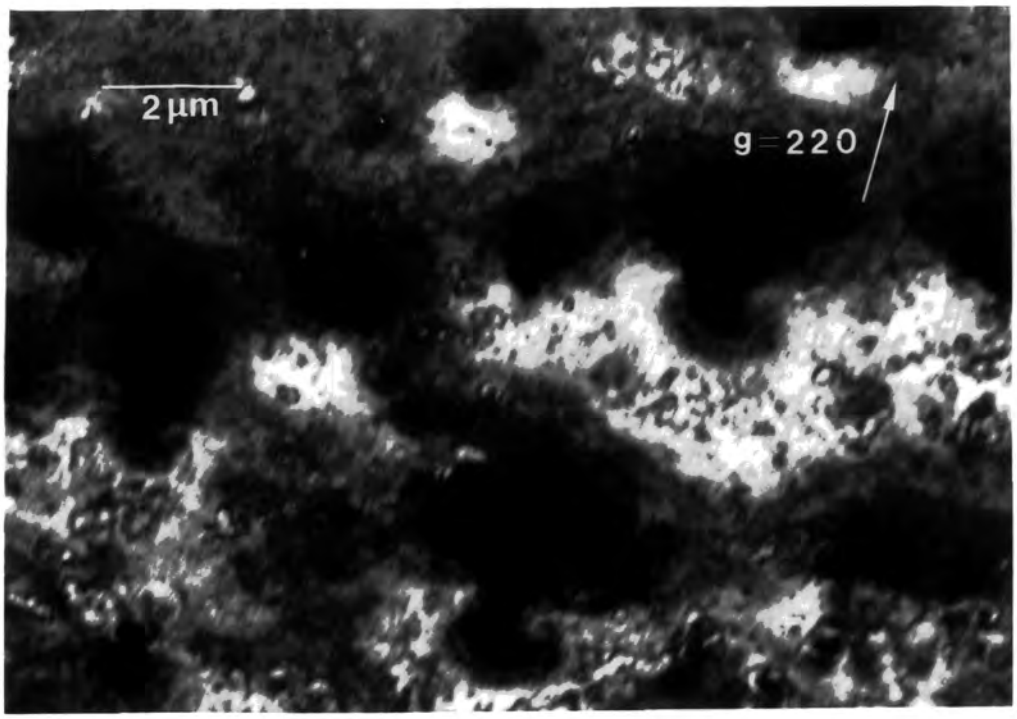

Figure 5.3 Transmission electron micrograph showing alumina particles.

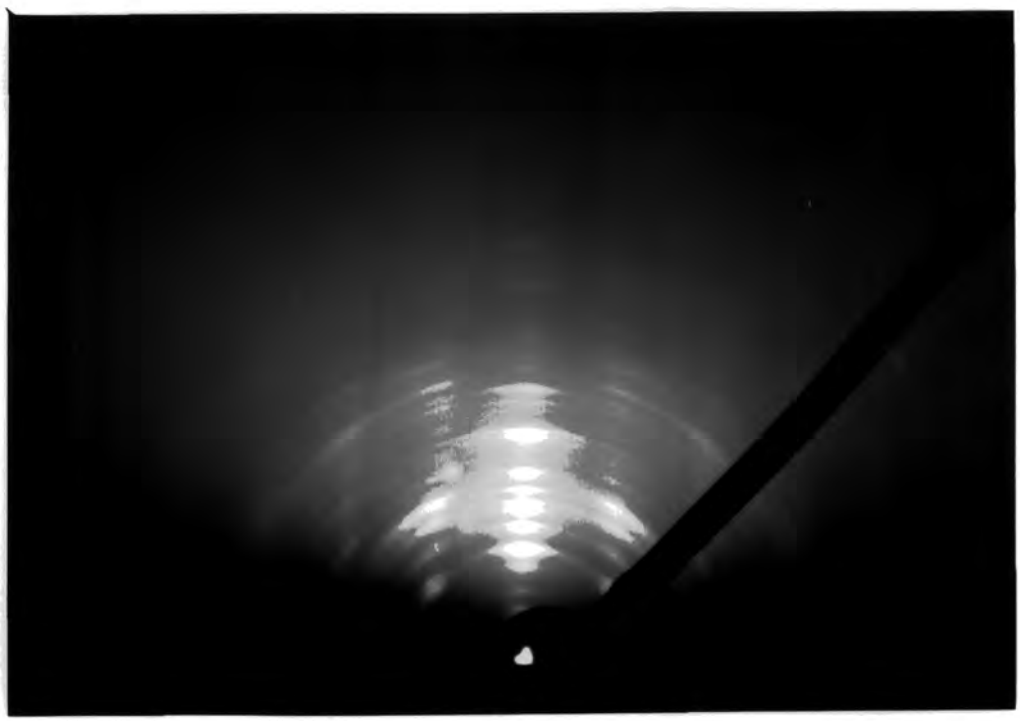

Figure 5.4 RHEED pattern taken from a bromine-methanol polished surface showing that a thin film is present.

It may be concluded that α-alumina particles become embedded in the crystal surface during mechanical polishing and persist as a surface contaminant during chemical polishing. Evidence of polycrystallinity and of the presence of particles embedded in the surfaces of other II-VI compounds which had been mechanically polished is provided by Russell et al [6].

The second effect observed on bromine-methanol polished surfaces using RHEED is a series of arcs, as shown in Figure 5.4, which persisted even after long periods of chemical polishing. This type of diffraction pattern could only be obtained when the beam was in the plane of the surface, which implies that the arcs are due to diffraction from a very thin surface layer. The arcing effect indicates that the film has a preferred crystalline orientation. Although the composition of the film has not been identified, it has been established that there are no reliable correspondences between the interplanar spacings calculated from the diffraction pattern in Figure 5.4 and the ASTM Powder File data for either Te or TeO_2. The film may be comprised of a compound of tellurium, bromine and oxygen as suggested by Werthen et al [5], but in the absence of any structural data for comparison, no definite assignment may be made.

While mechanical followed by chemical polishing is capable of producing damage-free surfaces which are relatively free from contaminants, this procedure has a number of disadvantages, namely:-

i) As indicated above, for the preparation of flat surfaces, mechanical polishing with an abrasive powder is essential prior to chemical polishing. This leads to the incorporation of abrasive particles in the crystal surfaces

which persist even after long periods of chemical polishing.

ii) Mechanically polished surfaces which are subsequently 'free' polished for long periods of time do not retain their flatness: their edges become severely bevelled and the slices become convex in shape.

iii) A thin surface layer, probably a tellurium-bromine-oxygen compound can develop during polishing.

The mechanochemical polishing method described in the next section was developed in order to overcome the problems arising from the mechanical polishing with abrasives which is necessary prior to 'free' polishing.

§5.2.3.3 Mechanochemical Polishing

In order to improve upon the quality of surfaces obtained by successive mechanical and chemical polishing procedures a mechanochemical polishing technique was developed. Basically this involves feeding the chemical polish onto a flat pad and placing the crystal sample in contact with the pad whilst moving either the pad, the workpiece, or both relative to one another.

To this end a mechanochemical polishing machine similar to that designed by Manfra and Calawa [11] was constructed. However, a number of design features were incorporated which make our polishing machine quite different from that described in the reference above : whereas Manfra and Calawa's machine operates by enabling a large sample holder to hydroplane on a high speed rotating pad, the apparatus built in this laboratory was designed to incorporate a slow polishing pad speed and a sample holder which is capable of holding individual substrates

[12] as illustrated in Figure 5.5.

The PTFE stub onto which the slices are fixed with wax is free to move in a vertical direction and thereby find its own level on the polishing pad during operation, a feature which ensures that the supply of reactants to the surface of the specimen is constantly replenished. A 1% solution of bromine in a mixture of methanol and ethelene glycol (4+1 by volume) was used for mechanochemical polishing since its viscosity reduces the possibility of the samples being scratched by the polishing pad. This solution dissolves CdTe at a rate of ∿35 μm per minute when used in the polishing machine. This rate is high compared to the polishing rate of 10-15 μm per minute encountered when free polishing using a 2% solution of bromine in methanol.

The mechanochemical polishing technique has a number of advantages over free polishing. Firstly, in most cases there is no need to perform any mechanical polishing prior to mechano-chemical polishing. This eliminates the presence of abrasive particles which act as a surface contaminant. Also the surfaces of samples polished on the mechanochemical polishing machine, although slightly bevelled at the edges, are reproducibly flat. It is significant that the thin contaminant film present on bromine-methanol polished surfaces which was observed by RHEED is less evident on mechanochemically polished surfaces. This may be due to its removal by the constant replenishment of the polishing solution encountered in mechanochemical polishing. Finally, the sample holder of the machine designed in the course of this work is capable of holding small samples or individual substrates, making it particularly suitable for use on a laboratory scale.

Figure 5:5 Mechanochemical Polishing Apparatus.

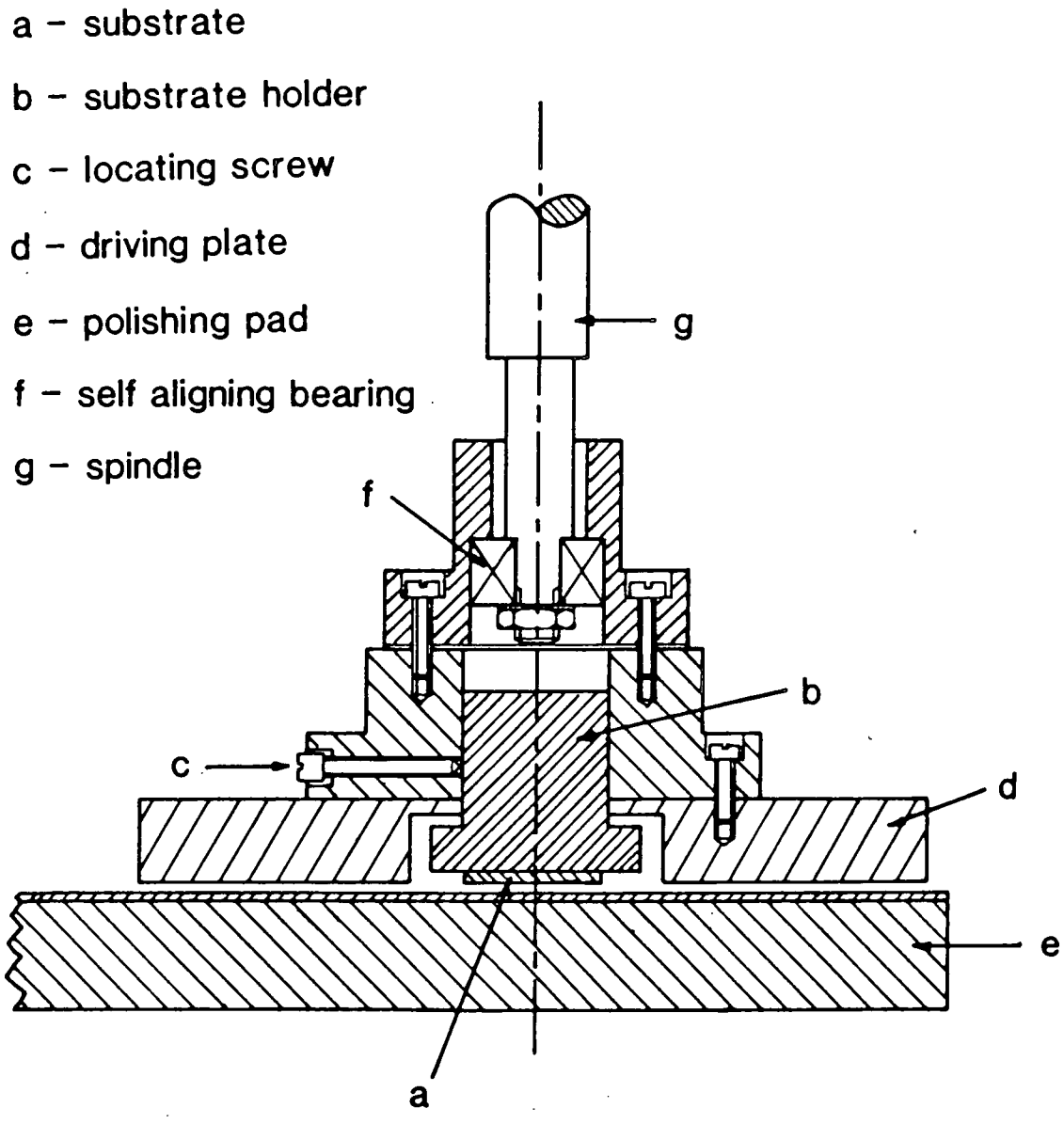

§5.3 Crystallographic Polarity

§5.3.1 Introduction

Crystallographic polarity in the sphalerite structure and its influence on a number of physical properties of crystals having this structure, including the growth of epitaxial layers of CdTe and $Cd_xHg_{1-x}Te$, has been mentioned in §4.2 in Chapter 4. In this section the use of chemical etchants to distinguish between the close packed polar faces of CdTe crystals is reviewed. Also the etching behaviour of two polar etching solutions which are reported in the literature are correlated with one another and the polar action of a new reagent which is capable of distinguishing between Cd(111) and Te($\bar{1}\bar{1}\bar{1}$) is described.

§5.3.2 Review of Polarity Identification in CdTe

The identification of the Cd(111) and Te ($\bar{1}\bar{1}\bar{1}$) faces of CdTe using the anomalous X-ray diffraction technique was first recorded by Warekois et al [13]. The two etches which are capable of distinguishing between the polar {111} faces and which are described in that work are i) HF + H_2O_2 + H_2O (3:2:1 by volume) and ii) HCl + HNO_3 (1:1 by volume). Etchant i) was found to leave the Te ($\bar{1}\bar{1}\bar{1}$) face heavily pitted and the Cd(111) face lightly pitted whereas etchant ii) leaves the Cd(111) face pitted and results in the build-up of a Te film on Te ($\bar{1}\bar{1}\bar{1}$). Fewster and Whiffin [14] subsequently reported that the latter etchant was ineffective.

Inoue et al [7] developed two etchants named EAg-1 and EAg-2 which are both comprised of $K_2Cr_2O_7$, HNO_3, H_2O but contain different amounts of $AgNO_3$. The different concentration of silver ions in the two etches (EAg-1 has a low and EAg-2 a high silver ion

concentration) controls their etching behaviour. Inoue et al [7] acknowledged that both etches are capable of distinguishing between polar faces and in a later paper [15] the results of correlating the action of EAg-1 with that of HF + H_2O_2 + H_2O (3:2:1 by volume) [13] are utilised. However, Inoue et al did not indicate which of the etch features obtained using EAg-1 are associated with which polar face.

Fewster et al [16] identified the polar faces of $Cd_xHg_{1-x}Te$ by anomalous X-ray diffraction and correlated their results with the action of the 'Polisar etch 2' [17]. However, these workers observed that epitaxial layers of $Cd_xHg_{1-x}Te$ grown on {111} CdTe surfaces were found to have reversed polarity with respect to their substrates (according to the definition of polarity due to Warekois et al [13]). This anomaly prompted Fewster and Whiffin [14] to reinvestigate the identification of the polarity of CdTe crystals by etching and anomalous X-ray diffraction. The etchant used in this work was Nakagawa's reagent [18] which consists of HF + H_2O + H_2O_2 (3:2:2 by volume). This reagent was found to produce a higher density of etch pits on the face which was identified as being the Cd (111) face by anomalous X-ray diffraction, than on the Te ($\bar{1}\bar{1}\bar{1}$) face. These findings contradict those of Warekois et al [13] and it was thus concluded that the work on CdTe reported in that reference is erroneous.

§5.3.3 Polarity Identification Using Etching Solutions

The action of three etching solutions on chemically polished {111} surfaces of CdTe crystals was investigated. The etchants used were that due to Nakagawa [14, 18], Inoue's EAg-1 reagent [7],

and a previously unreported etching solution consisting of equal volumes of HF, HNO_3 and CH_3COOH. The pitting produced on {111} faces by the Nakagawa etch and described by Fewster and Whiffin [14], has been correlated with that produced by the EAg-1 reagent by Lu et al [19] and Durose et al [20]. Photomicrographs of both types of {111} surfaces etched with each of these reactants are shown in Figures 5.6 a-d. The Inoue EAg-1 etchant produces small dark pyrimidal pits on Cd (111) (see Figure 5.6c) which is heavily pitted by the Nakagawa reagent (see Figure 5.6a). In contrast the Nakagawa reagent pits the Te ($\bar{1}\bar{1}\bar{1}$) face lightly (see Figure 5.6b) and EAg-1 develops flat bottomed triangular pits on it (see Figure 5.6d). It is worth pointing out here that the action of Inoue's EAg-1 reagent on the Cd (111) surface is not entirely consistent and that the well defined pits illustrated in Figure 5.6c do not always form: the etching is often patchy the pitted areas being interspersed with etched areas in which the pits are very small and indistinguishable from one another. For this reason an etched Cd (111) surface may sometimes look as if it is covered by a dark film after etching with this reagent. The distribution of these etch features within a given region could not always be reproduced when a slice was etched repeatedly and consequently the cause of this inconsistent etching is not known.

The results described above were used to define polarity in order to test the action of an etchant consisting of equal parts of HF, HNO_3 and CH_3COOH. An etch for 20s in this reagent followed by rinsing in water was found to leave a black coating on the Cd (111) face while the Te ($\bar{1}\bar{1}\bar{1}$) face became bright and shiny. The reaction of CdTe with this reagent is a vigorous

Figure 5.6 {111} polar surfaces etched with Nakagawa's and Inoue's reagents.

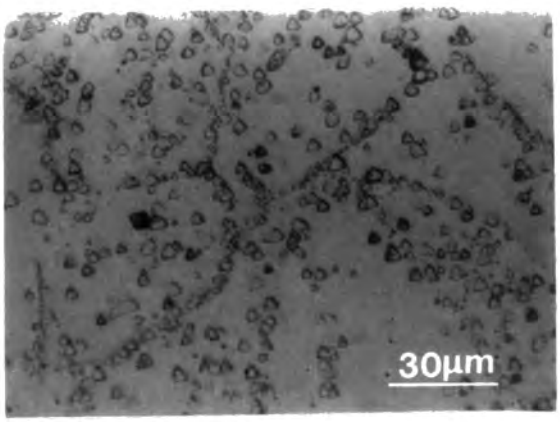

a) Cd (111) Nakagawa.

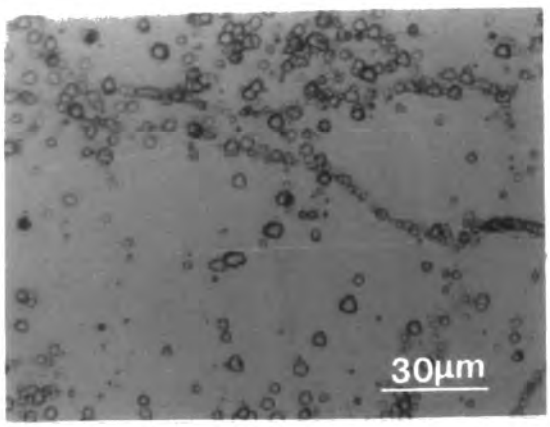

b) Te ($\bar{1}\bar{1}\bar{1}$) Nakagawa.

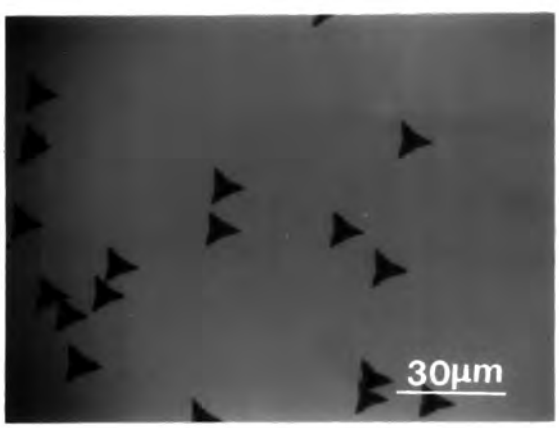

c) Cd(111) Inoue EAg-1.

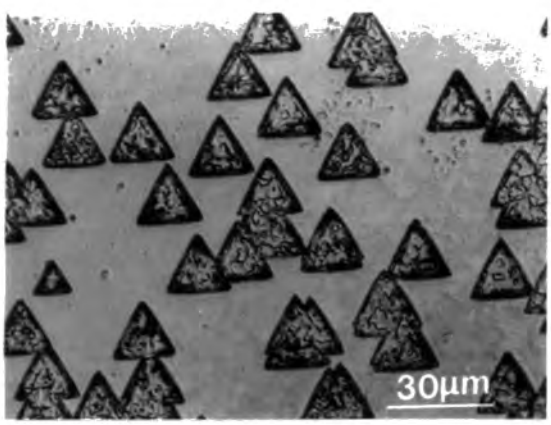

d) Te ($\bar{1}\bar{1}\bar{1}$) Inoue EAg-1.

one and is accompanied by the evolution of a brown gas which is probably NO_2 . The regions within the twin bands intersecting the Te $(\bar{1}\bar{1}\bar{1})$ faces of CdTe crystals etched were observed to be etched more slowly than the matrix orientation when using this reagent. In fact after etching for 20 s, etch steps about 50 μm in height are formed at the intersections of twin boundaries with the Te $(\bar{1}\bar{1}\bar{1})$ surface. This indicates that the etch rate of this reagent for the Te $(\bar{1}\bar{1}\bar{1})$ surface is high, probably of the order of 50 μm per minute.

It should be emphasised that throughout this thesis the crystallographic polarity of crystals of CdTe has been defined according to the work of Fewster and Whiffin [14] and hence in accordance with the etch features shown in Figure 5.6 a-d.

§5.4 Etching Solutions

§5.4.1 Introduction

An etching solution is characterised by its ability to chemically react in the regions of crystal defects at a different rate to that with which it dissolves the bulk crystal. The three etching solutions which have been used throughout this work are Nakagawa's reagent, a photoetch consisting of a solution of bromine in methanol and Inoue's EAg-1 etchant. The special features of each etchant are described below together with some experimental observations of their individual behaviour.

§5.4.2 Nakagawa's Reagent

The etchant which is commonly referred to as Nakagawa's reagent [18] consists of HF + H_2O_2 + H_2O in the ratio 3:2:2

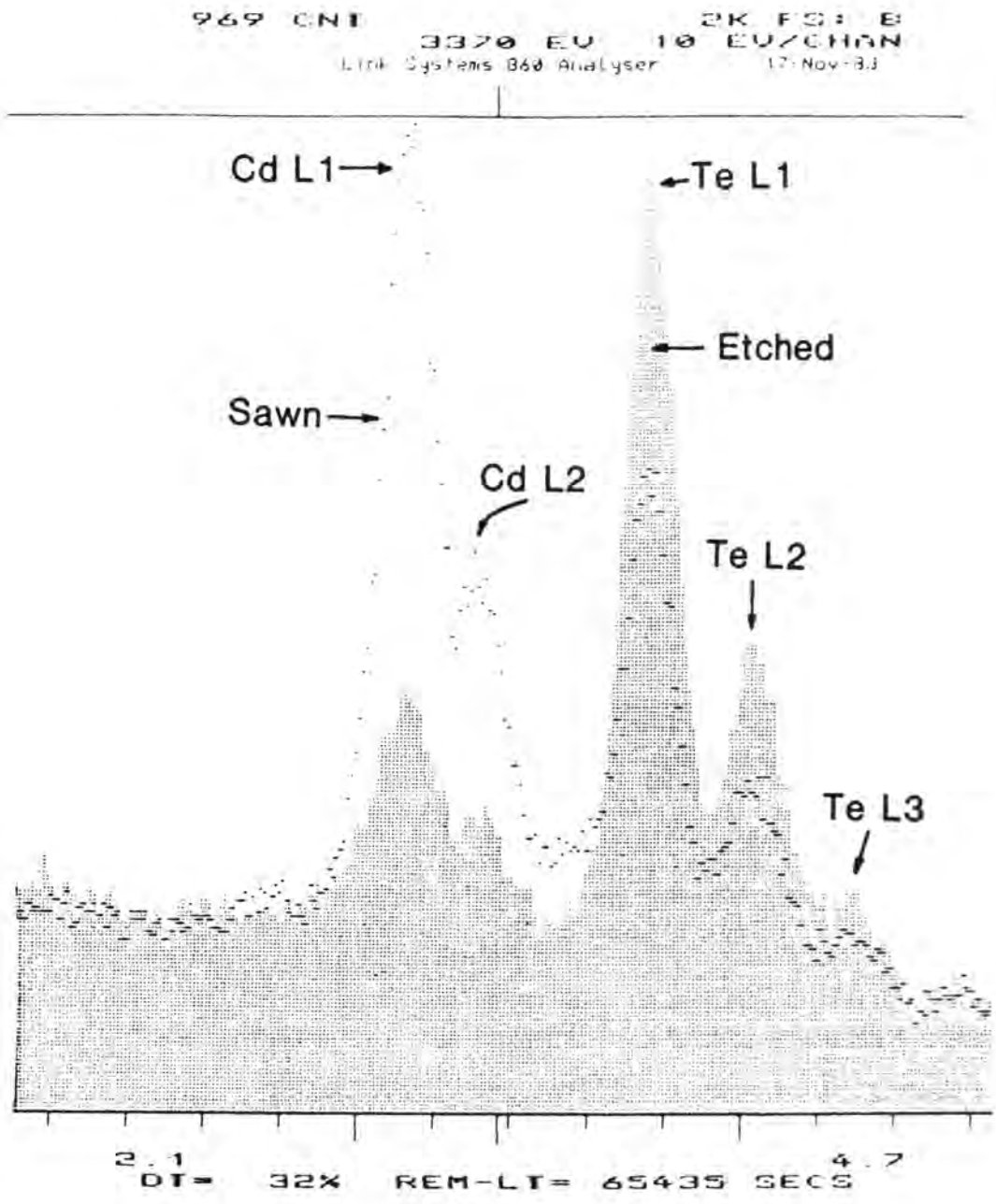

Figure 5.7 EDAX spectra accumulated from a surface etched with Nakagawa's reagent (full line) and from an untreated surface (dotted line).

Figure 5.8 RHEED pattern taken from a surface etched with Nakagawa's reagent.

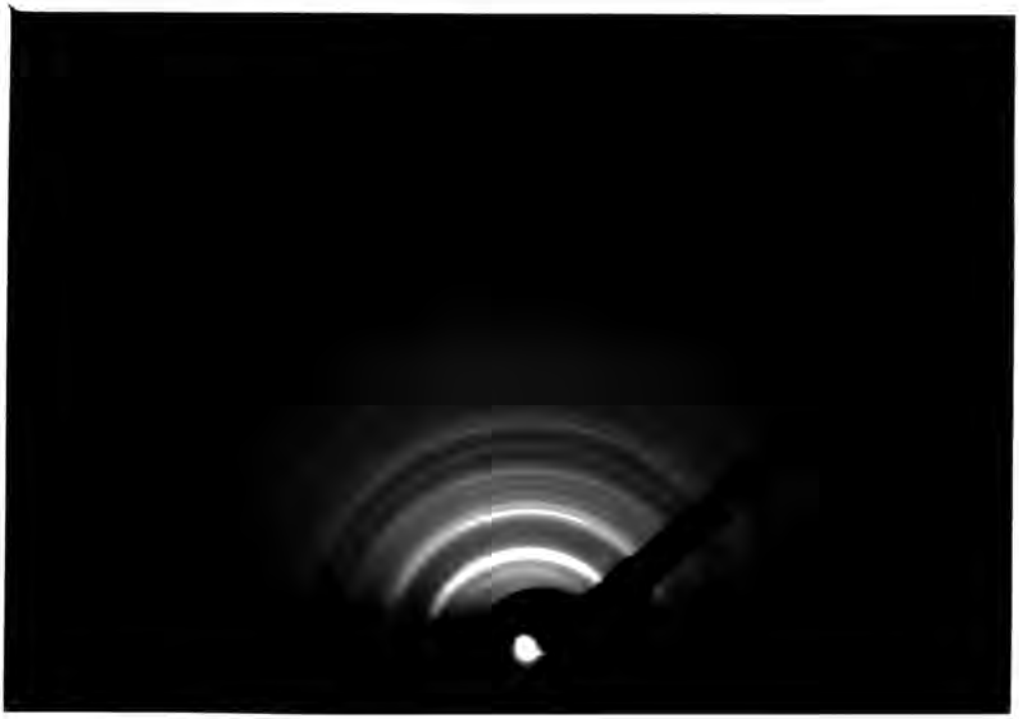

Table 5.2 Comparison of the d spacings calculated from the RHEED pattern above with those for Te from the ASTM Powder File.

Observed data			ASTM data	
Ring No.	d spacing Å	Intensity	d spacing Å	Intensity
1	3.942	medium	3.86	20
2	3.291	v. strong	3.230	100
3	3.385	strong	2.351	37
4	2.246	medium	2.223	31
5	2.103	weak	2.087	11
6	1.965	weak	1.980	8
			1.930	4
7	1.844	medium	1.835	20
8	1.789	weak	1.781	7
			1.758	2
9	1.621	weak	1.616	12
10	1.473	medium	1.479	13
			1.459	8
11	1.419	weak	1.417	8
12	1.374	weak	1.383	7
13	1.309	weak	1.309	6
			1.287	1
14	1.259	v.weak	1.257	4

by volume and is a variant of the etchant used by Warekois et al [13]. It produces etch pits on the Cd (111) face in greater density than on the Te ($\bar{1}\bar{1}\bar{1}$) face [14] and its use as a polar etchant has been described in §5.3. Nakagawa et al [18] found a 1:1 correspondence between the etch pits on the heavily pitted surface and the presence of dislocations which were imaged as dark spots by cathodoluminescence. This is the only widely accepted example of a 1:1 correspondence between etch pits and dislocations in CdTe.

After etching CdTe surfaces with the Nakagawa reagent for 1 minute, a surface film develops irrespective of the surface orientation. The colour of this film varies from black/brown to grey according to the orientation of the surface etched, thereby making this etchant particularly useful for identifying individual grains and twins. Analysis of the film by EDAX in the SEM (see Figure 5.7), shows that it contains a larger proportion of Te than an untreated sawn surface. Furthermore, RHEED patterns taken from the same etched surface contained a series of well defined polycrystalline rings (see Figure 5.8), and there is a good correspondence between the interplanar spacings calculated from this diffraction pattern and those obtained from the ASTM powder file data for Te as is shown in Table 5.1. Thus it may be concluded that the Nakagawa reagent depletes all orientations of CdTe surfaces of Cd leaving a thick layer comprised of elemental Te.

§5.4.3 Photoetching With ½% Bromine in Methanol

Although a 2% solution of bromine in methanol is a chemical

polish, a ½% solution acts as a defect etchant in the presence of illumination from a normal tungsten bulb [20,21]. The rate of dissolution of CdTe by this etchant is either inhibited or enhanced at the sites of defects depending upon both the electrical characteristics of the crystals and of the defects within them [21]. Extended defects such as grain boundaries, twin boundaries and polygonisation walls are therefore revealed either as raised or groove-like linear features. A unique feature of this etchant is that it is capable of revealing the presence of defects on all crystal surfaces, independant of their orientations.

§5.4.4 Inoue's EAg-1 Reagent

Inoue's EAg-1 reagent [8] consists of 20 ml H_2O + 10 ml conc. HNO_3 + 4g $K_2Cr_2O_7$ + 1.5 mg $AgNO_3$. This etching solution and EAg-2, which contains a higher Ag^+ ion concentration, have been the subject of a great deal of interest in the literature [see 8,15,19,20,22,23 and 24 for example]. Inoue's original work [8] with these etchants indicated that they produced etch pits which were directly related to the presence of dislocations. The evidence supporting this was i) the patterns of etch pits produced on pairs of opposite cleaved faces matched exactly, ii) the tips of etch pits formed continuous lines when depth profiled and iii) the density of etch pits was higher in deformed samples. A subsequent paper by Inoue et al [15] further shows how the two etchants are capable of distinguishing between α and β dislocations. In more recent work, [22] photomicrographs of etched pairs of opposite cleaved surfaces and of indentations, are presented which support Inoue's findings that the EAg etchants

reveal both fresh and grown-in dislocations. However, these results are not universally accepted. For example, Lu et al [19] were unable to trace the loci of etch pits by depth profiling and moreover were unable to find a correspondence between pits on either side of a 500 μm thick slice of CdTe by infra-red microscopy. Nakagawa [18] also states that the EAg etchants are incapable of revealing fresh dislocations, although it is not made clear in that work what efforts were made to ascertain this. It is worth mentioning here that the etching work presented in Chapter 8 describes arrays of etch pits produced by the Inoue EAg-1 reagent which are undoubtedly related to the presence of dislocations in sub-grain boundaries. However, in the present study attempts to observe a correspondence between the distribution of etch pits on pairs of cleaved {110} faces were not conclusive. Thus it is concluded that it is likely that the reliability of this reagent as a dislocation etchant may be variable due to:-

a) variability of the Ag^+ ion concentration which is known to influence the behaviour of this etchant,

b) the susceptibility of the etching action to differing degrees of agitation, and

c) the possibility of etching effects which are related to the decoration of dislocations with Te precipitates.

A particularly interesting feature of the Inoue EAg-1 reagent is its ability to produce etch pits having well defined crystallographic shapes on all crystal surface orientations. Inoue et al [8] found that the etch pits had facets comprised of tetrahedra of close packed planes. The scanning electron micrographs of etch pits on {100} surfaces presented by Iwanaga et al [24] firmly

support this view. Furthermore the {111} facets of the etch pits produced by EAg-1 have been identified as being Te $\{\bar{1}\bar{1}\bar{1}\}$ planes [20,23]. Evidence for this is found by simply noting that the flat bottoms of etch pits on a Te $(\bar{1}\bar{1}\bar{1})$ surface are parallel to that surface, and moreover that the edges of these pits lie along <110> directions. A model based on the formation of etch pits having facets comprised of tetrahedra of Te $\{\bar{1}\bar{1}\bar{1}\}$ planes is consistent with the appearance of pyrimidal etch pits on Cd {111} planes. Since such etch pits are visible on Cd {111} surfaces it is implicit that the rate of dissolution of the Te $\{\bar{1}\bar{1}\bar{1}\}$ planes is greater than that of the Cd {111} planes.

Describing the etch pits as being comprised of facets of Te $\{\bar{1}\bar{1}\bar{1}\}$ planes is equivalent to saying that the pits occupy spaces which may be filled with portions of tetrahedral crystallites comprised of Cd {111} facets. This suggests that cutting such a crystallite on a plane which is parallel to the etched surface under investigation is a convenient way of predicting the shapes of etch pits. This procedure is illustrated in Figure 5.9a for pits on {111} surfaces. It accounts for the main features of the flat bottomed and pyrimidal etch pits shown in the photomicrograph in Figures 5.6 c and d. However, the etch pits on Cd (111) have convex edges whereas those of the pits on Te $(\bar{1}\bar{1}\bar{1})$ are concave. These features are not accounted for by the model in Figure 5.9a. Deviations from the 'ideal' shapes of etch pits could be caused by there being a contribution to the dissolution process from the Cd {111} planes. This would imply that although the etching rate of Te $\{\bar{1}\bar{1}\bar{1}\}$ surfaces is higher than that of Cd {111} surfaces, the latter is not insignificant.

Figure 5.9 Generation of etch pit shapes by cutting a tetrahedral crystallite of {111} planes on

a) {111} and $\{\bar{1}\bar{1}\bar{1}\}$ planes, b) {511} and $\{\bar{5}\bar{1}\bar{1}\}$ planes

and c) on $\{5\ \bar{7}\ 13\}$ planes.

a)

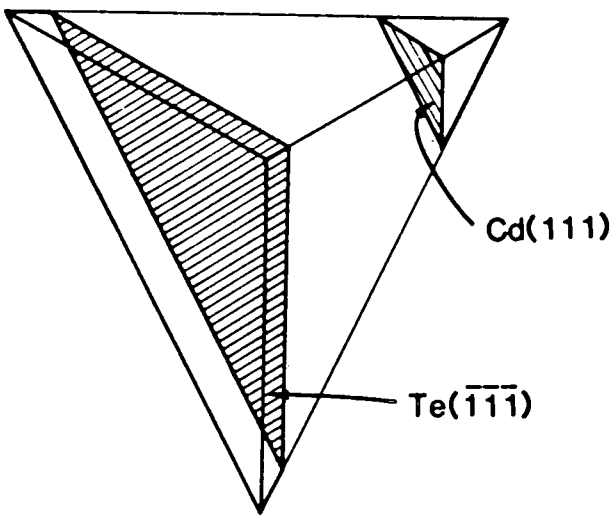

b)

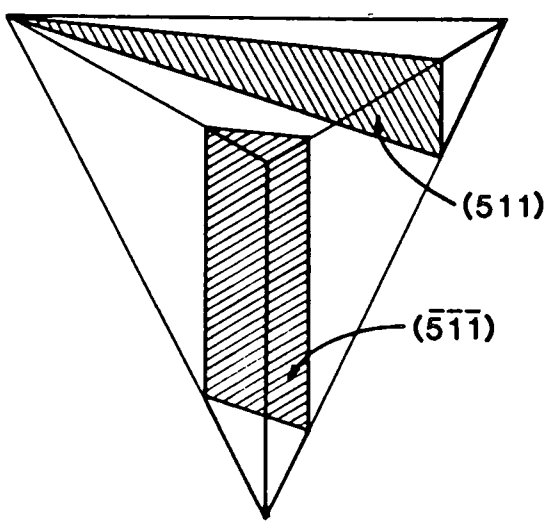

c)

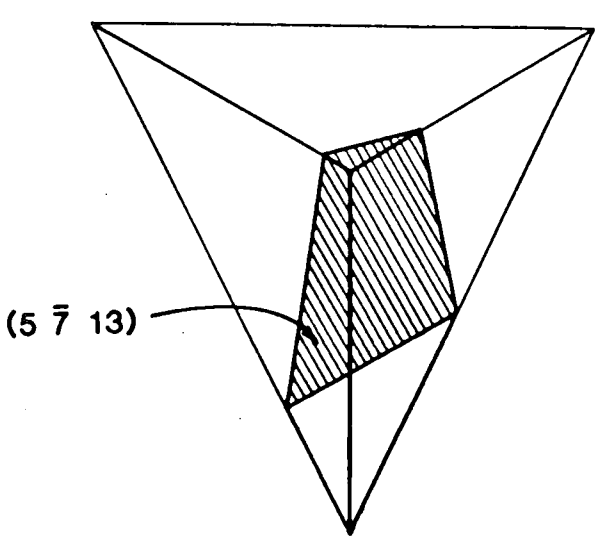

The shapes of etch pits on {511} surfaces were also investigated. Both the (511) and ($\bar{5}1\bar{1}$) orientations are readily available since these are first order twin orientations to Te ($\bar{1}1\bar{1}$) and Cd (111) respectively. The [511] direction is polar and different types of etch pit are predicted using the tetrahedral Cd {111} crystallite model, as illustrated in Figure 5.9b. The pits on ($\bar{5}1\bar{1}$) are expected to be trough shaped while those on (511) are expected to have the shapes of isosceles triangles. Pits having these shapes are observed in practice and are clearly visible on the twin bands in Figures 6.6a and b in Chapter 6. Figures 5.10a and b are photomicrographs showing these types of pits in greater detail. Their shapes are clearly similar to those predicted in Figure 5.9b and the apex angle of the isoscelese triangles was measured to be $\sim 22^{o}$ which is comparable to the calculated value of 22.62^{o}.

It was also possible to examine etch pits on the (5 $\bar{7}$ 13) plane since this is the second order twin orientation to Cd (111). Figure 5.11 shows a scanning electron micrograph of an etched surface which is intersected by a first order twin boundary which separates the ($\bar{5}1\bar{1}$) and (5 $\bar{7}$ 13) orientations. The pits on both of these planes are clearly visible and those on (5 $\bar{7}$ 13) have a distinctive shape. A further example of these pits is shown in the optical micrograph in Figure 5.12. The etch pit shape which is generated by the intersection of a {5 $\bar{7}$ 13} plane with the tetrahedral crystallite shown in Figure 5.9c corresponds well with that observed experimentally. This indicates that this model for predicting etch pit shape is valid, even for pits on irregular high index planes.

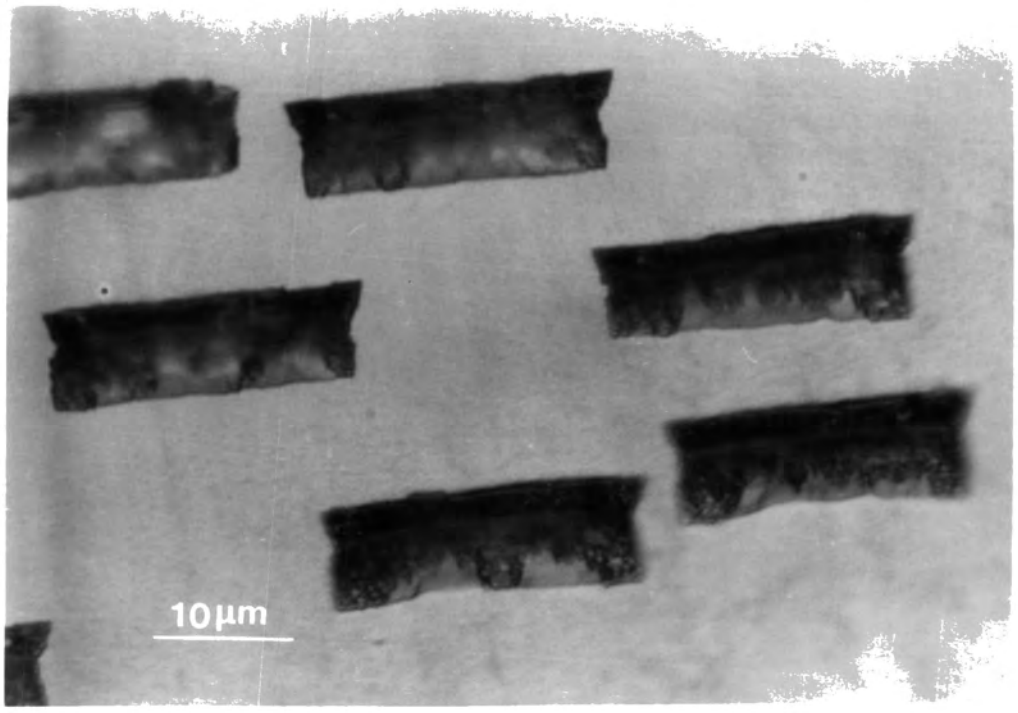

Figure 5.10 a) Etch pits on a $\{\bar{5}\bar{1}\bar{1}\}$ surface.

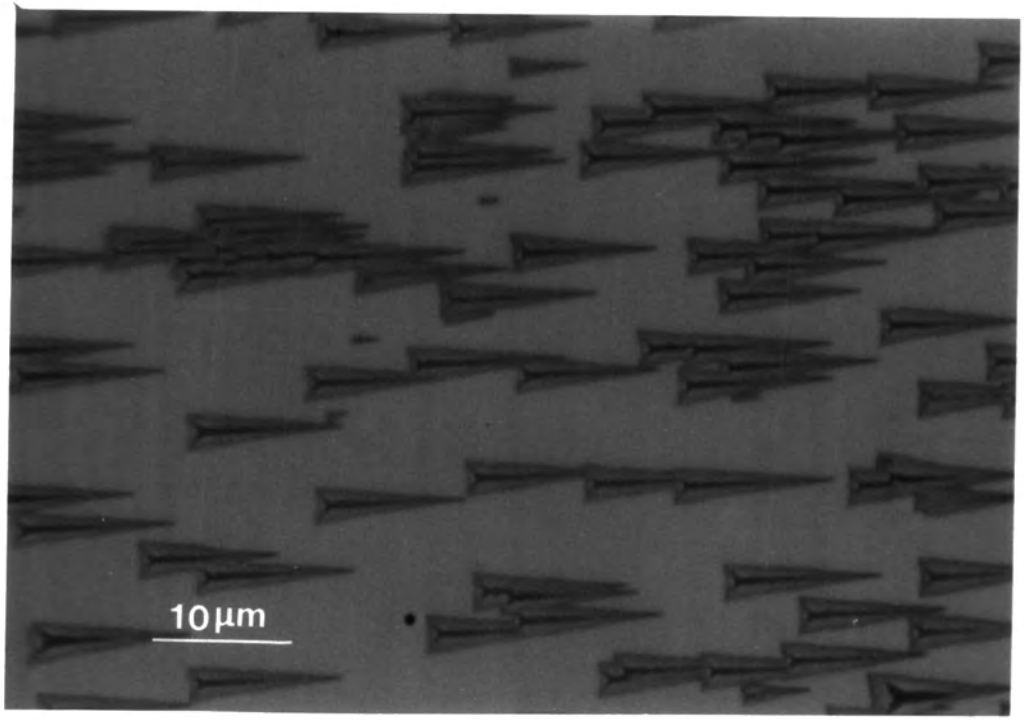

Figure 5.10 b) Etch pits on a {511} surface.

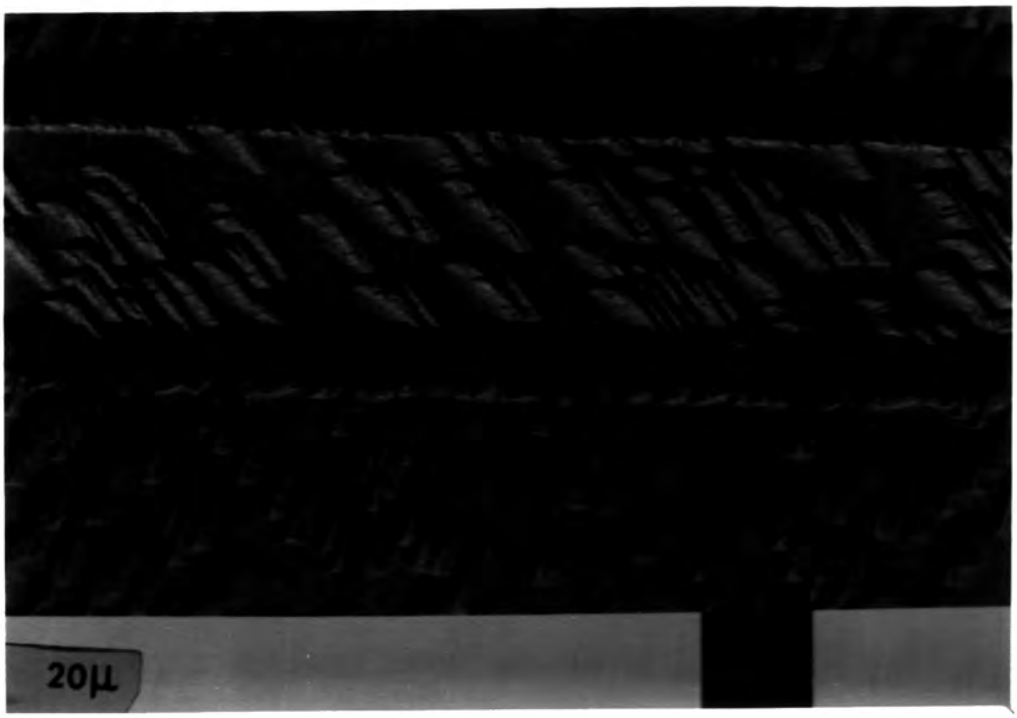

Figure 5.11 Scanning electron micrograph (backscattered mode) of an etched surface intersected by a twin boundary which separates the (511) and (5 $\bar{7}$ 13) orientations.

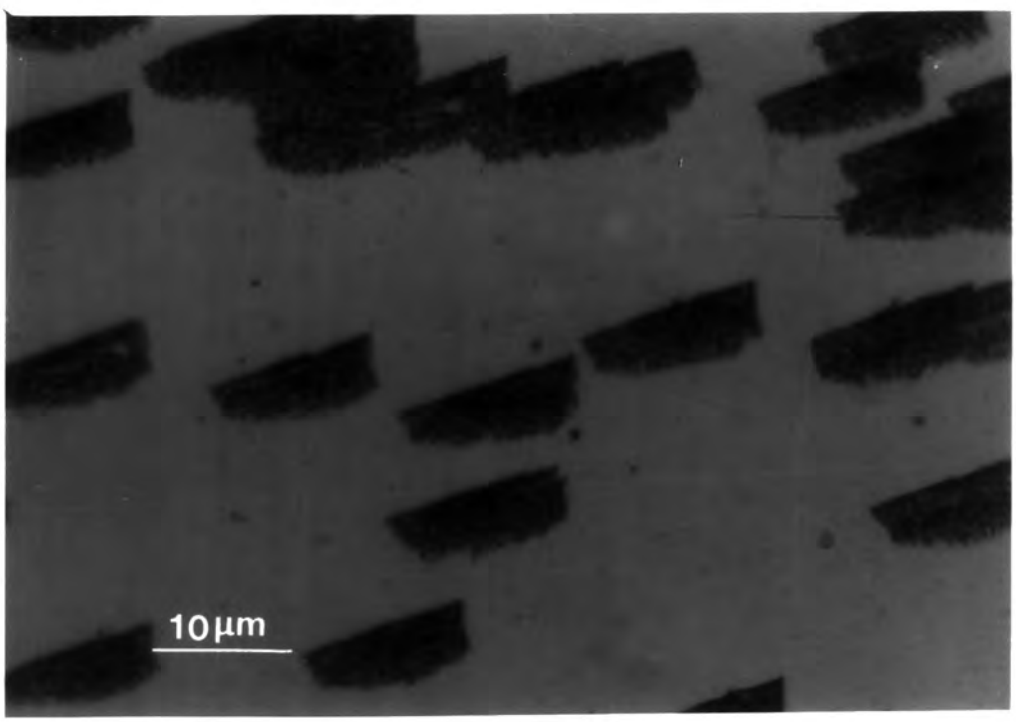

Figure 5.12 Photomicrograph of etch pits on a (5 $\bar{7}$ 13) surface.

§5.5 Summary of Conclusions

A 2% solution of bromine in methanol is a suitable chemical polishing reagent for CdTe substrates since it yields cleaner surfaces than many other chemical polishes (§5.2.3.1). Nevertheless, this polish does leave a thin layer of surface deposits which is variously reported in the literature as being comprised of Te, TeO_2, $TeBr_4$ and related compounds. A RHEED investigation of bromine-methanol polished surfaces (§5.2.3.2) revealed the presence of a thin film having a preferred crystalline orientation. The interplanar spacings calculated from the RHEED pattern did not correspond to those of either Te or TeO_2 and it is thought that the film may be comprised of a compound of tellurium, oxygen and bromine. A mechanochemical polishing machine (§5.2.3.3) has been developed for the preparation of CdTe substrates and this employs a 1% solution of bromine in a mixture of methanol and ethelene glycol (4+1 by volume) as a chemical polish. This machine has the following advantages over 'free' polishing:

i) Flat, polished surfaces may be obtained reproducibly.

ii) No mechanical polishing is necessary prior to mechano-chemical polishing. This obviates the need to use metallographic polishing powders such as 1 μm α-alumina which has been shown to become embedded in CdTe surfaces and to remain as a contaminant after 'free' polishing for as long as 40 minutes.

iii) The thin film left by bromine-methanol based polishes is less noticable on mechanochemically polished surfaces than on 'free' polished surfaces.

The mechanochemical polishing rate using the solution described

above is approximately 35 μm per minute which is 2-3 times that observed when free polishing using a 2% solution of bromine in methanol. This high rate of chemical polishing is caused by the constant replenishment of reactants at the substrate's surface during mechanochemical polishing.

The use of etchants to distinguish between the polar {111} surfaces was reviewed in §5.3.2 and the effects of two etches, the Nakagawa reagent and Inoue's EAg-1 etchant have been correlated with one another. The ability of a previously unreported etchant consisting of a mixture of HNO_3, HF and CH_3COOH (equal volumes of each) to identify polar surfaces is also described. The behaviour of all of these etches on {111} surfaces is summarised in Table 5.3.

Table 5.3 The Effects of Etching Solutions on the {111} Polar Surfaces of CdTe

Etchant	Cd (111)	Te ($\bar{1}\bar{1}\bar{1}$)
Nakagawa [22] (see Fewster and Whiffin [21])	High density of rounded pits and Te film.	Low density of rounded pits and Te film.
Inoue EAg-1 [17] (see Lu et al [19] and Durose et al [20])	Small pyramidal triangular pits.	Large flat bottomed triangular pits.
$HF/HNO_3/CH_3COOH$ (This work)	Black film.	Shiny, polished surface.

Throughout this work the determination of polarity was carried out in accordance with Table 5.3 and Figures 5.6 a-d, both of which are consistent with the work of Fewster and Whiffin [14].

The characteristics of three etchants which have been used to study crystal defects elsewhere in this thesis are described below:-

i) Nakagawa's reagent §5.4.2

This is a polar etchant which is known to produce dislocation etch pits on Cd (111) but does not pit any other surface reproducibly. The dark film which is left by this reagent on all CdTe surfaces has been identified in this work using EDAX and RHEED as being comprised of elemental Te.

ii) Photoetching with ½% bromine in methanol §5.4.3

Photoetching using this solution under illumination from a normal tungsten bulb is not widely reported in the literature. However the etchant effectively reveals extended defects, such as sub-grain , twin and grain boundaries, as raised or groove-like linear features on all surface orientations.

iii) Inoue's EAg-1 reagent §5.4.4

The ability of this etchant to reveal dislocations is disputed even though some clear instances of dislocation etching have been reported. The behaviour of this reagent is likely to be complicated by its strong dependance on the concentration of silver ions and possibly to the presence of Te precipitates associated with dislocations in some cases. Nevertheless, EAg-1 is an extremely useful etchant since it produces well defined, faceted etch pits on all surfaces. The facets of the etch pits have been shown to be Te $\{\bar{1}\bar{1}\bar{1}\}$ planes which indicates that these planes etch more quickly than the Cd {111} planes. From the behaviour of this etchant a model has been put forward to predict the shape of etch pits which might be expected to form on a number of different

crystal planes. This model has been tested experimentally and the observations have confirmed its validity. However, small deviations from the ideal shape of the etch pits observed on {111} planes occur and this is due to a contribution to the dissolution process from Cd (111) planes. This etchant was used extensively in the characterisation of twins which is the subject of the next Chapter.

REFERENCES FOR CHAPTER FIVE

1 B. Tuck, J. Mat.Sci. 10 (1975) p.321.

2 H. Hartmann, R.Mach and B. Selle in Current Topics in Materials Science, Volume 9 (1982) Ed. E. Kaldis, p.291.

3 P.M. Raccah and U. Lee, J. Vac.Sci.Technol.A1 (1983) p.1587.

4 J.P.Faurie, A. Million, R.Boch and J.T.Tissot, J.Vac.Sci.Technol. A1 (1983) p.1593.

5 J.G.Werthen, J.P.Haring, A.L.Fahrenbruch and R.H.Bube, J.Phys.D:Appl.Phys., 16 (1983) p.2391.

6 G.J.Russell, A.T.Fellows, S.Oktik, I.E.Ture and J.Woods, J.Mater.Sci.Lett.1 (1982) p.176.

7 P.Gaugash and A.G.Milnes, J.Electrochem.Soc.128 (4) (1981) p.924.

8 M.Inoue, I.Teramoto and S.Takayanagi, J.Appl.Phys.33(8) (1962) p.2578.

9 M.H.Patterson and R.H.Williams, J.Phys.D:Appl.Phys. 11 (1978) p.L83.

10 P.M.Amirtharajand F.H.Pollak, App.Phys.Lett.45(7) (1984) p.789.

11 M.J.Manfra and A.R.Calawa, Rev.Sci.Instrum,52(8) (1981) p.1256.

12 Patent applied for.

13 E.P.Warekois, M.C.Lavine, A.N.Mariano and H.C.Gatos, J.Appl.Phys.33(2) (1962) p.690.

14 P.F.Fewster and P.A.C.Whiffin, J.Appl.Phys.54 (1983) p.4668.

15 M.Inoue, I.Teramoto and S.Takayanagi, J.Appl.Phys.34(2) (1963) p.404.

16 P.F.Fewster, S.Cole, A.F.W.Willoughby and M.Brown, J.Appl.Phys.52(7) (1981) p.4568.

17 E.L.Polisar, N.M.Boinikh, G.V.Indenbaum, A.V.Vanyukov and V.P.Schastlivi, Izv. Visshikh. Uchebnikh, Zavedenii-Fixika, 6 (1968) p.81.

18 K.Nakagawa, K.Maeda and S.Takeuchi, Appl.Phys.Lett. 34(9) (1979) -.574.

19 Y-C.Lu, R.K.Route,D.Elwell and R.S.Feigelson, J.Vac.Sci.Technol A3(1) (1985) p.264.

20 K.Durose, G.J.Russell and J.Woods, Inst.Phys.Conf.Ser.No 72: Section 2 (1985) p.272.

21 D.J.Williams, private communication.

22 M.Nagabooshanam and H.V.Babu, Cryst.Res.Technol.19(5) (1984) p.643.

23 H.Iwanaga, T.Yoshiie, S.Takeuchi and M.Mochizuki, J.Crystal Growth, 61 (1983) p.691.

24 H.Iwanaga, A.Tomizuka, N.Shibata and K.Mochizuki, J. Crystal Growth, 74 (1986) p.113.

CHAPTER SIX

TWINS

§ 6.1 Introduction

Twins have been reported in bulk crystals of CdTe grown by the following techniques : Bridgman growth [1,2,3,4,5], modified Bridgman methods employing sealed capsules [6,7], travelling heater techniques with either Te [8] or Cd [9] molten zones, by the evaporation of Cd from a nonstoichiometric melt [5], liquid encapsulated Czochralski growth [5] and vapour growth [11,12,13,14,15,16]. The presence of twins in a boule greatly reduces its value as a substrate for epitaxy. For example, twin orientations in CdTe substrates readily propagate into CdTe and $Cd_xHg_{1-x}Te$ epilayers [17] and have a marked effect upon the quality of evaporated CdS layers [18]. In addition these inhomogeneities are also likely to be electrically active which could have important implications for device performance on such layers. The frequency of twinning in CdTe and its importance to device fabrication have prompted this detailed study of the twins present in material grown by the vapour phase technique. Table 6.1 lists the methods used in this work to study twins, the properties of these defects which make them visible and comments on the information obtained with each technique.

TABLE 6.1 Experimental Observation of Twin Bands and Boundaries.

METHOD OF OBSERVATION	PROPERTY MAKING TWINS VISIBLE	NOTES
Visual inspection of growth faces and sawn surfaces.	Variations of surface texture and orientation at twin bands. Steps are often seen at twin boundaries on growth surfaces.	Twin bands and boundaries are often easily visible by eye.
Optical microscopy of surfaces after etching with:-		
i) ½% Br_2 in methanol + illumination. [19]	The rate of dissolution of material at twin boundaries often differs from that of the surrounding material.	Twin boundaries are revealed as linear features on all crystal faces.
ii) Inoue's EAg-1 reagent [20]	The shape of the etch pits is characteristic of the surface orientation. Twin boundaries may also have special etch features associated with them.	Marked dependence of etch pit shape on surface orientation makes this etchant useful in the characterisation of twins.
iii) Nakagawa's etchant [21]	This etchant leaves a Te layer, the colour of which is dependant upon the orientation of the crystal surface as is the density of etch pits.	Twin bands are easily visible and their boundaries are sharply deliniated.
Transmission electron microscopy.	The orientation difference between twin and matrix gives rise to diffraction contrast.	Twins and the orientations of their boundary planes may be identified. Interfacial defects on twin boundaries may also be imaged by diffraction contrast.
Scanning electron microscopy (secondary emission mode)	Crystallographic contrast between twin and matrix orientations.	Twin bands visible.
Scanning electron microsopy (EBIC mode)	Recombination centres at boundaries.	Electrical activity of boundaries may be investigated.
RHEED	Diffraction from both the matrix and twin orientations occurrs.	RHEED patterns may be used to identify twins which intersect surfaces.

§ 6.2 General Morphology of Twins

During the course of this study the crystallography of twins in more than 30 crystal boules has been examined. Before describing the detailed characterisation work that has been undertaken it is appropriate to outline the general features and morphology of these defects. The incidence of twins in single crystals or boules comprised of large grains is usually confined to one set of {111} planes. The photograph of the growth face of a CdTe boule in Figure 6.1 shows this clearly. The twins are lamellae which have been seen to range in width from several microns to approximately one centimetre. An important observation made during this study is that the differently oriented grains in these crystals are often twin related.

Figure 6.1 Growth face of a boule showing twin lamellae.

A good example of this is depicted in Figure 6.2a which shows a photograph of a slice from a boule which has been etched with Inoue's EAg-1 reagent [20]. The structure and surface orientations of different regions of this slice are indicated in Figure 6.2b. The largest grains on the slice are the matrix of host crystal (A) and the first (B) and second order (C) twinned regions. Some third order twin lamellae (D) are also present as are first (a), second (b), third order (c) and lateral (d) twin boundaries. In boules which contain large numbers of small grains, twinning is more prolific. The density of twins is higher and grains often contain twins on more than one {111} plane. Similar observations have also been reported for material grown by a number of different techniques [5].

§ 6.3 First Order Coherent Twins

§ 6.3.1 Introduction

The simplest and most commonly observed type of twin boundary in the sphalerite structure is the first order coherent boundary. This is a low energy interface which bounds twin lamellae on {111} planes. This section is concerned with the experimental observation of such twins. Firstly their crystallography is characterised and in subsequent sections the effects of different etchants on twin bands and boundaries are described. Finally, transmission electron microscope observations of twin boundaries are presented.

§ 6.3.2 Characterisation of the Crystallography of Twins.

The two types of twin boundary which are geometrically possible in crystals having the sphalerite structure are described in § 4.4.2.2. The difference between these two types of twin is one of crystallographic polarity. In the case of the ortho-twin polarity is

Figure 6.2a {111} oriented slice of a 29mm in diameter boule showing several different types of twin boundary.

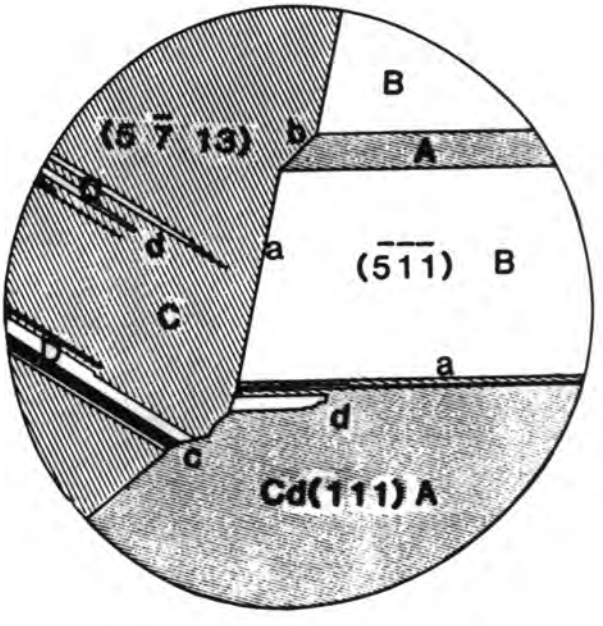

Figure 6.2b Sketch of Figure 6.2a showing twin boundaries and the surface orientations of different grains.

preserved on both sides of the boundary whereas it is reversed in the case of the para-twin. Alternatively the two types of twin may be described as <110> tilt boundaries having tilt angles of $\theta = 250^{o}32'$ (ortho) and $\theta = 70^{o}32'$ (para) [22].

From both of these descriptions it is implicit that simple etching experiments are capable of distinguishing between the two possible types of twin. Firstly the crystallographic polarity on either side of a twin boundary was found by etching a CdTe slice which had been cut so as to intersect a twin plane at a glancing angle. Inoue's EAg-1 reagent [20] was ideal for this experiment since it is capable of discriminating between polar faces, and develops etch pits having crystallographic facets on surfaces of all orientations.

The photomicrograph of the etched surface in Figure 6.3 shows that the pits on both sides of the boundary are of the same polar type, that is Te($\bar{1}\bar{1}\bar{1}$) but are rotated with respect to one another by 180^{o}. This is consistent with the ortho-twinning model. Secondly a cleaved {110} surface containing a twin band was etched with Inoue's EAg-1 reagent and the angle of rotation between the etch pits on the twin and matrix was measured. The angle of rotation observed was close to 250^{o} which is further confirmation that the twins in this material are of the ortho-type (see Figure 6.4).

§6.3.3 Observation of Twins Intersecting Surfaces

This section describes the observations of twin bands and boundaries by optical microscopy after etching with the Inoue EAg-1 or Nakagawa etchants. With experience, twin bands and even complex

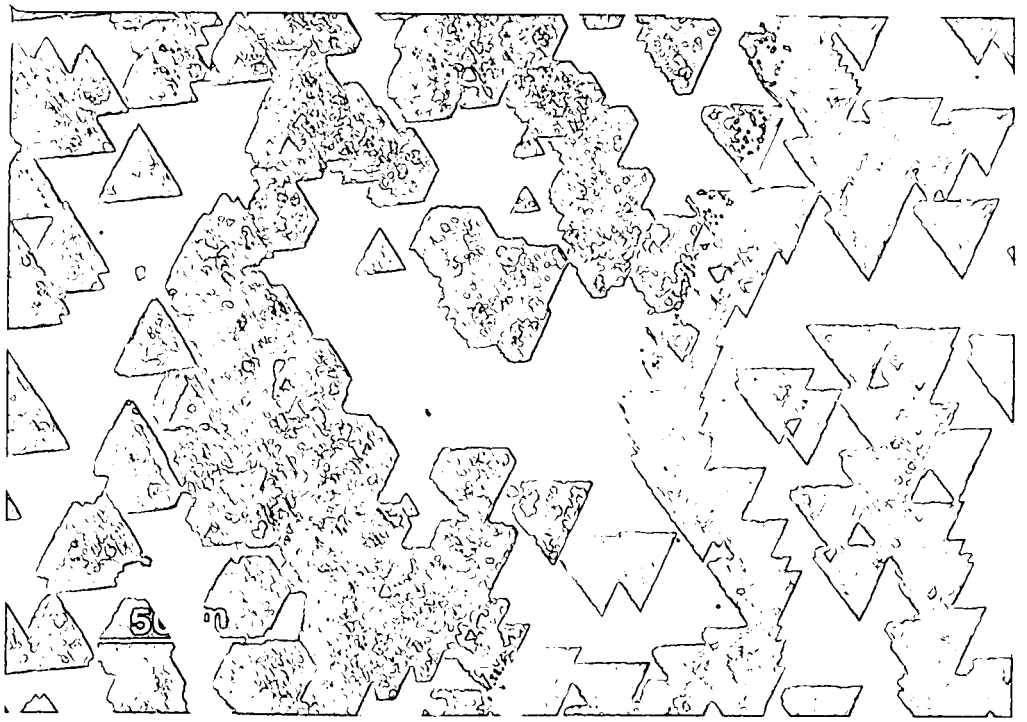

Figure 6.3 Photomicrograph of an etched surface intersecting a twin plane at an angle of $\sim 3^{o}$ showing the 180^{o} rotation of the etch pits on either side of the twin boundary.

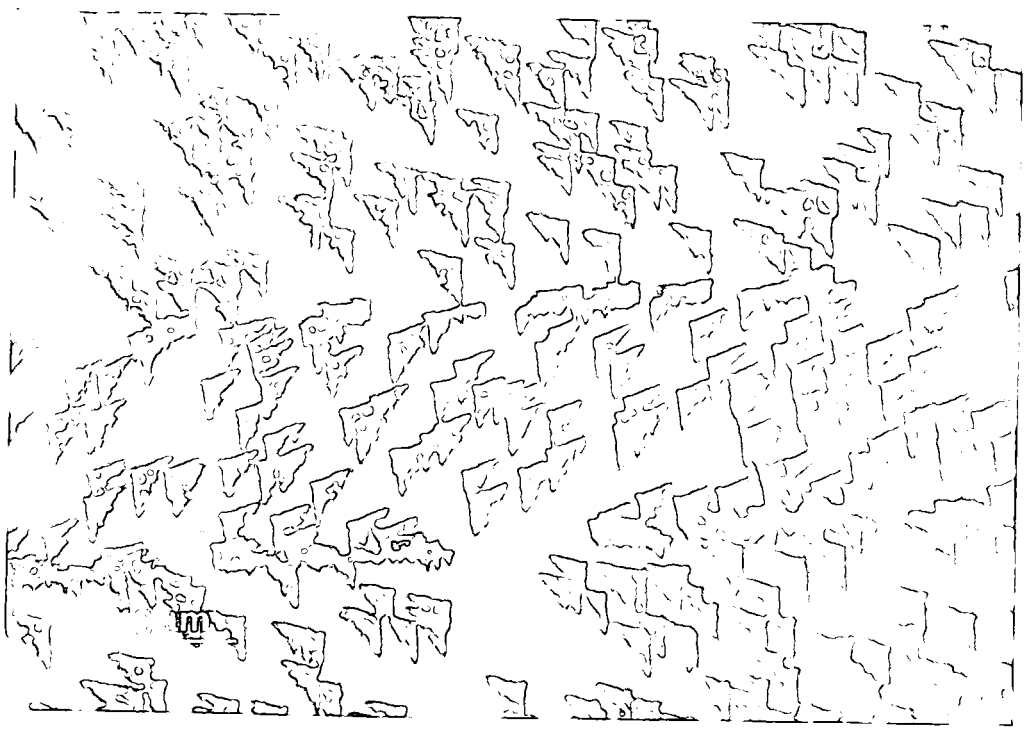

Figure 6.4 Photomicrograph of a cleaved {110} surface intersected by a twin band after etching. The etch pits on the twin band are rotated by $250^{o}32'$.

structures comprised of a number of twin related lamellae can be recognised on sight. Nevertheless the RHEED technique (see Chapter 2) is still a valuable aid to identifying twinned structures which intersect crystal surfaces, especially chemically polished substrates. For example, Figure 6.5 a/b shows a RHEED pattern taken from a {111} oriented surface with the beam direction parallel to <110> . Two sets of additional spots are present which occupy positions $\frac{1}{3}$ of the way between the matrix lattice spots and lie on two <111> directions. These extra spots correspond to two orientations of twin lamellae lying on the $(\bar{1}11)$ and $(\bar{1}1\bar{1})$ planes. The same slice was subsequently etched and it was found that the surface was indeed intersected by two sets of twins on two different twinning planes. Throughout this work the crystallographic information which can be obtained from RHEED has been used wherever necessary to complement the detailed information concerning the morphology of twins obtained from etching experiments.

Twins intersecting close packed surfaces have been the subject of detailed study in this work since the suitability of {111} surfaces of CdTe as substrate material for epitaxial growth is currently under investigation. Figures 6.6a and b are photomicrographs of twin bands which intersect Cd (111) and Te $(\bar{1}\bar{1}\bar{1})$ surfaces respectively. The etchant used was Inoue's EAg-1 reagent [20]. Using the matrix method described in §4.4.2.4 it was found that the surface planes of twin bands on Cd(111) have the $\{\bar{5}\bar{1}\bar{1}\}$ orientation whereas those on Te$(\bar{1}\bar{1}\bar{1})$ have the {511} orientation. Since [511] is a polar direction the etch pits on (511) and $(\bar{5}\bar{1}\bar{1})$ have different shapes which may be predicted by cutting a tetrahedron comprised of Cd close packed planes along the appropriate surface. This procedure is described

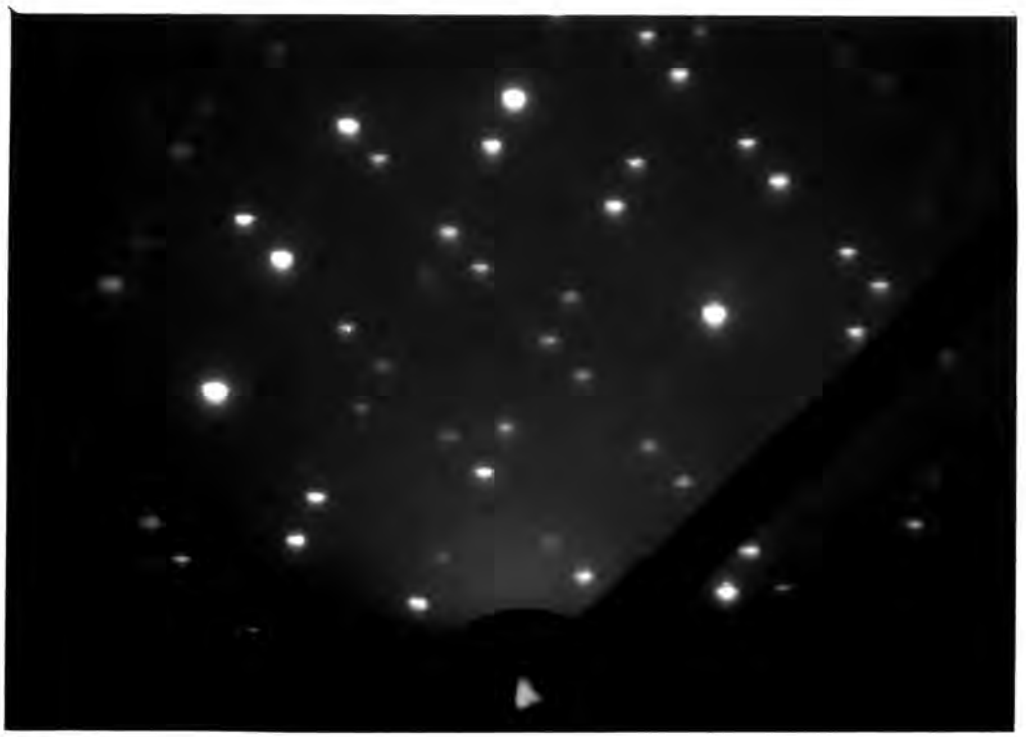

Figure 6.5a [110] RHEED pattern from a surface intersected by twins on the $(\bar{1}1\bar{1})$ and $(\bar{1}11)$ planes.

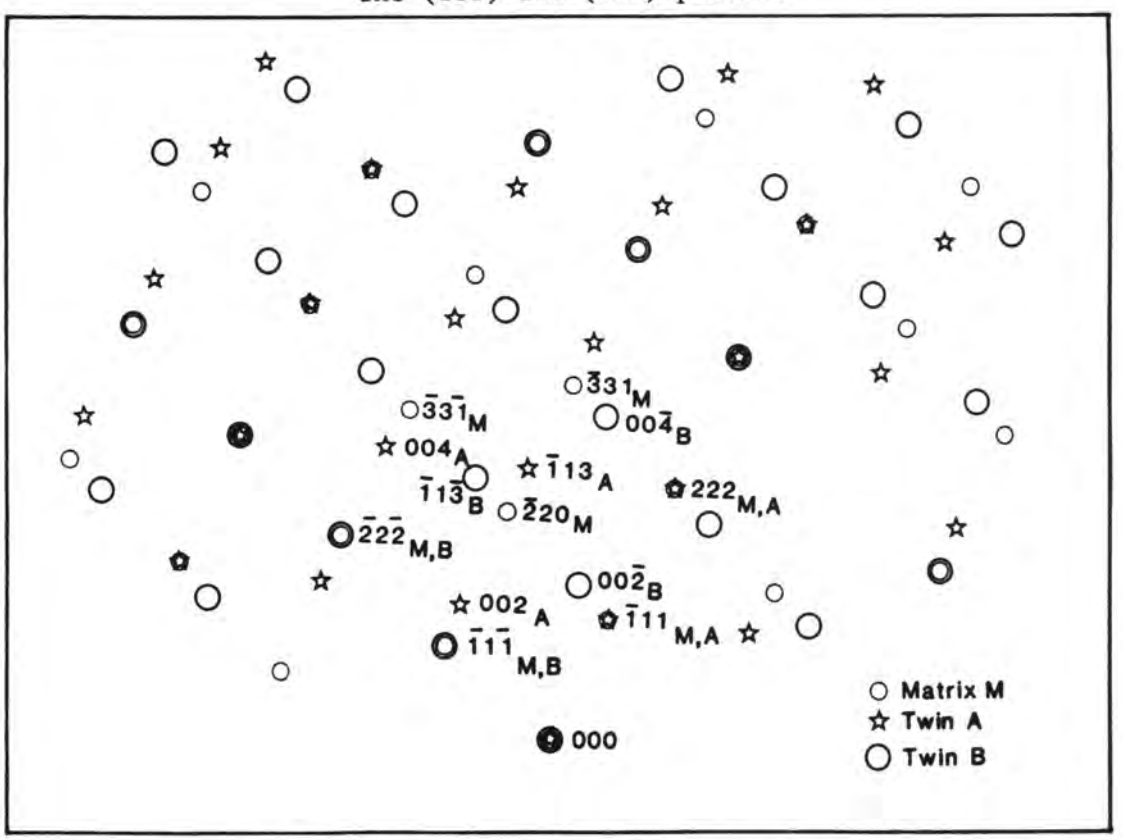

Figure 6.5b Indexed diffraction pattern as in 6.5a.

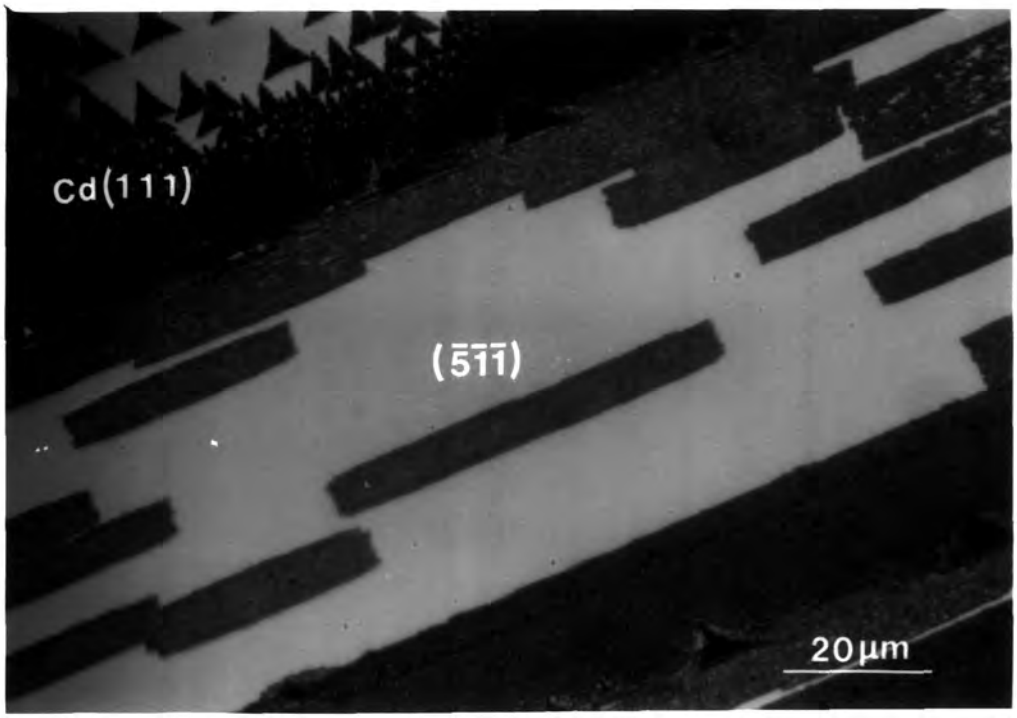

Figure 6.6a Photomicrograph of a twin band intersecting an etched Cd (111) surface.

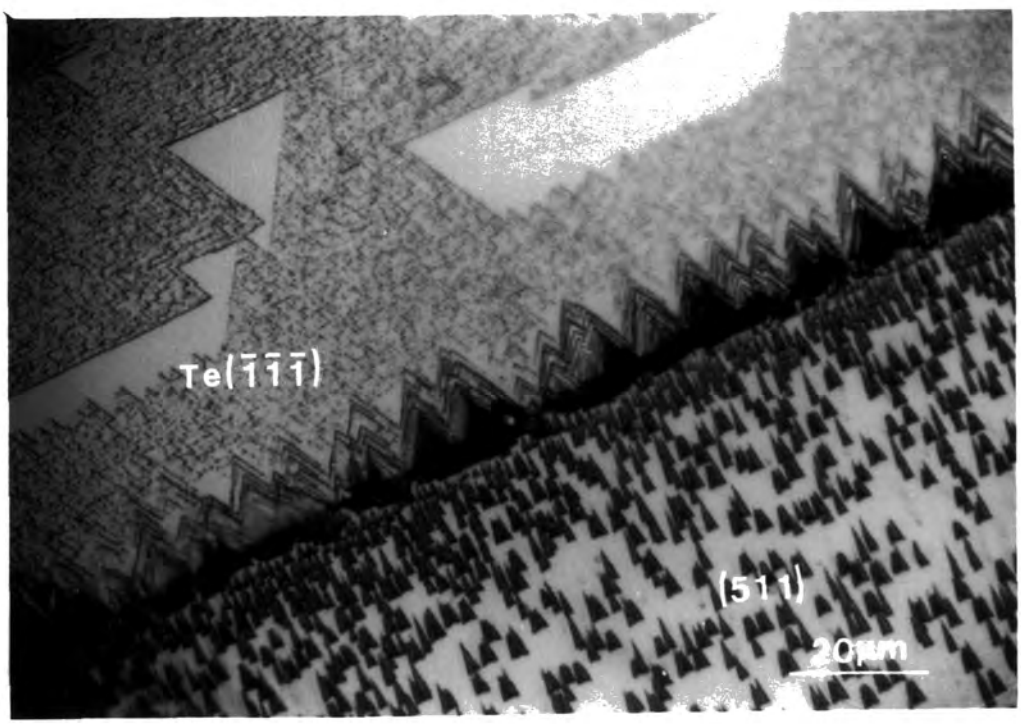

Figure 6.6b Photomicrograph of a twin band intersecting an etched Te (III) surface.

in § 5.4.4 The rectangular trough shaped pits on the twin band in Figure 6.6a are characteristic of the $(\bar{5}\bar{1}\bar{1})$ orientation whereas those on the opposite face (Figure 6.6b) have the shape of isosceles triangles and are typical of the (511) surface for this particular etchant.

In addition to the etch features just described which are related to the difference in orientation of twin bands there are three other types of etching behaviour which are specifically associated with twin boundaries.

Firstly the etching of {111} or {511} surfaces may be modified in the locality of twin boundaries. For example, on Te$\{\bar{1}\bar{1}\bar{1}\}$ surfaces shallow etched bands are always found adjacent to the twin boundaries on both sides of each twin lamella. One of the bands is consistently broader and is always found on the same side of the twin lamella, regardless of the inclination of the twin boundary beneath the surface. Such a band is present on the upper side of the boundary in Figure 6.6b. The surface of these etched bands is identical to that seen on the bottoms of the flat bottomed etch pits on Te$(\bar{1}\bar{1}\bar{1})$ surfaces.

Secondly, a high density of etch pits has sometimes been observed in the vicinity of twin boundaries. An example of this can be seen on the (511) orientation in Figure 6.6b.

The third etching phenomenon associated with twins is the presence of etch pits on the twin boundaries themselves. Such etch pits are visible on the boundaries in Figures 6.6a and b and clearly their shapes differ from those present to either side on the matrix or twin orientations. Furthermore, these etch pits are quite distinct from the etching effects associated with precipitates described in Chapter 9. The linear density and distribution of these interfacial etch pits varies considerably both along the length of a given

boundary and from one boundary to another : Both boundaries having a high density of indistinguishable pits and those having no pits have been observed. Similar patterns of pits on twin boundaries are revealed by etching with the Nakagawa reagent [21]. Figure 6.7 shows a scanning electron micrograph of the effect of this reagent on twin boundaries intersecting a Cd(111) surface. The pits on the boundaries are clearly different from those on the bulk Cd(111) material. Sections of boundary having no etch features are associated with a linear feature which SEM revealed to be a small step. This may be attributed to the higher chemical polishing rate of the twin orientation. Additional interfacial etching phenomena have been seen on faces other than {111} . Twin bands on {511} surfaces have either {11 11 1} or {5 7 13} orientation. For example, the first order twin boundary indicated in Figure 6.8 separates the $(\bar{5}\bar{1}\bar{1})$ and $(5\ \bar{7}\ 13)$ surface orientations. Etch pits which are characteristic of these orientations are clearly visible together with an interfacial etch feature at A. Figure 5.11 (Chapter 5) is a scanning electron micrograph of an identical twin boundary which shows how high densities of these differently shaped etch pits are sometimes seen to be associated with first order twin boundaries which intersect these surface orientations.

§ 6.3.4 TEM Studies of First Order Twin Boundaries

Twin boundaries are easily identified in the transmission electron microscope by selected area diffraction (SAD). An indexed diffraction pattern taken from a twinned region of a specimen with the beam direction, B = [101] is shown in Figures 6.9 a and b. The twin bands observed in this material are invariably broader than

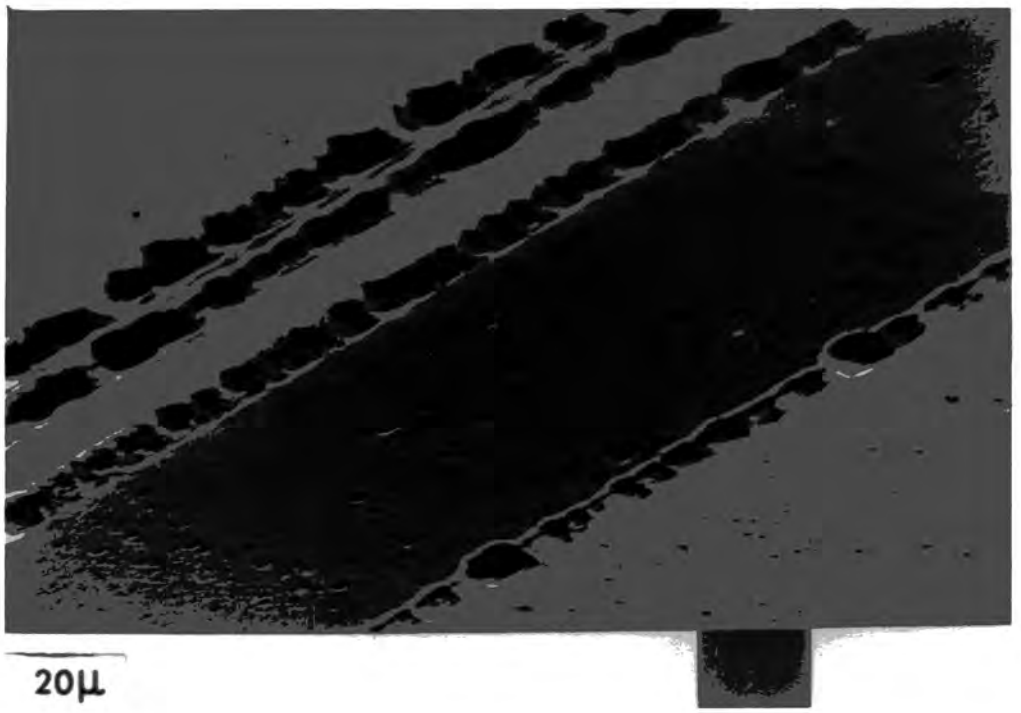

Figure 6.7 Scanning electron micrograph showing etch pits at twin boundaries.

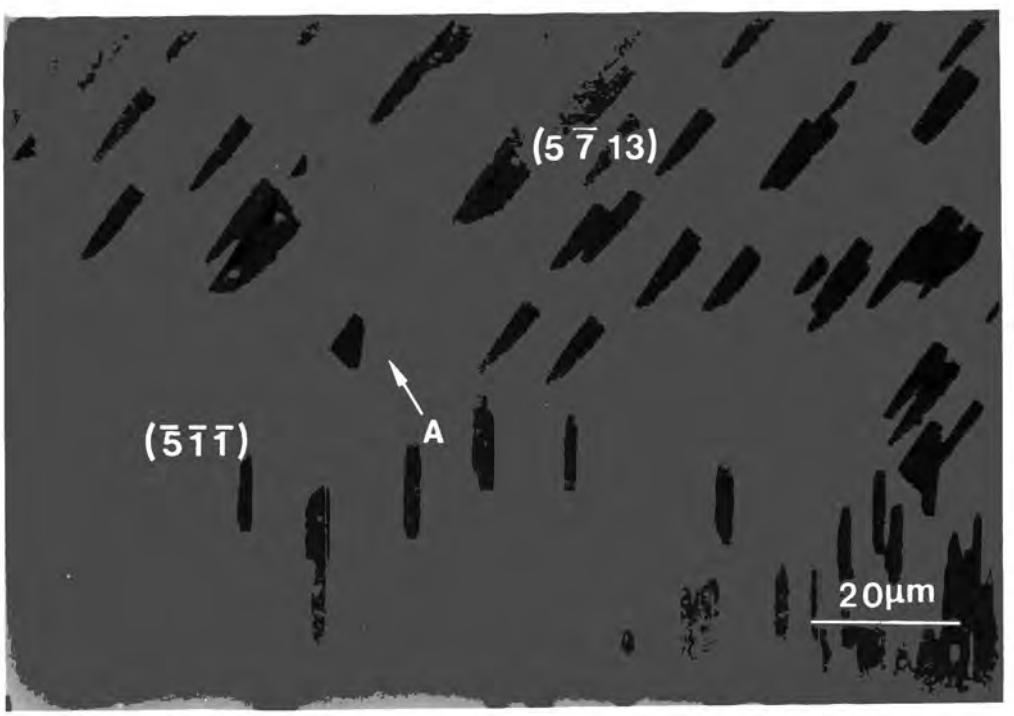

Figure 6.8 Photomicrograph of an etched first order twin boundary which intersects the ($\bar{5}\bar{1}\bar{1}$) and (5 $\bar{7}$ 13) orientations.

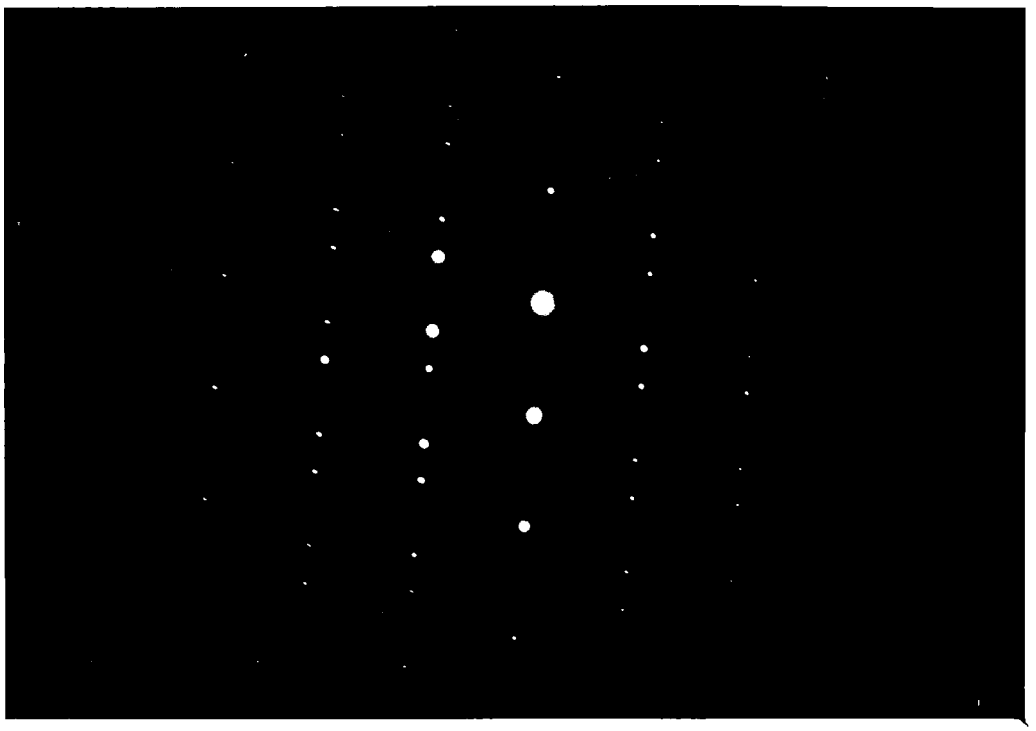

Figure 6.9a [101] Transmission electron diffraction pattern from a crystal which is twinned on $(\bar{1}11)$.

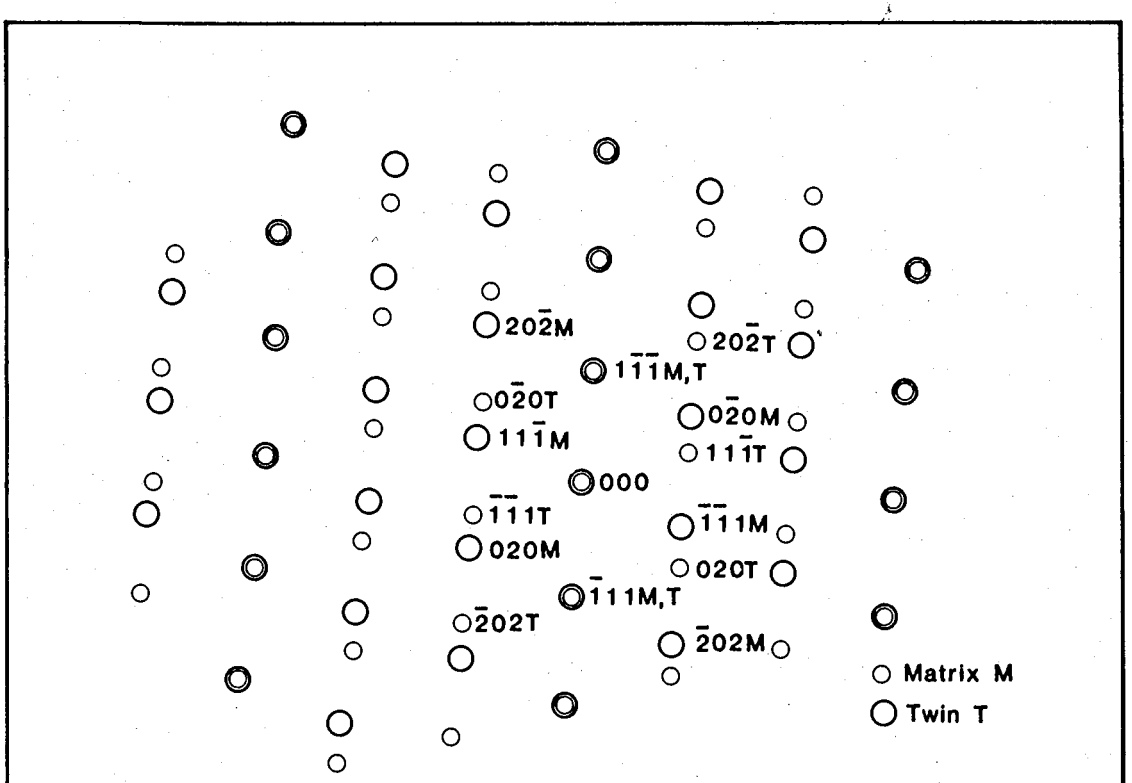

those seen in other II-VI crystals such as ZnS [23], ZnSe and ZnS-Se [24]. Consequently it was rare to be able to record both boundaries of a twin lamella in a single TEM micrograph. A particularly narrow twin band (for this material) is shown in Figure 6.10. The boundary plane of the twin in Figure 6.11a is $(\bar{1}11)$ and it was imaged in bright field using a two beam case with a $(1\bar{1}\bar{1})$ matrix reflection. The boundary is 'in contrast' and fringes parallel to the line of intersection of the boundary with the sample surface visible. They are interrupted by two dislocations lying on the twin plane itself. The dislocations were also imaged with the twin boundary 'out of contrast' with $\underline{g} = 20\bar{2}$ as in Figure 6.11b. A third dislocation which does not lie on the twinning plane is also present.

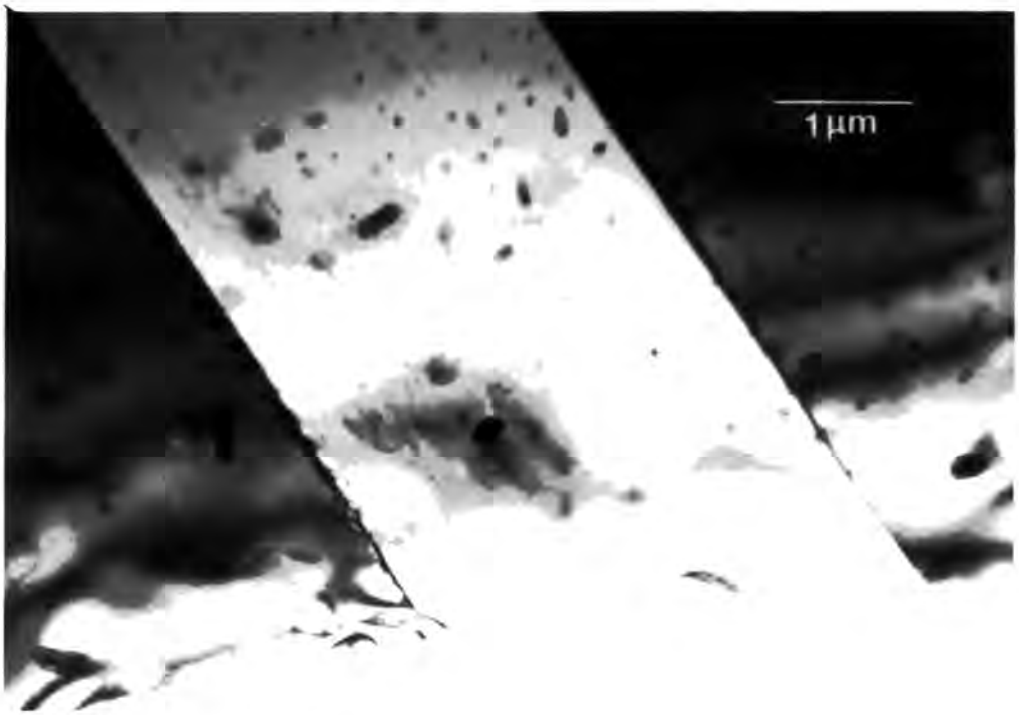

Figure 6.10 Transmission electron micrograph of a particularly narrow twin band.

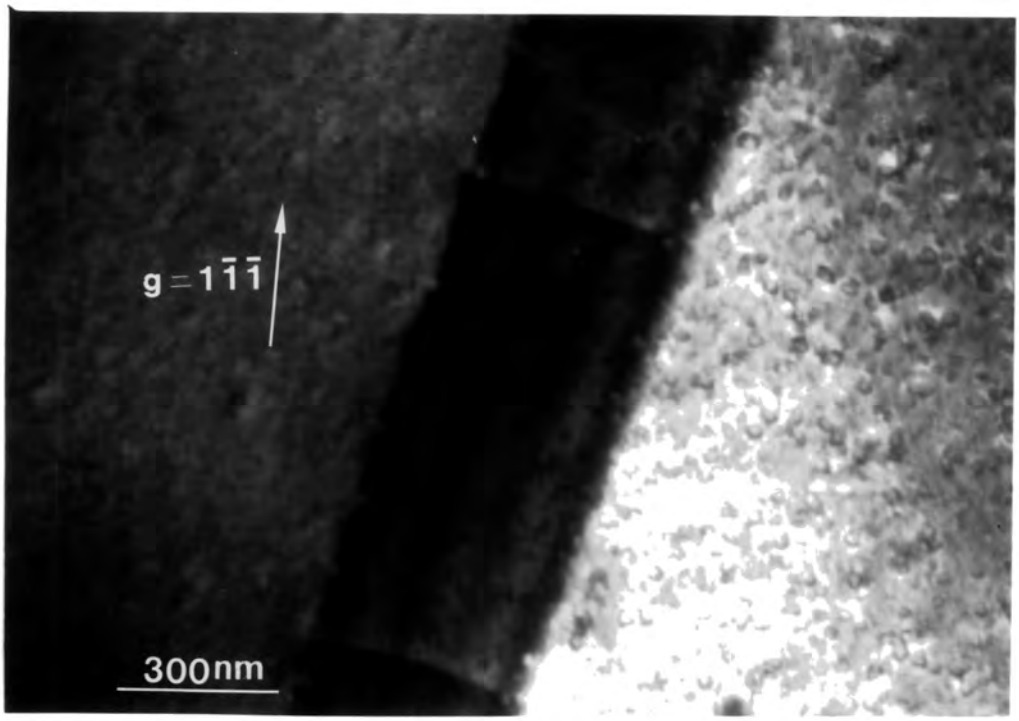

Figure 6.11a Transmission electron micrograph of a twin boundary. The boundary is in contrast and dislocations can be seen on it.

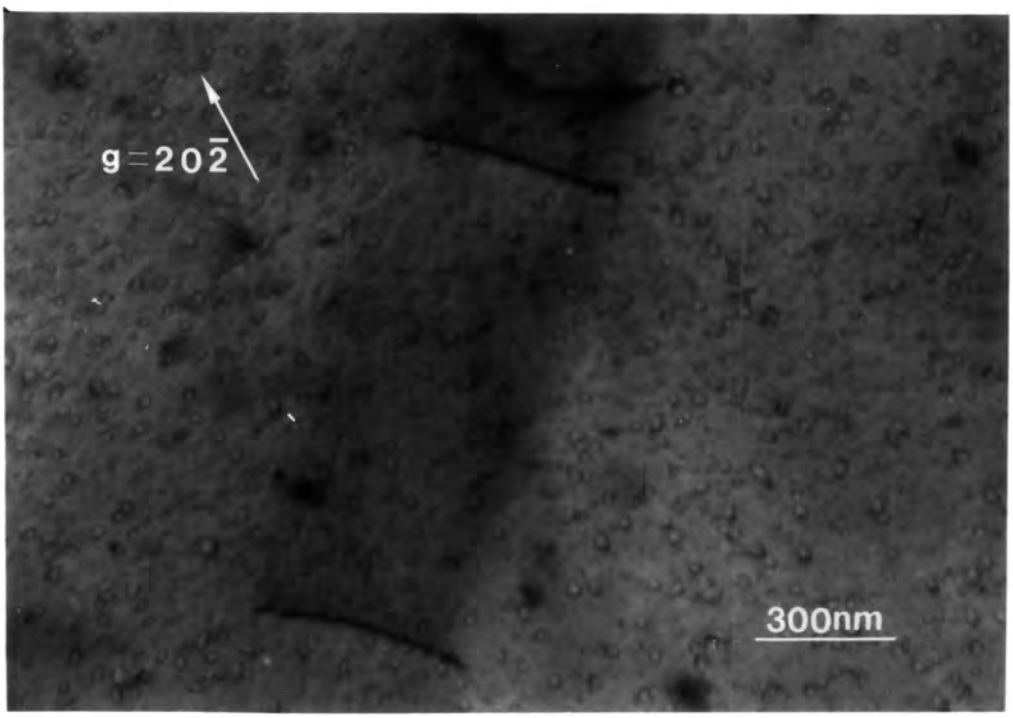

Figure 6.11b As 6.11a with twin boundary out of contrast.

Dislocations were observed on most of the twin boundaries examined and their density varied between about 1-70 per 5 μm length of boundary. The spacing between these dislocations only appeared to be regular when the dislocation density was high, as in Figure 6.12.

Isolated dislocations were occasionally seen in the vicinity of twin boundaries but no evidence of dislocation pile-ups was seen in the samples studied.

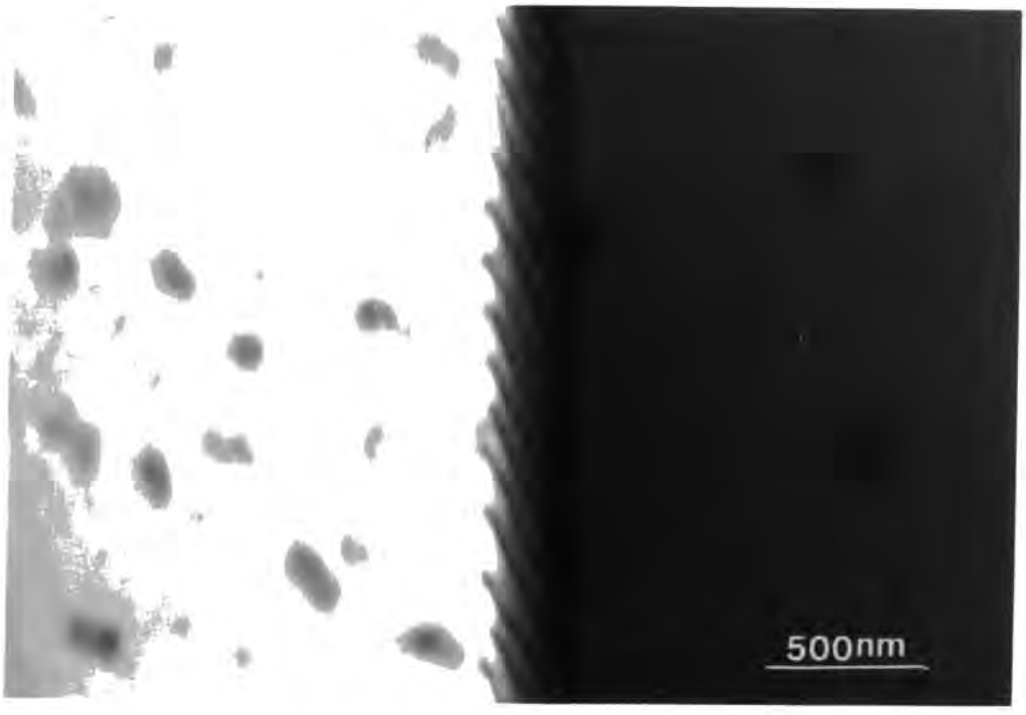

Figure 6.12 Transmission electron micrograph of a twin boundary with a high density of interfacial dislocations.

§ 6.3.5 Discussion

The following points arise from the studies of first order coherent twins:-

i) Ortho-twinning § 6.3.2

The incidence of ortho-twinning in CdTe is to be expected since ortho-twins are much more energetically favourable than para-twins (see § 4.4.2.2). Indeed, etching experiments have been carried out which have confirmed that the twins in InSb [25], GaAs [26], InP[27] and ZnSe [24] are all of the ortho-type.

ii) Interfacial defects. §6.3.3 and §6.3.4

The TEM study described in §6.3.4 showed that twin boundaries in CdTe grown by the vapour phase technique have interfacial dislocations associated with them. (See Figures 6.11a, 6.11b and 6.12) These are twinning dislocations of the a/6 <211> type which could arise during the formation of twin bands by either deformation or growth processes (see §4.3.2). The etch pits which appear at twin boundaries after etching with both the Inoue EAg-1 (Figures 6.6a and b) and Nakagawa reagents (Figure 6.7) are probably related to the dislocations which were observed on the boundaries by TEM. The distributions of dislocations and etch pits along twin boundaries are similar and the pits are clearly different from the other etch features associated with precipitates (see Chapter 9).

iii) Dislocation pile-up at twin boundaries § 6.3.3

The high density of etch pits which is sometimes observed near to twin boundaries (see Figure 6.6b) is likely to be related to the presence of dislocation pile-ups at the boundaries similar to those observed in liquid encapsulated Czochralski grown InP [27] using

X-ray topography. The failure to detect anything but isolated dislocations in the vicinity of twin boundaries by TEM probably reflects the small sampling areas available from TEM specimens rather than the absence of pile-up phenomena.

iv) Etched bands near to twin boundaries §6.3.3

Etched bands are always associated with twin boundaries intersecting Te ($\bar{1}\bar{1}\bar{1}$) faces after etching with the Inoue EAg-1 reagent (see Figure 6.6b). Since they appear consistently and are unrelated to the other boundary etch features, these bands are thought to be related purely to the twin boundaries themselves rather than to any other defects which may be associated with them.

The electrical activity of twin boundaries is discussed in §6.4.

§ 6.4 Lateral Twin Boundaries

§ 6.4.1 Introduction

Although many of the twins present are lamellae which extend across the full width of the boules, some terminate in the bulk of crystals, either at grain boundaries, twin intersections or lateral twin boundaries. Lateral twin boundaries are high energy variants of boundaries separating grains having a twinning relationship to one another. (see §4.4.2.3)

Such boundaries may also constitute steps on coherent (ortho) twin boundaries.

§ 6.4.2 Characterisation of Lateral Twin Boundaries

A number of lateral boundaries have been examined by optical and scanning electron microscopy after etching with the Nakagawa

reagent [21]. The orientations of the boundary planes were found by measuring the angles between the lateral and coherent boundaries on oriented surfaces. All of the lateral boundary planes examined corresponded to one of the four interfacial planes predicted using the coincidence site lattice model described in Chapter 7. Indexing with respect to both the twin and matrix orientations these are {115} -{ 111} , {112} - {112} , {110} - {114} and { 001} - {221}. Examples of each of these, which were found on a Te($\bar{1}\bar{1}\bar{1}$) surface after etching with the Nakagawa reagent, are shown in Figures 6.13 a-d. In all of the photomicrographs the twin bands are darker and less pitted than the matrix regions. The boundary in Figure 6.13a terminates a broad twin and is decorated at intervals by tellurium precipitates. These are described fully in Chapter 9 as are the arrays of etch-pits which indicate the presence of sub-grain boundaries in the same micrograph. In Figure 6.13b a twin is terminated by a boundary which changes orientation from {112} - {112} to {115} - {111} . A different situation is shown in Figure 6.13c in which the twin is observed to become progressively narrower by a series of lateral twin steps which are decorated by precipitates.

Finally, Figure 6.13d shows a lateral twin boundary which constitutes a step in a coherent boundary. The lateral boundary itself has some steps although the greater part of it lies on {001 }- {221 }.

The effect of the Nakagawa etchant on lateral twin boundaries was investigated by scanning electron microscopy. Lateral twin boundaries on both Cd(111) and Te($\bar{1}\bar{1}\bar{1}$) surfaces were preferentially etched out to a depth of several microns during a 1 minute etch. Furthermore, the chemical attack at these boundaries was always uniform, unlike that at coherent twins which varied from being heavily

Figure 6.13 Photomicrographs of lateral twin boundaries on twins intersecting a Te $(\bar{1}\bar{1}\bar{1})$ surface.

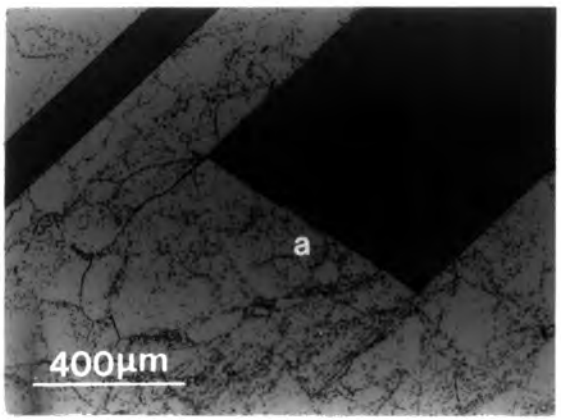

a) {115}-{111} boundary.

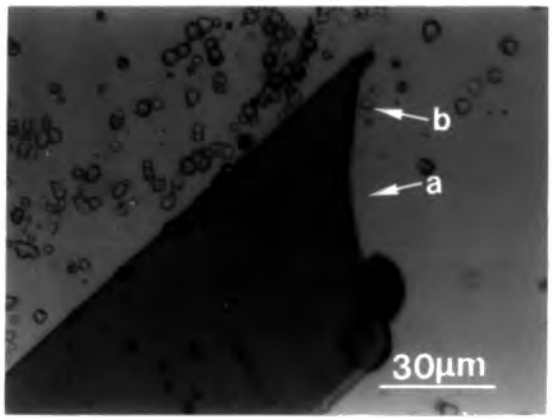

b) {112}-{112} boundary and a {115}-{111} boundary at (a).

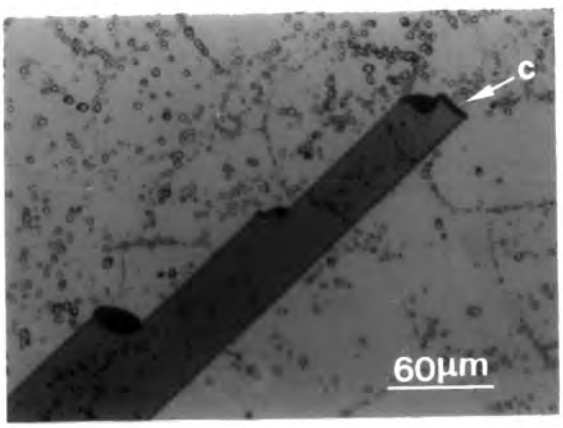

c) {110}-{114} boundary.

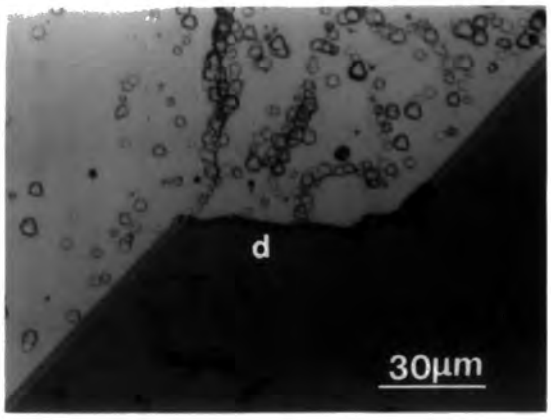

d) {001}-{221} boundary.

pitted (as in Figure 6.7) to being unpitted (in Figure 6.13a-d).

An investigation of the electrical activity of twin boundaries was carried out by EBIC (electron beam induced conductivity) in the SEM (see Chapter 2). Figure 6.14 shows an SEM/EBIC micrograph of a thin twin lamella ∿70 μm in width which is terminated by a lateral boundary. The background features are EBIC contrast due to recombination at dislocation networks (see Chapter 8). Both the coherent and lateral twin boundaries display EBIC contrast. However, the contrast at coherent boundaries is discontinuous (see Figure 6.14) and is probably due to the presence of the interfacial dislocations on the twinning plane which are described in §6.3.4. The EBIC signal from the lateral boundary in the figure is much stronger and this is consistent with the high density of recombination sites expected on this type of boundary.

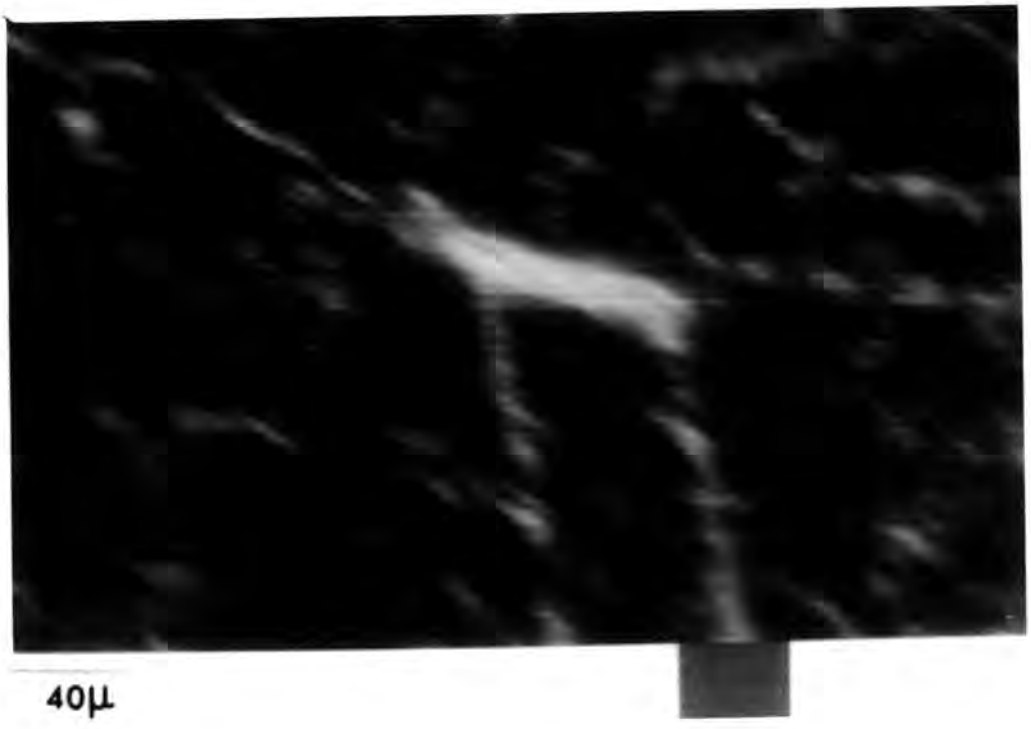

Figure 6.14 SEM/EBIC micrograph of a twin terminated by a lateral twin boundary.

§ 6.4.3 Discussion

In Chapter 7 a set of coincidence site lattice models of lateral twin boundaries is presented. These models are successful in that they predict all of the four lateral twin boundary planes which were observed in practice. The models also predict the atomic arrangements at the boundaries. While the exact details of these models are not unique, a feature which is common to all of them is the presence of wrong bonds of either the Te-Te or Cd-Cd type at the interfaces. These wrong bonds could account for the strong electrical activity of the boundaries observed by EBIC. The electrical activity of ortho-twin boundaries however, must arise from the presence of partial dislocations on the twinning planes since the ortho-structure contains no wrong bonds.

The relatively small areas of the lateral boundaries observed are indicative of their instability with respect to coherent twin boundaries. Indeed, for metals such as Cu, Cu-Al alloys, Ni and stainless steels the energy per unit area of the lateral boundaries γ_{TB} has been measured as being from 0.25 to 0.8 of the random grain boundary energy γ_{gb} whereas the coherent twin boundary energy γ_{tb} is only 0.01 to 0.04 γ_{gb}[28]. The defective bonding in the interfacial structure of lateral twin boundaries accounts for these energy differences, the stronger EBIC signal and the preferential chemical attack observed at these boundaries.

§ 6.5 Second Order Twin Boundaries

§ 6.5.1 Introduction

Second order twin boundaries, their relationship with first order twins and their formal description as tilt boundaries has been

described in §4.4.2.3. The structure of second order boundaries in the sphalerite structure is examined in detail using a coincidence site lattice model in §7.4. In this section experimental observations made of second order twin boundaries which intersect oriented surfaces after etching are reported. Detailed discussion of the ways in which interacting twinned structures are formed is delayed until §6.6 and §6.7.

§ 6.5.2 Characterisation of Second Order Twins

The second order twin boundary planes present in the boules examined have been characterised by measuring the angles that the intersections of these twins with oriented crystal surfaces make with known crystallographic directions. These directions were invariably either along the intersections of coherent first order boundaries or the edges of the etch pits developed by the Inoue EAg-1 reagent [20], both of which lie on <110> directions on {111} surfaces.

Figure 6.15 shows a Cd(111) face after etching with the Nakagawa reagent [21]. The two light bands are a pair of lamellar twins, the wider of which is crossed by another, narrower twin lamella. This is a second order twin. The two long boundaries of the second order twin are first order coherent boundaries whereas the two short and heavily etched boundaries at A and B are second order boundaries, that at A lying on {114} - {114} and that at B on {111}-{115}.

A second order boundary intersecting a Cd(111) surface which has been etched with Inoue's EAg-1 reagent is shown in Figure 6.16. The pits to the left of the boundary are characteristic of the action of this etchant on the Cd(111) surface, whereas those on the right are markedly different in shape. Using the matrix method for deter-

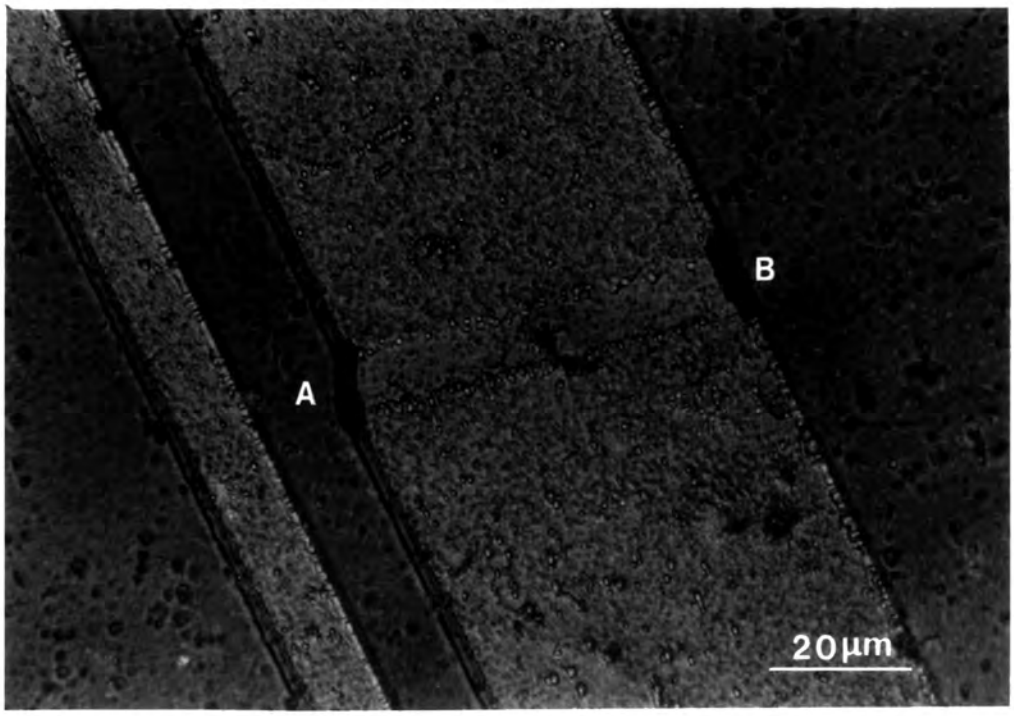

Figure 6.15 Second order twin on a first order twin lamella.

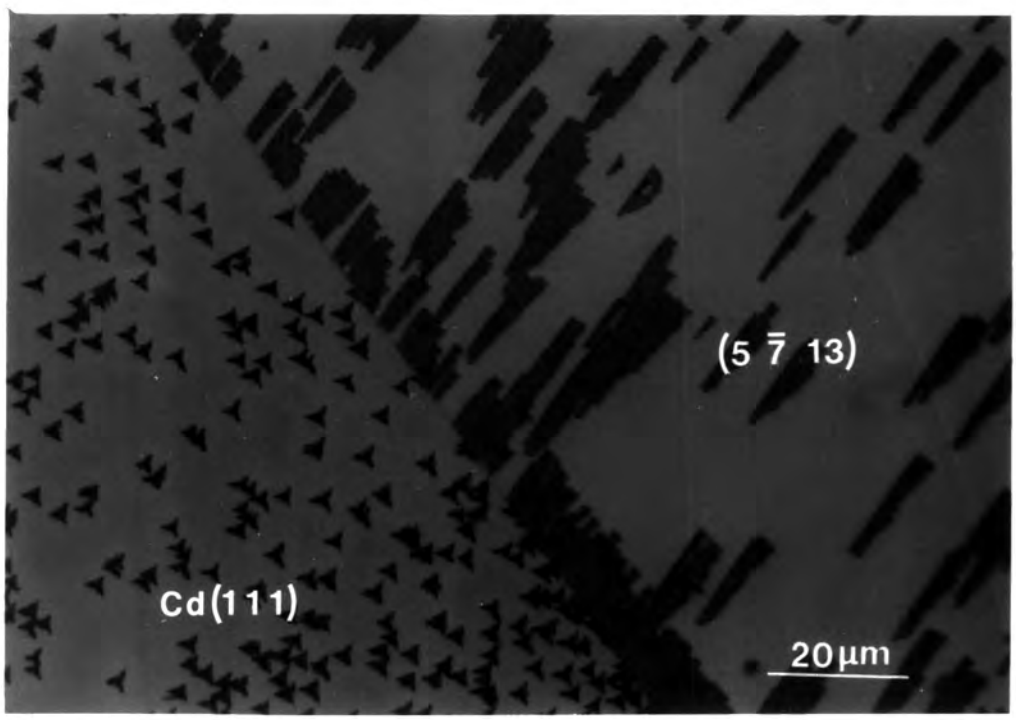

Figure 6.16 {114}-{114} type second order twin boundary.

mining the orientation of a surface following a twinning operation, the surface of the second order twin was found to be (5 $\bar{7}$ 13). Indeed, the pits on this particular surface orientation have the shape that is expected from cutting a tetrahedron of {111} planes along a (5 $\bar{7}$ 13) plane (see §5.4.4). The orientation of the boundary corresponds to {114} - {114} . The boundary itself was not heavily attacked by the Inoue EAg-1 reagent although there is a high density of etch pits on the (5 $\bar{7}$ 13) side of it. In contrast to this the {1 11} - { 11 5} boundary itself (shown in Figure 6.17) is deeply etched by the same reagent. These observations may be related to either selective etching at certain types of boundary or to the presence of defects on the boundaries, such as those observed on first order twin boundaries. A clear example of the intersection of two first order twin boundaries (A and B) and a second order one (c) is shown in Figure 6.18. The second order boundary lies on a {114} plane in both the matrix and twin and is decorated with Te precipitates. Precipitation is discussed in detail in Chapter 9. Figure 6.19 shows a more complex twinning situation in which twins (B) on the ($1\bar{1}1$) matrix planes and a broad twin (C) on the ($\bar{1}11$) matrix plane intersect one another. The orientations B and C in the figure are doubly twinned with respect to one another, the boundaries E and F being second order twin boundaries lying on planes of the forms {221}-{221} and {111} - {115} respectively. In addition, the broad twin orientation C contains three narrow second order twin bands on its ($1\bar{1}1$) planes which are labelled D. These twins have the (5 13 $\bar{7}$) surface orientation and are triply twinned with respect to the ($\bar{1}5\bar{1}$) orientation (B), the boundary at G being an example of a third order twin boundary.

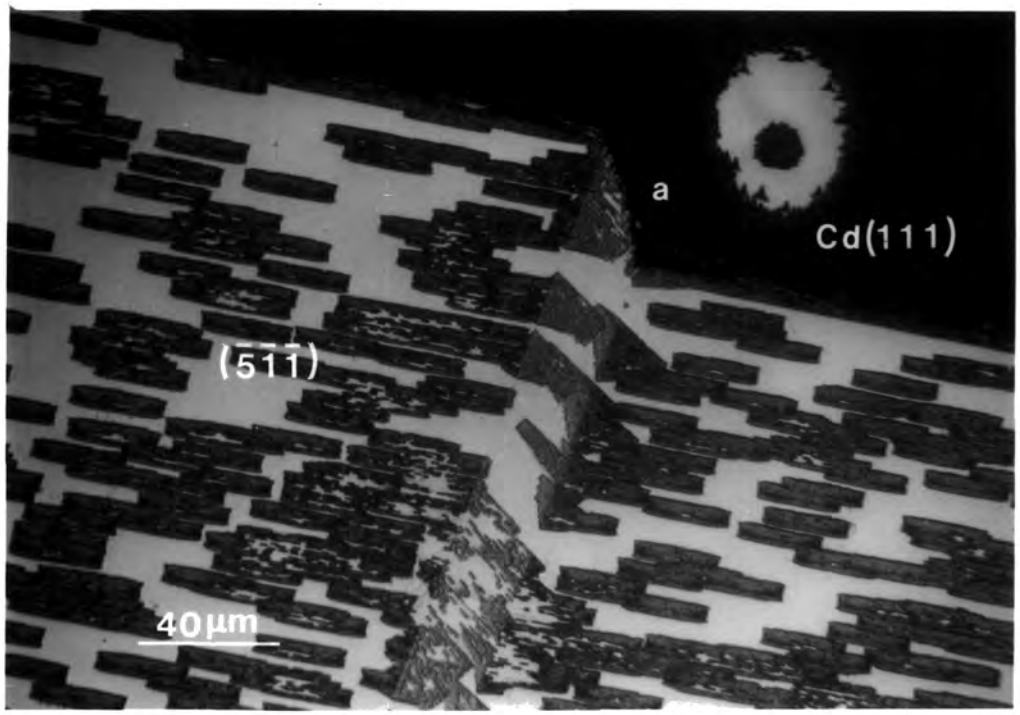

Figure 6.17 Second order twin on a first order twin lamella. (a) is a {111}-{115} type second order twin boundary.

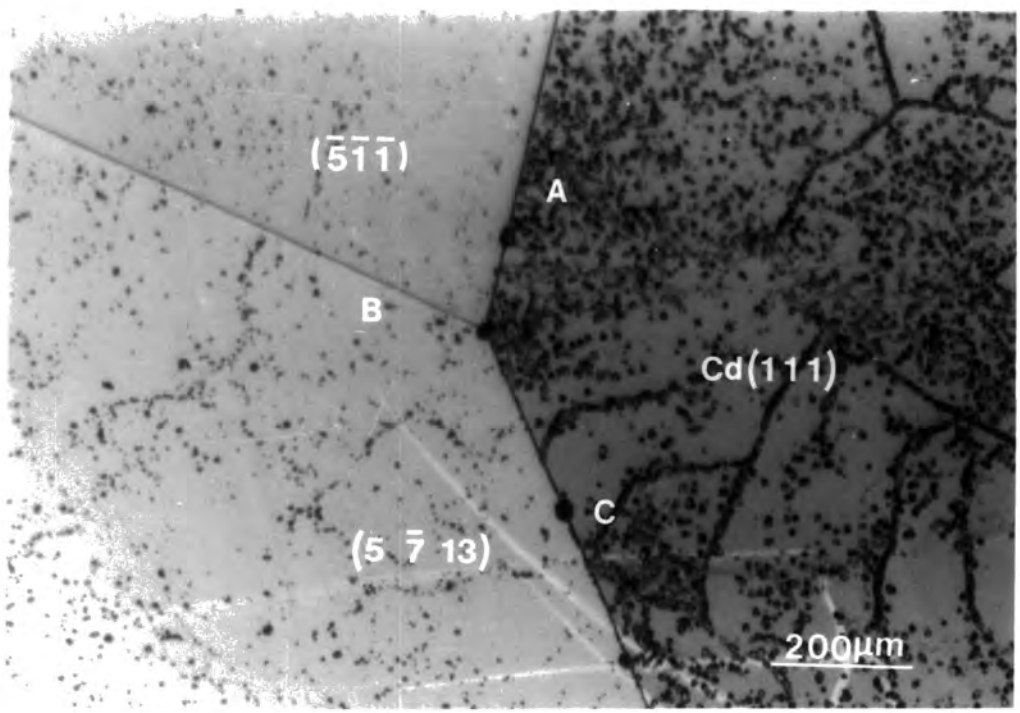

Figure 6.18 {114}- {114} type second order twin boundary (c) and two first order boundaries (A and B).

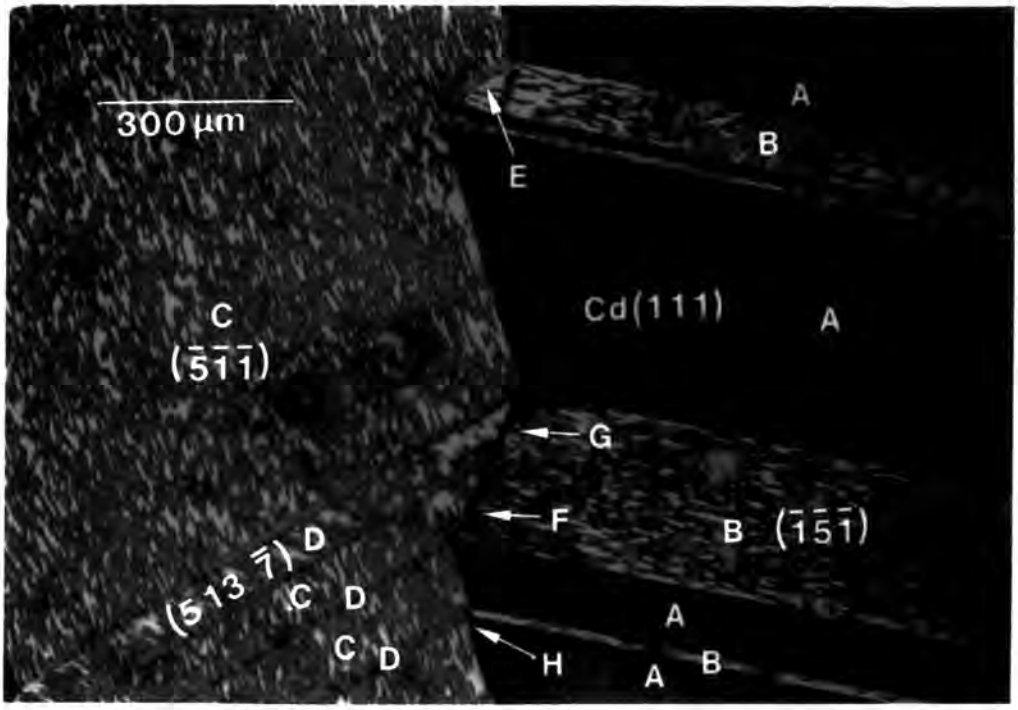

Figure 6.19 Intersecting twin lamellae.

§ 6.5.3 Discussion

All of the observed second order twin boundaries had boundary planes of the types {221}-{221}, {111}-{115} or {114}-{114}. These boundary planes are all predicted by the coincidence site lattice models developed in Chapter 7. The models also predict that wrong and/or dangling bonds are likely to be found at second order twin boundaries.

The presence of such defects implies that the energies of second order boundaries are likely to be much higher than those of first order coherent boundaries. As a result of this energy difference, second order twin boundaries are only seen in association with first order boundaries. It is the intersection of twins (Figure 6.19) and the presence of twin lamellae on other twins (Figures 6.2a, 6.15 and 6.17) which result in the formation of second order twin boundaries.

Since the formation of first order twin boundaries is a prerequisite to the formation of second order ones it follows that second order boundaries are statistically less likely to occur than first order ones. Similarly, the incidence of third and higher order twin boundaries becomes progressively more unlikely.

The preferential chemical attack by Inoue's EAg-1 reagent on a {111}-{115} second order boundary (Figure 6.17) and not a {114} - {114} boundary (Figure 6.16) deserves further attention. A systematic etching study of a number of second order twin boundaries of each orientation would establish whether the etching differences are genuinely caused by the different boundary orientations or by the presence of interfacial defects.

Mechanisms which are responsible for the formation of twins are discussed in §6.6 and detailed models of the formation of interacting twin structures in §6.7.

§ 6.6 The Origins of Twinning

Twins may form by either growth or deformation processes. Deformation twins are formed by the stress induced passage of $a/6\langle 211\rangle$ partial dislocations over successive {111} planes in a fcc, diamond or sphalerite crystal. Post growth stresses are likely to arise from interactions of the crystal boules with the walls of the silica growth capsules. Even though the boules are not generally seen to stick to the silica capsules the two are in close contact over a wide temperature range and stressing is likely to occur. Growth twins could develop as follows: As the charge material is transported a growth interface exists and the boule grows by adding successive layers to the interface which would ideally lie close

to a {111} plane. Accidents in the stacking sequence could be caused by disruptions at the (solid-vapour) growth interface and such events could cause individual stacking faults. If the stacking arrangement does not revert to the packing of the matrix after the nucleation of a stacking fault, then a twin lamella can be formed. If a significant thickness of material having the twin orientation accumulates the influence from the matrix orientation upon successive layers will be weak and the twin orientation will persist until another growth accident occurs. Alternatively growth twinning could arise by multiple grain nucleation, that is if adjacent grains happen to grow in the twin related orientations. The possibility of twins forming in this way is not insignificant : Meyers and Murr [28] have calculated that approximately 10% of randomly oriented grains in a polycrystalline boule of a fcc material are within 4^{o} of a twin orientation with respect to one of their neighbours.

There is no record in the literature of any experiment which proves conclusively that twinning in semiconductor materials is caused specifically by either growth or deformation processes. Vere et al [5] report that they were unable to introduce twins into CdTe bars by compressing them at temperatures up to 400 ^{o}C and thus concluded that twinning is a growth phenomenon. However, Cahn [29] points out that even though it may not be possible to produce deformation twins by applying stresses to crystals in a controlled manner this does not necessarily preclude their formation under the conditions in which they are grown.

In the absence of an unambiguous experimental method to distinguish between the two possible causes of twinning, the following is a phenomenological approach to the twinning problem. The most

important evidence against the growth twin model is that it cannot account for many of the lamellar twin structures frequently observed in the as-grown crystals. Three such examples are:-

i) twin lamellae which intersect the growth interface at a steep angle as in Figure 6.1.

ii) multiple twinning on different {111} planes as in Figure 6.20a; and

iii) second order twins which are present on other twin lamellae as in Figures 6.15, 6.17 and 6.19.

In each of these cases, twinning by a growth mechanism would require a complex growth interface which is capable of deviating from the growth axis normal, changing from one {111} plane to another or else is multi-faceted. For example, second order twins on first order twin lamellae such as that at B in Figure 6.15 could not have been formed by simple stacking accidents on a single {111} plane because the first order twin plane is not parallel to a {111} plane in the second order twin orientation. A growth model of the formation of this structure requires a second growth face on a close packed plane in the first order twin orientation.

In contrast deformation twinning can account for such structures with relative ease. A number of examples are discussed in more detail in §6.7. However, one problem does arise with the deformation model of twinning when boules containing large twinned grains are considered. Figure 6.2a/b shows such a boule in which there are three predominant orientations, the matrix, twin and second order twin. Since deformation twinning effectively involves shearing a lamella of material, matter must be displaced by the twinning operation. Furthermore, narrow twins intersecting the growth surfaces of boules are occa-

sionally seen to exhibit sloping facets which are a direct result of this shear. The constraints imposed by the silica growth capsule would tend to inhibit twin formation unless matter transport away from regions of displaced material, or indeed further twinning, could accommodate the shears involved. If deformation twinning were to occur during the earlier stages of growth then the twinned crystal might act as a seed for further growth. This provides a more reasonable explanation for the large grains in the twin orientation such as those observed in Figure 6.2a/b.

To summarise, deformation twinning is likely to be the dominant mechanism in the formation of lamellar twins and complex interacting twin structures. Dislocation models account for such structures easily and moreover, thermal stresses which are adequate to initiate twinning are more likely to arise during growth when the temperature is much higher than was the case in which a deformation experiment [5] failed to induce twinning. However, the deformation model cannot account for all twins observed in these crystals. For instance, in the case of large twins, the shears necessary in a deformation process would inevitably demand the displacement of amounts of matter significantly greater than those observed in practice. Consequently it is proposed that large twin related grains probably arise from crystals which are twinned during the early stages of growth and then act as seeds for further growth.

§6.7 The Morphology and Formation of Interacting Twin Structures.

Throughout §6.5 a number of systems containing interacting twins, and hence second order boundaries were examined. In this

Figure 6:20 Interacting Twin Structures.

a) Twin-twin intersections.

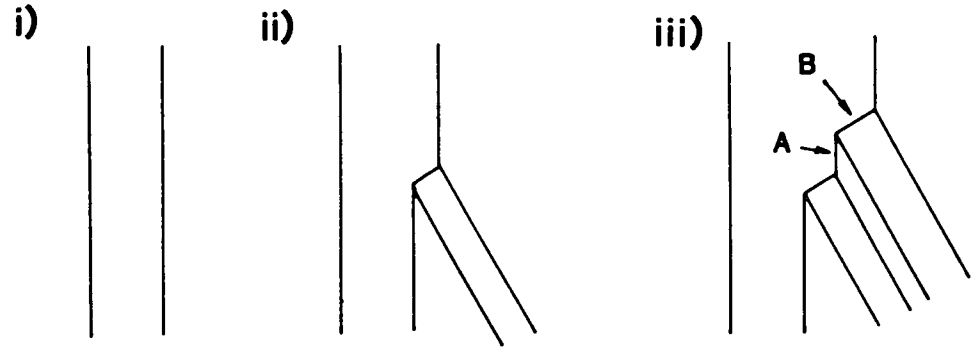

b) Twin bands incorporated on other twins.

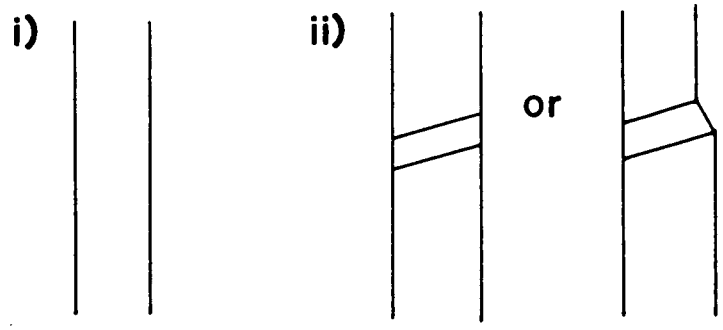

c) Twins crossing other twin bands.

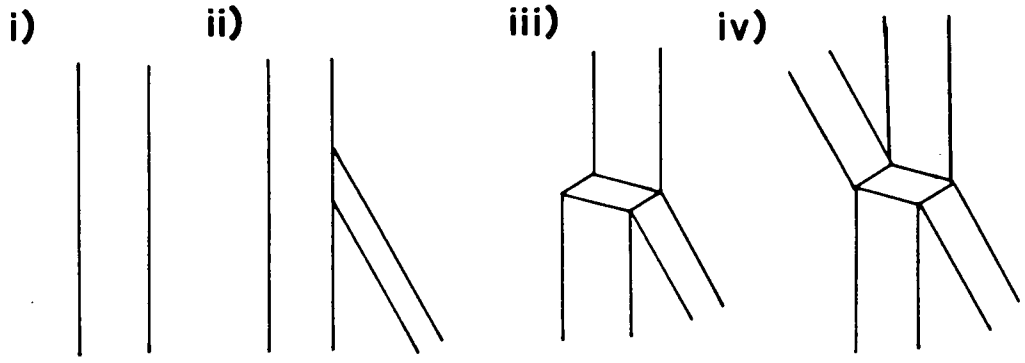

section, the morphologies of these interacting twin structures are described together with suggested mechanisms for their formation.

The three types of interacting twin structures which are frequently observed are shown schematically in Figure 6.20. They are:-

a) intersections between twins on different {111} planes.

b) twin bands which are present on other twin bands, and

c) cases where twins 'cross' other twin bands, that is combinations of a) and b).

The mechanisms which follow are proposed to explain the likely mechanisms of formation of the twinned structures in Figure 6.20a, b and c. It is assumed that the twins are deformation twins, that is they were formed by the passage of a/6<211> partial dislocations over successive {111} planes (see §4.4.2.2). The justification for this assumption was presented in §6.6.

a) Twin-twin intersections

i) The crystal is subjected to a stress which has a resolved component on a {111} slip plane which exceeds the critical shear stress necessary for the propagation of twinning dislocations (the critical shear stress for twinning). The stress is relieved by the passage of a/6<211> dislocations on successive {111} planes to form a stable lamellar twin.

ii) The activating stress changes to include a component which exceeds the critical resolved shear stress for twinning on another slip plane in the matrix. A new twin lamella which emanates from the first is formed when the partial dislocations passing on the original slip plane change to the new slip plane. The plane at which the dislocations transfer to the new slip plane becomes

a second order twin boundary such as that at E in Figure 6.19. An alternative view of the formation of the twin-twin intersection is obtained by reversing the sequence of events just described. In this way the dislocations forming the new twin lamella do not propagate from the original lamella but propagate towards it. When they reach the original lamella they transfer to its slip plane hence causing it to become wider.

iii) If the new twin orientation is not formed continuously but consists of two or more lamellae, then steps (first order twin boundaries as at A) will separate the junctions between the twins (second order twin boundaries as at B).

b) Twin bands incorporated on other twin bands

A model which involves the passage of partial dislocations over only one {111} slip plane in the matrix cannot account for the formation of both first and second order twin boundaries since the latter need not occur on slip planes. In order to form the second order twin orientations in Figure 6.20b twinning dislocations must cross successive slip planes present in the first order twin orientation. First order twinning is therefore a prerequisite for second order twinning. The formation model is as follows:-

i) A narrow twin lamella forms as in a)i.

ii) The stress which was responsible for the formation of this twin lamella changes to include a component which exceeds the critical resolved shear stress for twinning on a slip plane in the first twin lamella. When dislocations propagate over this slip plane the new twin orientation is generated.

iii) The original twin band becomes wider and the new twin band gets longer.

In stage ii above a stable second order twin may form which does not fully cross the first order twin lamella. Such twins are invariably narrow and are terminated by lateral twin boundaries.

c) Twin bands on different {111} planes crossing one another

Twins in the matrix are sometimes seen to propagate into other twin bands (or vice versa). The following formation mechanism is proposed:-

i) A twin lamella forms as in a) i.

ii) The stress which caused the first twin lamella to form changes to include a component which produces twinning on another matrix slip plane. Twinning dislocations propagate towards the original twin lamella.

iii) If the new component of stress is not relieved when the twin reaches the original twin lamella it may propagate through that lamella, providing that the resolved component of stress in the slip plane exceeds the critical shear stress for twinning. The energy penalty for this is the energy of formation of a third order twin boundary such as that at H in Figure 6.19.

An alternative to ii) and iii) would be for the second twin which crosses the first to originate in the broad lamellar twin and propagate into the matrix.

iv) In this figure both twins cross one another completely and two third order twin boundaries are present.

§ 6.8 Conclusions

Twinning is known to occur frequently in crystals of CdTe grown by a variety of techniques and is undesirable since the presence of twins in boules greatly reduce their value as sources of substrates for epitaxy. The twins in crystal boules grown by the 'Durham' sealed capsule vapour phase technique are most often present in the form of lamellae which range in width from several microns to approximately one centimetre. The grains in polycrystalline boules consisting of only several large grains were often found to be related to one another by twinning operations. In general the incidence of lamellar twinning was found to be higher in polycrystalline boules, a fact which was noted by Vere et al [5] who studied twins in CdTe boules grown by a variety of techniques.

First order, first order lateral, second order and occasionally third order twin boundaries have all been identified in the boules examined. First order twin boundaries lying on {111} planes are the most common and they have been identified as being of the low energy ortho-type. The ortho-twin is characterised by a rotation of $\Theta = 250^{o}32'$ about a <110> axis. Transmission electron microscopy has revealed the presence of twinning dislocations on first order twin boundaries. It is these dislocations which are responsible for the etch pits and the discontinuous electrical activity observed by EBIC in the SEM which are associated with the boundaries.

Four orientations of first order lateral twin boundaries have been characterised by examining oriented etched surfaces. These lie on the planes {115} - {111} , {112} - {112} , {110} - {114}

and {001}-{221} and correspond to those boundaries predicted by the coincidence site lattice models presented in Chapter 7. These boundaries are preferentially attacked by various chemical etchants and display strong contrast when imaged in the EBIC mode of the SEM - properties which reflect the distorted nature of the bonding which is to be expected at such boundaries.

Three orientations of second order boundary lying on the planes {111}-{115}, {114}-{114}and {221}-{221} were observed in practice and these also correspond to those predicted by the models proposed in Chapter 7. Second order twin boundaries were only seen in association with first order ones for example at twin-twin intersections or where twin lamellae act as host lattices for other first order twins. Since second order twin planes are not close packed, a simple mechanism (involving a single set of {111} planes) such as those associated with growth and deformation twinning, cannot be responsible for the simultaneous formation of both first and second order twins. First order twinning is therefore a prerequisite for second order twinning. Furthermore, a straight forward growth mechanism cannot account for the formation of sets of intersecting twin lamellae and other intersecting twin structures such as those in Figure 6.19. Deformation twinning mechanisms can be used to explain the presence of these defects relatively easily and a number of examples are given in § 6.8. However, the amounts of material that would be displaced by the shears necessary to create lamellae up to ∿1 cm in width by this mechanism cannot be achieved in practice due to the constraints of the walls of the silica growth capsules. It is therefore proposed that large twinned grains form as a result of seeded growth from twinned orientations which were produced by deformation processes during the early stages of growth.

REFERENCES FOR CHAPTER SIX

1 O. Oda, K. Hirata, K. Matsumoto and I. Tsuboya, J. Crystal Growth 71 (1985) p.273

2 M. Inoue, I. Teramoto and S. Takayanagi, J. Appl. Phys. 33 (1962) p.258

3 Y.C. Lu, R.K. Route, D. Elwell and R.S. Feigleson, J. Vac. Sci. Technol. A 3(1) (1985) p.264

4 J. Auleytner, Z. Liliental, E. Mizera and T. Warminski, Phys. Stat. Sol. (a) 55 (1979) p.603

5 A. W. Vere, S. Cole and D. J. Williams, J. Electronic Materials 12 (3) (1983) p.551

6 N. R. Kyle, J. Electrochem. Soc. 118 (1971) p.1790

7 M. R. Lorenz, J.App. Phys. 33 (11) (1962) p.3304

8 R. Schoenholz, R. Dian and R. Nitsche, J. Crystal Growth 72 (1985) p.72

9 R. Triboulet, R. Legros, A. Heurtel, B. Sieber, G. Didier and D. Imhoff, J. Crystal Growth 72 (1985) p.90

10 A. W. Vere, V. Steward, C.A. Jones, D.J. Williams and N. Shaw, J. Crystal Growth 72 (1985) p.97

11 I. Teramoto, Phil. Mag. 8 (1963) p.357

12 R. T. Lynch, J. App. Phys. 33 (3) (1962) p.1009

13 W. A. Kutagawa and K. Zanio, J. Crystal Growth 11 (1971) p.191

14 H. Iwanaga, A. Tomizuka, N. Shibata and K. Mochizuki, J. Crystal Growth 74 (1986) p.113

15 K. Durose, G. J. Russell and J. Woods, J. Crystal Growth 72 (1985) p.85

16 K. Durose, G. J. Russell and J. Woods, Inst. Phys. Conf. Ser. No. 76 . Section 6 (1985) p.233

17 J. Hails, to be published in J. Cryst. Growth.

18 G. R. Awan, PhD Thesis, University of Durham

19 D.J. Williams, private communication

20 M. Inoue, I. Teramoto and S. Takayanagi, J. Appl. Phys. 32 (1962) p.2578

21 K. Nakagawa, K. Maeda and S. Takeuchi, Appl.Phys. Lett. 34 (9) (1979) p.574

22 D. B. Holt, J. Phys. Chem. Solids 30 (1969) p.1297

23 G.J. Russell and J. Woods, J. Crystal Growth 47 (1979) p.647

24 J.R. Cutter, G.J. Russell and J. Woods, J. Crystal Growth 32 (1976) p.179

25 K.F. Hulme and J.B. Müllin, Solid State Electronics 5 (1962) p.211

26 A. Steinemann and U. Zimmerli, Solid State Electronics 6 (1963) p.597

27 S. Tohno and A. Katsui, J. Crystal Growth 74 (1986) p.362

28 M.A. Meyers and L.E. Murr, Acta Metall. 26 (1978) p.951

29 R.W. Cahn, Advances in Physics 3(12) (1954) p.363.

CHAPTER SEVEN

TWIN BOUNDARIES IN THE SPHALERITE STRUCTURE

§7.1 Introduction

This chapter is principally concerned with the construction of models of first and second order twin boundaries in the sphalerite structure. In §7.2 some of the existing work on models of twin boundaries in the diamond and sphalerite structures is reviewed and coincidence site lattice models of first order lateral twin boundaries in the sphalerite structure are developed in §7.3.2. Variations of the structure of the {112}-{112} boundary are explored in §7.2.2 with reference to recent work on the structure of this boundary in the diamond lattice. The physical implications of the proposed boundary structures and their relevance to real boundaries observed in CdTe crystals is discussed in §7.2.3. Coincidence site lattice models of second order twin boundaries are presented in §7.3.1 and discussed in §7.3.2. The conclusions of the work are summarised in §7.4.

§7.2 A Review of Some Models of Twin Boundaries

§7.2.1 Coincidence Site Lattice Models

A number of models of twin boundaries in the diamond structure have been devised. The earliest of these owed their success to the concept of the coincidence site lattice (CSL) description of grain boundaries which was first proposed by Friedel [1] and later, independantly, by Ellis and Treuting [2]. The CSL may be described as follows: If the lattices of two adjacent grains are superimposed then certain points common to both grains may

exist. For some special orientations these coincidence points will form a regular lattice, the CSL. This is characterised by Σ, the Friedel or grain boundary index, which is simply the ratio of the density of lattice points to that of coincidence lattice points (see §4.3).

Ellis and Treuting [2] and Kohn [3] noted some important properties of coincidence boundaries and the coincidence site lattice. These are:-

i) Coincidence boundaries i.e. those which are associated with a CSL, are special low energy grain boundaries. In practice, the E-θ curves calculated for tilt boundaries (see §4.4.1) are expected to contain cusps or minima when angles corresponding to coincidence orientations are encountered.

ii) For a given crystallographic relationship between adjacent grains, the energy of a grain boundary varies according to its orientation with respect to the coincidence site lattice. Kohn [3] explains in detail that low energy boundaries firstly lie along directions in the CSL having a high density of coincidence points, and secondly are chosen such that the normal arrangement of bonds in the material is distorted as little as possible by the presence of the boundary.

iii) First and higher order twin boundaries may be described as tilt boundaries having a <110> tilt axis. These are all coincidence boundaries, the Friedel index of an nth order twin being $\Sigma = 3^n$.

Kohn [3] systematically applied the CSL model to first,

second and third order twin boundaries in the diamond structure. In general atomically linear boundaries do not satisfy both of the requirements of a coincidence boundary specified by Kohn and outlined in ii) above. Some vectors which join CSL points do however fulfil both conditions. Kohn identified all of the possible simple boundary segments for each CSL and assembled them to form boundaries. Each boundary constructed in this way is characterised by a periodic array of atomic scale facets which correspond to CSL vectors. Atoms on one side of the boundary adopt the matrix positions and those on the other, the twin positions.

§7.2.2 First Order Lateral Twin Boundaries in the Diamond Structure

The CSL for first order twinning in diamond is generated by rotating two <110> projections of the lattice by $70^{o}32'$ with respect to one another about a common origin [2]. Kohn [3] used this CSL to derive four models of lateral twin boundaries lying on different {hhl} planes. Indexing with respect to both the matrix and twin orientations these are {115}-{111}, {112}-{112}, {001}-{221} and {110}-{114}. These boundaries are all faceted and are comprised of a combination of 5, 6 and 7 membered rings. A significant feature of all the models is that two atoms per period of each boundary have abnormal coordination, one having 3 and the other 5 nearest neighbours, compared to 4 in the undistorted diamond structure. This implies that there will be two dangling bonds in each period of each boundary. These are also present in an atomically linear, rather than faceted variant of the {112}-{112} boundary. Kohn recognised that atomic relaxations at the boundaries are likely to take place in order to reduce

the incidence of dangling bonds.

Hornstra [4] reinterpreted Kohn's model of the {112}-{112} boundary as being comprised of an array of partial dislocations. Nevertheless, Hornstra's model of this boundary does not differ greatly from that of Kohn and it too contains two dangling bonds per period.

More recent investigations of the structure of the {112} -{112} first order coherent twin boundary in the diamond cubic structure have benefited from the availability of modern TEM techniques. The 'α-fringe' technique has been used by Vlachavas and Pond [5] to reveal the relative positions of the matrix and twin lattices in the vicinity of a {112} - {112} boundary. It was found that the twin and matrix crystals are displaced by a distance corresponding to 1.38 x the (111) interplanar spacing. This 'rigid body translation' has been observed directly using high resolution TEM (HRTEM) by Bourret and Bacmann [6]. These workers examined coherent steps on {112} - {112} lateral twin boundaries and found dislocations located at the junctions between the lateral and coherent boundaries and these accomodate the displacement associated with the rigid body translation.

Pond et al [7] developed a relaxed model of the {112}-{112} boundary which incorporates the rigid body translation observed experimentally by Vlachavas and Pond [5]. The boundary is comprised of five and seven membered rings and contains neither abnormally coordinated atoms nor dangling bonds. For this reason it is expected that this model will have an interfacial energy which is significantly lower than that of the models due to either Kohn [3] or Hornstra [4].

§ 7.2.3 Second Order Twin Boundaries in the Diamond Structure

Kohn [3] modelled second order twin boundaries using a $\Sigma = 9$ CSL which was derived by rotating two <110> projections of the lattice by $38^{o}57'$ about a lattice point which is common to both. Three second order boundaries having the interfacial planes {111} - {115}, {114} - {114} and {221} - {221} were constructed by assembling segments of boundary which conformed to the criteria of high coincidence site density and minimum lattice distortion as described in §7.2.2. The {221} - {221} boundary structure is comprised of five and seven membered rings which have bonding that is distorted from the regular tetrahedral bonding of the diamond structure. All of the atoms at the interface have four nearest neighbours and there are no dangling bonds. However, Kohn concluded that both the {111} - {115} and {114} - {114} boundaries are comprised of five, six and seven membered rings and contain two dangling bonds per period of the boundary.

Hornstra [4] reinterpreted Kohn's {221} - {221} boundary as being comprised of a "zig-zag" array of dislocations and also proposed a structure consisting of a symmetrical array of double dislocations.

§ 7.2.4 Twin Boundaries in the Sphalerite Structure

The structure of first order coherent twin boundaries in sphalerite was first discussed in detail by Aminoff and Broomé [8]. In that work a variety of twin boundary structures were constructed by assembling {111} layers of close packed atoms in various stacking sequences. The work took into account the crystallographic polarity of the sphalerite structure and both

the 'ortho-' and 'para-' configurations (see § 4.4.2.2) of the first order twin were recognised. Aminoff and Broomé considered the stacking sequences of {111} planes which are characteristic of twinning to arise during the growth of the crystals.

Holt [9] conducted a systematic appraisal of <110> tilt boundaries in the sphalerite structure. This work took account of crystallographic polarity by utilising two tilt angles, θ and $\Theta = \theta + 180^{o}$ which represents the two polar variants of each type of boundary (see § 4.4.2.2). In this way the ortho- and para-twins were represented by tilt angles of $\Theta = 250^{o}32'$ and $\theta = 70^{o}32'$ respectively (see Figures 4.9a and b in Chapter 4). However, in that work Holt [9] did not consider first order lateral or second order twin boundaries.

§7.3 Models of First Order Lateral Twins in the Sphalerite Structure

§7.3.1 Introduction

While the structures of different types of twin boundary in the diamond structure have been discussed in detail [3,4,5,7] no examples of first order lateral or higher order twin boundaries in the sphalerite structure are available in the literature. Consequently this section attempts to rectify this ommission by taking the models of these boundaries in the diamond structure and employing the methods used in their construction as a basis for the construction of the analogous models of these boundaries in the sphalerite structure.

§7.3.2 First Order Lateral Twin Boundaries

In this section the CSL method (see §7.2.1) has been used

to construct models of first order lateral twin boundaries in the sphalerite structure. Variations of the structure of one particular boundary are also considered. The CSL for the ortho-twinning configuration was generated by superimposing two <110> projections of the sphalerite lattice and rotating one lattice relative to the other by an angle of $\Theta = 250^{o}32'$ about a common origin. The presence of ortho-twins in CdTe was confirmed experimentally (see § 6.4.2). The CSL illustrated in Figure 7.1 has a Friedel index of $\Sigma = 3$ and is analogous to Kohn's CSL for first order twinning [3]. Four types of atomic positions are used in all of the figures, and these represent Cd and Te atoms which are either in or out of the plane of the diagram as indicated in Figure 7.1. An alternative CSL may be generated by rotating through an angle of $\theta = 70^{o}32'$ about the same origin. This CSL corresponds to para-twinning and has only half of the density of CSL points as the CSL which corresponds ortho-twinning. These points are either all black (Cd) or all white (Te), depending upon the colour of the CSL point chosen as the origin. The lines joining CSL points which are labelled 1,2,2' and 3 in Figure 7.1 were chosen as suitable segments of twin boundaries according to Kohn's criteria which are outlined in §7.2.1. (Segment 2' is related to segment 2 by symmetry but has a different environment in the CSL). The three segments can be assembled to form the four different low index boundaries of the {hhl} type which are illustrated in Figure 7.1. In order to form the complete boundary structures, lattice points in the twin and matrix orientations are placed on either side of these boundaries. The four boundaries constructed in this way lie on the planes {115} - {111} (Figure

7.2), {112}-{112} (Figure 7.3), {001}-{221} (Figure 7.4) and {110}-{114}(Figure 7.5) and these are analogous to those drawn by Kohn [3] in the diamond lattice.

Four types of atomic positions on these boundaries are of interest. These are labelled in the diagrams as:-

a - 3 coordinated atoms having one bond rotated into the plane of the figure by $57^{o}1'$.

a'- 5 coordinated atoms having one bond rotated out of the plane of the figure by $57^{o}1'$. Two of the nearest neighbours of such atoms are not in the planes represented in the figures.

b - The site of a Te-Te or Cd-Cd wrong bond. The bonds from both atoms in the equivalent diamond structure are rotated by $19^{o}28'$ in the plane of the figure and are approximately 6% shorter than normal.

c - 4 coordinated atoms with normal undistorted tetrahedral bonding.

All four lateral first order twin boundaries contain one a and one a' atom per period of boundary. The presence of these abnormally coordinated atoms implies that these boundaries all contain two dangling bonds per period, as is the case in the diamond structure. As pointed out by Kohn it is expected that the coincidence structures presented here will relax in order to relieve the abnormal coordinations and hence saturate the dangling bonds. One b site which is associated with a wrong bond in the sphalerite structure is found in each period of each of the four boundaries. All of the wrong bonds in any given boundary will be of either the Cd-Cd or Te-Te type. The geometrically identical position in the diamond structure is simply a shortened bond. In both the diamond and sphalerite structures tetrahedrally coordinated

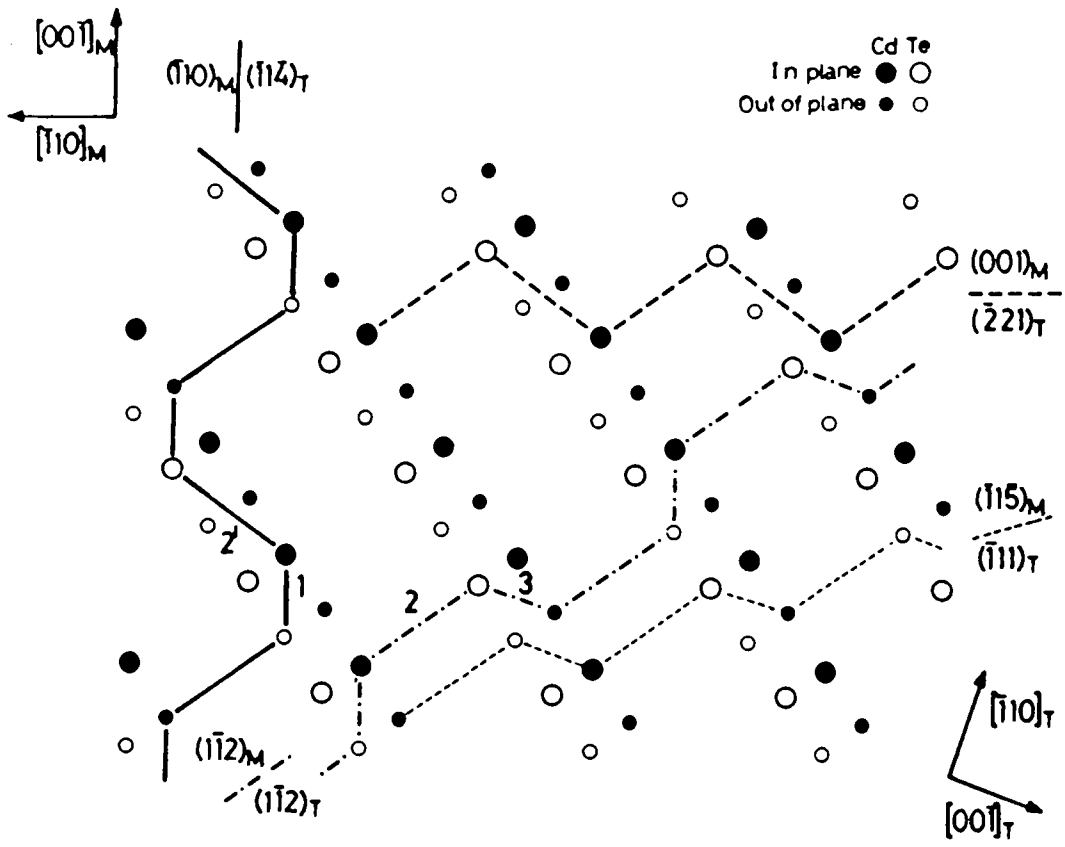

Figure 7.1 The $\Sigma = 3$ coincidence site lattice in the sphalerite structure.

atoms with undistorted bonding (labelled c in the diagrams) are only found in the {001}-{221} and {110}-{114} boundaries. Such atoms are associated with the structural unit labelled 2' in Figure 7.1.

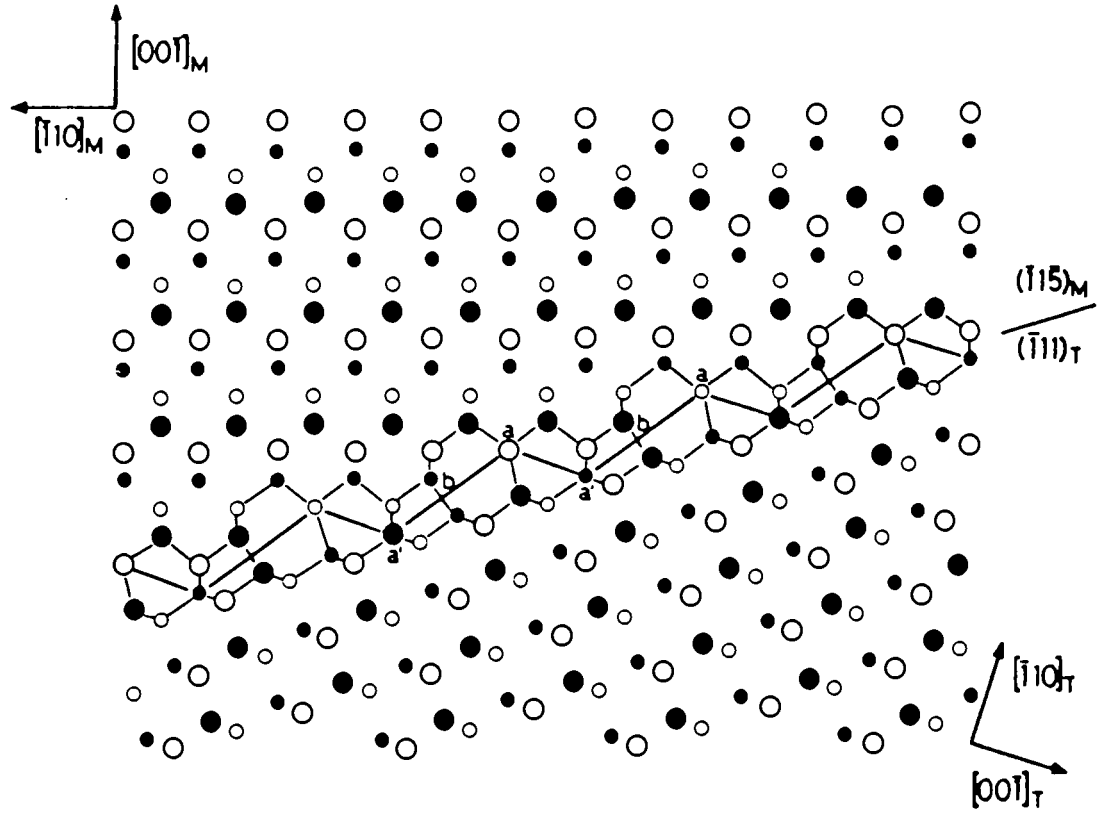

Figure 7.2 {115}-{111} lateral twin boundary.

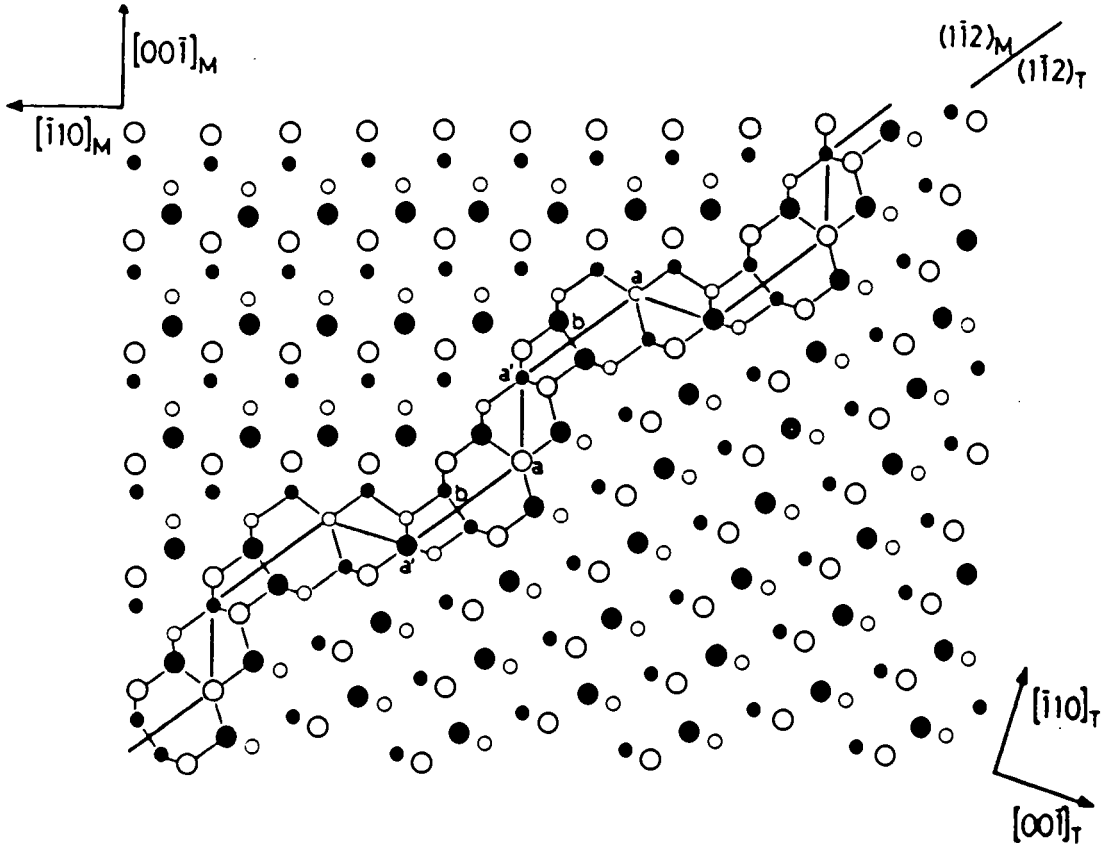

Figure 7.3 {112}-{112} lateral twin boundary.

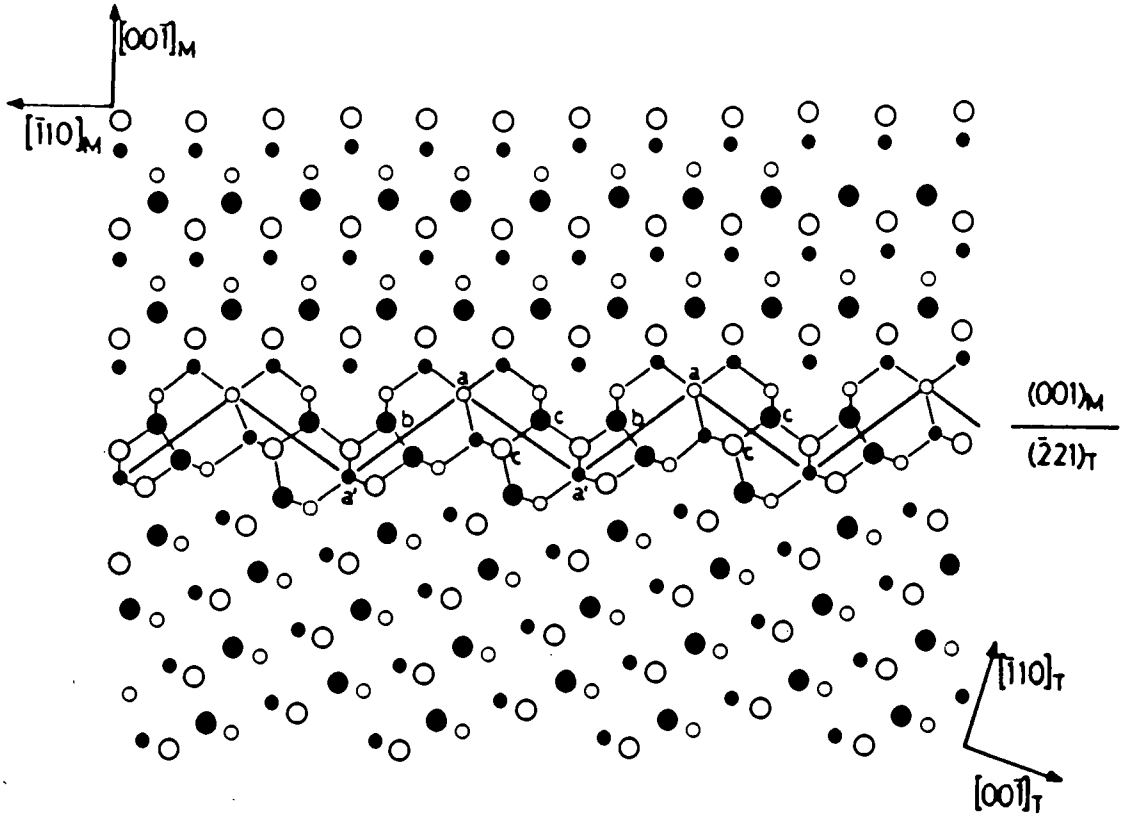

Figure 7.4 {001}-{221} lateral twin boundary.

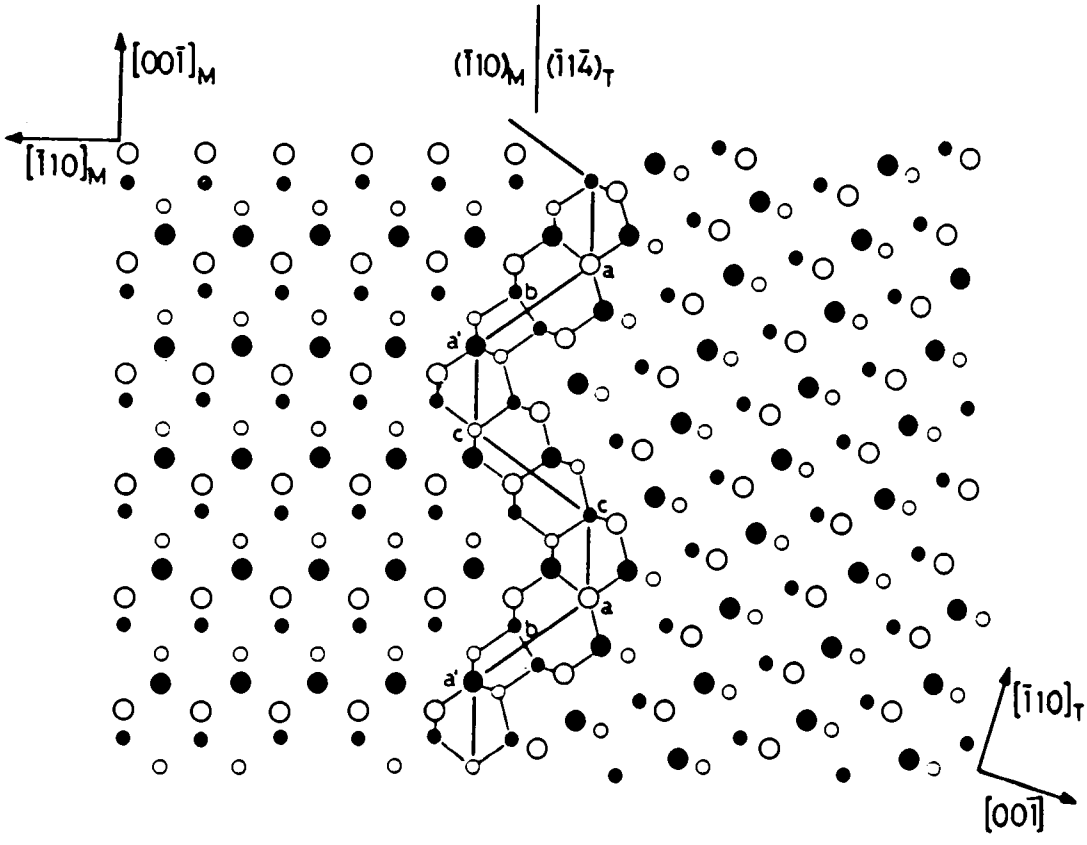

Figure 7.5 {110}-{114} lateral twin boundary.

§ 7.3.3 The {112}-{112} Boundary

The structures of the four coincidence boundaries illustrated in Figures 7.2 to 7.5 are not unique and different combinations of the structural units 1,2,2' and 3 can yield equivalent boundaries. For example, the faceted {211} - {211} boundary in Figure 7.3 can be replaced by an atomically linear boundary as in Figure 7.6. This new boundary contains the same structural features as the old one: For example, two dangling bonds are present in each period of the boundary and are associated with the abnormally co-ordinated atoms at L(≡ a) and R(≡ a'). Wrong bonds are also present in equal densities in the two boundaries.

The model of the {112}-{112} boundary in the diamond structure devised by Pond et al [7] contains no abnormally co-ordinated atoms and hence no dangling bonds (see § 7.2.2). The relaxation necessary to achieve this is made possible by the introduction of a rigid body translation between the matrix and twin lattices and a certain amount of atomic relaxation along the plane at which they meet. A boundary in the sphalerite structure which is analogous to one proposed by Pond et al [7] for the diamond structure is drawn in Figure 7.7. It is related to the atomically linear boundary in Figure 7.6 in the following way: The abnormally coordinated atoms L and R debond and one atom, L, becomes associated with the twinned lattice, while the other, R, becomes associated with the matrix lattice. Atom L subsequently bonds to P, T and T' in the matrix and atom R to Q, S and S' in the twin (S' and T' occupy positions vertically above S and T). The twinned lattice is then displaced by a rigid body translation of 1.38 times the $(\bar{1}1\bar{1})$ interplanar spacing as indicated in Figure 7.7. (The positions

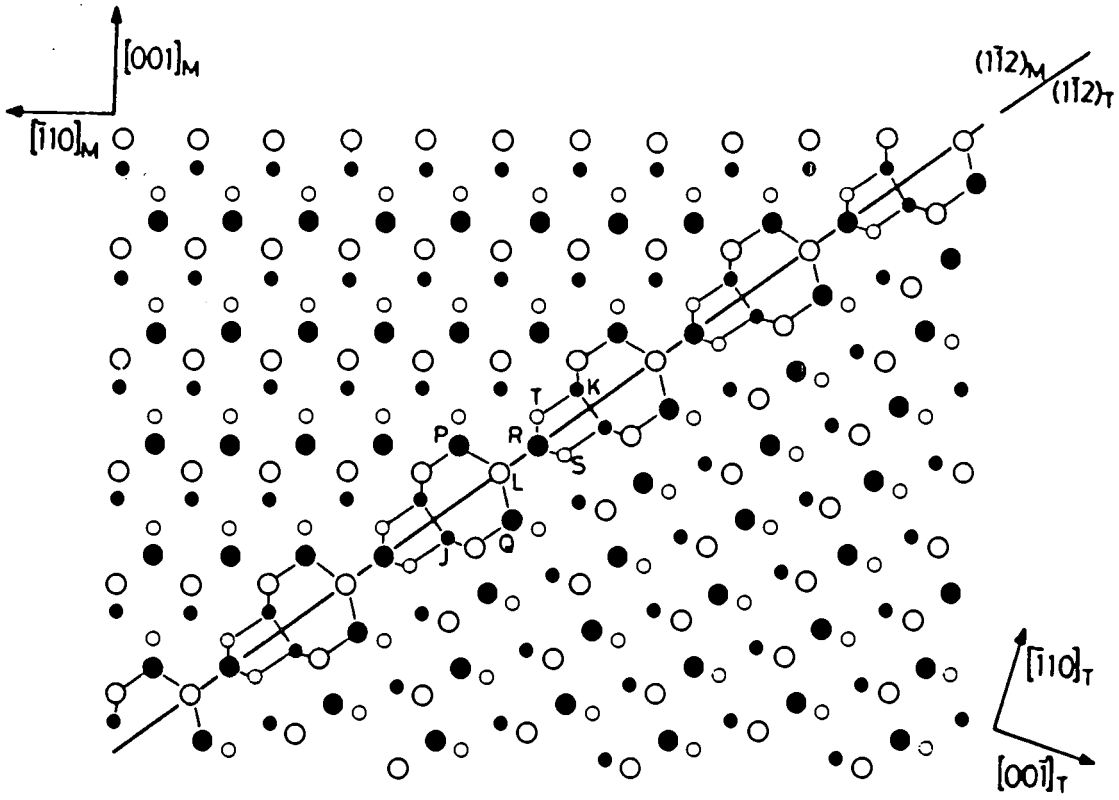

Figure 7.6 An atomically linear {112}-{112} lateral twin boundary.

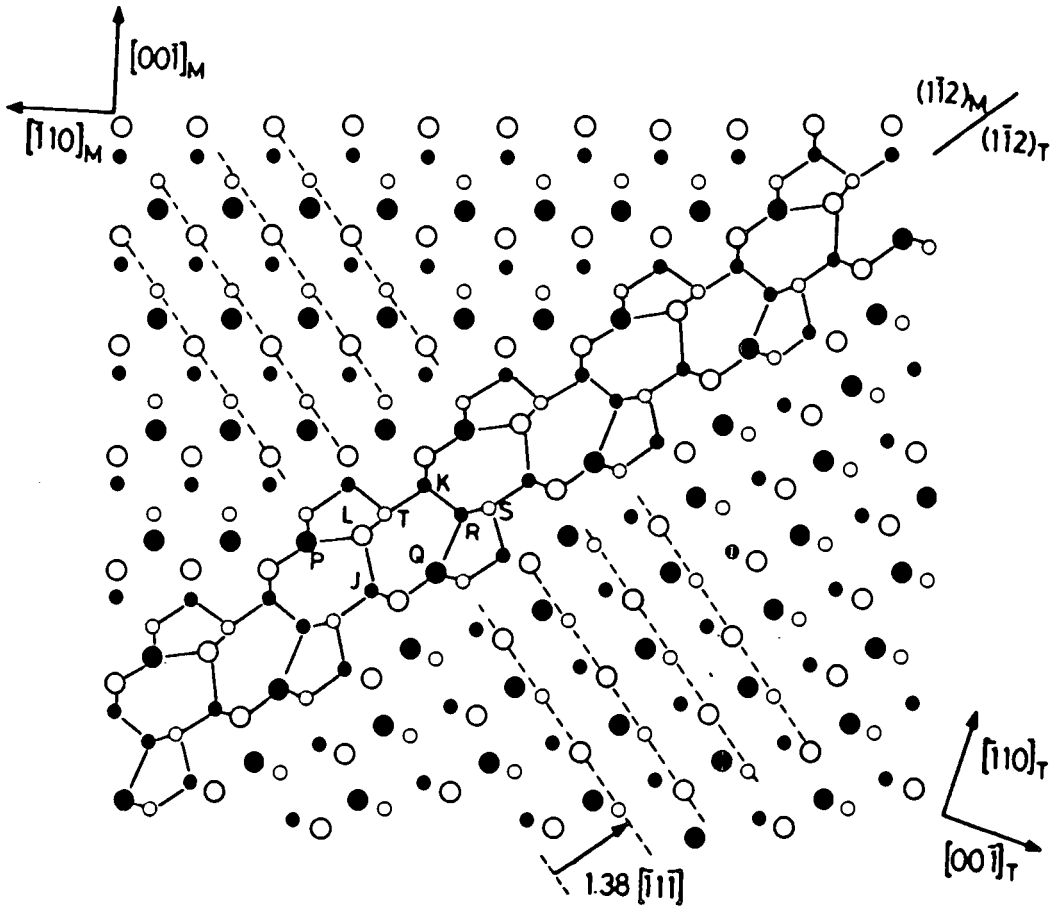

Figure 7.7 A relaxed {112}-{112} lateral twin boundary.

of the $(\bar{1}1\bar{1})$ planes are indicated by the dashed lines in the figure). The atoms L and R then become fully coordinated by forming bonds across the interface to atoms J and K respectively, as shown in Figure 7.7.

§ 7.3.4 Discussion

Whereas there is only one possible electrically active structural defect in the diamond lattice, the dangling bond, Holt [9] points out that there are four in the sphalerite structure. These are α (Cd) or β (Te) dangling bonds and α (Cd-Cd) or β (Te-Te) wrong bonds. The electrical properties of these defects in the sphalerite structure may therefore be expected to be more important than those in the diamond structure. Certainly the unrelaxed coincidence boundaries illustrated in Figures 7.2 to 7.6 all contain α and β type dangling bonds at a and a' and either α or β wrong bonds at b. The introduction of the boundary relaxations into the structure of the {112} - {112} lateral twin which are appropriate to the diamond structure does not eliminate the presence of electrically active defects in the same boundary in sphalerite: The rigid body translation introduced into the boundary illustrated in Figure 7.7 enables boundary relaxations to compensate for abnormal coordinations at the expense of creating an extra wrong bond per period of boundary. This relaxed structure not only retains the electrical activity of the coincidence boundary but also has a boundary configuration which is likely to be of higher energy than that of the unrelaxed structure.

The models described in §7.2 clearly indicate that it is highly likely that first order lateral twin boundaries are inherently

electrically active. Indeed this has been confirmed by the strong EBIC signals which have been obtained from these boundaries (see §6.4.2). This electrical activity has important implications for devices fabricated from epitaxial layers deposited on twinned substrates: Lateral twin boundaries which propagate into the epilayers will undoubtedly be electically active and it is obviously undesirable to grow epilayers on substrates which contain these defects. However, even when epitaxial layers of CdTe and $Cd_xHg_{1-x}Te$ have been grown by MOVPE on twin-free (111) oriented substrates [10] they have been found to contain a high density of 'islands' which have the twin orientation with respect to the rest of the epilayer. These twinned islands are irregular in shape and SEM reveals that their boundaries appear to be curved even when they are imaged at high magnification. Nevertheless these 'double positioning' boundaries are likely to be comprised predominantly of facets which lie on low energy planes, that is on coherent and lateral twin boundary planes. The double positioning boundaries may therefore be expected to be electrically active and hence deleterious to the performance of devices fabricated on such layers.

The experimental observation of lateral twin boundary planes in CdTe described in §6.4.2 supports the validity of the twin boundary models described in §7.3.2: All four orientations of lateral twin boundary planes predicted by the models were identified on the etched surfaces of oriented crystals. Furthermore, no other boundary orientations were discovered.

§7.4 Models of Second Order Twin Boundaries in the Sphalerite Structure

§7.4.1 Second Order Twin Boundaries

Models of second order twin boundaries in the sphalerite structure can be constructed using a <110> projection of a $\Sigma = 9$ CSL. This may be generated by rotating one <110> projection of the lattice with respect to another about a common origin through an angle of $\Theta = 218^{\circ}57'$. This CSL is analogous to that of the first order ortho-type twin boundary and is illustrated in Figure 7.8. Indeed, as in the case of first order ortho-twins there is a variant of the second order twin boundary which may be obtained by reversing the crystallographic polarity of one of the grains. This boundary is a <110> tilt boundary having a tilt angle of $\theta = 38^{\circ}57'$. Two CSLs can be generated by this rotation, one comprised of Cd atoms (black) and the other of Te atoms (white) - the type depends upon the identity of the atom at the origin of the CSL. Both of these CSLs have half the density of lattice points found in the $\Theta = 218^{\circ}57'$ CSL and it is not therefore expected that boundaries of this type will be observed in practice. For the $\Sigma = 9$ CSL only two boundary segments, labelled 1,2, and 2' in Figure 7.8 can be chosen to conform to Kohn's criteria [3] of high coincidence site density and minimum structural distortion (see §7.2.1). Segment 2' in the figure is symmetrically equivalent to segment 2. The three boundary segments may be assembled to form the three low index {hhl} boundaries indicated in Figure 7.8. In order to form the complete boundary structures lattice points in the matrix orientation are drawn on one side of the boundary and those in the twin orientation are drawn on the other as was done for first order twin boundaries. The boundaries

lie on planes of the forms {111} - {115} (Figure 7.9), {114} - {114} (Figure 7.10) and {221} - {221} (Figure 7.11) and are analogous to those drawn by Kohn [3] in the diamond structure. Positions labelled a, a' and b in Figures 7.9 to 7.11 are identical to those labelled similarly in the first order lateral twin boundaries (§7.3.2). None of the second order boundaries contain any atoms having undistorted bonding and unchanged coordination. Both the {111} - {115} and the {114} - {114} boundaries contain one wrong bond and two dangling bonds at a and a' in each boundary period. In practice boundary relaxations are expected to take place in order to saturate the wrong bonds to some extent and to lower the interfacial energy of the boundary. The {221} - {221} boundary is exceptional in that it contains no abnormally coordinated atoms and hence no dangling bonds. However, it does contain two wrong bonds per period, one Cd-Cd and one Te-Te type. The atoms in this boundary which are labelled d in Figure 7.11 are unique to the {221} - {221} boundary, the cross boundary bonds being rotated alternately clockwise and anticlockwise by $31^{o}35'$ in the plane of the figure. A similar tetrahedrally coordinated site with distorted bonding exists in the analogous boundary in the diamond structure.

§7.4.2 Discussion

The boundary sites labelled a, a' and b (that is abnormally coordinated atoms, associated with dangling bonds, and wrongly bonded atoms) which occurred in the unrelaxed CSL models of first order lateral twin boundaries are also found in the CSL models of second order twin boundaries. Two of the three coincidence

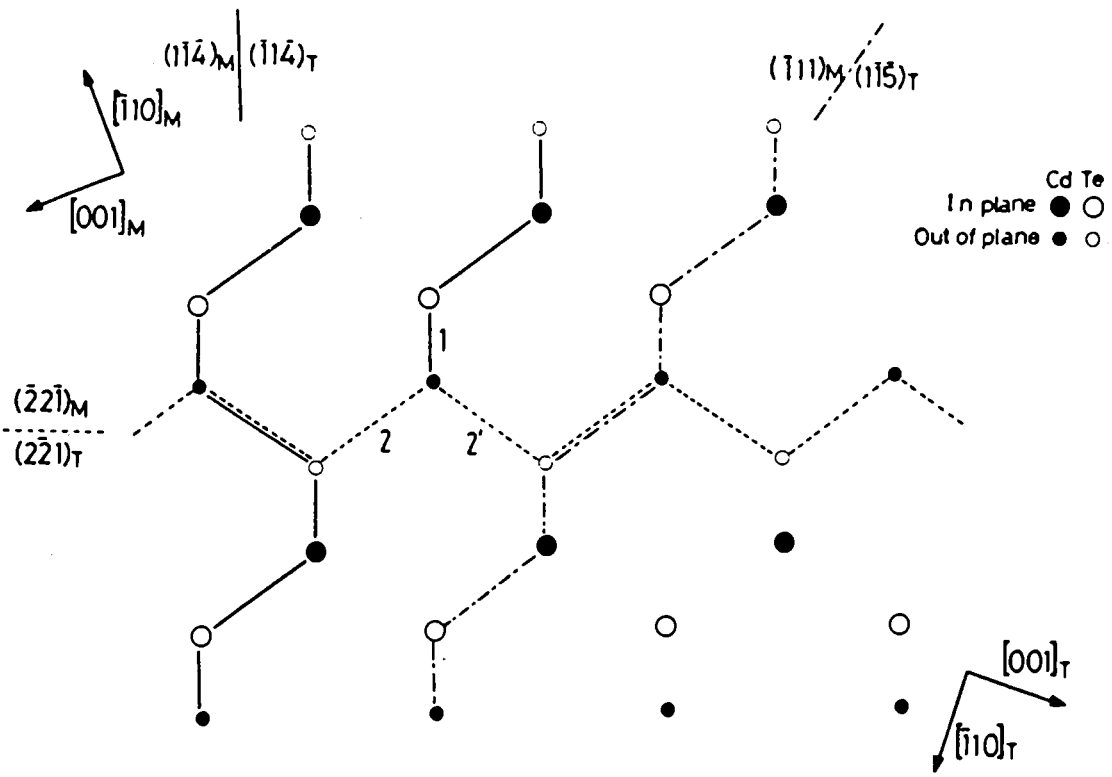

Figure 7.8 The Σ = 9 coincidence site lattice in the sphalerite structure.

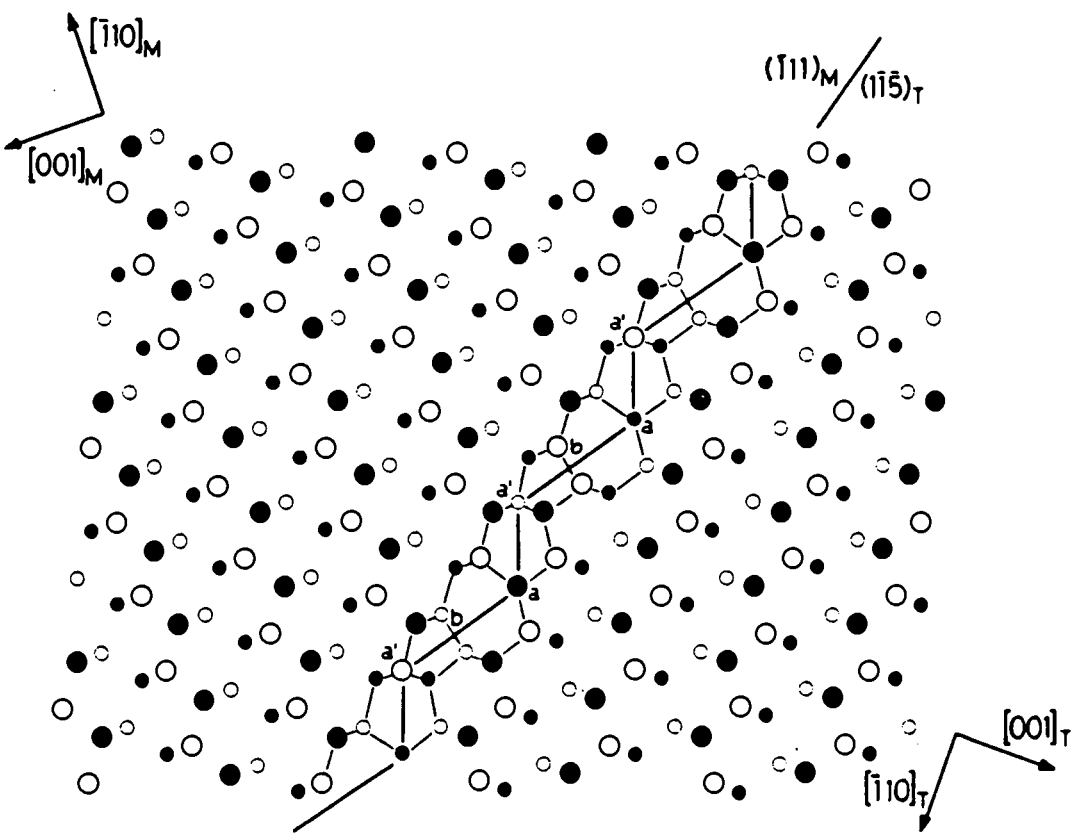

Figure 7.9 {111}-{115} second order twin boundary.

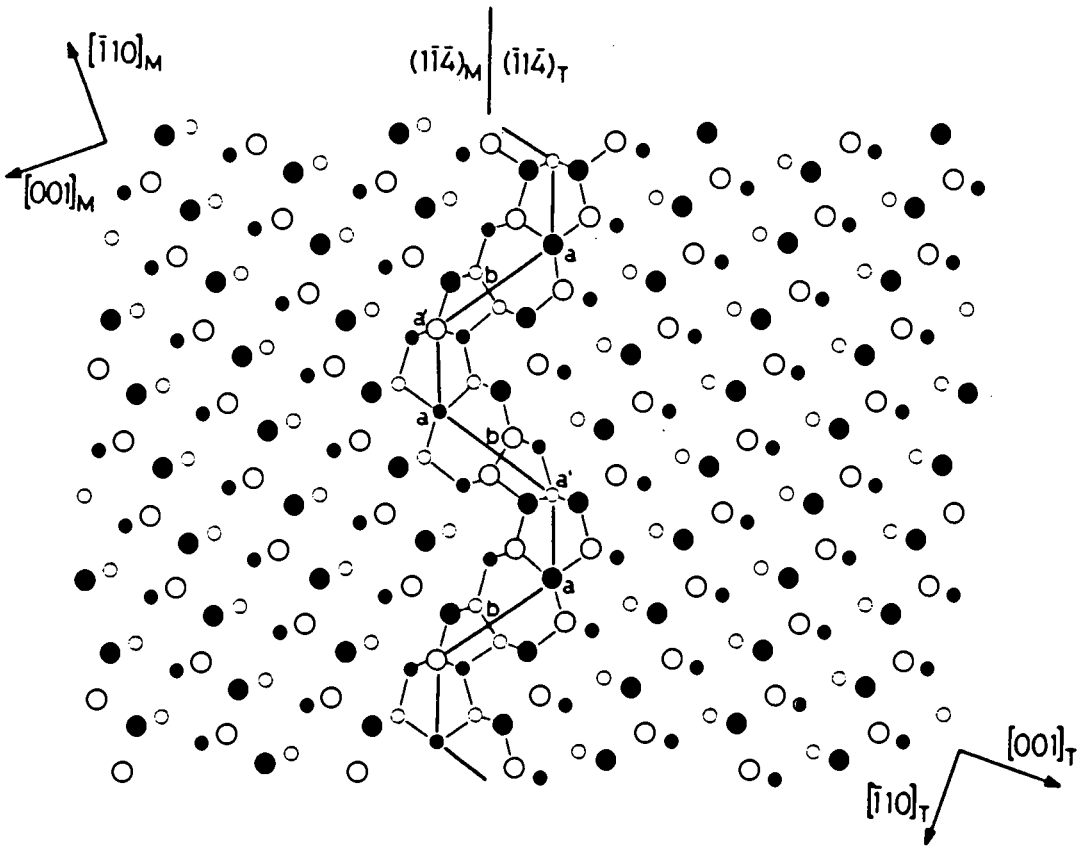

Figure 7.10 {114}-{114} second order twin boundary.

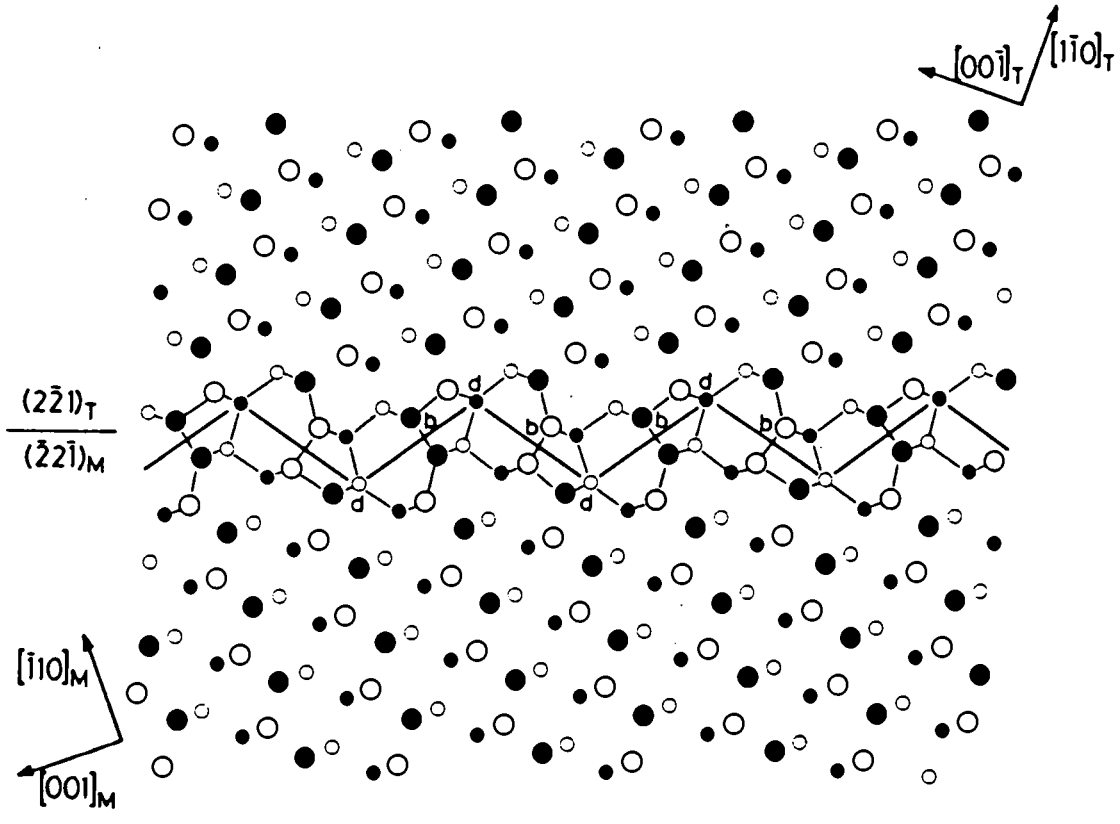

Figure 7.11 {221}-{221} second order twin boundary.

models contain two dangling bonds (a and a' sites) and one wrong bond per period. The third, the {221} - {221} boundary, contains two wrong bonds per period but is free from dangling bonds. It also contains one unusual tetrahedrally coordinated atom per period which has distorted bonding. Although the precise nature of the atomic arrangements at the interfaces will be altered in practice by boundary relaxations, it is likely that some wrong or dangling bonds will remain, also rendering these boundaries to be electrically active.

The CSL model is highly successful in that all of the boundaries which have been observed experimentally in CdTe (see §6.5.2) correspond to one of the three {hhl} boundary planes predicted. Furthermore, no second order boundaries on other planes have been discovered.

§ 7.5 Conclusions

For both first and second order boundaries in the sphalerite structure there are two possible CSLs. These represent the two forms of each boundary made possible by the crystallographic polarity of the sphalerite structure and which correspond to tilt angles about <110> of θ and $\Theta = \theta + 180^{\circ}$. The most densely populated CSLs were those corresponding to tilt angles of $\Theta = 250^{\circ}32'$ ($\Sigma = 3$ ortho-twin) and $\Theta = 218^{\circ}57'$ ($\Sigma = 9$ second order twin). The CSLs corresponding to the tilt angles $\theta = 70^{\circ}32'$ and $\theta = 38^{\circ}57'$ contained only half of the CSL points present in the $\Theta = 250^{\circ}32'$ and $\Theta = 218^{\circ}57'$ CSLs and furthermore the lattice points were either black or white, depending on the colour of the lattice point at the origin of the CSL. In summary, the following features concerning the models are of particular significance:-

1 First order lateral twin boundaries §7.3

The four interfacial planes identified for these boundaries using the CSL model were of the types {115}-{111}, {112}-{112}, {001}-{221} and {110}-{114}. Unrelaxed models of the structures of these boundaries are illustrated in Figures 7.2 to 7.5. All of these contain two dangling bonds per period, which are associated with abnormally coordinated atoms. One wrong bond of the Cd-Cd or Te-Te type is also present in each period of all three boundaries.

The atomically linear version of the {112}-{112} coincidence boundary in Figure 7.6 also contains one wrong bond and two dangling bonds per period. The {001} - {221} and {110}-{114} boundaries contain two atoms per period which have undistorted tetrahedral bonding. In practice it is thought that relaxations of the boundary atoms from the positions occupied in these CSL models will occur in order to reduce the number of boundary defects. A relaxed version of the {112}-{112} lateral twin boundary (Figure 7.7) which is related to the atomically linear boundary by a rigid body translation contains no dangling bonds. However, it contains twice the density of wrong bonds found in the unrelaxed coincidence boundary. From studies of these models it seems inevitable that lateral twin boundaries are likely to contain wrong bonds and/or dangling bonds making them inherently electrically active. Indeed the strong EBIC signals observed at lateral twin boundaries (see §6.4.2) confirm this.

2 Second order twin boundaries §7.4

The three boundary planes identified using the coincidence site

lattice model for second order twinning were of the types {111}-{115}, {114}-{114} and {221}-{221}. Unrelaxed coincidence models of these boundaries are illustrated in Figures 7.9 to 7.11. The {111}-{115} and {114}-{114} boundaries contain one wrong bond and two dangling bonds per period, the dangling bonds being associated with abnormally coordinated atoms. However, the {221}-{221} boundary contains no dangling bonds but has two wrong bonds, one Cd-Cd and one Te-Te type, per period. The presence of a high density of wrong bonds in this boundary is thought to be energetically unfavourable. These models indicate that second order twin boundaries are likely to contain electrically active wrong or dangling bonds.

It is suggested that any first order lateral or second order twin boundaries which become incorporated into epilayers a) by growth through from twinned substrates or b) as part of the intrinsic defect structures of the epilayers, will have an important effect upon the electrical properties of any devices fabricated using the layers.

A significant success of the models of both first order lateral and second order twin boundaries developed in this Chapter is that all of the boundary planes predicted by the model have been identified in practice (see §6.4.2 and §6.5.2). Moreover, no additional boundary planes have been observed.

REFERENCES FOR CHAPTER SEVEN

1 G. Friedel. Leçons de Cristallographie Ed. Berger Levrault Paris 1926.

2 W.C.Ellis and R.G. Treuting. Jour Metals 3 (1951) p.53.

3 J.A. Kohn. Amer. Mineralogist 43 (1958) p.263.

4 J. Hornstra. Physica 25 (1959) p.409.

5 D.S. Vlachavas and R.C. Pond. Inst.Phys.Conf.Ser. No.60 (1981) p.159.

6 A. Bourret in Polycrystalline Semiconductors Ed. G. Harbeke. Springer-Verlag (1985).

7 R.C.Pond, D.J. Bacon and A.M. Bastaweesy. Inst.Phys.Conf.Ser.No.67 (1983) p.253.

8 G. Aminoff and B. Broomé. Zeitschrift für Kristallographie und Mineralogie. (Leipzig) 80 (1931) p.335.

9 D.B. Holt. J.Phys.Chem.Solids 25.

10 J.E.Hails, G.J.Russell, A.W.Brinkman and J. Woods. In press in J.Crystal Growth.

CHAPTER EIGHT

SUB-GRAINS IN CdTe AND $Cd_{0.95}Zn_{0.05}Te$

§ 8.1 Introduction

In this Chapter the properties of dislocations in CdTe and $Cd_{0.95}Zn_{0.05}Te$ crystals grown by the 'Durham' method, and also in CdTe grown by the modified Piper-Polich method (see §2.2.2 and §2.2.3) are reported. In particular, the organisation of dislocations into arrays, that is sub-grain boundaries, in these materials has been investigated. Throughout the literature dislocations in CdTe crystals grown by all techniques are invariably reported as being concentrated into arrays which form a cellular structure, the density of dislocations within the cells (sub-grains) being comparatively low (see references [1-5] for example). An introduction to sub-grain boundaries and the phenomenon of polygonisation is given in §4.3.3 and §4.3.4.

§8.2 Sub-grain Boundaries in CdTe

§8.2.1 CdTe Grown by the 'Durham' Method

§8.2.1.1 Etching Studies

This section reports the investigations made using three different etchants on sub-grains in CdTe crystals grown using the 'Durham' technique (see §2.2.2). The reagents employed were:- i) Nakagawa's etch [6], ii) Inoue's EAg-1 etchant [7] and iii) a photoetch consisting of a 0.5% solution of bromine in methanol [3,5]. The capability of each of these reagents to etch CdTe is described in §5.4. The etch pit densities typically obtained for these crystals with the first two of these reagents

were 2 x 10^4 pits cm^{-2} on Cd(111) with approximately half this number on Te ($\bar{1}\bar{1}\bar{1}$) using Nakagawa's reagent, and 10^4 - 10^5 pits cm^{-2} on both {111} faces using EAg-1. While etch pit densities are frequently quoted as an indication of the quality of CdTe crystals (see reference [8] for example), such figures give no indication of the nature of the sub-grain boundaries present in this material. These boundaries are of considerable importance since they contain a high proportion of the native dislocations in CdTe crystals. Figures 8.1 and 8.2 show how such boundaries are revealed as closely packed rows of pits after etching for one minute in the Nakagawa and Inoue etches respectively (the features at the bottom of Figure 8.1 are twin boundaries). The preferred etchant for sub-grain boundaries is the 0.5% bromine in methanol photoetchant which reveals patterns of boundaries such as that shown in Figure 8.3 after about 10 minutes. The special feature of this reagent is that it produces etch features on surfaces of all orientations. All three of the photomicrographs just presented indicate an average sub-grain size of about 150 μm which has been found to be typical for this material. Figure 8.4 shows a higher magnification photomicrograph of sub-grain boundaries etched with the bromine-methanol photoetch. It is apparent from the photomicrograph that some sub-grain boundaries, such as that at A, are delineated more heavily than others, such as that at B for example. This indicates that the photoetch acts in different ways on different boundaries and thus it seems likely that a variety of types of sub-grain boundary exist in any one crystal boule.

Whereas the cellular structure depicted in Figure 8.4 is typical of this material, elongated sub-grains such as those in

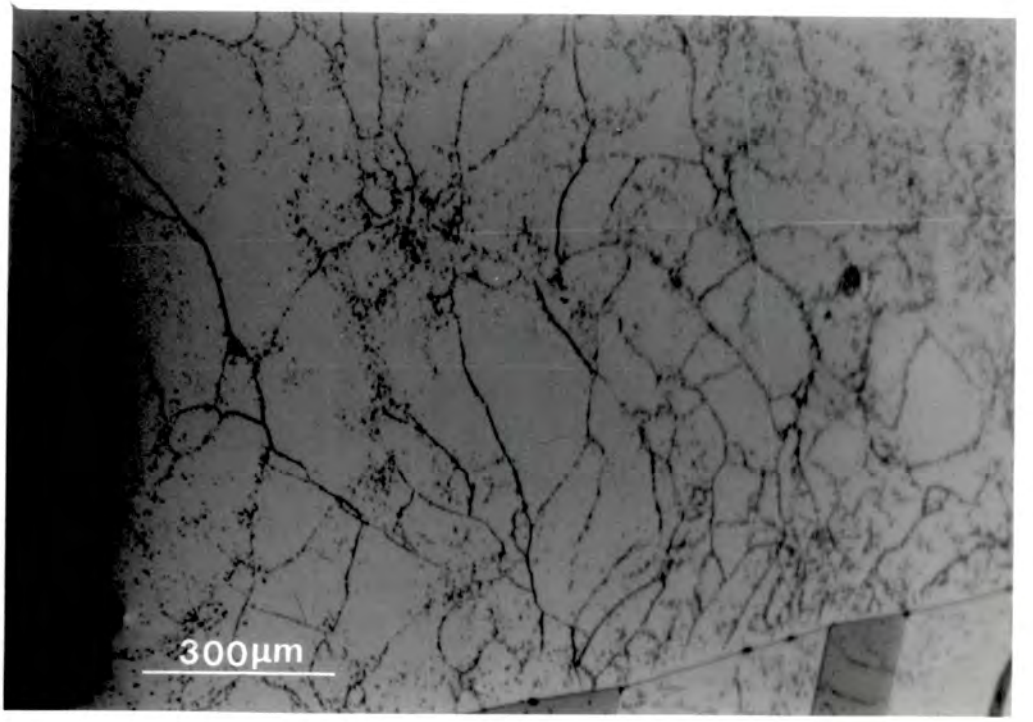

Figure 8.1 Sub-grain boundaries etched with Nakagawa's reagent.

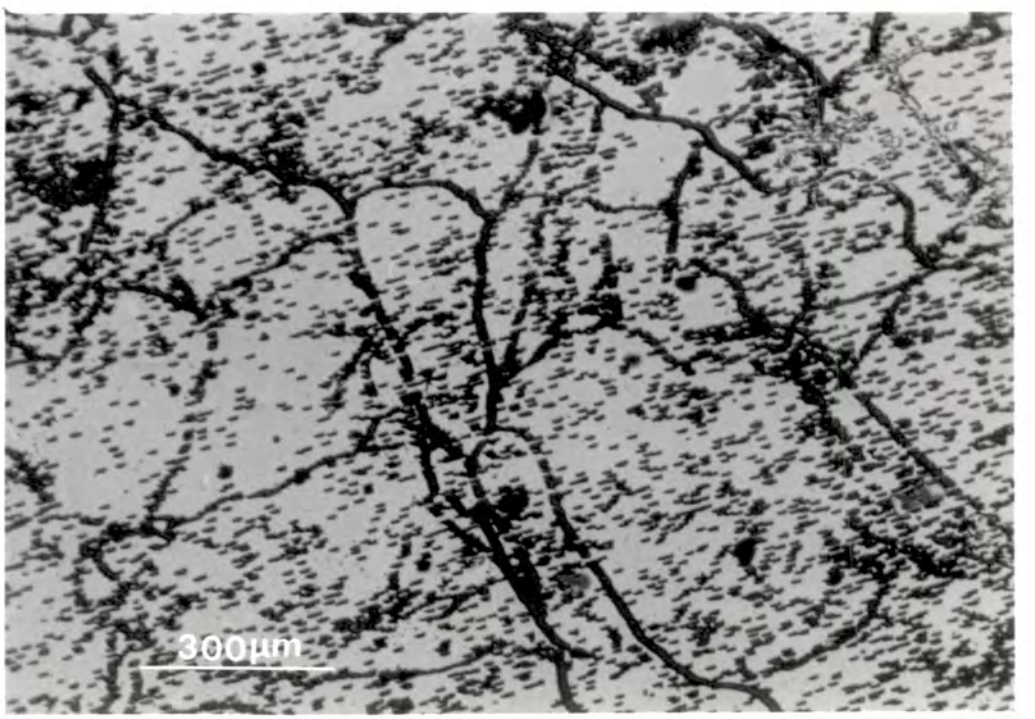

Figure 8.2 Sub-grain boundaries etched with Inoue's EAg-1 reagent.

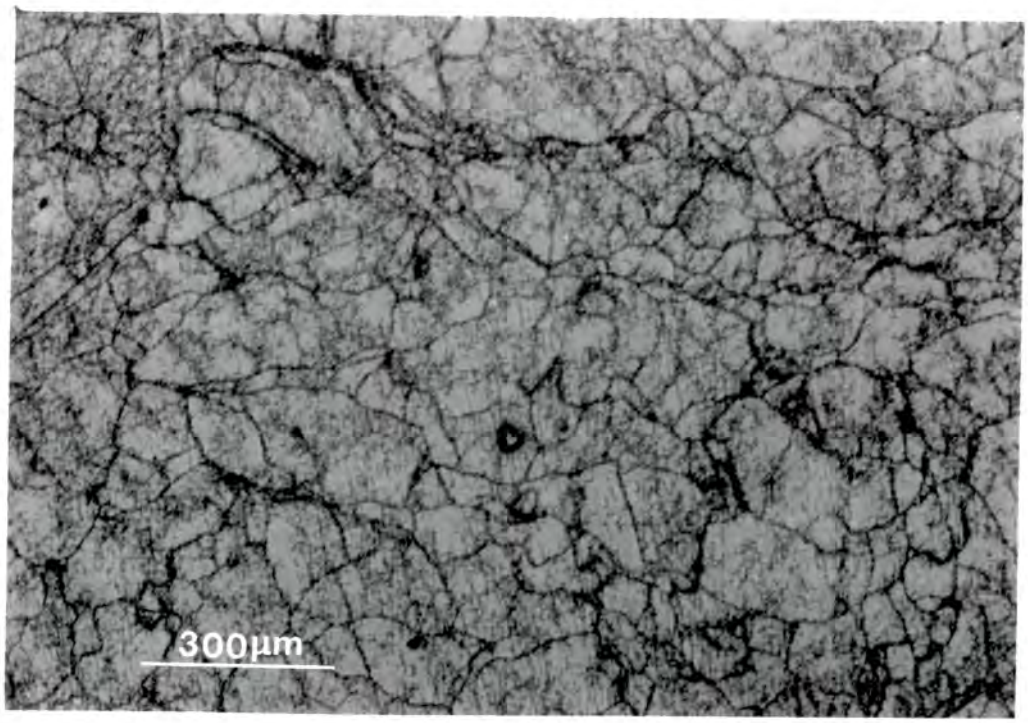

Figure 8.3 Sub-grain boundaries photoetched with a 0.5% solution of bromine in methanol.

Figure 8.5 were occasionally present. The long straight boundaries of these sub-grains are reminiscent of polygonisation walls in cold-worked annealed metals which were described in §4.2.3. The shapes, sizes and distribution of sub-grains were often seen to vary throughout a given boule and were related to the presence of other crystal defects. For example, the high angle grain boundary which runs from the top right to the bottom left of Figure 8.6 separates regions of high and low sub-grain boundary densities. Detailed examination of the region labelled A in this figure showed that the high concentration of sub-grain boundaries at that point is related to the presence of Te precipitates which are associated with the high angle grain boundary. The twin boundaries in Figure 8.7 are crossed by sub-grain boundaries in some places, as at A in the figure, although twin boundaries may sometimes terminate sub-grain boundaries, as at B. Sub-grain

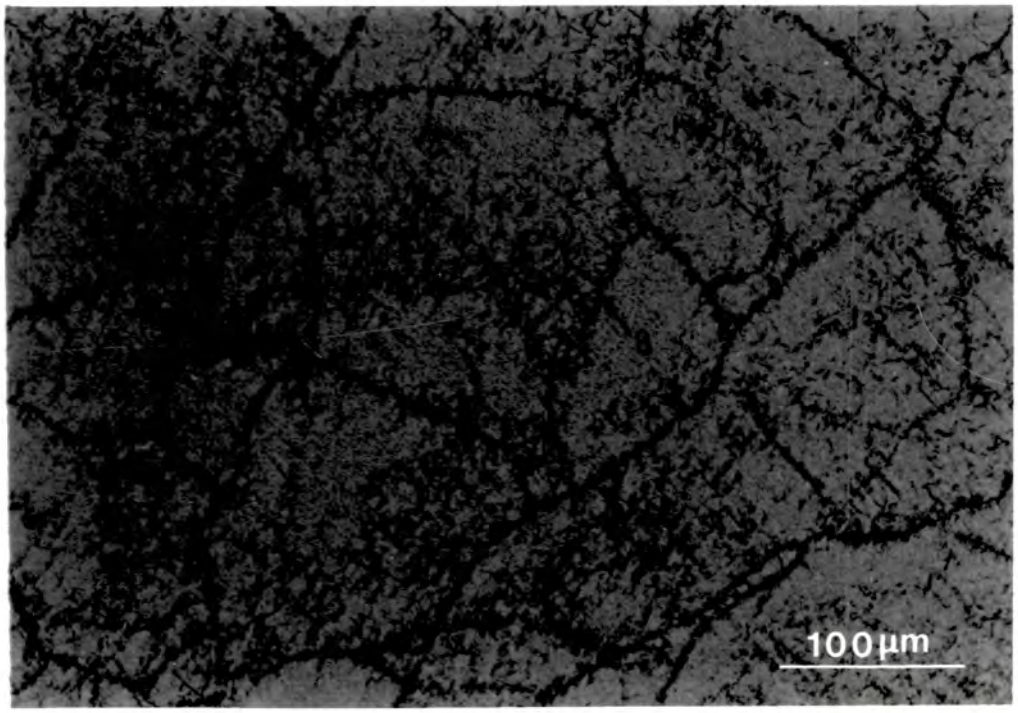

Figure 8.4 Typical sub-grains in CdTe.

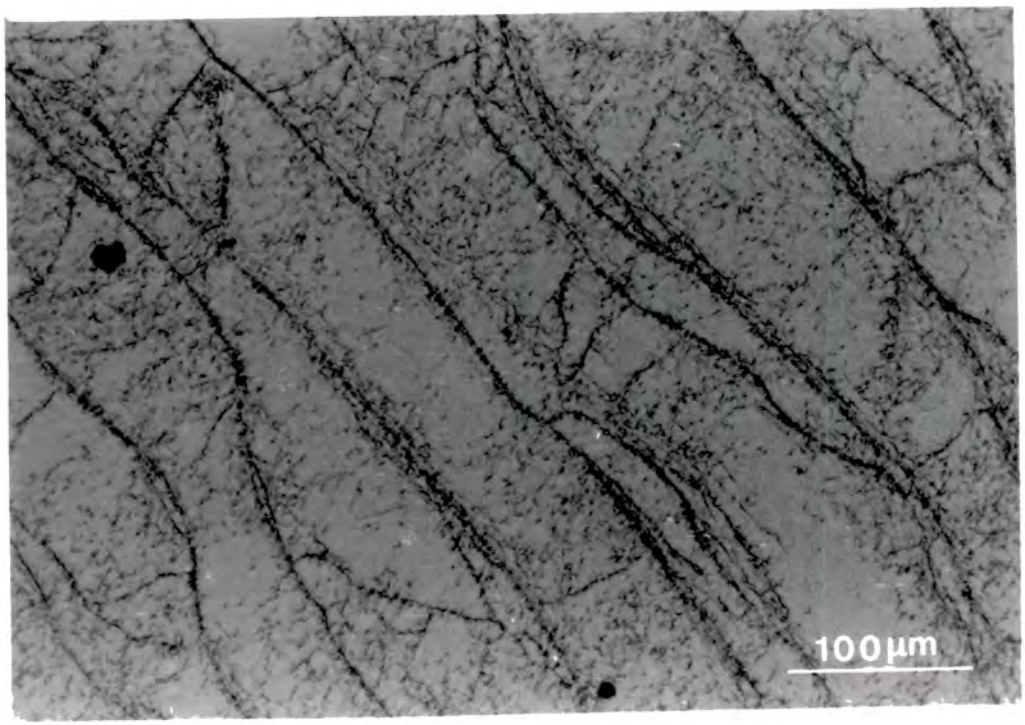

Figure 8.5 Elongated sub-grains in CdTe.

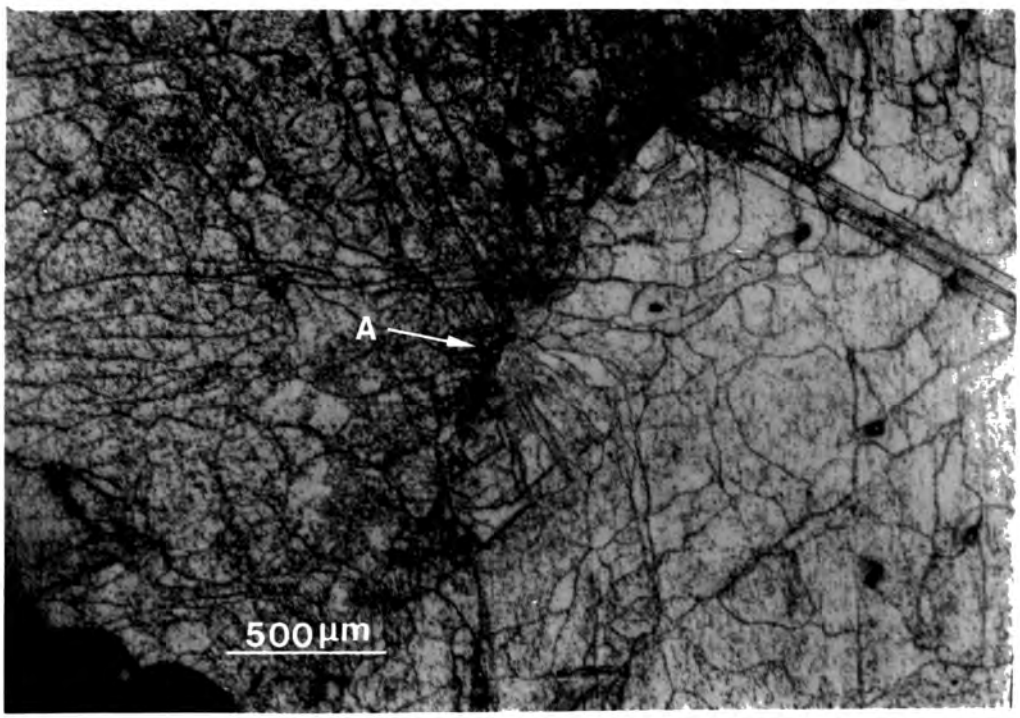

Figure 8.6 Sub-grain boundaries near a high angle grain boundary which is decorated with Te precipitates.

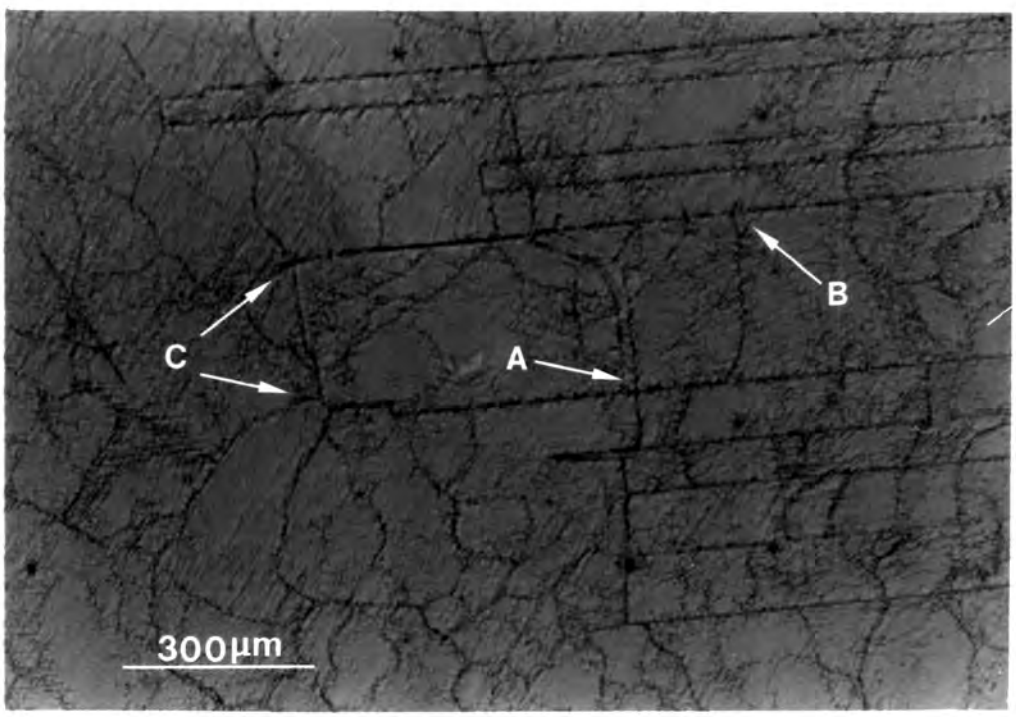

Figure 8.7 The interactions of sub-grain boundaries with twin boundaries.

boundaries were frequently observed to be associated with the junctions between lateral and first order coherent twin boundaries, as at the points labelled C in Figure 8.7. A similar association of sub-grain boundaries and the junctions between first and second order twin boundaries has also been observed. Slip lines lying on {111} planes such as those in the photomicrograph in Figure 8.8 were sometimes observed after photoetching, although they were seen very infrequently during the study of these crystals.

(Figure 8.8 is on the next page).

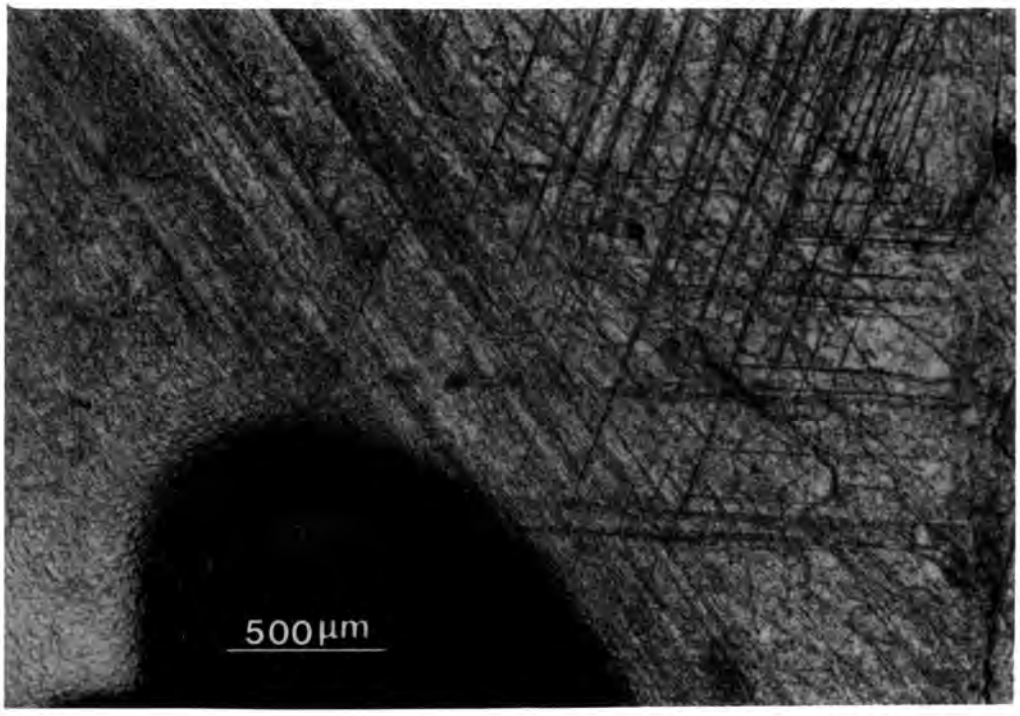

Figure 8.8 Slip lines near to the edge of a boule.

§8.2.1.2 TEM Studies

Isolated dislocations were rarely observed in the thin sections prepared for examination in the transmission electron microscope from CdTe boules which were grown by the 'Durham' method. Sub-grain boundaries were only occasionally encountered since the spacing between them is large in comparison to the size of the electron transparent areas of thin samples. However, a number of boundaries were examined and examples are shown in Figures 8.9-8.11. The speckled features in the background of each of these micrographs are artefacts arising from contamination of the sample surface during preparation and the parallel linear features on the left hand side of Figure 8.9 are slip traces which were introduced by thermal stresses generated by the electron beam during examination in the TEM. The boundaries in Figures 8.9 and 8.10 are predominantly comprised of a series of parallel dislocations each having the

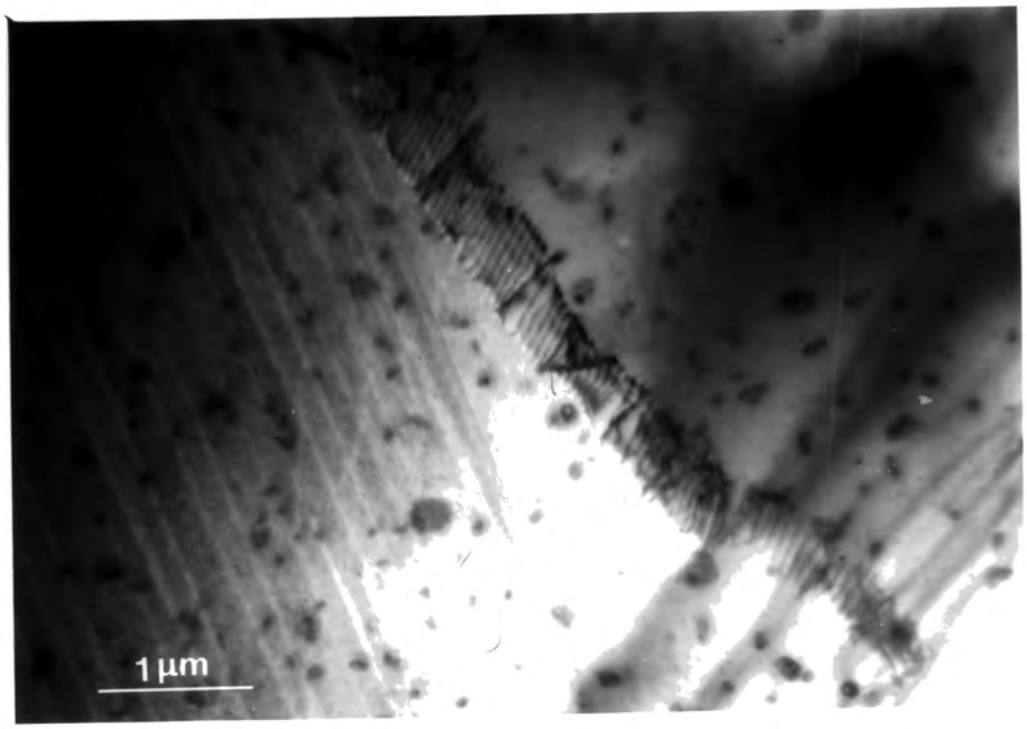

Figure 8.9 Transmission electron micrograph of a sub-grain boundary containing a high density of dislocations.

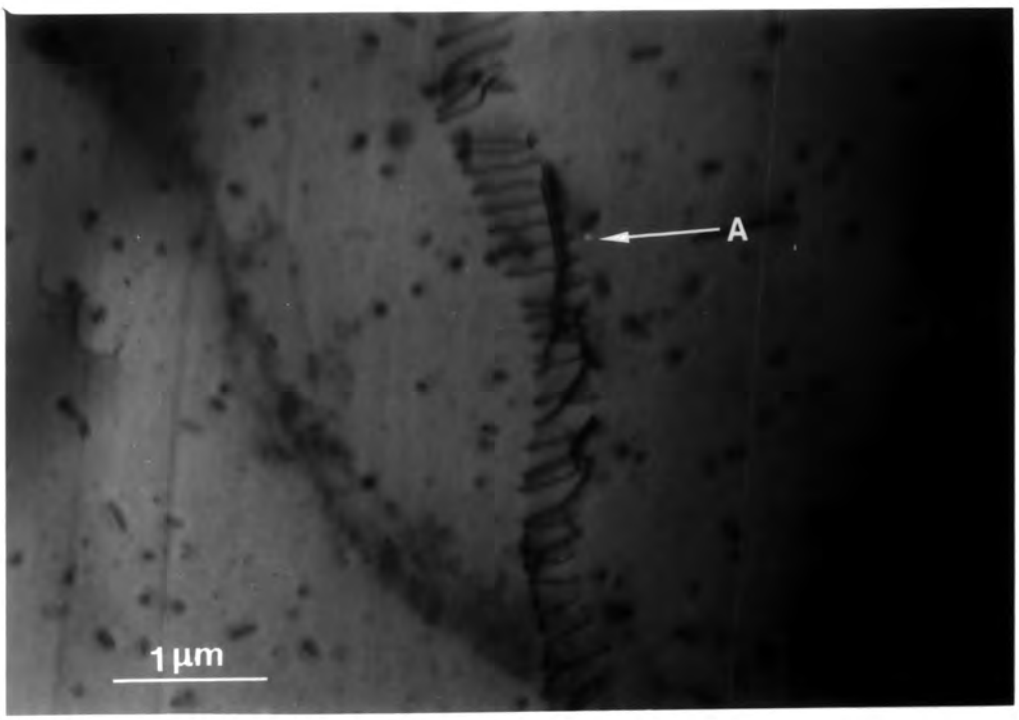

Figure 8.10 Transmission electron micrograph of a sub-grain boundary.

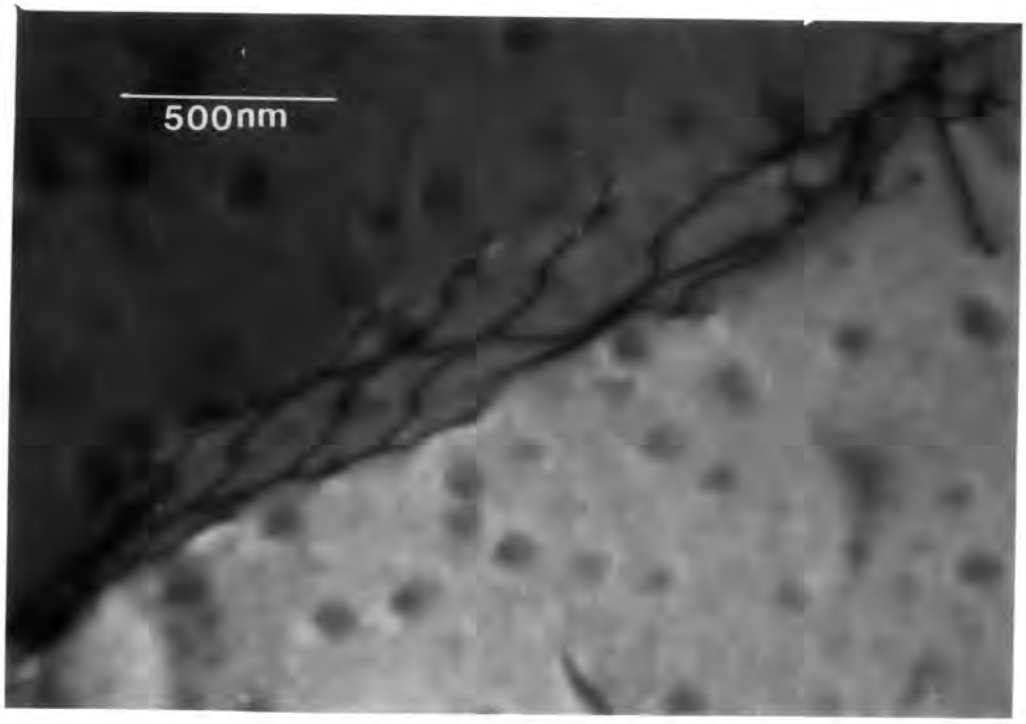

Figure 8.11 Transmission electron micrograph of a sub-grain boundary comprised of a network of dislocations.

same Burgers vector, although a few other types were invariably found in most of the boundaries examined. For example, the dislocation labelled A in Figure 8.10 has a double image whereas the other dislocations in the boundary appear as single images, which implies that this dislocation has a different Burgers vector from that of the other dislocations in the boundary. Boundaries similar to those illustrated in Figures 8.9 and 8.10 were observed which had dislocation densities ranging from about 2 to 16 dislocations per micron. The misorientations between adjacent sub-grains were estimated by measuring the displacements of Kikuchi lines from the diffraction spots in patterns taken from either side of the sub-grain boundaries. In this way the misorientation associated with the boundary in Figure 8.9 was found to be around 0.3^{o}. However, most of the boundaries observed were associated with smaller misorientations than this. A different type of

boundary which consists of a network of dislocations and is associated with a misorientation of approximately 0.05^{o} is shown in the electron micrograph in Figure 8.11. Boundaries comprised of dislocation networks such as this were seen only rarely in comparison to those of the type illustrated in the previous two figures.

§8.2.1.3 SEM/EBIC Studies

Schottky diodes for examination by SEM/EBIC were prepared by depositing Au and In contacts on chemically polished {110} surfaces of CdTe. A cellular structure of sub-grains reminiscent of that revealed by etching was imaged using this technique and an example is shown in Figure 8.12. The average sub-grain size was found to be approximately 150 μm, which corresponds to the size found by etching. The boundaries were not imaged as continuous lines but rather as patterns of bright speckled contrast features. It is suggested that this type of contrast might be attributed to the decoration of sub-grain boundaries with impurity species rather than to the imaging of individual dislocations.

§8.2.2 CdTe Grown Using the Modified Piper-Polich Method

Dislocations in crystals of CdTe grown by the modified Piper-Polich method (see §2.2.3) were also investigated during this work. Etch pitting by both the Inoue EAg-1 and Nakagawa reagents showed less of a tendancy to reveal discreet boundaries although sub-grain boundaries were clearly deliniated by photoetching with bromine in methanol. Transmission electron microscopy revealed irregular arrangements of dislocations having a variety of orienta-

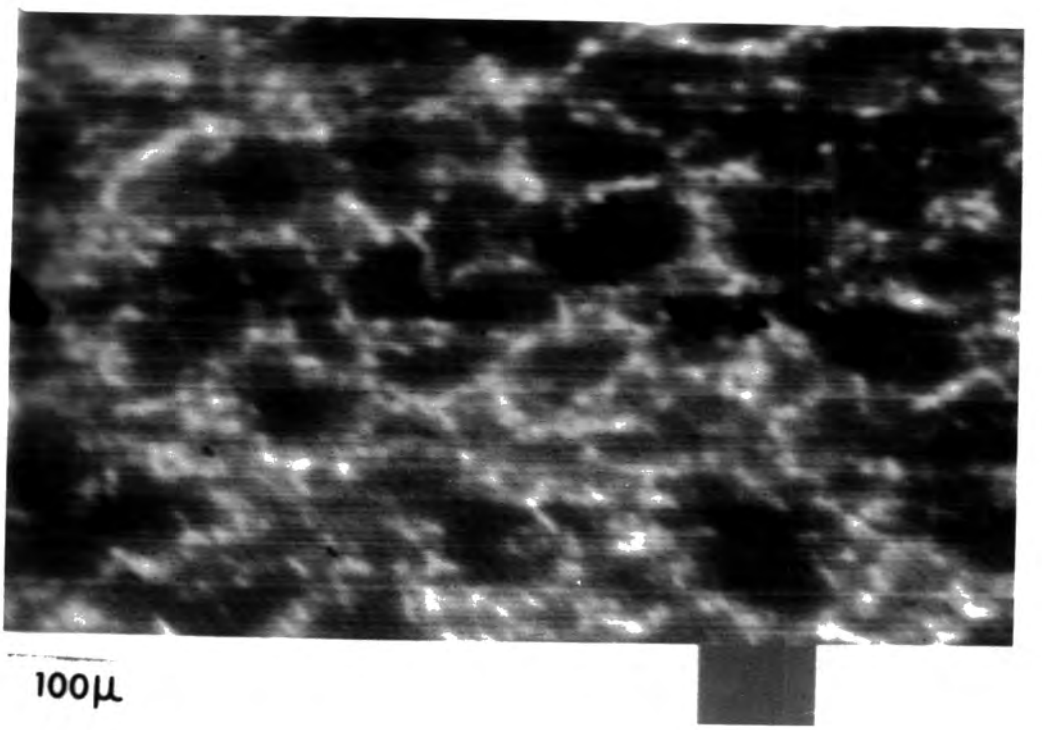

Figure 8.12 SEM/EBIC micrograph of a network of sub-grain boundaries.

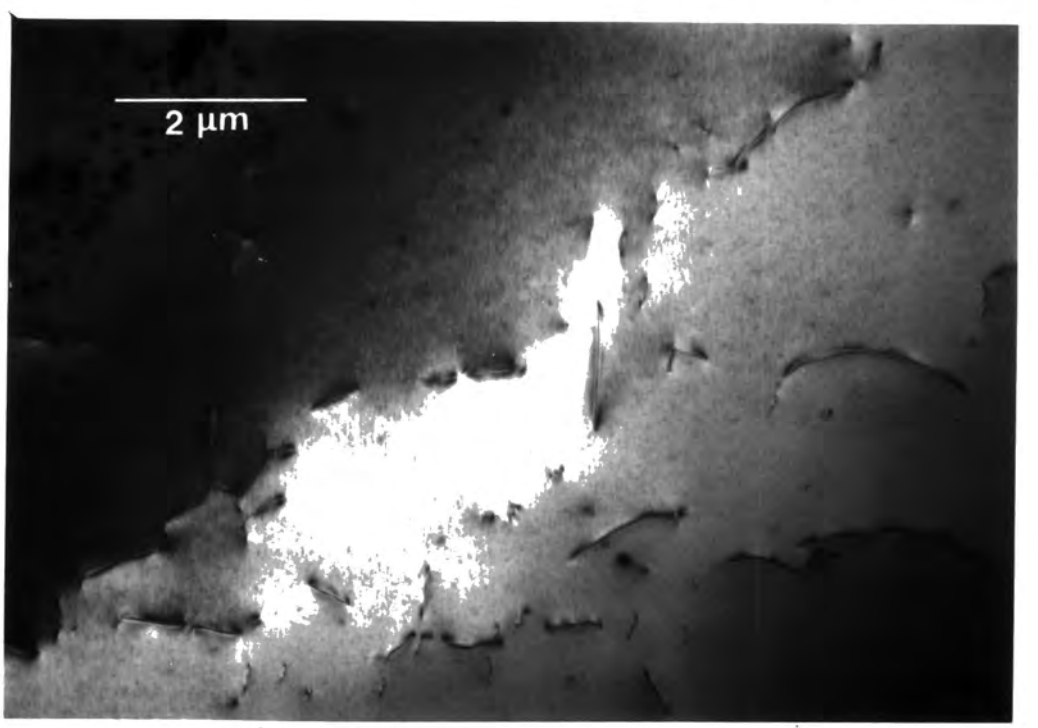

Figure 8.13 Transmission electron micrograph of dislocations in 'Piper-Polich' CdTe.

tions, as shown in Figure 8.13. In these crystals there was no tendancy for the dislocations to form regular closely packed arrays resembling the boundaries which were observed in the material grown by the 'Durham' method.

§8.2.3 Discussion

The observations of both elongated sub-grains (Figure 8.5) and of slip lines (Figure 8.8) suggests a mechanism for the formation of sub-grain boundaries in this material. Slip lines in CdTe have been observed by other workers [4,5] and are thought to arise from stresses incurred during crystal growth. In the case of both the 'Durham' and the modified Piper-Polich growth methods the stresses necessary to promote slip might easily arise if the boules stick to the silica growth capsules either during growth or in the post-growth cooling period since the rate of thermal contraction of CdTe ($5.5 \times 10^{-6}\ ^{o}C^{-1}$) is much higher than that of silica ($5.4 \times 10^{-7}\ ^{o}C^{-1}$)[9]. Williams and Vere [5] report that slip-lines in CdTe crystals are replaced by sub-grain boundaries if the crystals are annealed at temperatures as low as $440^{o}C$. Sub-grains in the material studied in this work are therefore thought to result from a polygonisation process which involves both the slip and climb of dislocations. Since CdTe crystals grown by the 'Durham' technique are held at high temperatures for several days during growth, there is ample opportunity for this polygonisation process to occur. Indeed, the long straight sub-grain boundaries shown in Figure 8.5 are reminiscent of those

illustrated in Figure 4.6b which result from polygonisation in metal crystals after slip has occurred on only one close packed plane (see §4.3.4). The annealing of crystals which have undergone slip on more than one plane, such as that illustrated in Figure 8.8, will undoubtedly result in more complex sub-grain shapes, such as those illustrated in Figures 8.1 - 8.4.

The most frequently observed arrangement of dislocations in those sub-grains examined in the TEM (see §8.1.2) was the low energy configuration described in §4.3.3. Electron micrographs of dislocation arrays in CdTe which are predominantly comprised of one type of dislocation are shown in Figures 8.9 and 8.10. The variations in the densities of dislocations observed in these boundaries and the fact that some boundaries are comprised of a network of dislocations may account for the variations in their etching behaviour (see Figure 8.4). The average sub-grain size of $\sim$ 150μm in this material suggests that its quality is comparable with that of some Bridgeman grown crystals [1,2,5] although better quality Bridgeman material having an average sub-grain size of several hundred microns has been produced in certain cases [2,4].

The bright spots of EBIC contrast deliniating sub-grain boundaries in the 'Durham' material are not present in such high densities as the dislocations in these boundaries. This would suggest that the electrical activity of these boundaries is due to some alternative defects such as impurities, rather than to the native states of the dislocations themselves. Similar conclusions were made by Williams and Vere [5]. However, the TEM study of

sub-grain boundaries carried out in this work has failed to reveal any association of Te precipitates with boundary dislocations. Thus it is suggested that the origin of the EBIC contrast might be attributed to small concentrations of impurity atoms which have become associated with these dislocations.

The observed association of dislocation arrays with the junctions between twin boundaries (see Figure 8.7) and with large Te precipitates situated on high angle grain boundaries (see Figure 8.6) can probably be attributed to the interactions between the lattice strains caused by the defects concerned. In fact such interactions may well act to reduce the overall elastic strain energy of the system.

From these studies it has become apparent that high angle grain boundaries such as that in Figure 8.6 often separate regions of high and low sub-grain boundary density. This situation could arise if one of the grains had undergone more deformation during the growth process than its neighbour: if the grain boundary acts as a barrier to dislocation motion, then any subsequent recovery and polygonisation processes would be constrained to the individual grains thus producing the observed distribution of sub-grain boundaries.

The fact that some sub-grain boundaries are seen to cross twin boundaries (see Figure 8.7) indicates that dislocations on either side of them are able to interact with one another during or after the polygonisation process to form continuous dislocation arrays. The likelihood of such an interaction taking place will of course vary according to the local conditions during

crystal growth and cooling, and hence not all sub-grains will necessarily become associated with others in adjacent twin-related grains.

The comparatively low dislocation densities which are observed within sub-grains, and the association of sub-grain boundaries with other defects indicates that polygonisation is at a very advanced stage in these crystals. This is undoubtedly a result of growth by the 'Durham' technique which requires that these crystals must be maintained at high temperatures for extended periods of time.

In contrast to this, the reorganisation of dislocations in crystals grown by the modified Piper-Polich technique is far from complete. Dislocations with a variety of orientations and Burgers vectors are found throughout the crystals and no tendency for them to form arrays comprised of dislocations having the same Burgers vector was observed. The relatively high growth rate and the consequential short period ($\sim$ 24 hours) that the crystals are kept at high temperature during growth by the modified Piper-Polich technique (see §2.2.3) account for the differences between the dislocation structures in these crystals and in those grown by the 'Durham' method. While it is well-known that CdTe is inherently prone to the formation of polygonisation walls, this comparison has shown that the growth technique employed can have a considerable effect upon the extent to which polygonisation occurs.

§8.3 Sub-grain Boundaries in $Cd_yZn_{1-y}Te$

§8.3.1 Introduction

$Cd_yZn_{1-y}Te$ has been used as an alternative substrate to CdTe for the growth of epitaxial $Cd_xHg_{1-x}Te$ in a number of laboratories [see 10,11 and 12 for example]. CdTe and ZnTe form solid solutions for the entire range of compositions and, in addition, the ternary $Cd_yZn_{1-y}Te$ is known to obey Vegard's Law [13], that is its lattice parameter varies linearly with composition. The composition of $Cd_yZn_{1-y}Te$ may therefore be chosen to provide a good lattice match to $Cd_xHg_{1-x}Te$ in order to reduce the incidence of interfacial dislocations in epitaxial systems. The ideal substrate composition for the epitaxial growth of $Cd_{0.2}Hg_{0.8}Te$ is around $Cd_{0.95}Zn_{0.05}Te$ [14]. The quality of $Cd_yZn_{1-y}Te$ substrates is known to be higher than that of CdTe ones, the Nakagawa etch pit density of the ternary being on average an order of magnitude smaller than that of CdTe [11] and its X-ray rocking curves being only half as wide as those obtained from CdTe [11,12]. Furthermore, the rocking curves and surface morphologies of $Cd_xHg_{1-x}Te$ epitaxial layers grown on $Cd_yZn_{1-y}Te$ substrates are superior to those grown on CdTe substrates [11,12]. In this work the dislocation content of $Cd_{0.95}Zn_{0.05}Te$ crystals grown by the 'Durham' technique was examined.

§8.3.2 $Cd_{0.95}Zn_{0.05}Te$ Grown by the 'Durham' Method

A number of boules of $Cd_yZn_{1-y}Te$ having diameters of up to 29 mm were grown by the 'Durham' vapour phase method as described in Chapter 2. The composition of the ternary, that is the value

of y, was determined by measuring the lattice parameter of the crystals using the X-ray powder technique and applying Vegard's law. The crystals studied had compositions close to $Cd_{0.95}Zn_{0.05}Te$. Slices of this material were chemically polished using the same method as was used for CdTe and specimens were prepared both for examination in the TEM and for photoetching in a solution of 0.5% bromine in methanol. The photoetching revealed patterns of sub-grains which were very similar in appearance and size ($\sim$150 μm) to those observed in CdTe grown by the 'Durham' technique. However, a TEM study of the structure of sub-grains revealed an arrangement of dislocations which differed from that encountered in CdTe grown by either the 'Durham' or modified Piper-Polich techniques. The group of dislocations in Figure 8.14 is typical of those observed in this material: in this ternary compound there is a marked tendancy for them to form arrays which are comprised of dislocations having a variety of different Burgers vectors and which constitute networks having irregular and open structures. Although most of the dislocations are concentrated in these networks, isolated dislocations were often observed, as in the top left hand corner of Figure 8.14. The dislocation labelled A in Figure 8.15 was characterised by imaging it in two beam conditions with g = $\bar{2}20$, $3\bar{1}\bar{1}$ and 220, as shown in Figures 8.15, 8.16 and 8.17 respectively. In the figures corresponding to these different diffraction conditions the dislocation was seen to be imaged as a single line, a double line and in an out of contrast or 'extinguished' condition, indicating that the conditions g.b = 1,2 and 0 are operating in the three micrographs

respectively. These observations are compatible with the dislocation having a Burgers vector of $b = a/2[1\bar{1}0]$ or $b = a/2[\bar{1}10]$. Since the Burgers vector is perpendicular to the line of the dislocation (see Figure 8.15) this dislocation is of the pure edge type.

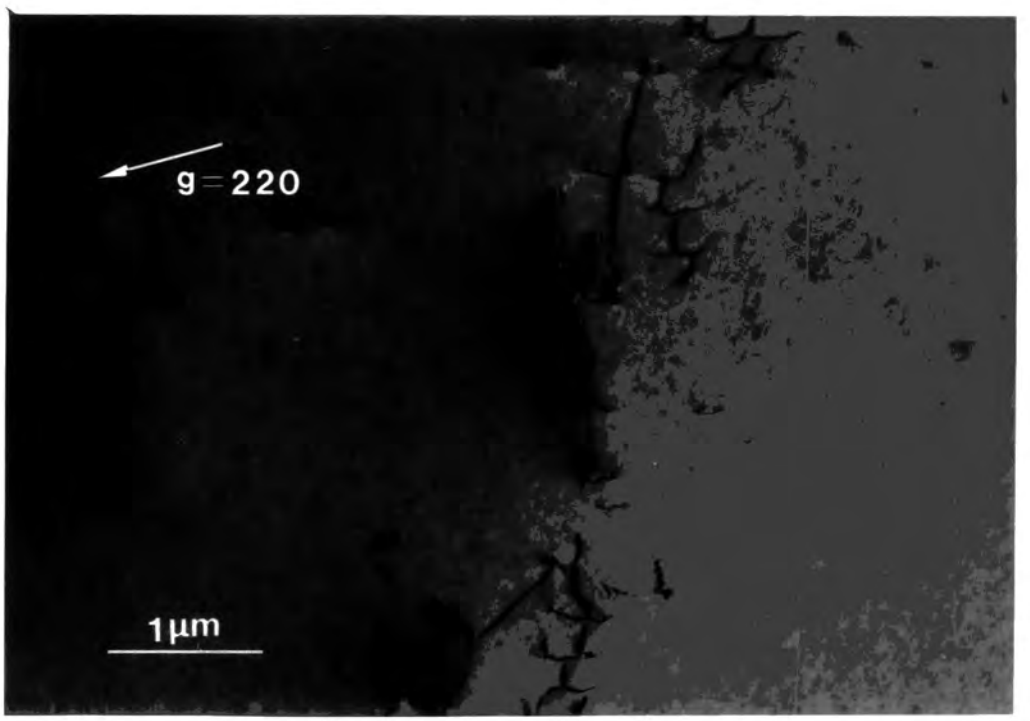

Figure 8.14 Transmission electron micrograph of dislocations in 'Durham' $Cd_{0.95}Zn_{0.05}Te$.

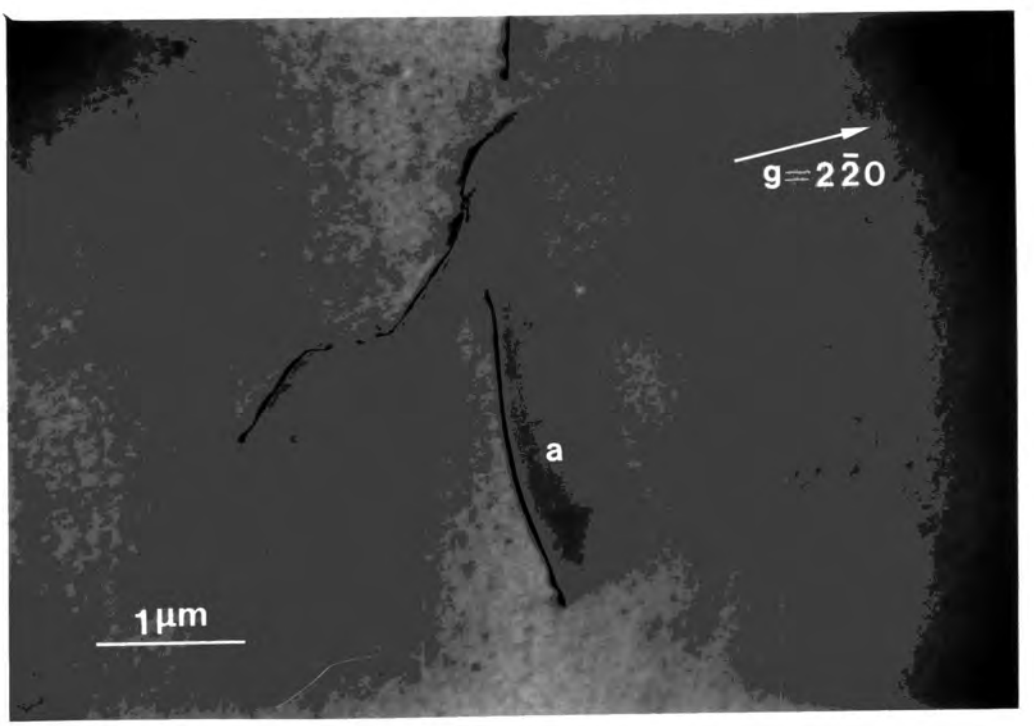

Figure 8.15 Image of a dislocation with g.b = 1.

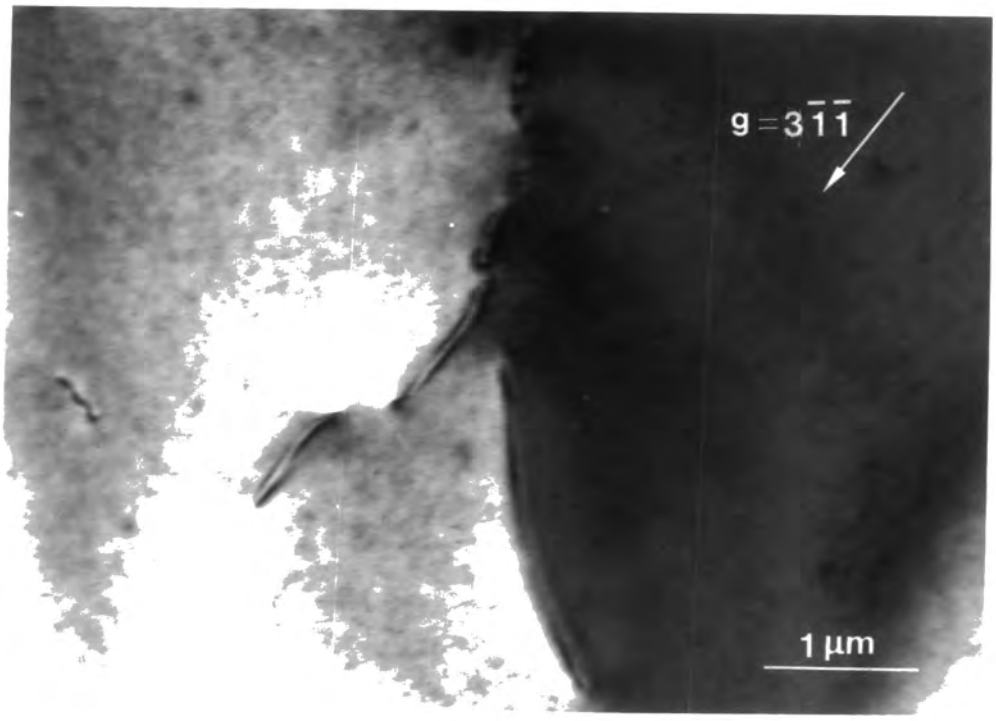

Figure 8.16 Double image of a dislocation with g.b = 2.

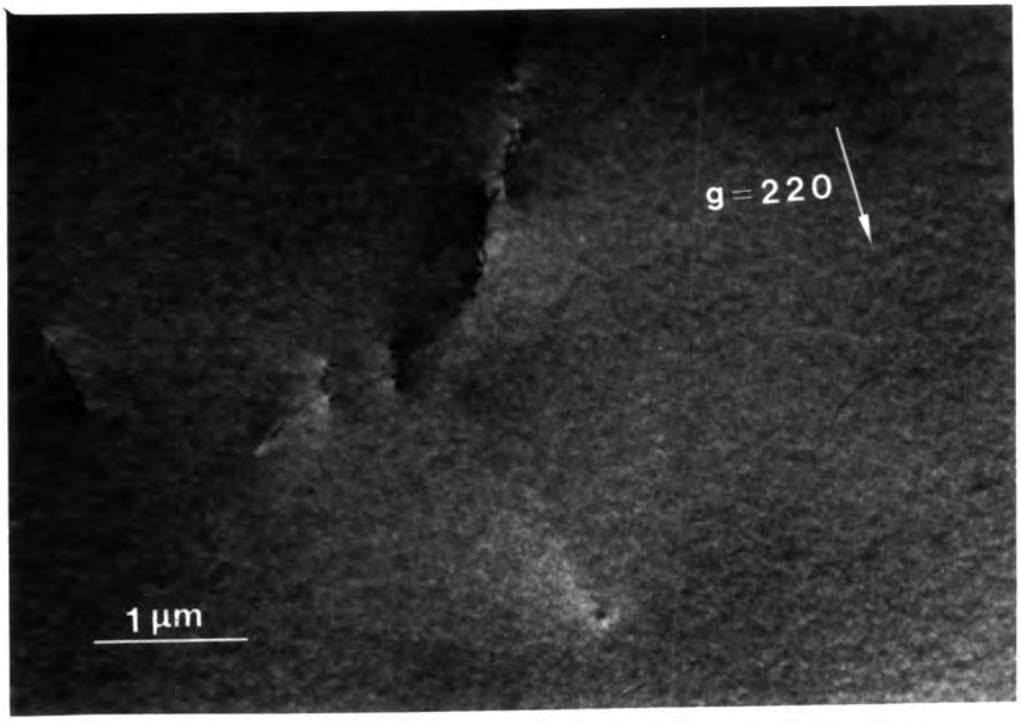

Figure 8.17 Dislocation out of contrast. g.b = 0.

§8.3.3 Discussion

The presence of open networks of dislocations in sub-grain boundaries in 'Durham' grown $Cd_{0.95}Zn_{0.05}Te$ (as compared to those in CdTe grown by the same technique) is consistent with the observation that the X-ray rocking curves obtained from $Cd_{0.95}Zn_{0.05}Te$ are narrower than those for CdTe [11,12]. The misorientations supported by the well formed sub-grain boundaries in CdTe are likely to be greater than those associated with the rather open dislocation arrays in $Cd_{0.95}Zn_{0.05}Te$: it is therefore apparent that the sub-grain formation in $Cd_{0.95}Zn_{0.05}Te$ is not nearly so advanced as that in CdTe crystals which had been grown in the same way using the 'Durham' technique, even though both types of crystals were subjected to similar amounts of stressing and annealing during growth. Hence it is concluded that the incorporation of ∿5 atomic % ZnTe in CdTe prevents the formation of highly developed polygonisation walls. This could be the result of two effects. Firstly, it is known that the incorporation of several atomic percent of In or Sb into GaAs crystals has the effect of reducing their grown-in dislocation densities [15,16]. This could account for the observation that $Cd_{0.96}Zn_{0.04}Te$ crystals have a lower Nakagawa etch pit density than CdTe [12]. Secondly, the so-called 'solution hardening' effects observed in ternaries may inhibit the motion of dislocations during the polygonisation process, thus leading to the formation of sub-grain boundaries which are only partially developed.

§8.4 Conclusions

The presence of slip-bands and elongated sub-grains in CdTe crystals which have been grown by the 'Durham' technique (see §8.2.1.1) suggests a mechanism which is likely to be responsible for the formation of sub-grain boundaries in this material. The thermal stresses which arise during and immediately following the growth of crystals by the 'Durham' technique are undoubtedly responsible for the introduction of dislocations and slip-bands into the crystals. Since these crystals are grown slowly, are maintained at a high temperature throughout growth and are cooled to room temperature very slowly there is ample opportunity for these grown-in dislocations to reorganise themselves into low energy configurations (polygonise) during the growth process. It is well known that the lowest energy configuration of a group of dislocations having the same Burgers vector is in the form of an array which constitutes a low angle grain boundary (see §4.3.3). A TEM investigation of these crystals (see §8.2.1.2) has shown that 'one dislocation' arrays of this type are indeed present in these CdTe crystals and that the misorientations associated with these arrays can be as large as 0.3^{o}. Although the shapes of sub-grains in this material are generally irregular, some elongated sub-grains having straight boundaries are occasionally observed. Such sub-grains are to be expected if dislocations which are confined to a single slip plane undergo polygonisation.

An important observation concerning sub-grain boundaries in this material is that they are associated with other defects which have strain fields of their own (see §8.2.1.1). For example,

these boundaries are often seen to terminate at the sites of Te precipitates and at the junctions between lateral and coherent twin boundaries. This indicates that the dislocation arrays are capable of migrating in order to achieve low energy positions with respect to other defects which are present in the crystals. Polygonisation in this material may therefore be regarded as having reached an advanced state.

In contrast to this, transmission electron microscopy has revealed that the distribution of dislocations in crystals of CdTe grown by the modified Piper-Polich technique (see §8.2.2) is quite different. The dislocation arrays in this material form loose networks which contain dislocations having a number of different Burgers vectors and orientations. A significant number of isolated dislocations were also observed. Differences in the arrangement of dislocations in this material are to be expected since the growth conditions used in the modified Piper-Polich technique differ markedly from those employed in the 'Durham' technique. The limited extent of polygonisation in this material can be directly attributed to the much shorter period taken to grow crystals by the modified Piper-Polich technique. This does not allow the grown-in dislocations to polygonise in the same manner as for the 'Durham' grown crystals.

Etching studies have shown that sub-grain boundaries also having an average size of $\sim 150\ \mu m$ are present in $Cd_{0.95}Zn_{0.05}Te$ grown by the 'Durham' technique (see §8.3.2). However, a TEM study has revealed that the dislocation structures are quite unlike the 'one dislocation' arrays observed in crystals of CdTe

grown using the same method. The dislocations are arranged in networks in the $Cd_{0.95}Zn_{0.05}Te$, although these do not have the open structures characteristic of those in CdTe grown by the modified Piper-Polich technique. Some isolated dislocations were also observed in this ternary compound.

The addition of 5 atomic % of Zn to CdTe is thought to inhibit the formation of polygonisation boundaries by i) reducing the density of grown-in dislocations present in the crystals, and ii) by impeding the mobility of dislocations during the annealing which accompanies crystal growth.

SEM/EBIC studies of sub-grain boundaries in crystals of CdTe grown by the 'Durham' technique have shown that these defects are electrically active (see §8.2.1.3). However, the appearance of the spotty contrast which is present at these boundaries suggests that this electrical activity may not be a result of the native states of the dislocations themselves, but is likely to be due to the presence of impurities which are thought to decorate these defects. Although the electrical activity of sub-grain boundaries in substrates prepared for the epitaxial growth of $Cd_xHg_{1-x}Te$ is in itself unimportant, the propogation of these defects into such epitaxial layers is potentially a serious problem: the presence of such electrically active defects in $Cd_xHg_{1-x}Te$ epilayers will undoubtedly have a deleterious effect upon the performance of any electronic devices fabricated from them.

REFERENCES FOR CHAPTER EIGHT

1 A.K.Chin, J.Electrochem.Soc., 129 (2) (1982) p.369.

2 O.Oda, K.Hirata, K.Matsumoto and I.Tsuboya, J. Crystal Growth, 71 (1985) p.273.

3 K.Durose, G.J.Russell and J.Woods, Inst.Phys.Conf.Ser.No.76 (6) (1985) p.233.

4 Y.C.Lu, R.S.Feigelson, R.K.Route and Z.U.Rek, J.Vac.Sci.Technol., A4 (4) (1986) p.2190.

5 D.J.Williams and A.W.Vere, To be published in J.Crystal Growth, (1986).

6 K.Nakagawa, K.Maeda and S.Takeuchi, Appl.Phys.Lett., 34 (1979) p.574.

7 M.Inoue, I.Teramoto,S.Takayanagi, J.Appl.Phys., 33 (1962) p.2578.

8 N.R.Kyle, J.Electrochem.Soc., 118 (11) (1971) p.1790.

9 L.S.Ladd, Infrared Phys, 6 (1966) p.145.

10 Y.Nemirovsky, S.Maraglit, E.Finkman, Y.Shackahm - Diamand and I.Kidron, J.Electron.Mater., 11(1) (1982) p.133.

11 S.L. Bell and S.Sen, J.Vac.Sci.Technol., A3 (1) (1985) p.112.

12 J.C.Tranchart, B.Lattore, C.Foucher and Y.Le Gouge, J.Crystal Growth, 72 (1985) p.468.

13 B.Woolley and B.Ray, J.Phys.Chem.Solids, 13 (1960) p.151.

14 H.Booyens and J.H.Basson, Phys.Stat.Sol., (a) 85 (1984) p.449.

15 G.Jacob, M.Duseaux, J.P.Farges, M.M.B. Van den Boom and P.J.Roksnoer, J.Crystal Growth, 61 (1983) p.417.

16 A.A.Ballman, A.M.Glass, R.E.Nahory and H.Brown, J.Crystal Growth, 62 (1983) p.198.

CHAPTER NINE

PRECIPITATION

§9.1 Introduction

The optical absorption coefficient of CdTe is not limited by intrinsic processes such as multiphonon absorption, but rather by the presence of native defects, notably Te precipitates [1]. The presence of such defects therefore impairs the performance of CdTe in optical applications such as infra-red windows.

Te precipitation is known to persist in crystals of CdTe grown by all techniques (see [2-6] for example) and may be observed readily by transmission infra-red microscopy [2,3,5,6,7] and metallographic techniques [2,4]. Inspection of the temperature-

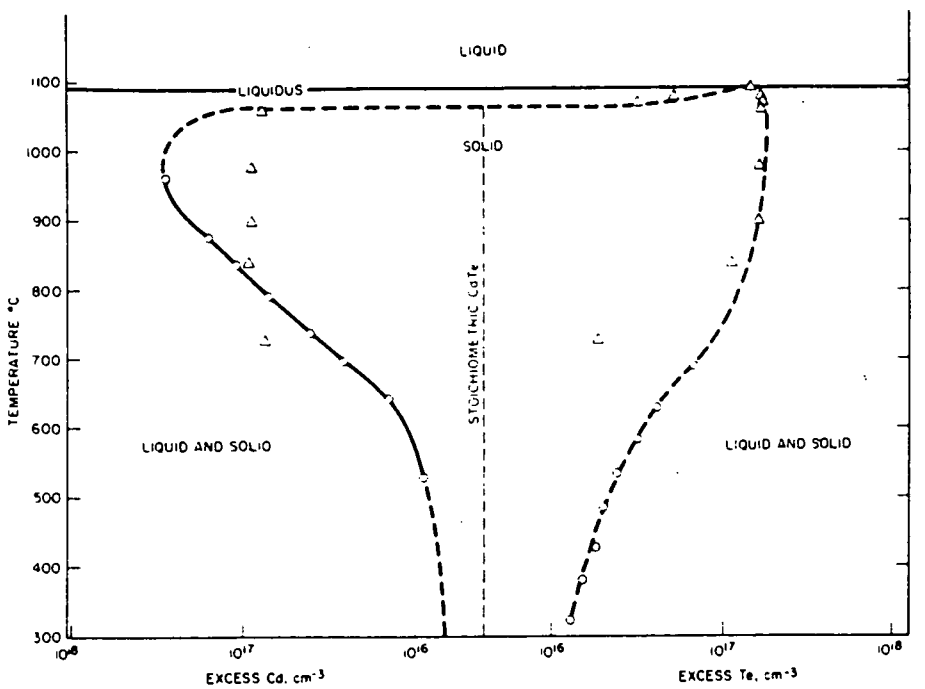

Figure 9.1 T-x phase diagram for CdTe (from ref.[23]).

composition (T-x) phase diagram of CdTe shown in Figure 9.1 [2] reveals the underlying reason for Te precipitation in this material: the diminishing ability of CdTe to accommodate excess Te in a solid solution with decreasing temperature (a phenomenon known as retrograde solid solubility [9]) ensures that any excess Te present in a solid solution at high temperatures precipitates out upon subsequent cooling.

In this Chapter the precipitates present in CdTe grown from the vapour phase using the 'Durham' and the modified Piper-Polich techniques are characterised (see sections §9.2 and §9.3 respectively). These two growth techniques are both described in Chapter 2. Comparisons between the precipitation in the crystals grown by the two methods are made in §9.4 and the conclusions of the Chapter are summarised in §9.5.

§9.2 Precipitates in CdTe Grown by the 'Durham' Technique

The incidence of precipitation in CdTe crystals grown by the 'Durham' technique has been investigated by etching. Figure 9.2 shows a typical low magnification photomicrograph of a Cd (111) surface after etching with Inoue's EAg-1 etchant [10]. The circular features present in the micrograph are precipitates having a density of ~ 100 per cm^2. Individual precipitates were examined more closely in the SEM and a representative micrograph of one of these features is shown in Figure 9.3. The EDAX spectrum in Figure 9.4 which was accumulated from the central part of the circular feature (labelled A in the figure) gave a high Te:Cd ratio, whereas a spectrum accumulated from the region labelled B was representative of stoichiometric CdTe. This demonstrates that while the precipitates

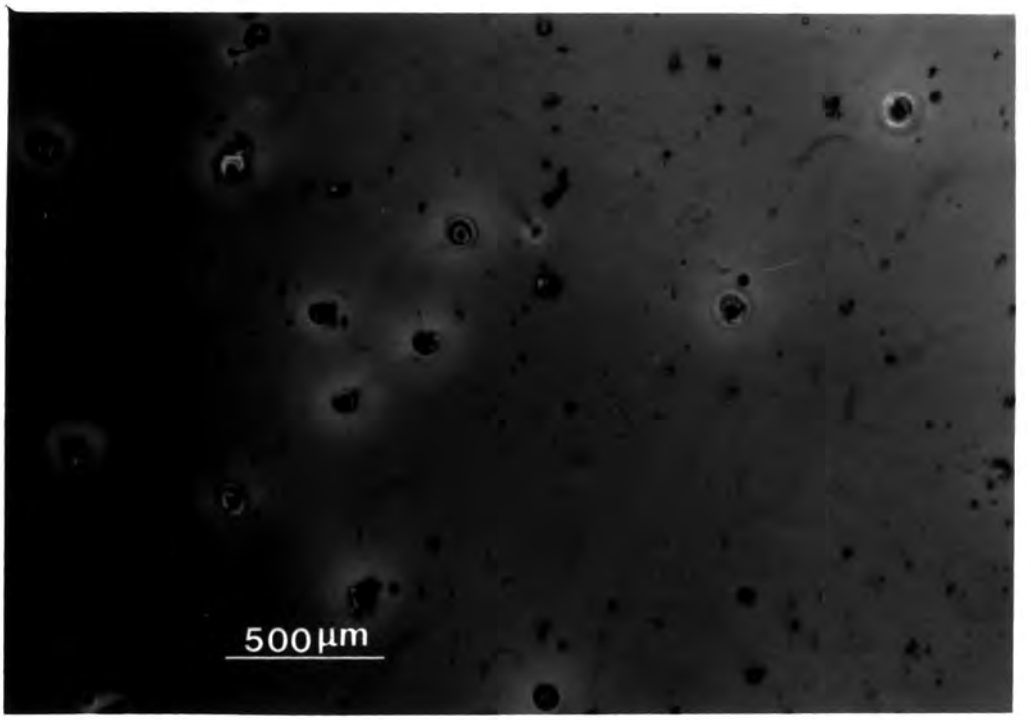

Figure 9.2 Photomicrograph of precipitates on a Cd(111) surface after etching with Inoue's EAg-1 etch.

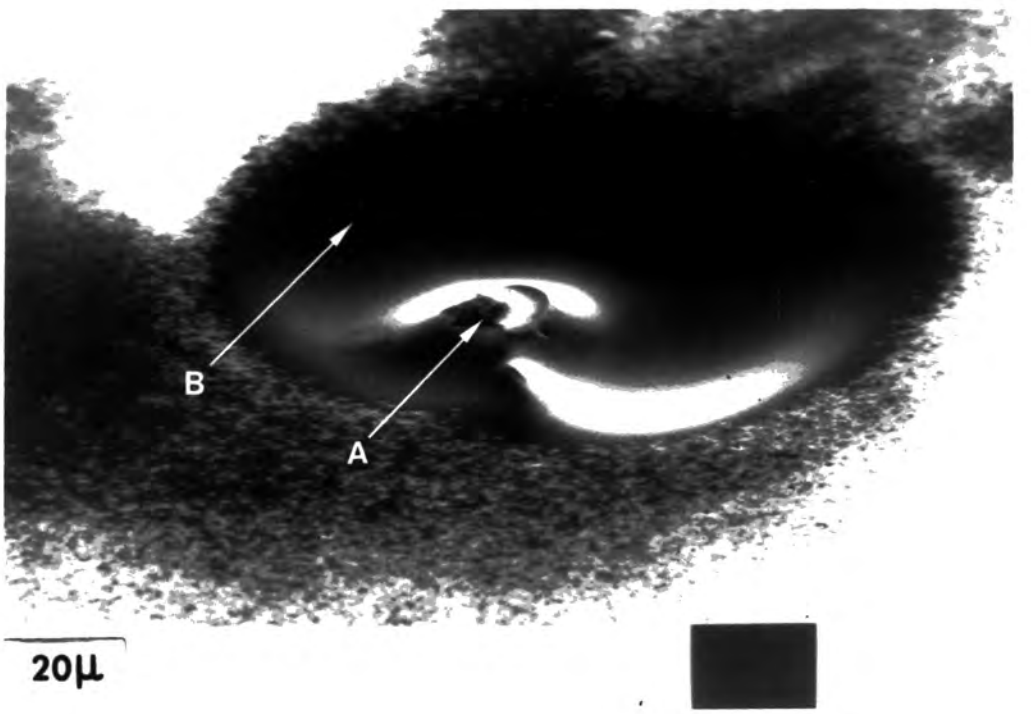

Figure 9.3 Scanning electron micrograph of one of the precipitates shown in Figure 9.2.

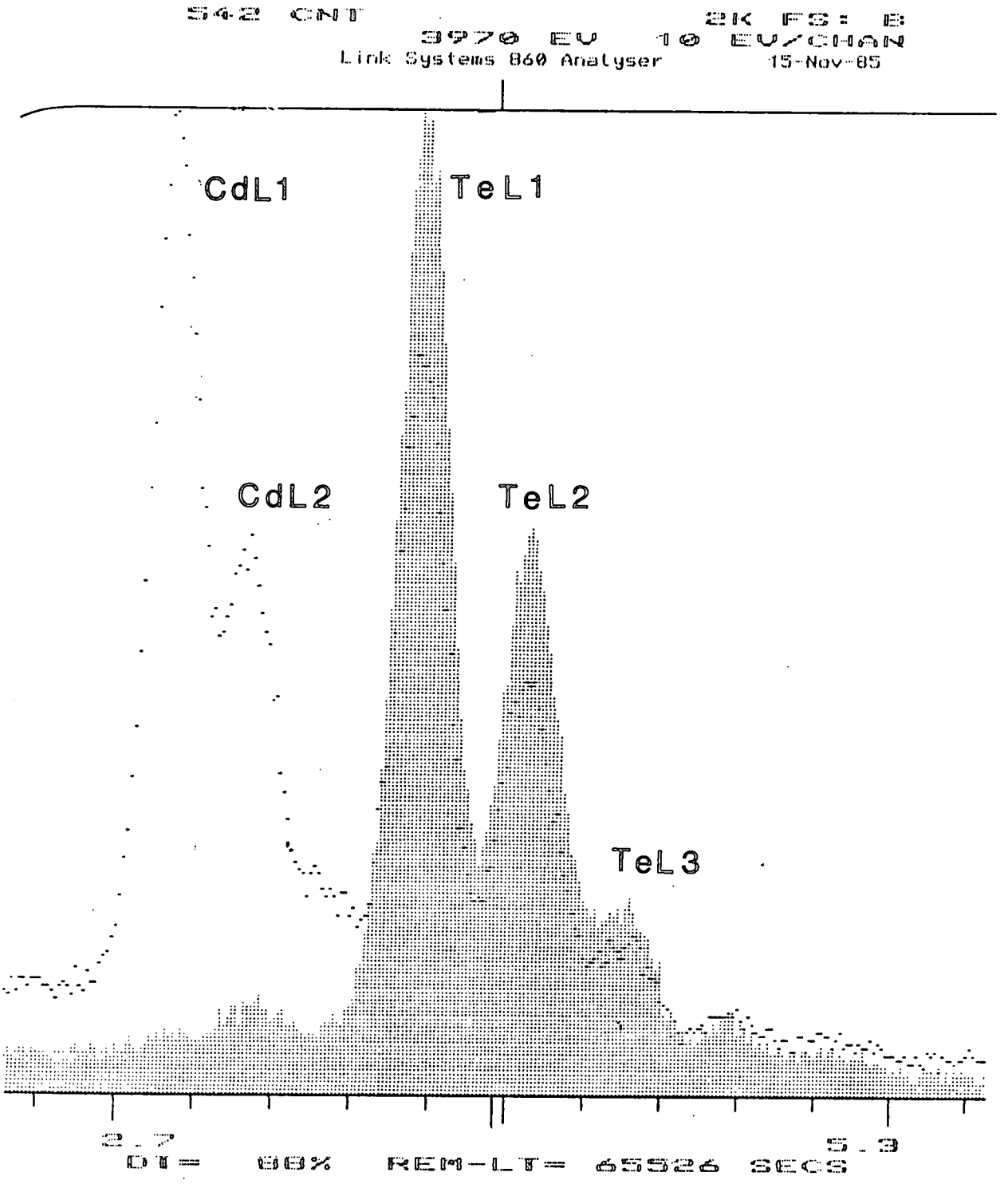

Figure 9.4 EDAX spectra accumulated from the precipitate in Figure 9.3 (shaded) and an adjacent region (open).

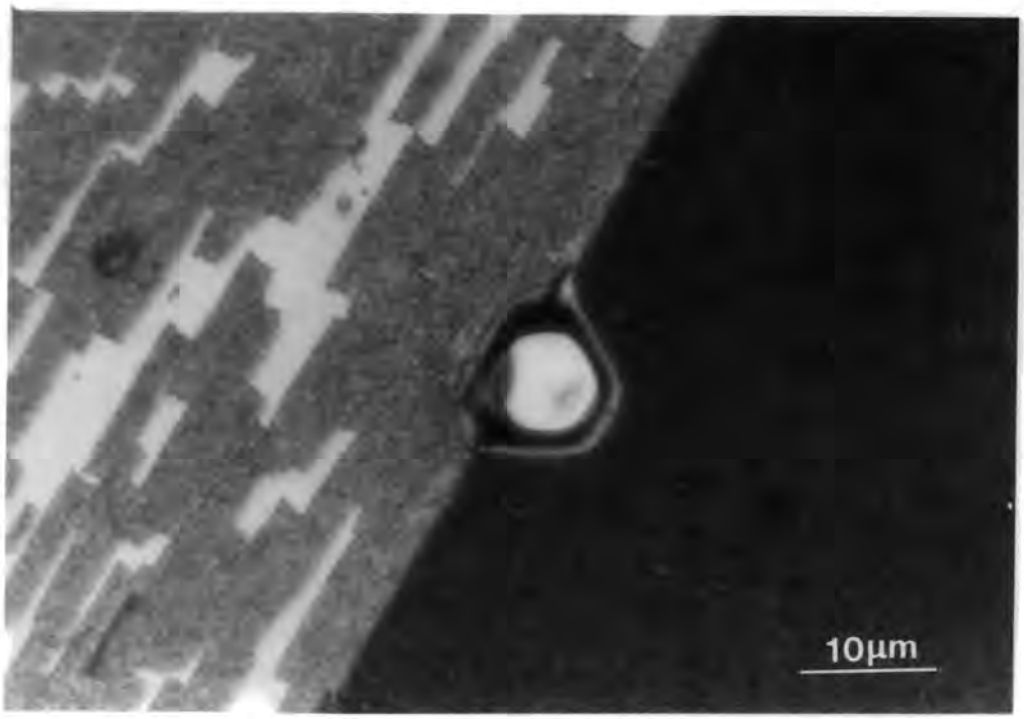

Figure 9.5 Photomicrograph of a Te precipitate on a first order twin boundary.

themselves are about 10 µm in width they are surrounded by much larger etch features after etching with Inoue's EAg-1 reagent.

Although precipitates were found within the bulk of this material they were more frequently seen to be associated with twin and grain boundaries within the crystal boules. Figure 9.5 shows a photomicrograph of a Te precipitate on a first order twin boundary after etching with Inoue's EAg-1 reagent. The precipitate itself is approximately 10 µm in diameter which is the average size of these features in this material. Te precipitation was more prolific at lateral twin boundaries than at first order twin boundaries. In fact these precipitates were clearly visible on all of the lateral boundaries in each of the photomicrographs of surfaces etched with the Nakagawa reagent [11] which are illustrated in Figures 6.13 a-d in Chapter 6. Figure 9.6 shows a surface which was also etched with the Nakagawa reagent

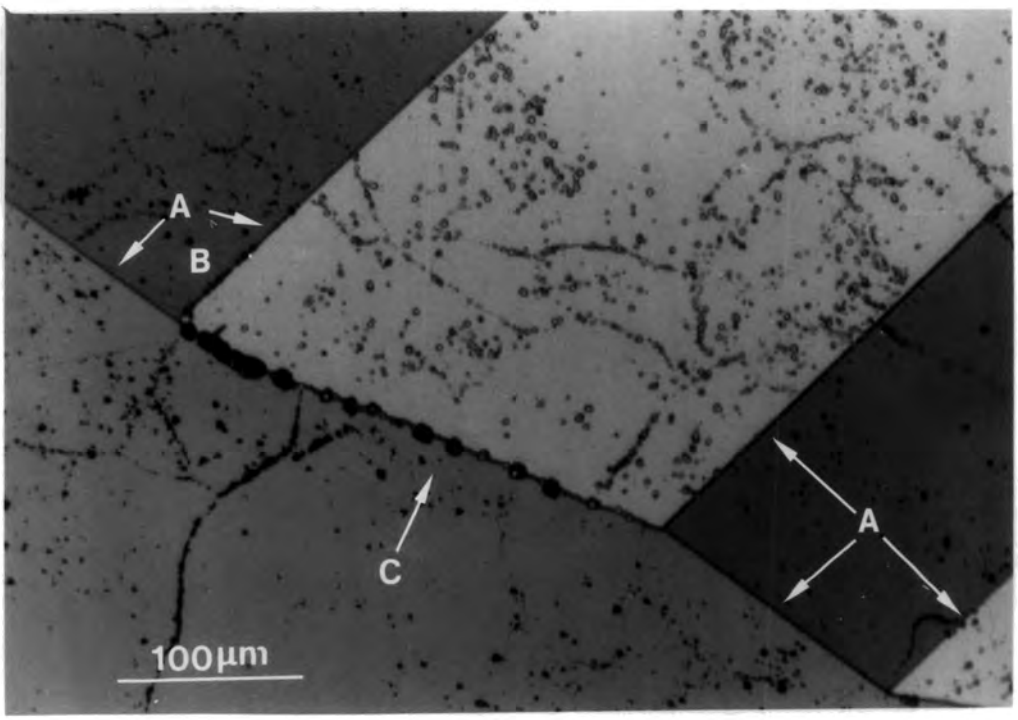

Figure 9.6 Preferential precipitation at a second order twin boundary etched with Nakagawa's reagent.

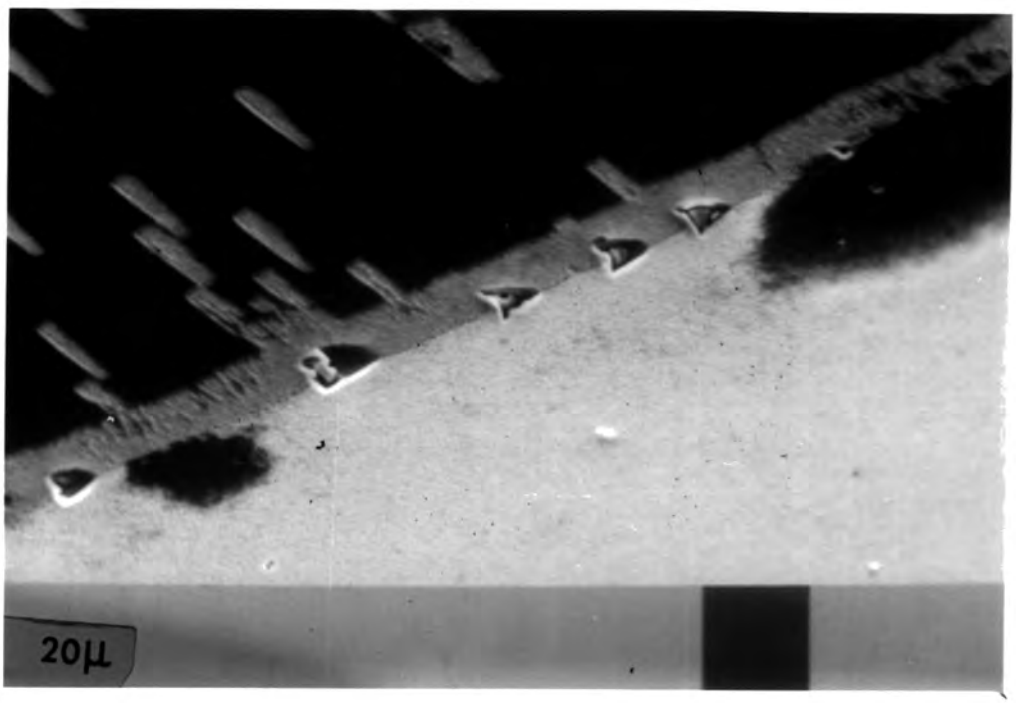

Figure 9.7 Precipitates on a second order twin boundary etched with Inoue's EAg-1 reagent.

and is intersected by a number of twin boundaries. It provides convincing evidence that precipitates accumulate preferentially at second order twin boundaries rather than at first order ones: the first order boundaries (labelled A) are largely free of precipitates (except at the region labelled B), whereas the second order boundary, labelled C, is heavily decorated along its whole length. The effect of Inoue's EAg-1 etch on a second order twin boundary which is decorated by precipitates is shown in Figure 9.7. An EDAX spectrum accumulated from one of the distinctive triangular precipitates in this micrograph was identical to that in Figure 9.4 which confirms that the precipitates are indeed comprised of Te. A high angle grain boundary found in one of the crystals is shown in Figure 9.8. The ½% bromine in methanol photoetch used on the surface

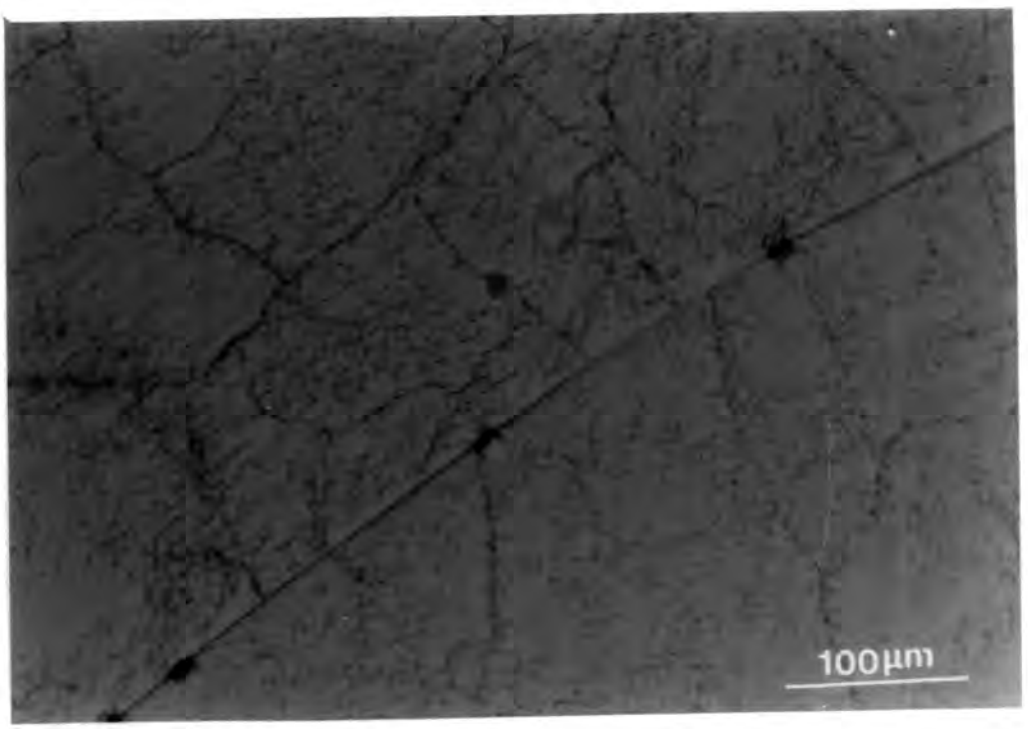

Figure 9.8 Precipitates at a random grain boundary.

shown in this photomicrograph has revealed both sub-grain boundaries and the long, curved high angle grain boundary which is decorated by several Te precipitates which are approximately 10 μm in width.

Thus for material grown by the 'Durham' technique it has been found that the preferential precipitation on boundaries in the crystals studied decreases according to the sequence:-

Random grain boundary	>	Second order twin boundary	>	Lateral twin boundary	>	First order twin boundary	>	Bulk CdTe

This sequence generally holds good, notwithstanding occasional local variations in the precipitate density.

The three etchants used in this study each have different effects upon Te precipitates: Whereas the ½% bromine in methanol photoetch [12] leaves them in tact, Nakagawa's reagent [11] dissolves them in preference to CdTe. The action of Inoue's EAg-1 reagent [10] is considerably more complex: the area immediately surrounding the precipitate shown in Figure 9.2 has been preferentially attacked by this reagent and is devoid of etch pits. Clearly in this case the presence of the precipitate has had a localised effect upon the behaviour of this etchant towards CdTe. However, the etchant has no similar effect upon the material surrounding those precipitates which lie on the first and second order twin boundaries shown in Figures 9.5 and 9.7.

§9.3 Precipitates in CdTe Grown by the Modified Piper-Polich Technique

Precipitation in crystals of CdTe grown using the modified Piper-Polich technique was investigated by transmission electron microscopy. A typical micrograph of precipitates in this material is shown in Figure 9.9. The precipitates themselves are imaged

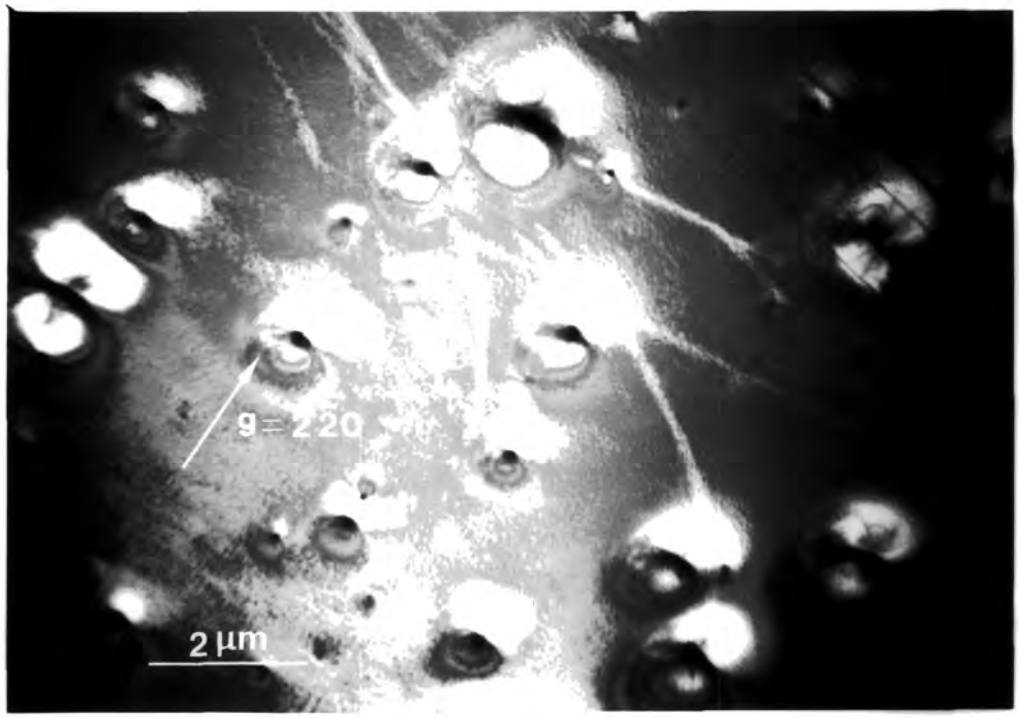

Figure 9.9 Strain associated precipitates in CdTe grown by the modified Piper-Polich method.

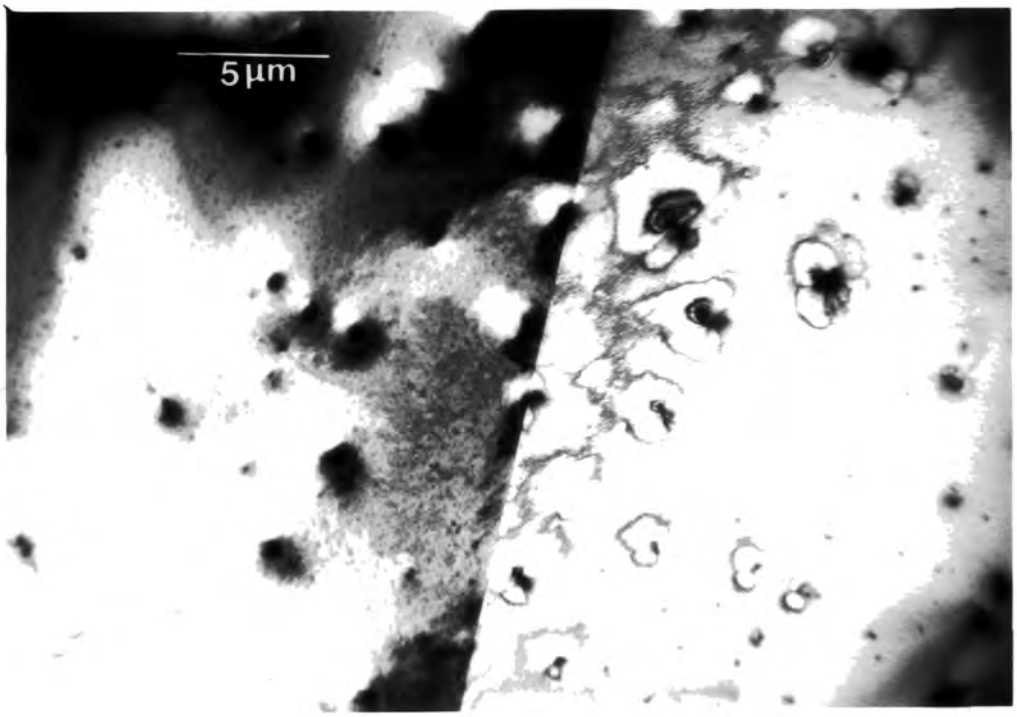

Figure 9.10 Precipitates in the vicinity of a first order twin boundary.

by absorption contrast as dark circular features approximately 0.1 to 0.5 μm in width. When imaged in a two beam condition in the electron microscope, the distinctive lobe-shaped contrast features present in Figure 9.9 became apparent. These typically consisted of a pair of black/white lobes which were separated by a 'line of no contrast' which is perpendicular to the diffracting vector, $g=2\bar{2}0$. These contrast effects closely resemble those which are associated with coherent spherical precipitates (see §3.3.6).

Precipitates in this material have been observed in the vicinity of a twin boundary and this is shown in the transmission electron micrograph in Figure 9.10. An important feature of this micrograph is that even though one or two precipitates are associated directly with the boundary, the majority do not appear to be influenced by its presence.

§9.4 Discussion

The most important finding of this Chapter is that the sizes and distributions of the precipitates in CdTe crystals grown by the 'Durham' and modified Piper-Polich methods differ considerably: precipitates in the former are approximately 10 μm in width and are to be found in relative abundance on crystal boundaries, while those in the latter are comparatively small (∿ 0.1 to 0.5μm in width) and are far less prone to association with other defects.

Thermodynamically it is expected that precipitates of a second phase within a solid material will, at equilibrium, become associated with other defects within that material such as dislocations, stacking faults and grain boundaries [13]. In systems in which precipitates become associated with crystal boundaries

the driving force for precipitation is the reduction of the free energy of the boundary resulting from its decoration with precipitates. Gleiter [14] found that the segregation of Cu at boundaries in Pb crystals was more enhanced at random than at coincidence boundaries. This implies that precipitation is more likely to be increasingly favoured at more disordered boundary structures since the free energy reduction is potentially the greatest at such boundaries. The free energy argument is able to explain qualitatively the extent to which precipitation occurs at various types of boundary in these crystals. From the sequence of precipitation densities in boundaries given in the previous section it is evident that precipitation is less favoured at twin boundaries than at random boundaries and this is in accordance with Gleiter's work on metallic systems [14]. Furthermore it is apparent that precipitation occurs preferentially at some coincidence boundaries rather than at others. For example, first order lateral twin boundaries are more disordered than are first order coherent twin interfaces and they undoubtedly have higher boundary energies. This is apparent from the coincidence site lattice models presented in Chapter 7. The free energy reduction associated with precipitation at lateral twin boundaries is therefore potentially greater than that for precipitation at first order boundaries. Preferential precipitation at lateral twin boundaries is therefore an indication of an equilibriated distribution of precipitates.

In contrast, transmission electron microscopy has shown that the small precipitates present in CdTe grown by the modified Piper-Polich technique do not show any marked tendancy to become associated with first order twin boundaries. If the sequence

of preferential precipitation densities found in CdTe crystals grown by the 'Durham' method is examined (see §9.2) then this observation is to be expected since, other than for the bulk material, first order twin boundaries have the lowest precipitate density. Nevertheless, the failure of the precipitates to become associated with the first order twin boundary in Figure 9.10, in spite of their close proximity to that twin boundary, is indicative of a considerable departure from the distribution of precipitates expected at equilibrium.

The different growth conditions employed in the 'Durham' and modified Piper-Polich techniques provide a reliable explanation for the differences in the precipitation effects encountered in the two types of material. In the 'Durham' method the crystal growth takes place over a period of 3-4 days and when growth is complete the crystals are cooled to room temperature in a controlled manner over a period of several days. Using the modified Piper-Polich technique both the growth and the post-growth cooling of the crystals each take place in approximately 24 hours. Clearly the crystals grown by the 'Durham' technique are maintained at high temperatures for longer periods of time than those grown by the modified Piper-Polich method. The absence of what is effectively an annealing stage during growth using the latter technique ensures that precipitates do not attain an equilibrium distribution within the crystals. The small precipitates which are nucleated within the bulk of the crystals during cooling are only likely to be mobile for a relatively short period of time. Consequently they are unable to become associated either with one another to form larger precipitates, or with other defects

such as twin boundaries, as was encountered in the 'Durham' material.

It is interesting to note that the behaviour of precipitates in the two materials parallels that of sub-grain boundaries in these materials which was described in the previous Chapter. Sub-grain boundaries in the 'Durham' material were found to be well-formed and associated with other defects whereas those in material grown by the modified Piper-Polich technique did not adopt the configuration expected at equilibrium. This comparison adds weight to the argument that the defect content of the two types of material is substantially affected by the growth conditions employed.

§9.5 Conclusions

The effects that three particular etching solutions have on 'Durham' grown crystals containing Te precipitates have been investigated. A photoetch consisting of ½% solution of bromine in methanol [12] dissolves the Te precipitates more slowly than it does bulk CdTe whereas the reverse is true for Nakagawa's etchant [11]. The effect of Inoue's EAg-1 reagent [10] is more complex: the regions in the immediate surroundings of the precipitates in the bulk of a CdTe crystal are etched in a way that is uncharacteristic of the action of this etchant on a precipitate-free region having the same orientation. This effect is not observed if the precipitates are present on crystal boundaries.

The significant differences observed in the forms and distributions of Te precipitates in CdTe crystals grown by the 'Durham' and modified Piper-Polich vapour phase techniques are a direct consequence of the differences in the growth conditions in the

two techniques. Crystals grown using the 'Durham' technique are kept at the growth temperature for an extended period of time during growth. The Te precipitates which form as a result of nonstoichiometry and the retrograde solid solubility of Te in CdTe are approximately 10 μm in width and are largely associated with crystal boundaries.

Notwithstanding the local variations which inevitably occur throughout a given boule, the preferential precipitation at crystal boundaries decreases according to the sequence:-

Random grain boundary	>	Second order twin boundary	>	Lateral twin boundary	>	First order twin boundary	>	Bulk CdTe

Preferential precipitation at interfaces is expected at thermodynamic equilibrium and, moreover the degree to which it occurs on a given boundary is representative of the free energy of that boundary. In this way high energy boundaries attract a greater density of precipitates than low energy ones.

The considerably shorter period taken to grow a crystal by the modified Piper-Polich technique ensures that Te precipitates do not achieve an equilibrium distribution. Consequently the precipitates in this material are small ($\sim$ 0.1 to 0.5 μm in diameter), coherent with the lattice, and do not become associated with coherent twin boundaries, even though they have been observed in close proximity to them.

The equilibrium and non-equilibrium distributions of precipitates in crystals grown by the 'Durham' and modified Piper-Polich materials respectively is analagous to the equilibrium and non-equilibrium arrangements of dislocations in sub-grain boundaries observed in these materials (see Chapter 8). This comparison indicates

that the differences between the defect content of the two materials can be adequately explained by considering the differences between the two growth techniques.

REFERENCES FOR CHAPTER NINE

1 G.H. Narayanan and S.H. Rustomji, J. Electrochem.Soc., 126 (1979) p.809.

2 K. Zanio, J. Electronic Materials, 3 (1974) p.327.

3 A.W. Vere, V.Steward, C.A.Jones, D.J. Williams and N.Shaw, J. Crystal Growth, 72 (1985) p.97.

4 K. Durose, G.J.Russell and J. Woods, Inst.Phys.Conf.Ser. No.76 Section 6, (1985) p.233.

5 J.B. Mullin and B.W. Straughan, Revue de Physique Appliquee, Tome 12 (2) (1977) p.105.

6 R.J.Dinger and I.L.Fowler, ibid, p.135.

7 S.Brelant, M.Elliott and G.Entine, ibid, p.141.

8 K.Zanio in Semiconductors and Semimetals Vol.13 'Cadmium Telluride'. Academic Press, New York 1978 Eds. R.K.Willardson and A.C.Beer, p.126.

9 R.G.Rhodes, International Series of Monographs on Semiconductors Vol.6 'Imperfections and Active Centres in Semiconductors'. Pergamon Press 1964 Ed. H.K.Henisch, p.214.

10 M. Inoue, I. Teramoto and S.Takayanagi, J.Appl.Phys.,33 (1962) p.2578.

11 K.Nakagawa, K.Maeda and S.Takeuchi, Appl.Phys.Lett., 34 (1979) p.574.

12 D.J.Williams, private communication.

13 L.E.Murr, 'Interfacial Phenomena in Metals and Alloys', Addison-Wesley, Reading, Massechusetts. (1975) p.240.

14 H.Gleiter, Acta Metallurgica,18 (1970) p.117.

CHAPTER TEN

CONCLUSIONS AND FURTHER WORK

§10.1 Summary of Conclusions

Large single-grained crystals of CdTe up to 29 mm in diameter and weighing up to 160 g have been grown successfully in this laboratory using the 'Durham' vapour phase technique (see [1,2] and §2.2.2). Twinning occurs frequently in these crystals [3,4] and the presence of these defects can reduce the value of boules which are to be used as substrate material for epitaxy. In large-grained boules the twins constitute lamellae which range in width from several microns to several millimeters. Polycrystalline boules were found to be more prone to twinning and generally contained a number of different types of twin boundaries (see §6.2). The twins in this material have been characterised in some detail in Chapter 6. A simple etching experiment (see § 6.3.2) was used to establish that first order twins in this material are related to the host crystal's orientation by rotation of $\Theta = 250^{\circ}\ 32'$ about a <110> axis. This implies that first order twin boundaries lying on {111} planes in this material are of the low energy 'ortho-type' rather than of the high energy, electrically active 'para-type' which contain a high density of Cd-Cd or Te-Te wrong bonds [4,5]. Four types of lateral twin boundary, that is first order boundaries which lie on planes other than {111}, have been characterised by examining their intersections with etched surfaces. These boundaries lie on planes of the forms {511}-{111}, {112}-{112}, {001}-{221} and {110}-{114} when indexed with respect to both the twin and the matrix orientations (see § 6.4 and §7.3.2).

Three types of second order twin boundary lying on planes of the forms {111}-{115}, {114}-{114} and {221}-{221} were also observed in the as-grown crystals (see §6.5 and §7.4.1). Twin lamellae were frequently seen to interact with one another. For example, in heavily twinned grains the twin lamellae were often seen to cross one another and sometimes twins were observed which acted as hosts to other twin lamellae (see §6.7).

Consideration of these types of twin structures indicates the likely origin of the twins in this material: whereas a growth accident model cannot explain the formation of complex arrangements of twins (see § 6.6) a deformation model in which twins form by the passage of a/6 <211> dislocations over successive close packed planes in the crystal can account for the presence of these structures with ease (see §6.7). The fact that transmission electron microscopy revealed the presence of dislocations on the interfacial planes of first order twins (see §6.3.4) would appear to confirm that twins in this material form as a result of deformation processes suffered during or after growth.

Coincidence site lattice models of first order lateral and second order twin boundaries in the sphalerite structure were developed in Chapter 7. These proved to be useful in characterising the twin boundaries observed in the as-grown crystals. Models of first order twin boundaries in the sphalerite structure were constructed using a <110> projection of a $\Sigma = 3$ coincidence lattice which is characterised by the tilt angle for 'ortho'-twinning which is $\theta = 250^{\circ}32'$ (see §7.3.2 and Figure 7.1). Four unrelaxed coincidence site boundaries were constructed on this lattice using four different boundary segments according to the rules specified by Kohn [6] (see §7.2.1). The model

predicts that stable lateral twin boundaries should lie on planes of the form {115}-{111}, {112}-{112}, {001}-{221} and {110}-{114}. Indeed, only lateral twin boundaries of these specific types were observed in practice. The unrelaxed models of these four boundaries presented in Figures 7.2 - 7.5 all contain atomic sites which differ from the usual tetrahedrally coordinated sites which are present in the sphalerite structure. For example, in each 'period' of each of the four boundaries there is one wrong bond (that is a Te-Te or Cd-Cd bond), and two abnormally coordinated atoms, one of these having three and the other five nearest neighbours. Clearly structures such as these are likely to undergo some form of relaxation in a real crystal in order to reduce the interfacial energies of the boundaries. An alternative configuration for the {112}-{112} boundary in the sphalerite structure which is based on the relaxed boundary model in the diamond lattice proposed by Vlachavas and Pond [7] was discussed in §7.3.3. The model of this boundary (see Figure 7.7) incorporates a rigid body shift of the twin with respect to the matrix which eliminates the presence of atoms at the boundary which have abnormal coordination numbers. However, the relaxed boundary contains twice the density of electrically active wrong bonds that is present in the unrelaxed boundary. For this reason it is expected that this particular boundary relaxation will not decrease the interfacial energy of this boundary in the sphalerite structure.

The presence of Te-Te or Cd-Cd wrong bonds in all of the models of lateral twin boundaries studied indicates that these defects are likely to be present in real boundaries in the sphalerite structure, making them electrically active. Indeed, the strong EBIC contrast observed at such boundaries (see §6.3.2) confirms this. The contrast

observed at first order 'ortho'-twin boundaries, which are expected to be electrically inactive, was weaker than that at lateral ones and was also discontinuous. It is considered that this electrical activity was not due to any native state of the boundaries themselves, but rather to defects which are associated with them, such as the interfacial dislocations described in §6.3.4.

Unrelaxed coincidence site lattice models of second order twin boundaries in the sphalerite structure were constructed using a <110> projection of a $\Sigma = 9$ coincidence site lattice which is characterised by a tilt angle of $\Theta = 218^{o}57'$ (see §7.4.1 and Figure 7.8). Three different boundary types, shown in Figures 7.9-7.11 were constructed and these lie on the planes of the form {111}-{115}, {114}-{114}and {221}-{221}. All three of these boundaries contain either Te-Te or Cd-Cd wrong bonds and hence it is likely that second order twin boundaries in the sphalerite structure will be electrically active. One of the boundaries, that which lies on {221}-{221}, is unique in that it does not contain any atoms which have abnormal coordination numbers, whereas the other two boundaries both contain three and five coordinated atoms. The absence of wrong bonds in the {221}-{221} boundary may make it an energetically favourable structure with respect to the other two boundaries.

Although coincidence site lattice models cannot be used to predict the precise details of the atomic arrangements which are actually present at twin boundaries, the models are highly successful in that they accurately predict the interfacial planes of these boundaries. The four lateral and three second order boundary types predicted by these models were all observed experimentally in the as-grown crystals and, moreover, no additional boundary types were found.

The etching studies presented in §8.2.1.1 have shown that the dislocations in CdTe grown by the 'Durham' technique are arranged in a cellular network of sub-grain boundaries, the average sub-grain size being ≃150 μm. Transmission electron microscopy has shown that the dislocations within each individual sub-grain boundary predominantly have the same Burgers vector and that the misorientation between adjacent sub-grains can be as large as 0.3^{o} (see §8.2.1.2). EBIC imaging in the SEM has shown that the sub-grain boundaries are electrically active. However, since the EBIC contrast at these boundaries is spotty it is thought that the electrical activity is not due to the native states of the dislocations themselves, but rather it is likely/to be related to impurity decoration [8]. The observation of slip-traces and elongated sub-grains in this material (see §8.2.1.1) suggests that the sub-grains formed as a result of the polygonisation of dislocations which were introduced into the crystals at some stage during growth. Since the sub-grain boundaries are mostly of the 'one dislocation' type and are frequently observed to be associated with other defects in these crystals (see § 8.2.1.1), it is evident that both the polygonisation and subsequent reorganisation of dislocations in this material are well-advanced processes. This is due to the fact that the crystals are held at high temperatures for extended periods of time during and immediately following growth by the 'Durham' method (see §8.2.3 and §2.2.2).

Dislocations have also been examined using transmission electron microscopy in crystals grown by the modified Piper-Polich technique which is described in § 2.2.3. This material contains open networks of dislocations having a variety of different Burgers vectors which are quite unlike the 'one dislocation' arrays encountered in CdTe

grown by the 'Durham' technique. Dislocation networks of this type (as opposed to the well-formed dislocation arrays observed in 'Durham'-grown CdTe) are expected, since growth by the modified Piper-Polich technique occurs in a much shorter time than is the case for growth by the 'Durham' technique. Crystals grown by the modified Piper-Polich technique are not held at high temperatures for sufficiently long periods of time to enable the grown-in dislocations to achieve the low-energy configurations observed in 'Durham'-grown material. Nevertheless, the open networks of dislocations are favourable since the misorientations between adjacent sub-grains is small. However, the poor grain sizes which are characteristic of CdTe crystals grown by the modified Piper-Polich technique make these crystals unsuitable for use as substrates for epitaxy.

A number of crystals of $Cd_{0.95}Zn_{0.05}Te$ have been grown by the 'Durham' method and etching and TEM studies have shown that this material contains sub-grains whose average size is also about 150 μm (see §8.3.1). However, the dislocations within the boundaries are arranged in networks (§ 8.3.2) which, although they are not nearly so open as those observed in CdTe grown by the modified Piper-Polich technique, are nevertheless considerably more disordered than those in 'Durham' grown CdTe. The misorientations between adjacent sub-grains in this material are therefore correspondingly reduced which implies that the observation of dislocation networks in $Cd_{0.95}Zn_{0.05}Te$ is consistent with the comparatively narrow X-ray rocking curves reported for this material by Bell and Sen [9]. The addition of 5 atomic % ZnTe to CdTe is thought to inhibit the formation of sub-grains by reducing both the density of grown-in dislocations in the ternary and their mobility during annealing (see §8.3.3).

The presence of Te precipitates in CdTe crystals which have been grown by a number of techniques is widely reported in the literature and is known to occur as a result of the strong retrograde solid solubility of this element in CdTe [10] (see § 9.1). Precipitates which have been identified as being comprised of Te are present in 'Durham'-grown CdTe and are readily observed both in the bulk material and in association with twin and grain boundaries (see § 9.2). The average size of precipitates in this material is ∿10 μm and the preferential precipitation at boundaries has been observed to decrease according to the sequence:-

Random grain boundary	> Second order twin boundary	> First order lateral twin boundary	> First order coherent twin boundary	> Bulk CdTe

Precipitates are expected to become associated with crystal boundaries at thermodynamic equilibrium since the decoration of interfaces reduces the free energies of those interfaces. Furthermore, since the free energy reduction associated with precipitate decoration will be greatest for the higher energy boundaries, the sequence of precipitate densities observed above, in which the higher energy boundaries are more heavily decorated than the lower energy ones, is expected [11].

The precipitates present in CdTe grown by the modified Piper-Polich technique are much smaller than those in 'Durham'-grown CdTe (∿0.1 to 0.5 μm in width) and are associated with coherency strains (see §9.3). An important observation is that these precipitates are not especially associated with first order coherent twin boundaries. Both the small size of these precipitates and their failure to become associated with twin boundaries indicates that the distribution of

precipitates in this material represents a significant departure from equilibrium. The differences in precipitate size and distribution in CdTe grown by the two methods may be directly attributed to the differences in the two growth techniques. Since the cooling of crystals grown by the 'Durham' method from the growth temperature is slow, precipitation is well advanced and the precipitates are able to reach an equilibriated distribution. This is not the case for crystal growth by the modified Piper-Polich technique which employs a relatively rapid cooling stage.

The use of CdTe as a substrate material for epitaxy demands that simple methods of polishing CdTe slices and of identifying the polarity of crystal faces should be available. During the course of this work a mechanochemical pad polishing machine which employs a bromine-methanol based chemical polish has been developed (see §5.2.3.3). This apparatus has been used to prepare pristine, optically flat surfaces, both rapidly and easily. It has been demonstrated that the crystallographic polarity of {111} surfaces of CdTe can be established by chemical etching with either Nakagawa's etch [12], Inoue's EAg-1 reagent [13], or with a previously unrecorded etchant which consists of equal volumes of HF, HNO_3 and CH_3COOH (see §5.3.3). The actions of these etchants on {111} surfaces of CdTe are summarised in Table 10.1, the information therein being consistent with the definition of crystallographic polarity given by Fewster and Whiffin [14] who used the Nakagawa reagent [12].

Table 10.1 The Effects of Etching Solutions on the {111} Polar Surfaces of CdTe

Etchant	Cd (111)	Te ($\bar{1}\bar{1}\bar{1}$)
Nakagawa [12] (see Fewster and Whiffin [14]).	High density of rounded pits and Te film.	Low density of rounded pits and Te film.
Inoue EAg-1 (see Durose [4] and Lu et al [15]).	Small pyrimidal triangular pits.	Large flat bottomed triangular pits.
$HF/HNO_3/CH_3COOH$ (This work).	Black film.	Shiny, polished surface.

The shapes of etch pits produced on polished CdTe surfaces by Inoue's EAg-1 reagent are discussed in detail in § 5.4.4. Although all three of the etchants listed in Table 10.1 may be used to determine crystallographic polarity, the most convenient reagent is $HF/HNO_3/CH_3COOH$. This etchant produces a distinctive film on the Cd (111) surface of CdTe which can be seen without the aid of a microscope. Furthermore, since this reagent has a very high etch rate, chemical polishing prior to its use is unnecessary. The use of a $\frac{1}{2}$% solution of bromine in methanol as a photoetch which is capable of revealing crystal defects such as twin and sub-grain boundaries on CdTe surfaces having all orientations has also been demonstrated.

§10.2 Further Work

The work described in this thesis points towards a range of topics which are suitable for further study. For example, little

is known about the relationship between the etch pits produced by Inoue's EAg reagents [13] and specific crystal defects. Although this etchant has been the subject of a number of papers there is no work which fully explains the factors which affect the incidence of the etch pits which are produced by it. Unfortunately a well-characterised etchant which is capable of revealing individual dislocations on all surface orientations of CdTe is not currently available.

While the work presented in this thesis has provided a sound understanding of the defects in CdTe bulk crystals grown by two different techniques, there has not been adequate time to make use of the knowledge gained to modify the present techniques so as to eliminate, or else reduce the incidence of the defects. This would require further analysis of the effects that the variations in the growth process and post-growth treatments have on the defects present.

The most important study which leads on from the work in this thesis is the assessment of the structural quality of the CdTe-related epitaxial systems which are being grown in this laboratory. To this end cross sections of epitaxial systems are currently being investigated by transmission electron microscopy in Durham.

REFERENCES FOR CHAPTER TEN

1 G.J.Russell, N.F.Thompson and J.Woods, J.Crystal Growth, 71 (1985) p.621.

2 K.Durose, G.J.Russell and J.Woods, J.Crystal Growth, 72 (1985) p.85.

3 A.W.Vere, S.Cole and D.J.Williams, J.Electronic Materials, 12 (3) (1983) p.551.

4 K.Durose, G.J.Russell and J.Woods, Inst.Phys.Conf.Ser.No 76: Section 6 (1985) p.233.

5 D.B.Holt, J.Phys.Chem.Solids, 25 (1964) p.1385.

6 J.A.Kohn, Am.Min., 43 (1958) p.263.

7 D.S.Vlachavas and R.C.Pond, Inst.Phys.Conf.Ser.No 60 (1981) p.159.

8 D.J.Williams and A.W.Vere, In press in J.Crystal Growth.

9 S.L. Bell and S.Sen, J.Vac.Sci.Technol. A3 (1) (1985) p.112.

10 K.Zanio in Semiconductors and Semimetals Vol.13. 'Cadmium Telluride'. Academic Press, New York, 1978, Eds. R.K.Willardson and A.C.Beer, p.6.

11 H.Gleiter, Acta metallurgica, 18 (1970) p.117.

12 K.Nakagawa, K.Maeda and S.Takeuchi, Appl.Phys.Lett., 34 (9) (1979) p.574.

13 M. Inoue, I.Teramoto and S.Takayanagi, J.Appl.Phys.33(8) (1962) p.2578.

14 P.F.Fewster and P.A.C.Whiffin, J.Appl.Phys, 54 (1983) p.4668.

15 Y-C Lu, R.K.Route, D.Elwell and R.S.Feigelson, J.Vac.Sci. Technol., A3(1) (1985) p.264.